

Analysis and Optimization of Single-Pad and Multi-Pad Air Foil Thrust Bearings

Zur Erlangung des akademischen Grades Doktor-Ingenieur (Dr.-Ing.)
Genehmigte Dissertation von Markus Eickhoff aus Leer (Ostfriesland)
Tag der Einreichung: 30. April 2024, Tag der Prüfung: 17. Juli 2024

1. Gutachten: Prof. Dr.-Ing. Bernhard Schweizer
2. Gutachten: Prof. Dr.-Ing. Wilfried Becker
Darmstadt – D 17



TECHNISCHE
UNIVERSITÄT
DARMSTADT

MASCHINENBAU
We engineer future



Analysis and Optimization of Single-Pad and Multi-Pad Air Foil Thrust Bearings

Genehmigte Dissertation von Markus Eickhoff

Tag der Einreichung: 30. April 2024

Tag der Prüfung: 17. Juli 2024

Darmstadt, Technische Universität Darmstadt

Bitte zitieren Sie dieses Dokument als:

URN: urn:nbn:de:tuda-tuprints-277894

URL: <https://tuprints.ulb.tu-darmstadt.de/id/eprint/27789>

Jahr der Veröffentlichung auf TUpriints: 2024

Dieses Dokument wird bereitgestellt von tuprints,

E-Publishing-Service der TU Darmstadt

<https://tuprints.ulb.tu-darmstadt.de>

tuprints@ulb.tu-darmstadt.de

This work is protected by copyright

<https://rightsstatements.org/page/InC/1.0/>

Erklärungen laut Promotionsordnung

§8 Abs. 1 lit. c PromO

Ich versichere hiermit, dass die elektronische Version meiner Dissertation mit der schriftlichen Version übereinstimmt.

§8 Abs. 1 lit. d PromO

Ich versichere hiermit, dass zu einem vorherigen Zeitpunkt noch keine Promotion versucht wurde. In diesem Fall sind nähere Angaben über Zeitpunkt, Hochschule, Dissertationsthema und Ergebnis dieses Versuchs mitzuteilen.

§9 Abs. 1 PromO

Ich versichere hiermit, dass die vorliegende Dissertation selbstständig und nur unter Verwendung der angegebenen Quellen verfasst wurde.

§9 Abs. 2 PromO

Die Arbeit hat bisher noch nicht zu Prüfungszwecken gedient.

Darmstadt, 30. April 2024

M. Eickhoff

Preface

This thesis presents a synopsis of the following publications in peer-reviewed journals. These publications are based on the work which has been accomplished during my employment as a research assistant at the Institute of Applied Dynamics at the Technical University of Darmstadt. Note that a change of name from Rieken to Eickhoff took place in 2021.

1. Markus Rieken, Marcel Mahner und Bernhard Schweizer. „Thermal optimization of air foil thrust bearings using different foil materials“. In: *Journal of Turbomachinery* 142.10 (2020), S. 101003 [1]
2. Markus Eickhoff, Andre Theile, Michael Mayer und Bernhard Schweizer. „Analysis of Air Foil Thrust Bearings with annular top foil including wear prediction, Part I: Modeling and simulation“. In: *Tribology International* 181 (2023), S. 108174 [2]
3. Markus Eickhoff, Johannis Triebwasser und Bernhard Schweizer. „Thermo-elasto-hydrodynamic analysis of bump-type air foil thrust bearings considering misalignment“. In: *Bulletin of the Polish Academy of Sciences. Technical Sciences* 71.6 (2023) [3]
4. Markus Eickhoff, Johannis Triebwasser, Andre Theile und Bernhard Schweizer. „Compensating thermal bending of the runner disk in hydrodynamic thrust bearings: Simple approach for passively improving the performance of gas bearings“. In: *Tribology International* (2024), S. 109632 [4]

A complete list of publications to which the author has contributed is found at the beginning of the main document.

Kurzfassung

Folienluftlager sind ein Maschinenelement aus der Kategorie nachgiebiger hydrodynamischer Lager, die ein zuverlässiges, wartungsarmes und umweltfreundliches Lagerelement für den Einsatz in Turbomaschinen darstellen. Aufgrund der Verwendung von Umgebungsluft oder anderen Gasen als Schmiermittel können sie in ölfreien Maschinen eingesetzt werden. Im Vergleich zu starren Luftlagern stellen sie eine kostengünstige und robuste Alternative dar. Die Analyse und Optimierung von axialen Folienluftlagern ist aufgrund der Kombination thermodynamischer, elastomechanischer und hydrodynamischer Gleichungen sowie ihrer Kopplung in detaillierten numerischen Modellen herausfordernd.

In dieser Arbeit werden axiale Folienluftlager untersucht, die grundsätzlich aus einer Grundplatte, gewellten Bump Foils und glatten Top Foils bestehen. Sie können in zwei verschiedene Design-Typen eingeteilt werden: erstens ein Mehrfolien-Design bestehend aus mehreren unabhängigen Lagersegmenten und zweitens ein Einfolien-Design, bestehend aus mehreren unabhängigen Bump Foils, aber einer einzigen zusammenhängenden, ringförmigen Top Foil. Die Unterschiede in den Modellierungsansätzen werden dargelegt. Es zeigt sich, dass die Analyse von axialen Folienluftlagern des Einfolien-Designs nur möglich ist, wenn die reale Foliengeometrie und der Verschleiß der Beschichtung des Top Foils in die Analyse einbezogen werden.

Darüber hinaus wird ein vollständiges Lagermodell, das jedes einzelne Segment des Mehrfolien-Designs im Falle von Schiefstellung von Welle und Lager berücksichtigt, mit einem reduzierten Ansatz unter Verwendung von Symmetriebedingungen und Betrachtung eines einzelnen Segmentes verglichen.

Das Temperatur-Management von axialen Folienluftlagern erweist sich als ein zentraler Punkt für die Optimierung von Tragfähigkeit und Verlusten. Der Einfluss der thermischen Biegung der Wellenscheibe, die durch axiale Temperaturgradienten verursacht wird, ist signifikant für die Lagerleistung. Die am weitesten verbreitete Methode zur Verringerung dieses Effekts ist die Einleitung eines Luftstroms unterhalb der Top Foil. Dies reduziert jedoch die Gesamteffizienz der Maschine. Neben dieser direkten Methode werden in dieser Arbeit die Wahl eines alternativen Folienmaterials mit hoher Wärmeleitfähigkeit und Kompensationsmechanismen basierend auf Zentrifugaleffekten vorgestellt.

Abstract

Air foil bearings are a type of compliant hydrodynamic bearing that feature a reliable, low-maintenance, and ecological machine element for high-speed turbomachinery. Due to the utilization of surrounding air or other gases as a lubricant, they can be used in oil-free machines. When compared against rigid air bearings, they present a low-cost and robust alternative. The analysis and optimization of air foil thrust bearings is challenging owing to the multiphysicality of thermodynamic, elastomechanic and hydrodynamic equations that have to be considered as well as their coupling in detailed numerical models.

In this thesis, bump foil thrust bearings, consisting of a base plate, corrugated bump foils and smooth top foils are examined. They can be categorized in two different design types: firstly, a multi-foil design consisting of several independent bearing pads, and secondly, a single-foil design comprising several independent bump foils, but a single, annular top foil. The differences in the modeling approaches are illustrated. It is concluded that single-foil bearing analysis is only possible when the real foil geometry and top foil coating wear are included in the analysis.

Furthermore, a full bearing model accounting for each individual pad of the multi-foil design in the case of misalignment is compared against a reduced approach using symmetry conditions.

The thermal management of foil thrust bearings turns out to be one of the prime tasks for the optimization of load capacity and losses. The thermal bending of the runner disk that is caused by axial temperature gradients is shown to have a significant effect on bearing performance. The most prominent solution is the application of a forced cooling flow underneath the top foil. However, this reduces overall machine efficiency. Apart from this straightforward method, choosing an alternative foil material with a high thermal conductivity and compensating mechanisms based on centrifugal effects are presented here.

Acknowledgments

First and foremost, I would like to thank my supervisor Prof. Dr.-Ing. Bernhard Schweizer. You introduced me to the field of air foil bearing research and made this dissertation possible. In the course of my employment, your integrity and support allowed me to overcome challenges and focus on research for a great share of my time. Many exciting projects and collaborations enabled me to extend research results to real-world problems. I would also like to thank Prof. Dr.-Ing. Wilfried Becker for reviewing this dissertation. The fundamentals for elastostatics and the advanced theories are taught in your lectures which lay the foundation of the detailed models presented in this thesis.

I would like to thank my colleagues at the Institute of Applied Dynamics for fruitful discussions and conversations and the invaluable amount of collaboration and help during projects, experiments and numerical studies. Among this group of people, I want to highlight the impact of Pascal Zeise who endured me as an office mate and companioned me all the way for the past 6 years.

I would like to thank Prof. Markert for his introduction into rotordynamics as well as his ongoing support which initially introduced me to the Institute for my Bachelor's thesis. Furthermore, without the help of Helga Lorenz and Maria Rauck in administrative regards, I wouldn't have been able to finish this dissertation.

I would like to thank the entire staff of our workshop for their help with designing and manufacturing prototypes for our testing. Also, I would like to thank our industry partners for their cooperation in challenging projects.

Last but not least I would like to express my gratitude towards my family and especially my wife Insa for their never-ending and loving support.

Inhaltsverzeichnis

Preface	v
Kurzfassung	vii
Abstract	ix
Acknowledgments	xi
Contents	xiv
Abbildungsverzeichnis	xvi
Publications	xvii
Author's contributions	xix
Nomenclature	xxi
1 Introduction	1
1.1 Fundamentals of Air Foil Thrust Bearing Analysis	1
1.2 Objectives and Structure of the Thesis	9
1.2.1 Outline of Paper 1	9
1.2.2 Outline of Paper 2	11
1.2.3 Outline of Paper 3	16
1.2.4 Outline of Paper 4	17
2 Results	21
2.1 Optimization results for AFTBs	21
2.2 Analysis of single-foil bearings including wear prediction	26
2.3 Influence of misalignment on the bearing performance	30
3 Conclusions	37

Bibliography	46
Paper 1	47
Paper 2	57
Paper 3	81
Paper 4	93

Abbildungsverzeichnis

1.1	Foil thrust bearing structure consisting of a base plate as well as bump and top foils.	2
1.2	Cut view of a rotor disk and a single-sided thrust bearing.	2
1.3	Comparison of (a) multi-foil and (b) single-foil bearing design. Left side: bearing assembly with base plate, bump foils and top foil(s). Right side: exaggerated height profiles of the top foils, (a) taper-land and (b) taper-step.	3
1.4	Main heat flow paths in a foil thrust bearing assembly.	9
1.5	Pseudocode of the wear algorithm.	14
1.6	(a) Definition of rotor boundary sections I to VIII. (b) Result plot section of CFD calculation for heat transfer coefficient determination.	16
1.7	Definition of the two misalignment values α_{mis} and β_{mis} of Eq. (1.19).	17
1.8	Thermal bending of the rotor disk (exaggerated) directed away from the hot bearing side resulting from the supported thrust force.	19
1.9	Comparison of the optimized rotor disk design O (top half) including an asymmetric mass distribution as well as a combination of a recess and a rounding at the base of the disk vs. the standard symmetric design S (bottom half).	19
1.10	Different technical approaches for compensating thermal bending.	20
2.1	Maximum top foil temperature increase ΔT_T for different foil materials over the rotational speed.	22
2.2	Thermally induced axial deformation v_z of the rotor disk for foil materials A, B, and C.	23
2.3	Maximum top foil temperature increase ΔT_T for different foil materials over cooling heat transfer coefficient α_C at 120 krpm.	23
2.4	Rotor disk bending mechanisms.	25
2.5	(a) Rotor disk temperature and deformation for standard (S) and optimized (O) rotor disk configuration and (b) rotor disk deformation on the interface to the air film.	27

2.6	(a) Second optimized design O2, (b) thrust load improvement over the minimal gap height H_{\min} , and (c) performance map.	28
2.7	(a) Height profile after assembly without load, (b) height function $H^{(0)} = H$ for a rotational speed of 120 krpm and a minimal gap height $H_{\min} = 2 \mu\text{m}$, (c) corresponding top foil deformation v_3 under pressure load showing a kink at the first bump row as well as a cyclic deformation profile.	31
2.8	Wear simulation series showing the height function (left), the pressure distribution (center), and the wear function H_{wear} . Rotational speed is 120 krpm and minimal gap height is $H_{\min} = 2 \mu\text{m}$	32
2.9	Performance map of the single-foil thrust bearing for two rotational speeds: power loss in W over the thrust force in N.	33
2.10	Pressure distributions $p_i - p_0$ for misalignment angle $\alpha_{\text{mis}} = 3 \times 10^{-4}$ rad.	34
2.11	Thrust load over the misalignment angle α_{mis}	35

Publications

The following list contains all publications to which the author has contributed. The publications that are submitted for this dissertation are marked in green color.

- Markus Rieken. *Numerical Investigations of a Rotor in Journal Bearings with Adjustable Geometry*. Bachelor's thesis, Technical University of Darmstadt. 2014 [5]
- Bastian Pfau, Markus Rieken und Richard Markert. „Numerische Untersuchungen eines verstellbaren Gleitlagers zur Unterdrückung von Instabilitäten mittels Parameter-Antiresonanz“. In: *First IFToMM DA-CH Conference 2015: 11. März 2015, TU Dortmund* [6]
- Markus Rieken. *The Finite Element Method Integrated with Floquet Theory for a Column with Harmonic Axial Forcing*. Master's thesis, Technical University of Darmstadt. 2018 [7]
- Eoin Clerkin und Markus Rieken. „FEM with Floquet Theory for Non-slender Elastic Columns Subject to Harmonic Applied Axial Force Using 2D and 3D Solid Elements“. In: *IUTAM Symposium on Recent Advances in Moving Boundary Problems in Mechanics: Proceedings of the IUTAM Symposium on Moving Boundary Problems, Christchurch, New Zealand, February 12-15, 2018*. Springer. 2019, S. 267–282 [8]
- Markus Rieken, Marcel Mahner und Bernhard Schweizer. „Thermal optimization of air foil thrust bearings using different foil materials“. In: *Turbo Expo: Power for Land, Sea, and Air*. Bd. 58691. American Society of Mechanical Engineers. 2019, V07BT34A031 [9]
- Pascal Zeise, Marcel Mahner, Marcel Bauer, Markus Rieken und Bernhard Schweizer. „A Reduced Model for Air Foil Journal Bearings for Time-Efficient Run-Up Simulations“. In: *Turbo Expo: Power for Land, Sea, and Air*. Bd. 58691. American Society of Mechanical Engineers. 2019, V07BT34A004 [10]

-
- Markus Rieken, Marcel Mahner und Bernhard Schweizer. „Thermal optimization of air foil thrust bearings using different foil materials“. In: *Journal of Turbomachinery* 142.10 (2020), S. 101003 [1]
 - P Zeise, M Mahner, M Bauer, M Rieken und B Schweizer. „A reduced semi-analytical gas foil bearing model for transient run-up simulations“. In: *12th International Conference on Vibrations in Rotating Machinery*. CRC Press. 2020, S. 575–587 [11]
 - Bernhard Schweizer, Marcel Bauer, Marcel Mahner, Markus Rieken und Pascal Zeise. *Gaslager und ein Verfahren zu dessen Herstellung*. Patent DE50 2019 004 472.2, 2020 [12]
 - M Rieken, P Zeise, M Bauer und B Schweizer. „Multiphysical Finite Element Model for Air Foil Thrust Bearing Optimization“. In: *25th International Congress of Theoretical and Applied Mechanics*. IUTAM, 2021, S. 1627–1628 [13]
 - Bernhard Schweizer, Marcel Bauer, Pascal Zeise und Markus Rieken. *Axiales federblechfreies Foliengaslager*. Patent DE10 2020 132 177.5, 2022 [14]
 - Markus Eickhoff, Andre Theile, Michael Mayer und Bernhard Schweizer. „Analysis of Air Foil Thrust Bearings with annular top foil including wear prediction, Part I: Modeling and simulation“. In: *Tribology International* 181 (2023), S. 108174 [2]
 - Andre Theile, Markus Eickhoff, Felix Foerster und Bernhard Schweizer. „Analysis of air foil thrust bearings with annular top foil including wear prediction, Part II: Experimental investigations“. In: *Tribology International* 188 (2023), S. 108742 [15]
 - Markus Eickhoff, Johannis Triebwasser und Bernhard Schweizer. „Thermo-elasto-hydrodynamic analysis of bump-type air foil thrust bearings considering misalignment“. In: *Bulletin of the Polish Academy of Sciences. Technical Sciences* 71.6 (2023) [3]
 - Andre Theile, Markus Eickhoff und Johannis Triebwasser. *Rotor mit Rotorscheibe, Strömungsmaschine mit Rotor sowie Verfahren zum Betreiben einer Strömungsmaschine*. Patent DE10 2022 120 067.1, 2024 [16]
 - Markus Eickhoff, Johannis Triebwasser, Andre Theile und Bernhard Schweizer. „Compensating thermal bending of the runner disk in hydrodynamic thrust bearings: Simple approach for passively improving the performance of gas bearings“. In: *Tribology International* (2024), S. 109632 [4]

Author's contributions

Markus Rieken, Marcel Mahner und Bernhard Schweizer. „Thermal optimization of air foil thrust bearings using different foil materials“. In: *Journal of Turbomachinery* 142.10 (2020), S. 101003

	Markus Rieken	Marcel Mahner	Bernhard Schweizer
Conceptualization	90%	5%	5%
Data acquisition	100%		
Analysis and Interpretation	90%	5%	5%
Manuscript preparation	90%		10%
Corrections	85%	5%	10%

Markus Eickhoff, Andre Theile, Michael Mayer und Bernhard Schweizer. „Analysis of Air Foil Thrust Bearings with annular top foil including wear prediction, Part I: Modeling and simulation“. In: *Tribology International* 181 (2023), S. 108174

	Markus Eickhoff	Andre Theile	Michael Mayer	Bernhard Schweizer
Conceptualization	85%	5%	5%	5%
Data acquisition	80%	20%		
Analysis and Interpretation	80%	10%	5%	5%
Manuscript preparation	80%	15%		5%
Corrections	85%	5%	5%	5%

Markus Eickhoff, Johannes Triebwasser und Bernhard Schweizer. „Thermo-elasto-hydrodynamic analysis of bump-type air foil thrust bearings considering misalignment“. In: *Bulletin of the Polish Academy of Sciences. Technical Sciences* 71.6 (2023)

	Markus Eickhoff	Johannis Triebwasser	Bernhard Schweizer
Conceptualization	90%	5%	5%
Data acquisition	100%		
Analysis and Interpretation	90%	5%	5%
Manuscript preparation	90%		10%
Corrections	80%	10%	10%

Markus Eickhoff, Johannes Triebwasser, Andre Theile und Bernhard Schweizer. „Compensating thermal bending of the runner disk in hydrodynamic thrust bearings: Simple approach for passively improving the performance of gas bearings“. In: *Tribology International* (2024), S. 109632

	Markus Eickhoff	Johannis Triebwasser	Andre Theile	Bernhard Schweizer
Conceptualization	85%	5%	5%	5%
Data acquisition	80%	15%	5%	
Analysis and Interpretation	85%	5%	5%	5%
Manuscript preparation	90%			10%
Corrections	85%	5%	5%	5%

Nomenclature

Abbreviations

AFTB	Air foil thrust bearing
EP	Externally pressurized bearing
FE	Finite element
O	Optimized rotor disk design
O2	Second optimized rotor disk design
S	Standard symmetric rotor disk design
TEHD	Thermo-elasto-hydrodynamic

Operators

Δ	Laplace operator
∇	Nabla operator
min	Minimum operator
ramp	Ramp function for wear algorithm

Vectors

\vec{n}	Normal vector
\vec{n}_l	Normal vector of leading edge
\vec{n}_t	Normal vector of trailing edge

Indices

0	Ambient/reference condition
A	Air film
b	Base plate
B	Bump foil
D	Rotor disk
l	Leading edge
R	Rotor
t	Trailing edge
T	Top foil

Greek symbols

α_C	Heat transfer coefficient of forced cooling
α_{mis}	Misalignment angle
β_{mis}	Misalignment angle
γ_R	Lamé constant of rotor and disk
ΔT	Disk temperature difference for thermal bending
ΔT_R	Disk temperature difference
δ_{wear}	Wear height increment
ϵ_R	Thermal expansion parameter of rotor and disk
η	Air viscosity
η_{RG}	Air viscosity in radial gap
λ	Thermal conductivity of air
λ_{RG}	Thermal conductivity of air in radial gap
$\lambda_{C,eff}$	Effective thermal conductivity
λ_R	Thermal conductivity of rotor and disk material
μ_R	Shear modulus of rotor and disk
ν	Poisson's ratio of top and bump foil
ν_C	Kinematic viscosity of cooling flow
ν_{CT}	Turbulent kinematic viscosity of cooling flow
ρ	Air density
ρ_C	Cooling flow density
ρ_R	Density of the rotor and disk
Ω	Angular velocity of the rotor

Latin symbols

A_{sec}	Sector area
B	Bending stiffness
c_p	Isochoric heat capacity of air
$c_{P,C}$	Isochoric heat capacity of cooling flow
D	Stretching stiffness
E	Young's modulus of top and bump foil material
G	Shear modulus of the rotor and disk material
Gt	Shear stiffness of top and bump foil
H	Air film height
$H^{(i)}$	Air film height in the i -th wear iteration step
H_{coat}	Film height deviations due to top foil coating defects
H_{min}	Minimal air film height

H_{mis}	Misalignment in height function
h_{par}	Amplitude of parabolic shape deviation of top foil
H_{par}	Parabolic shape deviation function of top foil
$H_{\text{wear}}^{(i)}$	Wear function for the top foil coating in the i -th wear iteration step
i	Wear iteration counter
i_{end}	Total number of wear iterations
k_S	Shear correction factor
$m^{\alpha\beta}$	Moment tensor of shell theory
$n^{\alpha\beta}$	Stress resultant tensor of shell theory
n_{sec}	Number of sectors
p	Air film pressure
p^i	External forces of shell theory for $i = 1, 2, 3$
P_{loss}	Power loss
q^α	Transverse shear stress of shell theory
$q_{\text{T,in}}$	Heat flux entering the top foil from the air film
$q_{\text{T,out}}$	Heat flux leaving the top foil into the base plate
r	Radial coordinate
R	Radius of curvature in shell theory
R_A	Gas constant of air
r_D	Outer disk radius
r_i	Inner top foil radius
r_m	Mean top foil radius
r_o	Outer top foil radius
Re	Reynolds number
T_1	Hot temperature of runner disk
T_2	Cold temperature of runner disk
T_A	Air film temperature
T_C	Cooling flow temperature
T_m	Height-averaged air film temperature
T_R	Temperature of the rotor and disk
t_{RG}	Initial gap width in radial gap
T_{RG}	Air temperature in radial gap
T_T	Top foil temperature
U	x -component of disk velocity
V	y -component of disk velocity
u	x -component of air velocity
u_C	Radial velocity of cooling flow

v	y -component of air velocity
v_C	Circumferential velocity of cooling flow
v_i	Translational deformations of the shell middle surface of top (T) and bump foil (B) for $i = 1, 2, 3$
v_r	Radial deformation of the rotor and disk
v_z	Axial deformation of the rotor and disk
W	Bearing load capacity
w_α	Rotational deformations of the shell middle surface of top and bump foil for $\alpha = 1, 2$
w_C	z -velocity of cooling flow
x	Cartesian coordinate
y	Cartesian coordinate
z	Axial coordinate
z_R	Axial position of rotor

1 Introduction

Air foil bearing technology had its first industrial application in the late 1960s where air cycle machines in planes were fitted with this type of bearing. They present an alternative for other bearing types like rolling element bearings or oil bearings, offering advantages like high reliability, high-speed operation, low losses and low maintenance needs [17, 18]. Moreover, they are able to use surrounding air or other gases as their working/lubricating fluid and enable an oil-free machine design with lower complexity due to the omission of an oil supply.

This section serves as an introduction into the topic of foil thrust bearings and the challenges that have to be overcome when designing and optimizing these bearings. At the same time, the motivation for the different studies that were conducted and published in the mentioned papers is given. This thesis presents a synopsis of these papers which is why the superordinate problems and challenges are explained in this introductory section. Later, the different outlines of the individual papers are shown for each paper. The main results and findings are combined and displayed in a synthesis section. Thereafter, final conclusions are drawn and an outlook is given for possible interesting future research projects and developments.

1.1 Fundamentals of Air Foil Thrust Bearing Analysis

Air foil thrust bearings (AFTBs) are a specific type of hydrodynamic bearing that are used in high-speed machines. The AFTB as a machine part is integrated in the stationary housing. The rotor that is mounted into the machine possesses a rotor disk (also referred to as runner disk) which can be an integral part of the rotor or (in multi-part rotor designs) can be fitted onto the rotor shaft. The general structure of AFTBs is displayed in Fig. 1.1. The AFTB consists of a rigid base plate on which the compliant bearing foils are mounted. Two kinds of foils have to be distinguished: the corrugated bump foils serve as a flexible understructure of the bearing. In comparison with rigid air bearings, this characteristic of a foil bearing allows for larger manufacturing tolerances. Furthermore, the compliance of these bearings results in increased admissible misalignments in machines which is a key

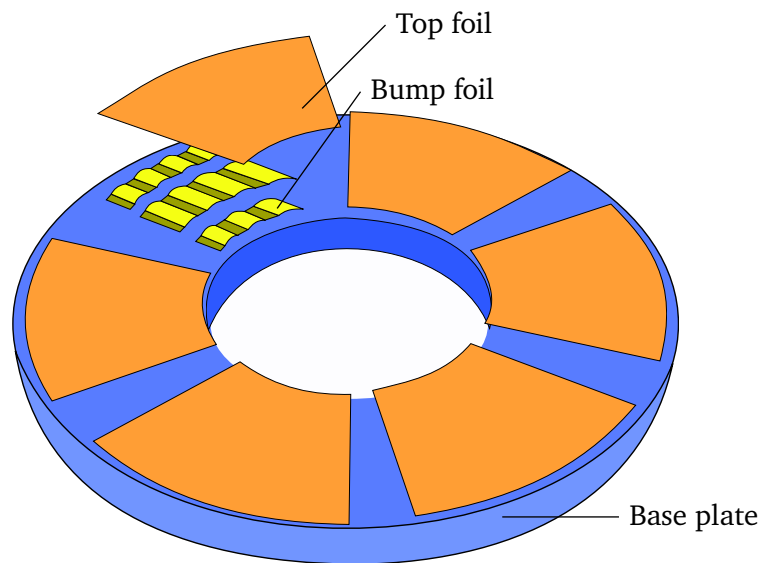


Abbildung 1.1: Foil thrust bearing structure consisting of a base plate as well as bump and top foils.

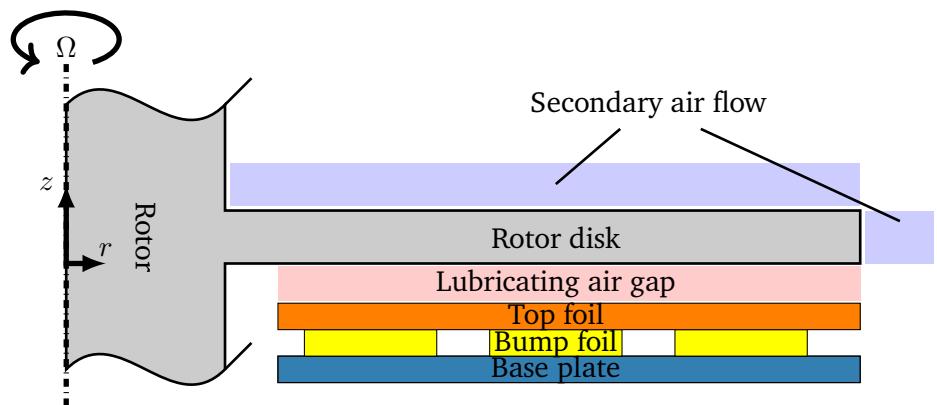
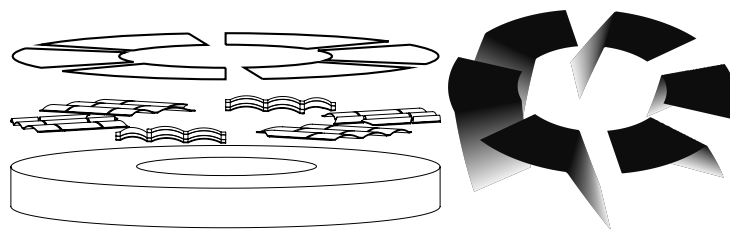
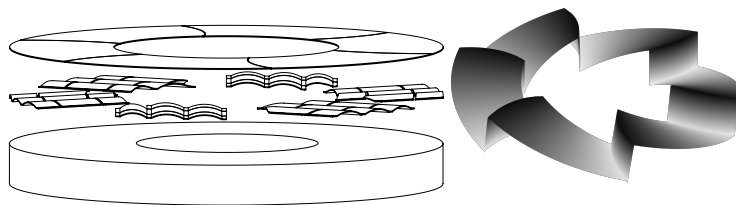


Abbildung 1.2: Cut view of a rotor disk and a single-sided thrust bearing.



(a) Multi-foil design.



(b) Single-foil design.

Abbildung 1.3: Comparison of (a) multi-foil and (b) single-foil bearing design. Left side: bearing assembly with base plate, bump foils and top foil(s). Right side: exaggerated height profiles of the top foils, (a) taper-land and (b) taper-step.

feature to reduce manufacturing costs. The compliant understructure in thrust bearings may also be achieved by the use of metal meshes [19] or leaf-type bearings [20]. In the works presented here, only bump-type bearings are considered. The second kind of foil is a flat and smooth top foil which is used to guide the airflow in the lubricating gap of the bearing. For the top foils as well as for the runner disk, coatings are used in order to reduce friction and wear at low rotor speeds [21, 22].

The shape of the top foil and the design of the bump foil with different bump heights can be used to tailor the topography of the gap between the runner disk and the top foil surface. In many cases, taper-land topologies are used where a wedge-shaped region (taper) with a converging gap height is combined with a region of nominally constant gap height (land). Due to the rotation of the runner disk, hydrodynamic pressure is generated in the lubricating gap which separates the top foil and the runner disk and supports axial loads of the rotor. For low speeds, mixed lubrication occurs which prohibits long-time operation of these bearings below a specific lift-off speed. For rotational speeds above the lift-off speed, full fluid lubrication is achieved between runner disk and top foil surface. In this thesis, two different bearing designs are investigated. The two designs are depicted in Fig. 1.3. The multi-foil bearing possesses individual bearing pads that each consist of a bump foil and a top foil, cf. Fig. 1.3a. Herein, the top foil is supported by bump foils with specifically designed bump heights. The bump heights imprint the aforementioned taper-land topography. By varying the bump heights, the nominal gap profile can be manipulated.

By contrast to this bearing design, the single-foil design of Fig. 1.3b possesses a single annular top foil that is supported by multiple bump foils with constant bump height. Furthermore, the top foil is embossed so that a taper-step topography is achieved. In combination with a thrust load, the top foil deforms and a taper-land-like topography is accomplished as well with this bearing type. For details, please see Sec. 1.2.2.

Many studies investigate dynamic characteristics of AFTBs including stiffness parameters, e.g. [23–27]. The focus of the studies presented here lies in the thermo-elasto-hydrodynamic (TEHD) static behavior of AFTBs with a focus on the thermal balances and optimization of foil thrust bearings with regard to load capacity, power loss, and thermal properties. A detailed literature review of the relevant works that deal with the design, analysis, and optimization of foil thrust bearings [28–50] can be found in the publications that are attached to this synopsis.

The analysis of AFTBs presented here is based on several fundamental equations and assumptions. The components of a thrust bearing (see Fig. 1.2) and the relevant properties in a thermo-elasto-hydrodynamic model are:

- Base plate: rigid, constant temperature.

- Bump foil: deformations are calculated via a Reissner-Mindlin type shell theory, thermal properties are represented by a thermal resistance.
- Top foil: deformations are calculated via a Reissner-Mindlin type shell theory, temperature is calculated via a heat diffusion equation.
- Lubricating air film: air pressure is calculated via a compressible 2D Reynolds equation, air temperature is calculated via a 3D energy equation.
- Rotor and runner disk: deformations are calculated with 2D Navier-Lamé equations including centrifugal forces and thermal stresses, temperature is calculated with a 2D heat diffusion equation.

The most important equations are highlighted here. They are generally solved using a fully coupled finite element model. For the calculation of the air film pressure $p(x, y)$, the Cartesian generalized compressible Reynolds equation [51] is used:

$$\begin{aligned} & \frac{\partial}{\partial x} \left[\frac{\rho(p, T_m) H^3}{12\eta(T_m)} \frac{\partial p}{\partial x} \right] + \frac{\partial}{\partial y} \left[\frac{\rho(p, T_m) H^3}{12\eta(T_m)} \frac{\partial p}{\partial y} \right] \\ & = \frac{\partial}{\partial x} \left[\frac{\rho(p, T_m) U H}{2} \right] + \frac{\partial}{\partial y} \left[\frac{\rho(p, T_m) V H}{2} \right]. \end{aligned} \quad (1.1)$$

The air density ρ and the air viscosity η are evaluated for a film height-averaged fluid temperature $T_m(x, y)$ [30, 46], the temperature dependent variables are defined in Tab. 1.1 for a temperature range from 20 °C bis 500 °C. The variables U and V describe the velocity of the disk in the Cartesian x - and y -direction. The height function H is very important for the performance of hydrodynamic bearings. It is influenced by the rotor axial movement, the nominal gap topography and the component deformations. Moreover, it might be influenced by the wear of the top foil coating, cf. Sec. 1.2.2, or misalignment, cf. Sec. 1.2.3. Regarding boundary conditions of the Reynolds equation (1.1), the specific bearing design and the extent of the model (single-pad model vs. full bearing model) both have a significant influence.

For the air temperature field $T_A(x, y, z)$, a 3D energy equation is solved, cf. for example [52]:

$$\begin{aligned} \rho c_P \left[u \frac{\partial T_A}{\partial x} + v \frac{\partial T_A}{\partial y} \right] & = \left[\frac{\partial}{\partial x} \left(\lambda \frac{\partial T_A}{\partial x} \right) + \frac{\partial}{\partial y} \left(\lambda \frac{\partial T_A}{\partial y} \right) + \frac{\partial}{\partial z} \left(\lambda \frac{\partial T_A}{\partial z} \right) \right] \\ & + \left[u \frac{\partial p}{\partial x} + v \frac{\partial p}{\partial y} \right] + \eta \left[\left(\frac{\partial u}{\partial z} \right)^2 + \left(\frac{\partial v}{\partial z} \right)^2 \right]. \end{aligned} \quad (1.2)$$

Tabelle 1.1: Energy equation parameters

Variable	Value	Description
ρ	$\frac{p}{R_A T_{m,i}}$	Density
R_A	0.287 kJ/(kg · K)	Gas constant of air
η	$\left[-1.75 \times 10^{-11} \left(\frac{T_{m,i}}{[K]} \right)^2 + 5.68 \times 10^{-8} \left(\frac{T_{m,i}}{[K]} \right) + 3.06 \times 10^{-6} \right] [\text{kg}/(\text{m} \cdot \text{s})]$	Viscosity
c_P	$\left[2.43 \times 10^{-4} \left(\frac{T_{A,i}}{[K]} \right)^2 - 7.7 \times 10^{-2} \left(\frac{T_{A,i}}{[K]} \right) + 1008 \right] [\text{J}/(\text{kg} \cdot \text{K})]$	Heat capacity
λ	$\left[-2.1 \times 10^{-8} \left(\frac{T_{A,i}}{[K]} \right)^2 + 8.46 \times 10^{-5} \left(\frac{T_{A,i}}{[K]} \right) + 2.89 \times 10^{-3} \right] [\text{W}/(\text{m} \cdot \text{K})]$	Heat conductivity

Equation (1.2) includes convective heat transfer, diffusive heat transfer (conduction), power of pressure forces, and dissipation resulting from shear forces. λ describes the heat conductivity, c_P is the specific heat capacity of air. u and v are the Cartesian fluid velocities, respectively [51]. Generally, for AFTBs, the conductive heat transfer in z -direction is significantly larger than the convective heat transfer due to the small dimensions of the air gap. Note that planar heat diffusion in the lubricating gap is usually neglected, cf. [50], but can be included in order to be able to formulate consistent boundary conditions for single-foil bearing analysis. Again, the specific boundary conditions depend on the application and the bearing design.

The deformations of the top and bump foil are calculated using a Reissner-Mindlin type shell theory [53, 54]. Each shell possesses 5 degrees of freedom (DOFs), namely 3 translational DOFs $v_1(x, y)$, $v_2(x, y)$, and $v_3(x, y)$ in x -, y -, and z -direction, respectively, as well as 2 rotational DOFs denoted by $w_1(x, y)$ and $w_2(x, y)$. Equations (1.3) to (1.7) are used for the calculation of the deformations of a cylindrical shell with radius of curvature R along the x -direction under the external loads p^1 , p^2 , and p^3 in x -, y -, and z -direction,

respectively:

$$\begin{aligned}
& \frac{\partial}{\partial x} \left[D \left(\frac{\partial v_1}{\partial x} + \nu \frac{\partial v_2}{\partial y} + \frac{1}{R} v_3 \right) \right. \\
& \quad \left. + \frac{B}{R} \left(\frac{\partial w_1}{\partial x} + \nu \frac{\partial w_2}{\partial y} + \frac{1}{R} \frac{\partial v_1}{\partial x} + \frac{1}{R^2} v_3 \right) \right] \\
& \quad + \frac{\partial}{\partial y} \left[D \frac{1-\nu}{2} \left(\frac{\partial v_2}{\partial x} + \frac{\partial v_1}{\partial y} \right) \right. \\
& \quad \left. + \frac{B}{R} \frac{1-\nu}{2} \left(\frac{\partial w_2}{\partial x} + \frac{\partial w_1}{\partial y} + \frac{1}{R} \frac{\partial v_1}{\partial y} \right) \right] \\
& = -\frac{Gtks}{R} \left(w_1 + \frac{\partial v_3}{\partial x} - \frac{1}{R} v_1 \right) - p^1,
\end{aligned} \tag{1.3}$$

$$\begin{aligned}
& \frac{\partial}{\partial x} \left[D \frac{1-\nu}{2} \left(\frac{\partial v_2}{\partial x} + \frac{\partial v_1}{\partial y} \right) \right] \\
& \quad + \frac{\partial}{\partial y} \left[D \left(\frac{\partial v_2}{\partial y} + \nu \frac{\partial v_1}{\partial x} + \frac{\nu}{R} v_3 \right) \right] \\
& = -p^2,
\end{aligned} \tag{1.4}$$

$$\begin{aligned}
& \frac{\partial}{\partial x} \left[Gtks \left(w_1 + \frac{\partial v_3}{\partial x} - \frac{1}{R} v_1 \right) \right] \\
& \quad + \frac{\partial}{\partial y} \left[Gtks \left(w_2 + \frac{\partial v_3}{\partial y} \right) \right] \\
& = \frac{D}{R} \left(\frac{\partial v_1}{\partial x} + \nu \frac{\partial v_2}{\partial y} + \frac{1}{R} v_3 \right) \\
& \quad + \frac{B}{R} \left(\frac{\partial w_1}{\partial x} + \nu \frac{\partial w_2}{\partial y} + \frac{1}{R} \frac{\partial v_1}{\partial x} + \frac{1}{R^2} v_3 \right) - p^3,
\end{aligned} \tag{1.5}$$

$$\begin{aligned}
& B \left[\frac{\partial}{\partial x} \left(\frac{\partial w_1}{\partial x} + \nu \frac{\partial w_2}{\partial y} + \frac{1}{R} \frac{\partial v_1}{\partial x} + \frac{1}{R^2} v_3 \right) \right. \\
& \quad \left. + \frac{\partial}{\partial y} \left(\frac{1-\nu}{2} \left(\frac{\partial w_1}{\partial y} + \frac{\partial w_2}{\partial x} + \frac{1}{R} \frac{\partial v_1}{\partial y} \right) \right) \right] \\
& = Gtks \left(w_1 + \frac{\partial v_3}{\partial x} - \frac{1}{R} v_1 \right),
\end{aligned} \tag{1.6}$$

$$\begin{aligned}
& B \left[\frac{\partial}{\partial x} \left(\frac{1-\nu}{2} \left(\frac{\partial w_1}{\partial y} + \frac{\partial w_2}{\partial x} + \frac{1}{R} \frac{\partial v_1}{\partial y} \right) \right) \right. \\
& \left. + \frac{\partial}{\partial y} \left(\frac{\partial w_2}{\partial y} + \nu \frac{\partial w_1}{\partial x} + \frac{\nu}{R} \frac{\partial v_1}{\partial x} + \frac{\nu}{R^2} v_3 \right) \right] \\
& = Gt k_S \left(w_2 + \frac{\partial v_3}{\partial y} \right).
\end{aligned} \tag{1.7}$$

This formulation contains the stretching stiffness D , the bending stiffness B and the shear stiffness Gt with Young's modulus E , Poisson's ratio ν and the shell thickness t . The top foil is usually considered an approximately flat metal sheet with $R \rightarrow \infty$, while the bump foil possesses cylindrical bumps (constant radius R) combined with flat bridges ($R \rightarrow \infty$). The equations become nonlinear when contacts between the base plate and the bump foil as well as between the bump foil and the top foil are considered.

For the top foil temperature T_T , a 2D heat diffusion equation

$$-\lambda_T t_T \Delta T_T = q_{T,\text{in}} + q_{T,\text{out}} \tag{1.8}$$

with thermal conductivity λ_T , thickness t_T and heat fluxes $q_{T,\text{in}}$ into the top foil from the lubricating gap and $q_{T,\text{out}}$ from the top foil into the bump foil and the base plate.

Deformations $v_r(r, z)$ in radial and $v_z(r, z)$ in axial direction of the rotor and the runner disk are calculated via a thermoelastic axisymmetric model. The deformations are obtained by solving the Navier-Lamé equations including centrifugal forces and thermal stresses as in Ref. [55]:

$$\begin{aligned}
\mu_R \left(\nabla^2 v_r - \frac{v_r}{r^2} \right) + (\gamma_R + \mu_R) \frac{\partial}{\partial r} \left(\frac{1}{r} \frac{\partial}{\partial r} (r v_r) + \frac{\partial v_z}{\partial z} \right) - \epsilon_R \frac{\partial \Delta T_R}{\partial r} &= -\rho_R r \Omega^2, \\
\mu_R \nabla^2 v_z + (\gamma_R + \mu_R) \frac{\partial}{\partial z} \left(\frac{1}{r} \frac{\partial}{\partial r} (r v_r) + \frac{\partial v_z}{\partial z} \right) - \epsilon_R \frac{\partial \Delta T_R}{\partial r} &= 0,
\end{aligned} \tag{1.9}$$

where γ_R is the Lamé constant and μ_R is the shear modulus. The constant ϵ_R describes thermoelastic stresses with ΔT_R being the disk temperature difference with respect to a reference temperature. Further, ρ_R is the density of the rotor material. It is assumed that the influence of the fluid film pressure and the fluid film shear stresses on the rotor disk are negligible.

The temperature of the rotor disk $T_R(r, z)$ is calculated with the energy equation

$$\frac{\partial}{\partial r} \left[\lambda_R r \frac{\partial T_R}{\partial r} \right] + \frac{\partial}{\partial z} \left[\lambda_R r \frac{\partial T_R}{\partial z} \right] = 0 \tag{1.10}$$

with the thermal conductivity λ_R of the rotor material.

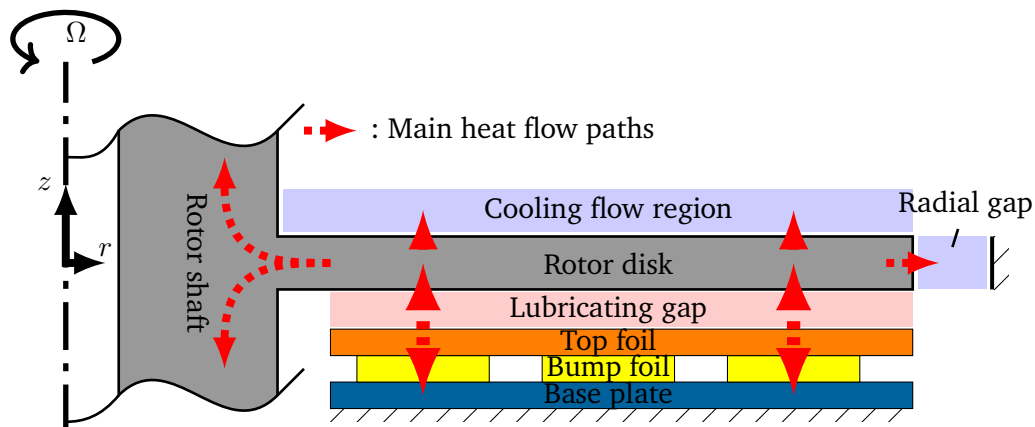


Abbildung 1.4: Main heat flow paths in a foil thrust bearing assembly.

1.2 Objectives and Structure of the Thesis

The fundamental equations displayed in Sec. 1.1 represent the basis of the TEHD models used to analyze and optimize AFTBs in this thesis. In the upcoming sections, the focus of the individual contributions that are summarized in this synopsis are explained. This thesis is based on the four publications [1–4]. They all deal with different aspects of AFTB analysis and optimization. Paper 2 presents an analysis of single-foil bearings, while Papers 1, 3, and 4 investigate multi-foil bearing designs, cf. Fig. 1.3.

1.2.1 Outline of Paper 1

Paper 1 [1] aims at describing the heat flow paths in an AFTB and showcasing the effect of different foil materials on the bearing performance. Through dissipation, high temperatures occur in the lubricating gap owing to the high circumferential velocity of the rotor disk. It is important to understand the mechanisms of heat transfer inside the thrust bearing in order to optimize the bearing behavior. The heat generated in the lubricating gap is mainly flowing into the foil sandwich on the one hand and into the rotor disk on the other hand which leads to thermally induced bending of the rotor disk. These deformations reduce the load capacity of the thrust bearing. The main heat flow paths are illustrated in Fig. 1.4. In order to reduce thermal bending, the heat flow into the foil sandwich can be increased. The first and most widespread method is introducing a radial cooling flow under the top foil that reduces the top foil temperature and at the same time

Tabelle 1.2: Foil material parameters.

Dimension	Material A	Material B	Material C
E in GPa	210	180	147.5
ν	0.3	0.3	0.325
λ in W (mK)^{-1}	12	55	250
Top foil thickness in μm	100	105.3	112.5
Bump foil thickness in μm	75	79.0	84.4

lowers the heat flux into the rotor disk. This has a positive effect on the load capacity, cf. [37, 50]. The approach of the current study is to decrease the thermal resistance of the foil sandwich by introducing alternative materials for the bump and top foils (typically, a superalloy like INCONEL[®] X-750 is used). Due to dynamic loads, spring materials are typically utilized which need to have specific properties: high bending fatigue strength, high tensile strength and resiliency.

If alternative materials are to be considered for the bump and top foils, their maximum operation temperature needs to be higher than the bearing operation temperature as well. With increasing temperature, metals suffer from a weakening of the above mentioned properties and may experience effects like creep which are to be avoided [56]. For high-temperature applications as in [57], only specific steels are contemplable. For lower temperature applications, the use of other materials with significantly higher thermal conductivities, albeit with lower maximum operating temperatures, can become feasible. Therefore, a comparison is drawn here between INCONEL[®] X-750 (Material A), DURACON[®] 17A (Material B) and CuNi1Si (Material C) as foil materials. The relevant material parameters are given in Table 1.2. It is important to note that in order to make up for the lower Young's modulus of the different materials, the foil thicknesses are increased accordingly to create equal bending stiffnesses at room temperature. The increased foil thickness alongside the higher thermal conductivity contribute to a lower thermal resistance. A lower thermal resistance of the bump foil leads to increased heat fluxes into the base plate which in turn decrease the thermal load of the runner disk.

In this model, only a single-sided bearing is considered. At the free backside of the rotor disk, the disk rotation causes an airflow. The heat flux that leaves the disk is calculated from the temperature $T_C(r, z)$ in the cooling region which is obtained from the energy

equation (assuming axisymmetry):

$$\begin{aligned} \frac{\partial}{\partial z} \left[\lambda_{C,eff} \frac{\partial T_C}{\partial z} \right] &= \rho_C c_{P,C} \left[u_C \frac{\partial T_C}{\partial r} + w_C \frac{\partial T_C}{\partial z} \right] \\ &- \rho_C (\nu_C + \nu_{CT}) \left[\left(\frac{\partial u_C}{\partial z} \right)^2 + \left(\frac{\partial v_C}{\partial z} \right)^2 \right]. \end{aligned} \quad (1.11)$$

Here, $\lambda_{C,eff}$ is an effective thermal conductivity according to Ref. [58], ρ_C the density, $c_{P,C}$ the isochoric heat capacity and ν_C and ν_{CT} are the kinematic viscosity and the turbulent kinematic viscosity according to Cebeci and Smith [59]. The velocity field consisting of the radial velocity u_C , the circumferential velocity v_C and the velocity w_C in z -direction is calculated from the boundary layer equations for steady incompressible axisymmetric flow (neglecting a radial pressure gradient), see Ref. [59].

In the radial gap between the rotor disk and the housing, the disk rotation also causes an airflow. It is assumed to be laminar with purely circumferential flow (Couette flow) and with linearly decreasing velocity over the radial coordinate (disk speed at the inner boundary, zero speed at the outer boundary). This simple assumption is made as the initial gap width t_{RG} is 200 μm and decreases below 100 μm at high rotational speeds due to centrifugal effects. The estimated maximal Reynolds number for the flow is $Re \approx \Omega r_D t_{RG} \rho / \eta \approx 700 - 800$. Thus, the 2D energy equation

$$\frac{\partial}{\partial r} \left[\lambda_{RG} r \frac{\partial T_{RG}}{\partial r} \right] + \frac{\partial}{\partial z} \left[\lambda_{RG} r \frac{\partial T_{RG}}{\partial z} \right] = -r \eta_{RG} \left[\frac{\Omega r_D}{t_{RG}} \right]^2 \quad (1.12)$$

including dissipative heating is solved to obtain the temperature profile $T_{RG}(r, z)$ in the radial gap. In Eqn. (1.12), λ_{RG} is the thermal conductivity, η_{RG} is the dynamic viscosity of air in the gap, r_D is the disk radius and t_{RG} is the gap width with account for disk deformations.

With the help of this model, the impact of the different foil materials on the bearing temperatures, the thermal bending of the runner disk and the load capacity is investigated and compared against conventional forced cooling.

1.2.2 Outline of Paper 2

Paper 2 [2] is the first of two papers describing the analysis of single-foil thrust bearings. While the second paper [15] focuses on the test rig and measurements, this work gives insight into the modeling of this type of bearing. A fully coupled TEHD model for stationary simulations for single-foil AFTBs with an annular, one-part top foil is presented. The model

takes into account thermoelastic deformations of the rotor due to thermal stresses and centrifugal effects, a detailed thermodynamic model for the rotor temperature with a heat transfer model from CFD analysis, air film temperature and pressure through a 3D energy equation and a 2D Reynolds equation, respectively, elastomechanic deformations of top and bump foil via a nonlinear shell model including normal and tangential contact forces, as well as a detailed model for the top foil temperature and the heat transfer through the bump foil and the air gap between top foil and base plate.

A direct implementation of the full bearing would require extreme simulation times which would not allow for parameter studies and optimizations. Therefore, a reduction approach is presented which makes use of the cyclic symmetry. The cyclic coupling conditions for the top foil and the air film are derived and explained in detail. Of course, misalignment may not be considered in this case.

The cyclic boundary conditions for the shell equations of the top foil (index T) are formulated for the leading (index l) and trailing edge (index t):

$$\begin{aligned} \vec{n}_l v_{\alpha, T, l} \vec{e}_\alpha &= \vec{n}_t v_{\alpha, T, t} \vec{e}_\alpha, & v_{3, T, l} &= v_{3, T, t}, & \vec{n}_l w_{\alpha, T, l} \vec{e}_\alpha &= \vec{n}_t w_{\alpha, T, t} \vec{e}_\alpha, \\ \vec{n}_l n_{T, l}^{\alpha\beta} \vec{e}_\alpha &= \vec{n}_t n_{T, t}^{\alpha\beta} \vec{e}_\alpha, & q_{T, l}^\alpha &= q_{T, t}^\alpha, & \vec{n}_l m_{T, l}^{\alpha\beta} \vec{e}_\alpha &= \vec{n}_t m_{T, t}^{\alpha\beta} \vec{e}_\alpha. \end{aligned} \quad (1.13)$$

\vec{n}_l and \vec{n}_t describe the normal vectors at the leading and trailing edge, respectively, and \vec{e}_α is the unit vector. The transverse shear stress is q^α , the moment tensor $m^{\alpha\beta}$, and the stress resultant tensor $n^{\alpha\beta}$ according to [54]. Note that this design possesses independent bump foils which are therefore not coupled cyclically.

A direct comparison of simulation results with measurements shows large discrepancies. It is observed that significant wear occurs upon the loading of the bearing, especially for the first break-in. Therefore, an appropriate algorithm for the simulation of wear is derived and incorporated into the model.

The quasi-static wear algorithm that has been developed allows to take into account gap height changes due to wear. With this TEHD model, stationary simulations of the bearing components can be carried out. The minimal gap height $\min |H(x, y)|$ is used as a limit criterion for plausible bearing operation. In this work, $\min |H(x, y)| = H_{\min} = 2 \mu\text{m}$ is chosen as the transition point between fluid lubrication and mixed lubrication. The integrated pressure field at this specific point represents an approximation of the load capacity of the bearing,

$$W = n_{\text{sec}} \iint (p - p_0) dA_{\text{sec}} \quad (\text{for } H_{\min} = 2 \mu\text{m}). \quad (1.14)$$

If the thrust load on the rotor is further increased, the disk will get closer to the top foil and $\min |H(x, y)| < H_{\min}$. The assumptions for a continuous air flow are no longer met in

this case and mixed lubrication is expected to occur.

In experiments, several significant wear marks on the coating are observed during the run-in process. In order to represent this effect in the simulation, a quasi-static wear algorithm is developed. It assumes that the top foil coating is soft compared to the rotor disk and will instantaneously be worn when mixed lubrication occurs.

For the wear algorithm, the function $H_{\text{wear}}(x, y)$ is defined as the wear depth of the top foil. This means that worn areas possess a positive value according to the height of abraded coating, while unworn areas have a wear depth of 0. Initially, H_{wear} is set to zero and a stationary simulation of the bearing is carried out until $\min |H(x, y)| = H_{\text{min}}$ is met, yielding amongst others a load capacity $W^{(0)}$ for the unworn state according to Eq. (1.18). Note that reaching a specific value of the minimal gap height is achieved by changing the axial position of the rotor z_R . Now, all areas of the height function with $H \geq -(H_{\text{min}} + \delta_{\text{wear}})$ with a small user-defined δ_{wear} are stored in the wear function

$$H_{\text{wear}}^{(1)} = \text{ramp}(H + H_{\text{min}} + \delta_{\text{wear}}) = \begin{cases} H + H_{\text{min}} + \delta_{\text{wear}}, & H + H_{\text{min}} + \delta_{\text{wear}} \geq 0 \\ 0, & H + H_{\text{min}} + \delta_{\text{wear}} < 0 \end{cases} \quad (1.15)$$

In the upcoming sections, $\delta_{\text{wear}} = 1 \mu\text{m}$ has been chosen. It represents the wear height increment of each wear step. Note that the bracketed superscript index denotes the wear iteration, ranging from 0 (unworn state) to i_{end} (fully worn state).

While the base iteration with $i = 0$ is carried out with the height function H of Eq. (1.18), the new height function for iteration step $i = 1$ and the corresponding height functions for the upcoming iteration steps now read

$$\begin{aligned} H^{(0)} &= H, \\ H^{(1)} &= H - H_{\text{wear}}^{(1)}, \\ &\vdots \\ H^{(i)} &= H - H_{\text{wear}}^{(i)}, \\ &\vdots \\ H^{(i_{\text{end}})} &= H - H_{\text{wear}}^{(i_{\text{end}})}. \end{aligned} \quad (1.16)$$

After each incrementation of H_{wear} , a new simulation of the bearing is conducted. In the proceeding incrementation steps, the old wear result is added to the new contribution of

```

program WEAR ITERATION
Iteration number  $i = 0$ 
while  $W \leq 100 \text{ N}$ 
    set initial value of  $z_R$ 
    calculate foil and disk deflections
    while  $\min |H(x, y)| \neq H_{\min}$ 
        update  $z_R$ 
        calculate foil and disk deflections
    end while
    calculate  $H_{\text{wear}}^{(i)}$ 
     $H_{\text{wear}}^{(i)} = H_{\text{wear}}^{(i-1)} + \text{ramp}(H^{(i-1)} + H_{\min} + \delta_{\text{wear}})$ 
    increment  $i$ 
end while
 $i = i_{\text{end}}$ 
end program WEAR ITERATION

```

Abbildung 1.5: Pseudocode of the wear algorithm.

the current step i , i.e.

$$\begin{aligned}
 H_{\text{wear}}^{(0)} &= 0, \\
 &\vdots \\
 H_{\text{wear}}^{(i)} &= H_{\text{wear}}^{(i-1)} + \text{ramp}(H^{(i-1)} + H_{\min} + \delta_{\text{wear}}), \\
 &\vdots \\
 H_{\text{wear}}^{(i_{\text{end}})} &= H_{\text{wear}}^{(i_{\text{end}}-1)} + \text{ramp}(H^{(i_{\text{end}}-1)} + H_{\min} + \delta_{\text{wear}}).
 \end{aligned} \tag{1.17}$$

Figure 1.5 shows the program sequence in a pseudocode representation. It shows the outer while loop for the wear iteration index i and the inner iteration loop for the minimal gap height iteration to H_{\min} .

The top foil geometry as well as the coating topography deviate significantly from their nominal design values. Therefore, the real geometry of top foil and coating is included in the model. Without the use of the real top foil topography and the consideration of wear, bearing performance cannot be analyzed by the model. With the extended model, numerical results agree well with experimental data.

A detailed experimental investigation of the real top foil geometry yields the following

results:

- The step at the border of adjacent sectors is not ideally vertical but rather extended over a small region. An average step width of 0.66 mm is observed in real top foils.
- In the ideal geometry, the top foil possesses no radial slope or curvature; the ideal taper is a function of the angular position only. Through the embossing process, however, the top foil is also deformed into a parabolic shape. This shape deviation is observable in radial direction, meaning that the inner and outer foil edge (at the inner and outer radius) is bent upwards. Therefore, radial cuts of the top foil do not yield straight lines. Measurements show that this shape deviation in radial direction can be sufficiently approximated by the parabola expression $H_{\text{par}}(r) = h_{\text{par}}(r - r_m)^2 / (r_i - r_m)^2$ with $r_m = (r_i + r_o) / 2$ and $h_{\text{par}} = 20 \mu\text{m}$.
- The top foil is coated with a PTFE layer with a mean coating thickness of $25 \mu\text{m}$. Measurements show that this coating is not uniform. A detailed analysis of the coating thickness reveals that, towards the inner and outer foil edges at $r = r_i$ and $r = r_o$, coating accumulations of $\Delta h_{\text{coat}} = 12 \mu\text{m}$ beyond the mean coating thickness are observed. Measurements further show that the variation of coating height in the circumferential direction is negligible. Consequently, the coating height distribution in radial direction, in the following denoted by $H_{\text{coat}}(r)$, is considered in the simulation model with a spline representation.

These 3 deviations are systematic due to the manufacturing process of the top foil and the coating application. They were found in all the test specimen.

The first two items of the list above—namely the finite step width of 0.66 mm and the parabolic shape deviation in radial direction—are geometrical deviations of the metal foil due to the embossing process in comparison with the ideal geometry.

It is interesting to note that each sector of the one-part top foil deforms from the initial taper-step geometry (cf. Fig. 1.3b) into a taper-land configuration under pressure load during operation.

Another fundamental aspect of the TEHD model lies in the formulation of consistent boundary conditions, especially for the heat transfer from the bearing and rotor to the surrounding. For the test rig that is used to validate the numerical model of this study [15], a CFD analysis is conducted to analyze the heat flow from the rotor to the surrounding air, see Fig. 1.6.

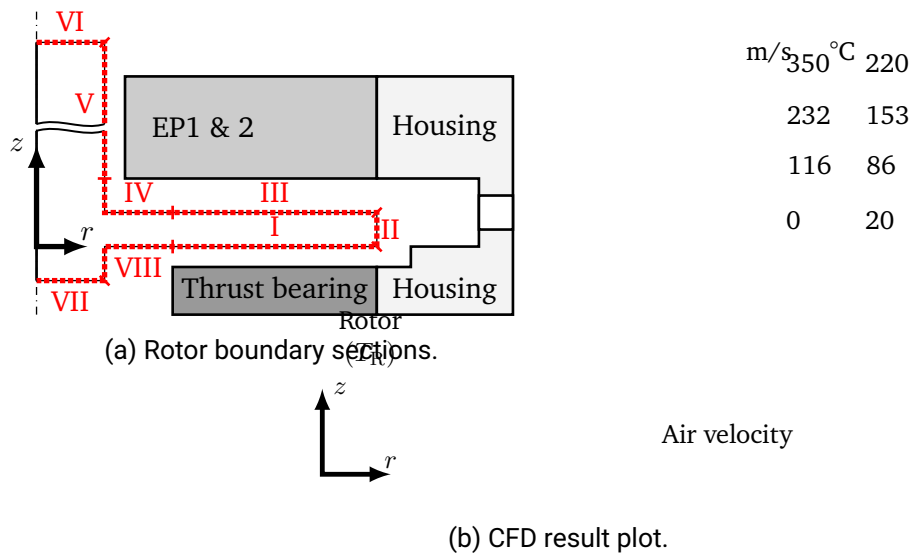


Abbildung 1.6: (a) Definition of rotor boundary sections I to VIII. (b) Result plot section of CFD calculation for heat transfer coefficient determination.

1.2.3 Outline of Paper 3

Paper 3 [3] displays the influence of misalignment on the thrust bearing performance. A detailed TEHD FE model is utilized which has the following substantial extensions:

- When considering misalignment, the height function of each bearing pad is individual.
- Each bearing pad exerts a different pressure load and power loss.
- Therefore, the analysis of a single bearing pad as a representation for the overall bearing behavior is no longer valid. The successive calculation of each bearing pad individually is sufficient only for the isothermal case. For the thermal model of the bearing, the fully coupled model of all individual air films presented in this paper can solve this issue.
- Through the use of a single rotor model combined with multiple individual bearing pads (air films and foil understructure), the case of misalignment is adequately represented in the thrust bearing model.
- This extension displays huge additional computational expenses. In comparison with a reduced model where only a single bearing pad is taken into account, computation times are increased by a factor of 8-10 when considering a bearing with six bearing pads.

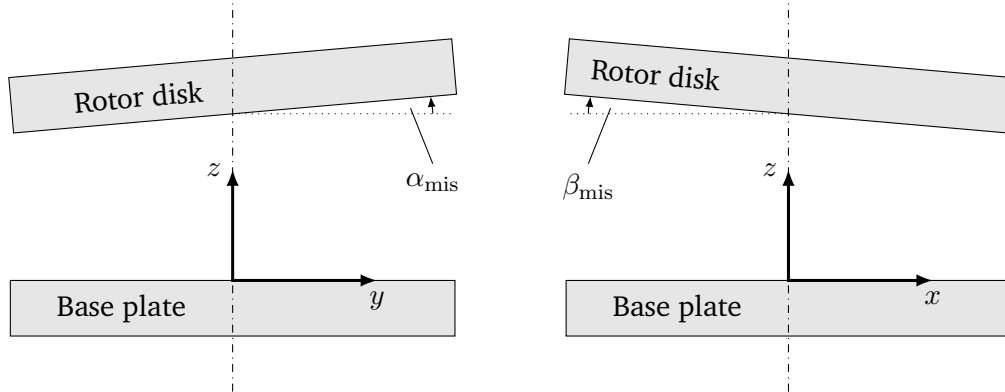


Abbildung 1.7: Definition of the two misalignment values α_{mis} and β_{mis} of Eq. (1.19).

For the numerical analysis of the thrust bearing, the film height function $H(x, y)$ is crucial. It is affected by the bearing design, but also includes the deformations of the bearing components. Each bearing pad possesses an individual height function $H_i(x, y)$:

$$H_i(x, y) = z_R - v_{3,T,i} + v_z(z = 0, r) + H_{\text{mis}}. \quad (1.18)$$

Herein, $v_{3,T,i}$ is the deformation of the i -th top foil and is individual for each pad. The remaining values are the same for each bearing pad: z_R displays the axial position of the rotor, $v_z(z = 0, r)$ is the deformation of the rotor disk underside, and H_{mis} represents the misalignment between the rotor disk and the bearing:

$$H_{\text{mis}} = -\tan(\beta_{\text{mis}})x - \frac{\tan(\alpha_{\text{mis}})}{\cos(\beta_{\text{mis}})}y. \quad (1.19)$$

The two misalignment values α_{mis} and β_{mis} are displayed in Fig. 1.7.

1.2.4 Outline of Paper 4

In paper 4 [4], compensation approaches for the commonly observed thermal bending phenomenon of the rotor disk in thrust bearings are presented using passive effects without additional expenditure of energy. The heat fluxes from dissipation in the lubricating gap that enter the runner disk cause an axial temperature gradient which in turn causes thermoelastic bending deformations of the runner disk directed away from the bearing. This bending changes the shape of the lubricating gap and reduces the load capacity of the bearing, which can lead to even higher temperatures and machine failure (thermal

runaway), cf. Fig. 1.8.

The main idea to compensate this effect is to make use of centrifugal forces that generate a bending moment in the rotor disk that causes a deformation counteracting the thermal bending effect. Different measures can be considered in order to generate a compensating effect.

- Using asymmetric rotor disk mass distributions causing a bending moment through centrifugal forces, see Fig. 1.9. The resulting centrifugal force does not act along the rotor disk centerline depicted by the dotted line, therefore causing a bending moment for the rotor disk.
- Applying recesses or asymmetrically placed radii or notches at the base of the rotor disk causing a bending moment through centrifugal forces.
- Implementing isolation layers or cuts to reduce the axial temperature gradient and reduce thermal bending.
- Utilizing different materials (with different densities or thermal expansion properties) for dual-material rotor disks and making use of centrifugal and thermal expansion effects.

The design changes that are proposed here are summarized in Fig. 1.10. A fully coupled air foil thrust bearing finite element (FE) model is presented incorporating a standard rotor disk geometry S as well as a new proposed optimized design O in order to compensate the thermal bending of the rotor disk.

Detailed results of the fully coupled TEHD thrust bearing model including pressure distributions, height functions and rotor temperatures at high rotational speeds and loads are presented.

A direct comparison is drawn between the standard design S and different optimized designs. Temperatures, deformations, thrust loads and power losses are shown in order to evaluate the benefit of the proposed design changes.

The impact of changes in single design parameters is investigated and a second optimization step for maximum load capacity of the bearing is presented.

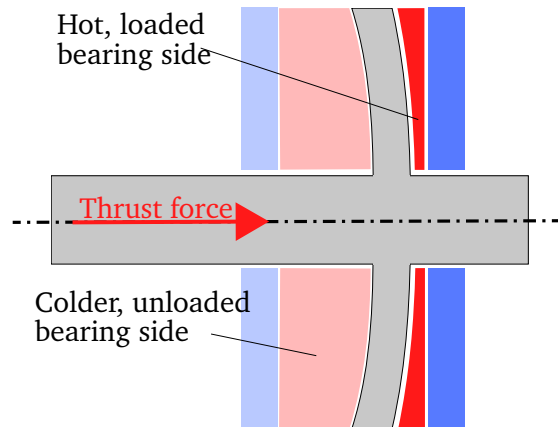


Abbildung 1.8: Thermal bending of the rotor disk (exaggerated) directed away from the hot bearing side resulting from the supported thrust force.

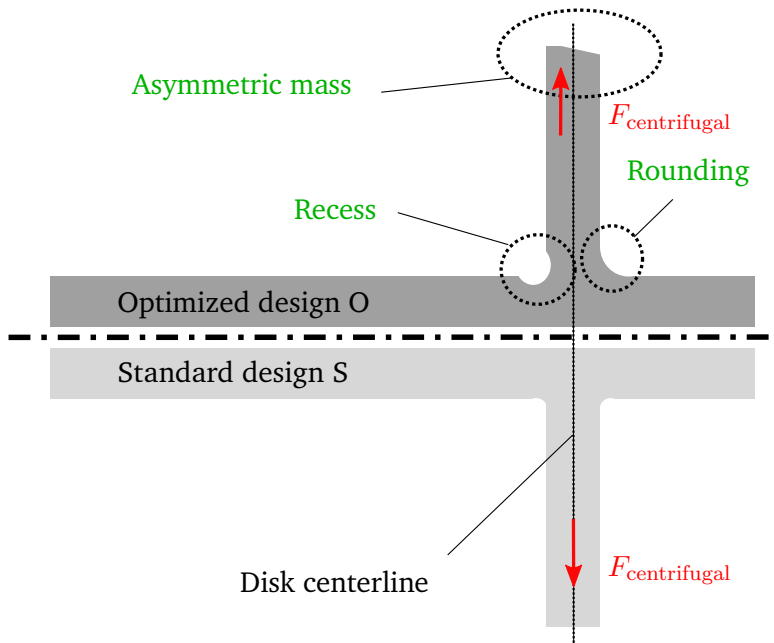


Abbildung 1.9: Comparison of the optimized rotor disk design O (top half) including an asymmetric mass distribution as well as a combination of a recess and a rounding at the base of the disk vs. the standard symmetric design S (bottom half).

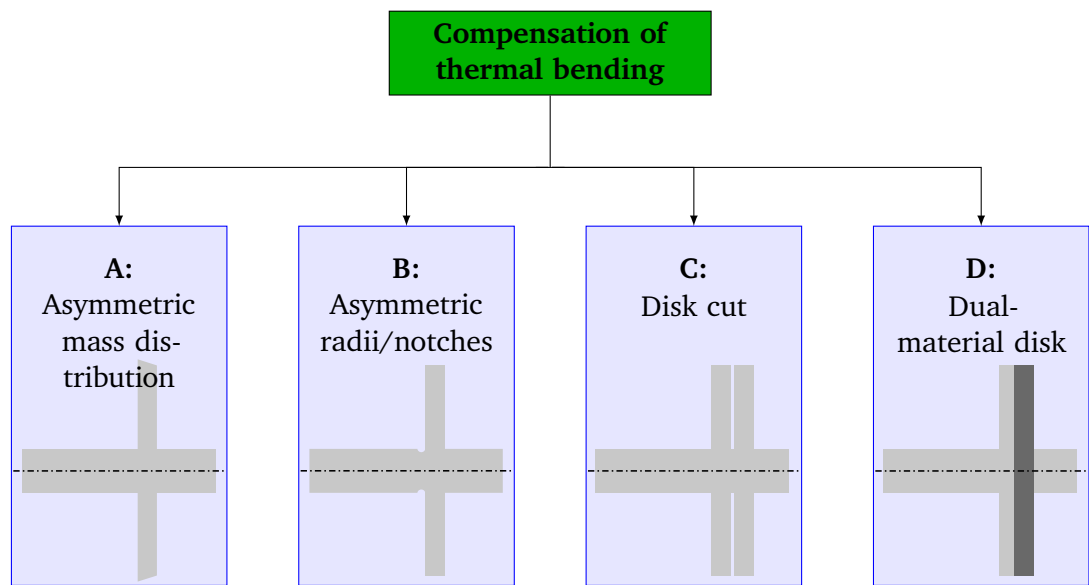


Abbildung 1.10: Different technical approaches for compensating thermal bending.

2 Results

This section of the synopsis serves as a synthesis of the aforementioned publications. Here, the results of the different works are brought together and discussed in detail. Their contribution to the overarching scientific problem of the analysis and optimization of air foil thrust bearings with single-foil and multi-foil design are displayed.

Papers 1 and 4 [1, 4] display two different passive approaches to optimize the thermal management on the one hand and reduce or compensate the thermal bending of the runner disk in AFTBs on the other hand. These results are summarized and discussed in Sec. 2.1.

While the two aforementioned publications investigate the behavior of multi-foil bearings, paper 2 [2] presents in-depth results for a single-foil bearing design which are displayed in Sec. 2.2. It is shown why the wear of the top foil coating is prominent in this design and has to be taken into account.

Paper 3 [3] extends the single-sector models of the other publications towards a full bearing model. Single-sector models utilize symmetry conditions of the different bearing sectors and are therefore not able to predict the performance of foil thrust bearings under misaligned conditions. However, the misalignment of the bearing and the runner disk can markedly impact the bearing load capacity and power loss. The results are summarized in Sec. 2.3.

2.1 Optimization results for AFTBs

The use of different foil materials that has been outlined in Sec. 1.2.1 with higher thermal conductivities is aimed towards the reduction of overall bearing temperatures. Similar to the commonly applied forced cooling of thrust bearings with a cooling air flow that is guided through the foil sandwich, this passive approach may improve heat transfer away from the hot lubricating gap. Figure 2.1 displays the maximum top foil temperature increase with respect to ambient temperature for the three different foil materials that are considered over the rotational speed. It is obvious that—with increasing rotational speed—the power loss of the thrust bearing is increased and bearing temperatures rise.

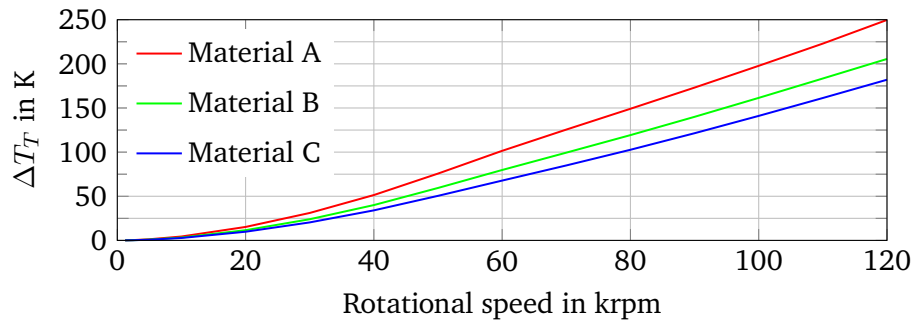


Abbildung 2.1: Maximum top foil temperature increase ΔT_T for different foil materials over the rotational speed.

For the maximum rotational speed of 120 krpm, the standard foil material A shows a temperature increase of around 250 K, while this maximum temperature increase for material C with the highest thermal conductivity ranges up to 180 K. This corresponds to a reduction of the maximum temperature increase of 27%.

The reduced bearing temperatures also decrease the thermal bending of the rotor disk. With a lower axial temperature gradient, the thermo-elastic deformations are also smaller. Figure 2.2 displays the thermal bending deformations of the runner disk for the different foil materials at the highest load and rotational speed. The deformation is evaluated at the interface between rotor disk and lubricating gap. Between the inner bearing radius r_i and the outer bearing radius r_o , these deformations increase progressively towards the outer radius. It can be seen that the maximum axial deformation can be reduced to below 11 μm for foil material C, while the bearing with the standard foil material A shows a maximum deformation of over 15 μm .

Figure 2.3 compares the influence of the foil material against the commonly applied method of installing a forced cooling flow. The cooling flow is represented by a uniform heat transfer coefficient α_C that is applied to the top foil domain. In order to size the effect, the maximum top foil temperature increase is examined. It is evident that the change from the standard foil material A to material C is equivalent to a cooling heat transfer coefficient α_C between 300 and 400 $\text{W (m}^2\text{K)}^{-1}$ which corresponds to a medium cooling flow level. Furthermore, it is interesting to notice that even for the highest cooling flow investigated here, the maximum top foil temperature increase is still markedly affected by the higher thermal conductivity of materials B and C.

The resulting load capacity at maximum speed may be increased by up to 10% by using a different foil material for the considered bearing geometry. Likewise, for a similar bearing,

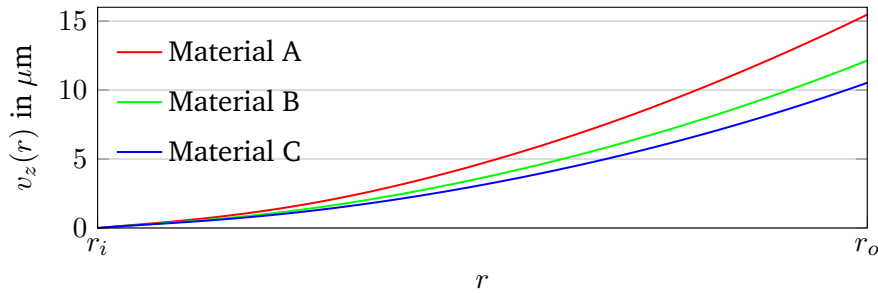


Abbildung 2.2: Thermally induced axial deformation v_z of the rotor disk for foil materials A, B, and C.

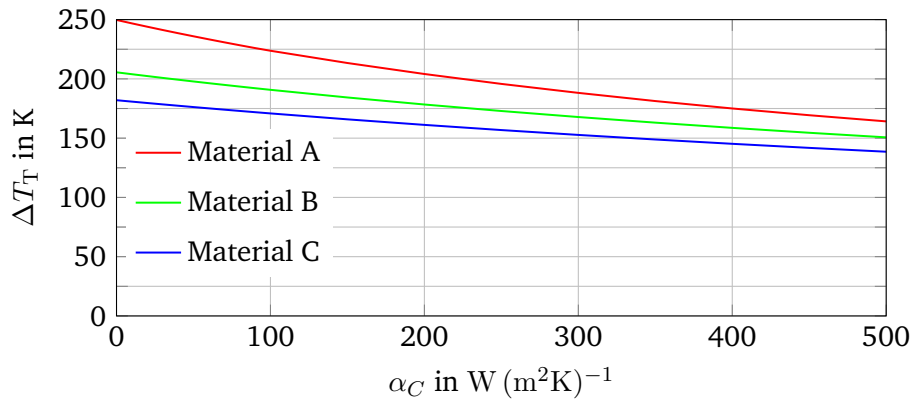


Abbildung 2.3: Maximum top foil temperature increase ΔT_T for different foil materials over cooling heat transfer coefficient α_C at 120 krpm.

the effect of an optimized rotor geometry has been investigated as described in Sec. 1.2.4. The quantitative influence of an axial temperature difference on the bending deformations of the rotor disk are illustrated in Fig. 2.4a. At standstill (0 rpm), a high temperature T_1 is imposed to the bottom edge of the symmetric runner disk which is located at the loaded bearing side of the rotor-bearing assembly (red line). This line represents the interface between the runner disk and the hot air film. The top edge refers to the cooler, unloaded bearing side with the colder temperature T_2 (blue line). All remaining boundaries of the rotor disk are assumed to be adiabatic. The imposed temperature difference $\Delta T = T_1 - T_2$ causes an axial temperature gradient and consequently thermal bending deformations of the runner disk of up to $25 \mu\text{m}$ at the outer disk radius for $\Delta T = 40 \text{ K}$.

Through the alteration of the symmetric rotor disk design S of Fig. 1.9 according to the approaches in Fig. 1.10, the rotor disk deforms due to centrifugal effects when it is rotating. In order to illustrate the impact of the suggested geometry changes, Fig. 2.4b shows the deformation of modified runner disks for three different mass overhangs (outer radius $r_D = 31, 32, 33$ mm) which represent different mass overhangs. The resulting deformation lines can be observed on the right side of Fig. 2.4b. All calculations were carried out at the maximum rotational speed of $n = 120$ krpm. The disk deformation is directed towards the thrust bearing surface with a progressive slope towards the outer diameter. Of course, the larger mass overhangs produce larger disk deformations. For an outer radius of $r_D = 33$ mm, the disk deflects up to 30 μm at the outer radius.

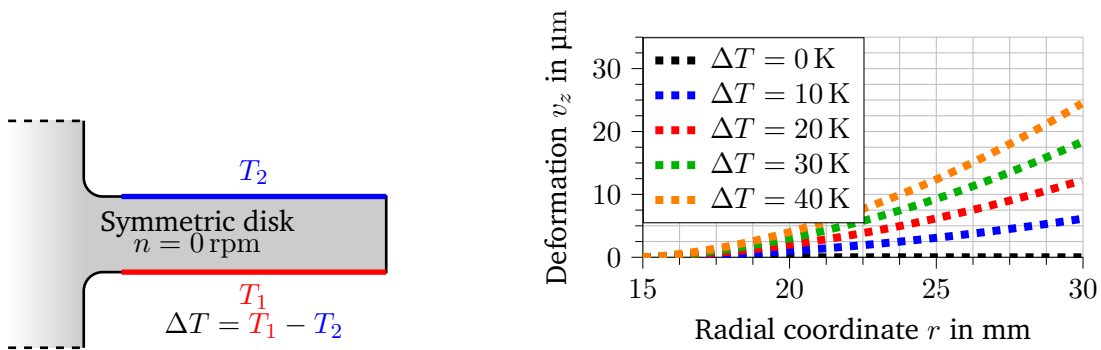
Figure 2.4c shows the resulting deformation of the runner disk of the optimized design O with a mass overhang and a recess. It is again evaluated at the interface to the air film for different rotational speeds. For increasing rotational speeds, the resulting disk deformations increase nonlinearly. The shape of the deformation lines is again showing increasing slopes towards the outer radius of the runner disk as in Fig. 2.4b.

The combination of the unwanted thermal bending deformations with these opposite centrifugal deformations of the runner disk may improve the shape of the lubricating gap height towards a more uniform shape. It should also be mentioned that the increase of these deformations with speed is rather convenient as the thermal bending deformations are also increasing with higher temperatures (connected to higher speeds) and are of a very similar—but opposite—shape. This is the reason why the rotor disk design changes may be used to compensate thermal bending deformations passively.

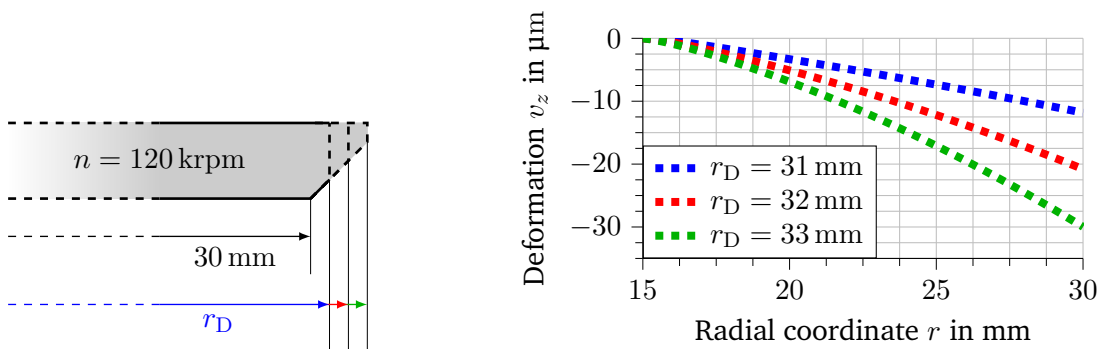
Figure 2.5 presents a comparison of the standard design S and the optimized design O with regard to the rotor temperature, rotor deformations and the global bearing performance parameters, namely thrust load and power loss.

In Fig. 2.5a, the rotor temperature is displayed for both designs at a thrust load of 95 N. Short remark on the chosen operating point: The thrust load of 95 N represents the limit thrust load for the standard design S with $H_{\min} = H_{\min, \text{limit}} = 2$ μm . In order to achieve a fair comparison of the two rotor designs, the same thrust force (95 N) is applied to the bearing with the optimized rotor disk design O. This means that the minimal gap height H_{\min} in the simulation of the optimized design O is larger than 2 μm . Specifically, for a load of 95 N, the minimal gap height is $H_{\min} = 5.3$ μm for the optimized design O.

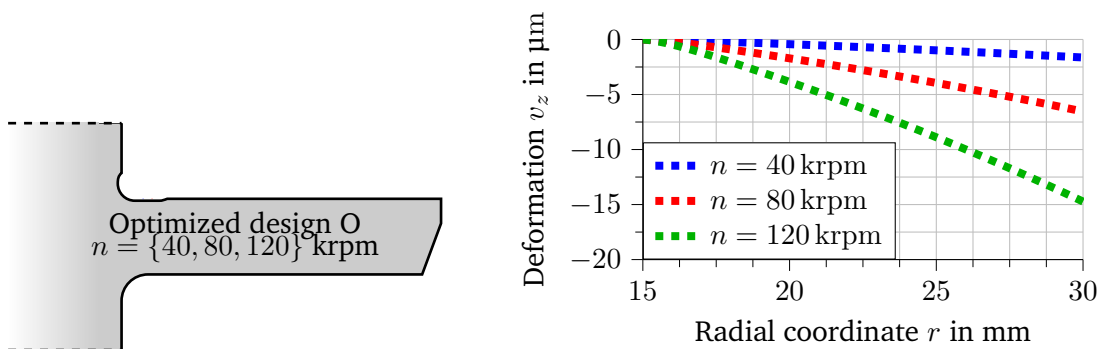
The plot also shows the rotor deformations for the standard rotor design S with two symmetric roundings on the left and the optimized rotor design O with a combination of rounding, recess and asymmetric mass distribution on the right. It is obvious that the rotor temperatures for the standard rotor design S are substantially higher than with the optimized design O. This is the case because—at the same thrust load—the corresponding power loss is higher for the standard rotor design S.



(a) Thermal bending caused by an axial temperature gradient.



(b) Centrifugal bending caused by different mass overhangs.



(c) Influence of the rotational speed on centrifugal bending.

Abbildung 2.4: Rotor disk bending mechanisms.

The bending deformation of the rotor disk, evaluated at the air film interface, is shown in Fig. 2.5b for two different operating points, namely $H_{\min} = 7 \mu\text{m}$ and $H_{\min} = 2 \mu\text{m}$. The deformation of the standard rotor disk S has a progressive slope and reaches a maximum value of $9.3 \mu\text{m}$ for $H_{\min} = 7 \mu\text{m}$ and $18.9 \mu\text{m}$ for $H_{\min} = 2 \mu\text{m}$. The deformation of the optimized rotor disk O (blue) is a combination of the thermal bending deformations with the compensating deformations from centrifugal forces. For the highest load configuration at $H_{\min} = 2 \mu\text{m}$, the maximum rotor deformation $v_z(z = 0, r = r_D)$ is reduced by $7 \mu\text{m}$. For the medium load at $H_{\min} = 7 \mu\text{m}$, a large part of the thermal bending is compensated so that only a maximum deformation of $2.7 \mu\text{m}$ remains. It can be concluded that, with the optimized rotor disk design O, the compensating effect is largest for the case $H_{\min} = 7 \mu\text{m}$, while thermal bending deformations are still present for the case $H_{\min} = 2 \mu\text{m}$.

Figure 2.6 displays the simulation results for a second optimized design. In Fig. 2.6a, the second optimized geometry O2 is shown which combines a large mass overhang ($R_D = 33 \text{ mm}$) with a deep recess (0.26 mm) and the standard notch depth (0.2 mm). With this design, a very high load capacity of approximately 136 N can be achieved, which is equal to a 43% increase compared to the standard rotor disk design S. The corresponding load improvement curve in Fig. 2.6b has its maximum very close to the limit gap height of $H_{\min} = H_{\min, \text{limit}} = 2 \mu\text{m}$, meaning that the compensating effect of the asymmetric rotor disk design is optimal near the limit load.

The performance map of Fig. 2.6c also shows a marked improvement in load capacity when comparing the second optimized design O2 with the previous optimized design O of Fig. 2.5a and with the standard design S. While the second optimized design O2 of Fig. 2.6a reveals a very little increase in power loss for low loads, a significant increase of the load capacity by 24 N in comparison to the optimized design O of Fig. 2.5a and 41 N with regard to the standard design S is achieved.

2.2 Analysis of single-foil bearings including wear prediction

The single-foil thrust bearing with an annular, single-part top foil shows distinct features when compared against multi-foil thrust bearings. After assembly of the bearing and for the case that pressure forces are absent, i. e. at $\Omega = 0 \text{ rad/s}$, the height function possesses a taper-step topography, depicted in Fig. 2.7a. Herein, deformations of the top foil and deformations of the rotor disk are absent, $v_{3,T} = v_z = 0$. The figure shows the characteristic taper profile and the real foil geometry defects, namely the parabolic shape deviation in radial direction and the extended step width as well as the coating accumulations at the inner and outer radius. Furthermore, it should be stressed that the leading edge and the trailing edge have an equal slope in the circumferential direction.

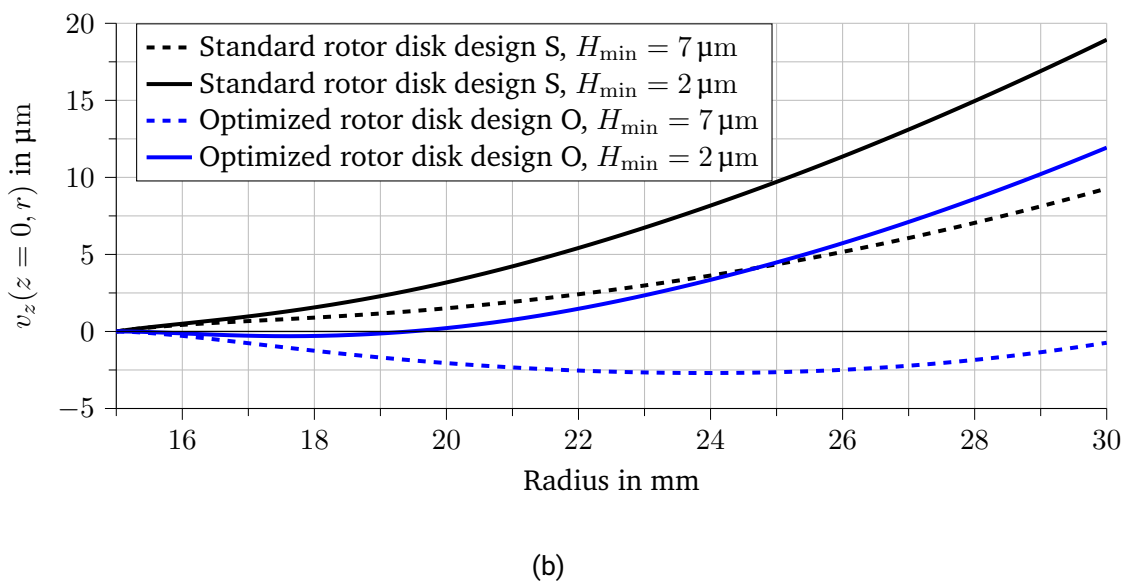
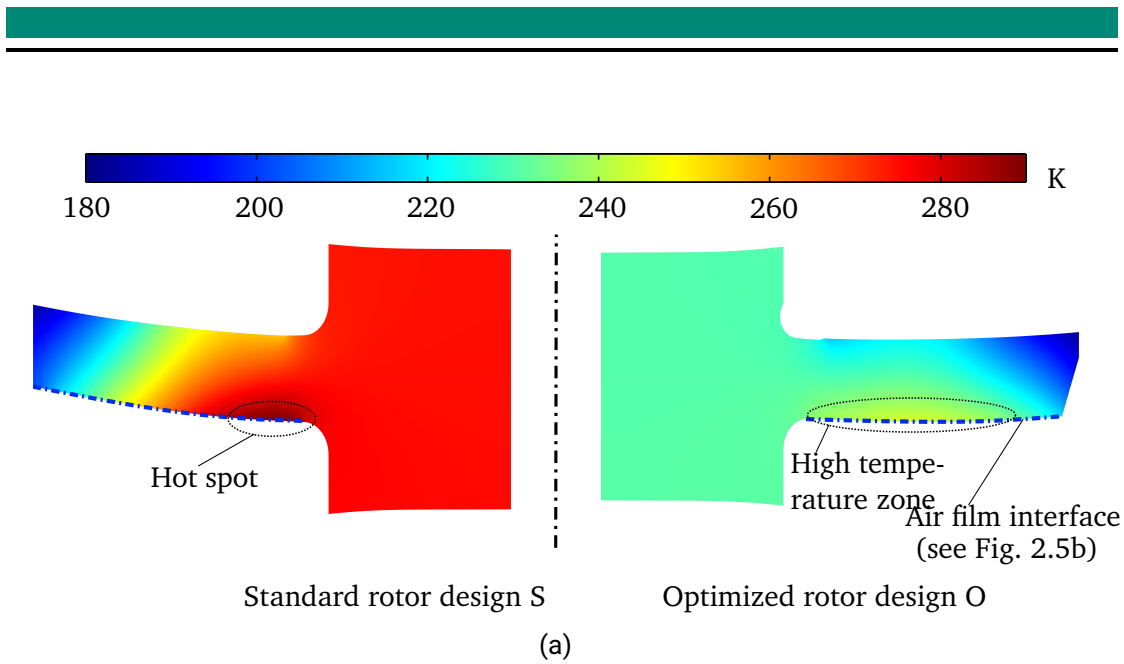
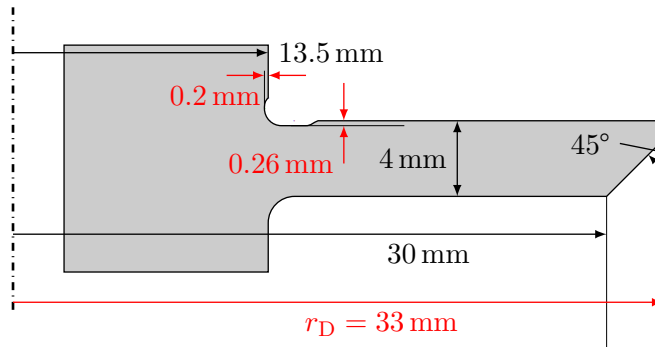
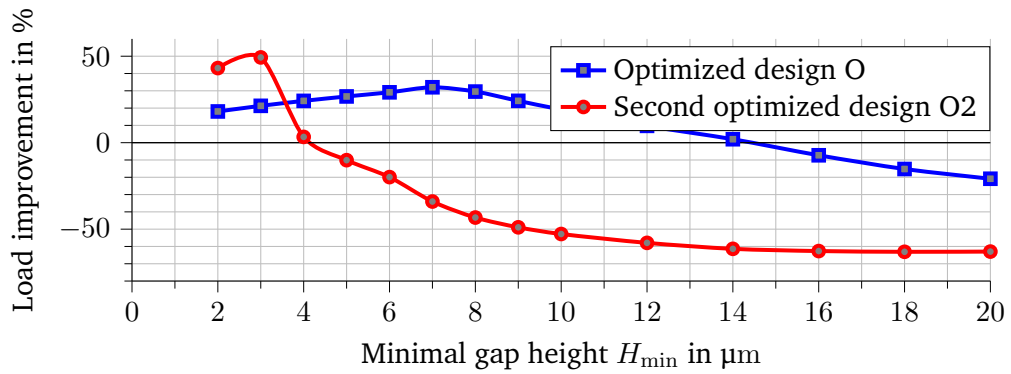


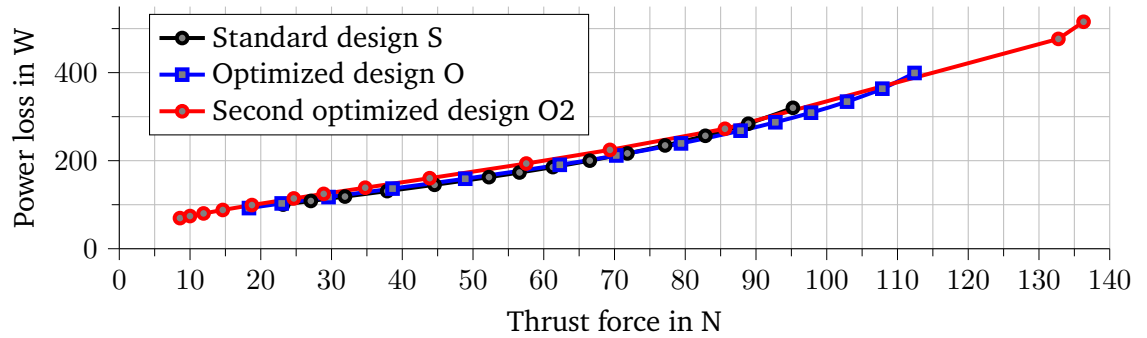
Abbildung 2.5: (a) Rotor disk temperature and deformation for standard (S) and optimized (O) rotor disk configuration and (b) rotor disk deformation on the interface to the air film.



(a) Second optimized design O2.



(b) Load improvement curves.



(c) Power loss vs. thrust force.

Abbildung 2.6: (a) Second optimized design O2, (b) thrust load improvement over the minimal gap height H_{min} , and (c) performance map.

This is a result of the embossing process during manufacturing and is of high relevance for the understanding of the upcoming analysis.

A distinct feature of the presented bearing type is the fact that the unloaded height profile of Fig. 2.7a transforms into a taper-land configuration upon loading, i.e. air film pressure acting on the top foil. The height function $H^{(0)}$ for the loaded case ($\Omega = 120$ krpm) is depicted in Figure 2.7b. In comparison with the unloaded assembly state of Fig. 2.7a, the height function here is mainly changed by the large deformations of the top foil, shown in Fig. 2.7c. Rotor deformations also contribute, but are significantly smaller. The gap height profile (Fig. 2.7b) shows a classical taper-land-type topography, with a converging gap at first and an approximately constant gap height towards the trailing edge. However, at the trailing edge, the height profile converges again right before the beginning of the step. This behavior—the rising at the trailing edge—is typical for bearings with an annular top foil. It is caused by the top foil being bent upwards near the trailing edge. It can be explained as follows:

- In the unloaded, assembled state of the bearing, the top foil contacts the bump foil only at the first bump row due to the initial taper geometry.
- When the bearing is loaded and air film pressure pushes the top foil down onto the bump foil, the top foil is bent at the first bump row, cf. Fig. 2.7c.
- In the course of the loading, the top foil deforms further and eventually contacts the second and the third row of bumps of the bump foil. It should be stressed again that the bumps are of the same height so that the initial gap between the top and bump foil is therefore larger at the second and third bump row.
- When the trailing edge is deformed down, the leading edge is also pulled down by the trailing edge of the adjacent sector. In the simulation model, this effect is achieved via the cyclic coupling of the leading and trailing edge, cf. Eq. (1.13).
- The step is acting as a stiff connector both between the leading and the trailing edge in terms of the deflection $v_{3,T}$ as well as for the slope. If the leading edge is pulled down, the slope has to increase due to the contact to the bump foil. Consequently, the slope at the trailing edge has to increase as well, causing the trailing edge to rise.

Note that—due to the high stiffness of the step—the height difference between the leading and trailing edge is nearly constant (initial value h_s).

The upwards bending at the trailing edge is clearly seen in Fig. 2.7c. The load capacity for the unworn top foil is only $W^{(0)} = 7.5$ N with a power loss of $P_{\text{loss}}^{(0)} = 51.5$ W.

Figure 2.8 shows the height function $H^{(i)}$, the pressure distribution $p^{(i)} - p_0$ and the wear function $H_{\text{wear}}^{(i)}$ for the 3 iteration indices $i = \{13, 16, 20\}$ of the wear simulation. All plots are generated for a rotational speed of 120 krpm and a minimal gap height of $H_{\text{min}} = 2 \mu\text{m}$.

In the height function of the slightly worn state of Fig. 2.8a ($i = 13$), only a small peak at the inner radius near the trailing edge reaches the minimal gap height, while the other areas possess much larger film heights and do not substantially contribute to the pressure generation. Therefore, the entire wear in Fig. 2.8a occurs at this very spot.

In the following iterations, wear increases further at this spot. Afterwards, additional wear occurs towards the middle of the sector at the inner and outer radius, cf. Fig. 2.8b and Fig. 2.8c.

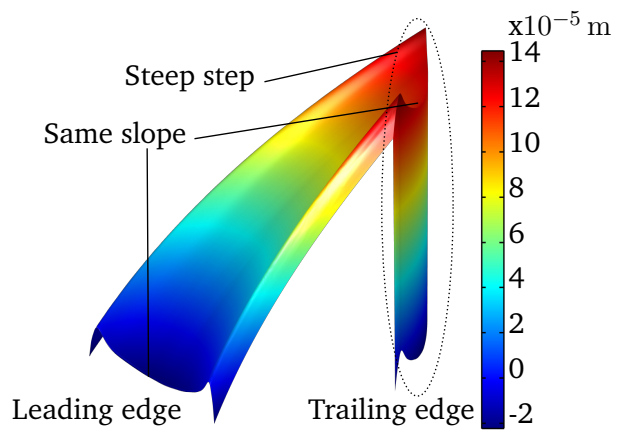
In all 3 iteration steps, the pressure profiles show an increasing peak at the trailing edge. The contribution of the remaining sector area to the load capacity is growing continuously and is most developed in the last wear step of Fig. 2.8c.

Figure 2.9 displays the correlation between power loss P_{loss} in W and thrust force W in N for the considered bearing, cf. Eq. (1.14). Results are shown from simulations and experiments for rotational speeds of 120 krpm and 90 krpm. In experiments, these characteristic curves are recorded after the initial break-in. At a constant rotational speed, the worn bearing is then subjected to a range of loads of up to 100 N. The simulation results were obtained by choosing different values of H_{min} at constant angular velocities Ω and using the wear height function $H_{\text{wear}}^{(23)}$ of the 23rd iteration step.

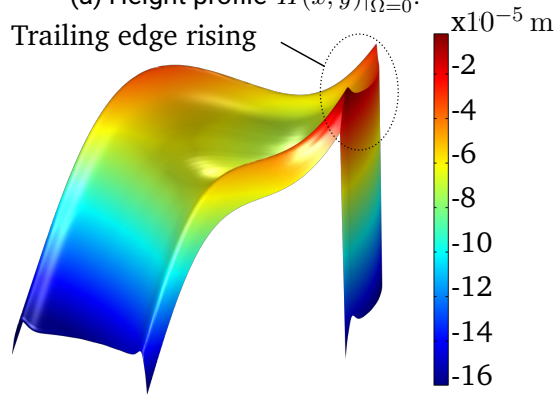
A near linear increase in power loss is observed with a slight bend towards higher power loss for high loads. The power loss is 50 to 80 W higher at 120 krpm in comparison with 90 krpm for the considered load range. For all considered loads and rotational speeds, the agreement of the results of the numerical simulation and the experiment are good. In the end, this was achieved by not only incorporating a real top foil topography into the model, but also accounting for the coating wear that occurs during operation of the bearing.

2.3 Influence of misalignment on the bearing performance

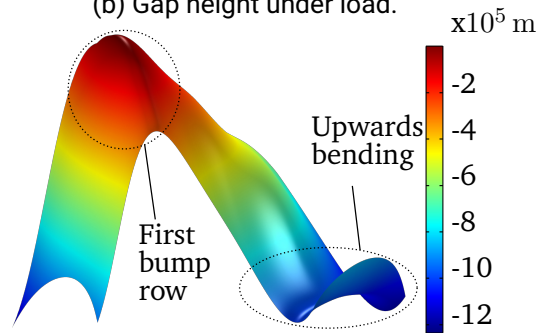
In paper 3 [3], a full bearing TEHD model is used in order to predict the impact of misalignment on the bearing performance. In the case without misalignment between the rotor disk and the bearing, identical pressure distributions across all bearing pads are observed. In general, the highest pressures are observed in the land region of the pad with distinct pressure peaks at the contact lines between top foils and bump foils. These contact lines are marked by black lines in Fig. 2.10. Please note again that the direction of rotation of the rotor disk in the displayed views is counter-clockwise (positive z -direction).



(a) Height profile $H(x, y)|_{\Omega=0}$.

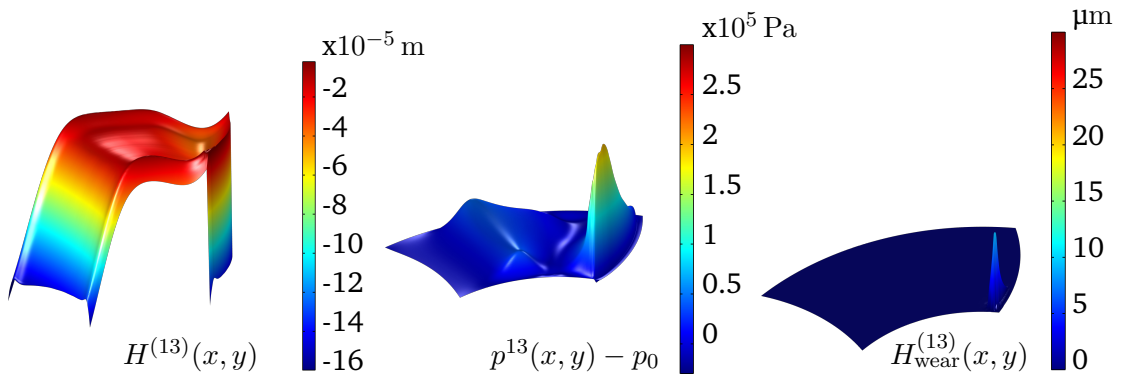


(b) Gap height under load.

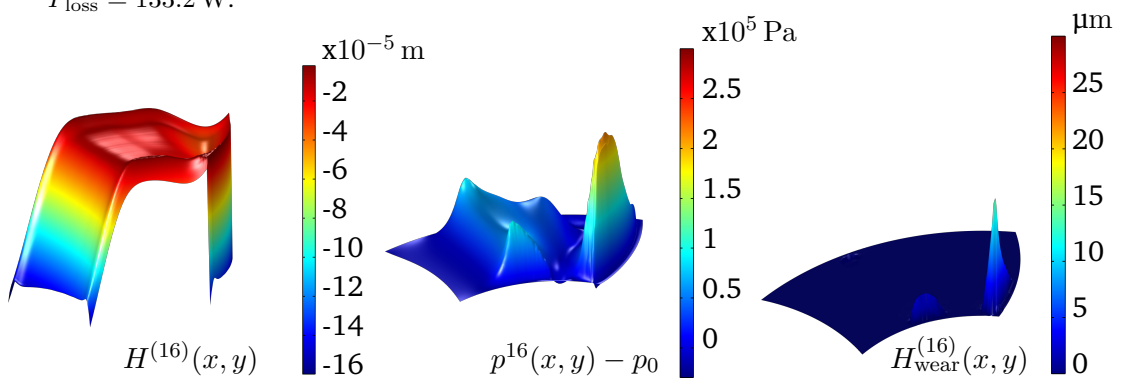


(c) Deformation $v_{3,T}$ of the top foil.

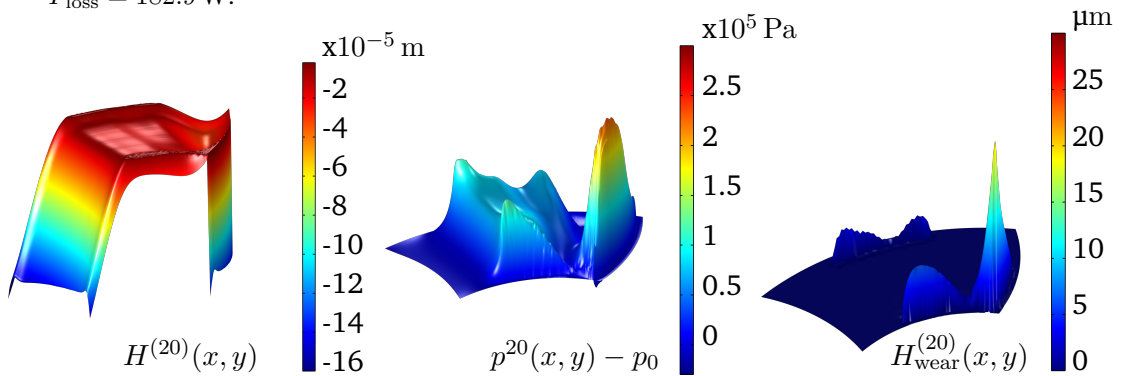
Abbildung 2.7: (a) Height profile after assembly without load, (b) height function $H^{(0)} = H$ for a rotational speed of 120 krpm and a minimal gap height $H_{\min} = 2 \mu\text{m}$, (c) corresponding top foil deformation v_3 under pressure load showing a kink at the first bump row as well as a cyclic deformation profile.



(a) Height function, pressure distribution and wear height function for $i = 13$. $W = 30.0$ N and $P_{\text{loss}} = 133.2$ W.



(b) Height function, pressure distribution and wear height function for $i = 16$. $W = 47.5$ N and $P_{\text{loss}} = 182.9$ W.



(c) Height function, pressure distribution and wear height function for $i = 20$. $W = 65.0$ N and $P_{\text{loss}} = 234.7$ W.

Abbildung 2.8: Wear simulation series showing the height function (left), the pressure distribution (center), and the wear function H_{wear} . Rotational speed is 120 krpm and minimal gap height is $H_{\text{min}} = 2 \mu\text{m}$.

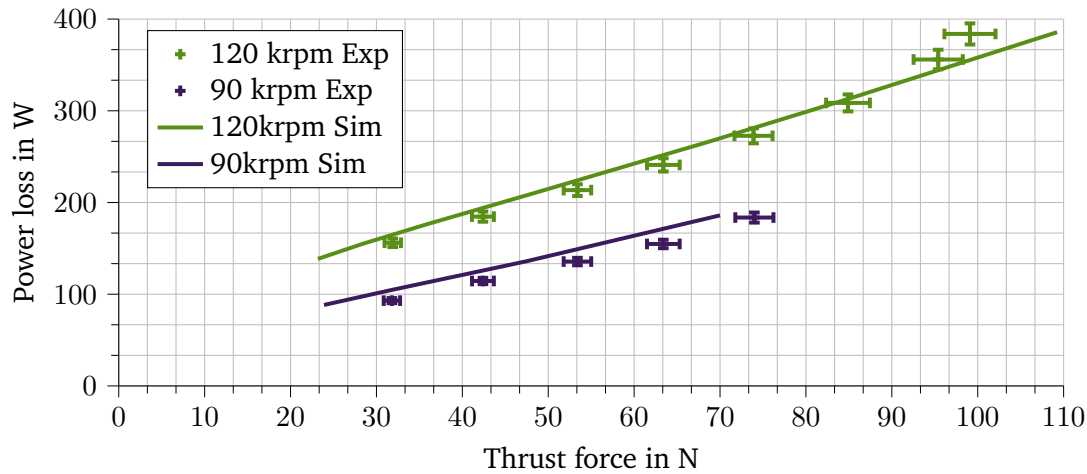


Abbildung 2.9: Performance map of the single-foil thrust bearing for two rotational speeds: power loss in W over the thrust force in N.

When the misalignment angle is increased, the rotor disk tilts towards the lower half of the bearing (negative y -direction). For comparability, all simulations were carried out with a constant minimal air gap height. All six bearing pads show a spot where this minimal gap height is observed while no misalignment is applied. For the case with misalignment, the minimal gap height is only reached on the bottom left pad in Fig. 2.10. It is interesting to notice that—by contrast to rigid thrust bearings—the compliant foil thrust bearing can compensate a portion of the misalignment. This is why the bearing pads in the top half of Fig. 2.10 still show significant pressure buildup. For the case of Fig. 2.10 with $\alpha_{\text{mis}} = 3 \times 10^{-4}$ rad, the pad with the highest load generates two times as much load capacity as the least loaded pad on the top right. However, the overall load capacity of the bearing is very similar with a value of 55 N at a rotational speed of 100 krpm at a minimal gap height of $5 \mu\text{m}$ when compared to results without misalignment. Figure 2.11 shows the thrust load over the misalignment angle α_{mis} . For the investigated misalignment angle range, the thrust load is nearly constant. Simultaneously, through the uneven loading of the bearing, the exerted power loss increases by approximately 6.5% to 164 W.

Short remark on the misalignment angles displayed in this manuscript: A misalignment configuration with $\alpha_{\text{mis}} = 1 \times 10^{-4}$ rad and $\beta_{\text{mis}} = 0$ rad refers to a maximum misalignment of $3 \mu\text{m}$ at the outer radius of the thrust bearing.

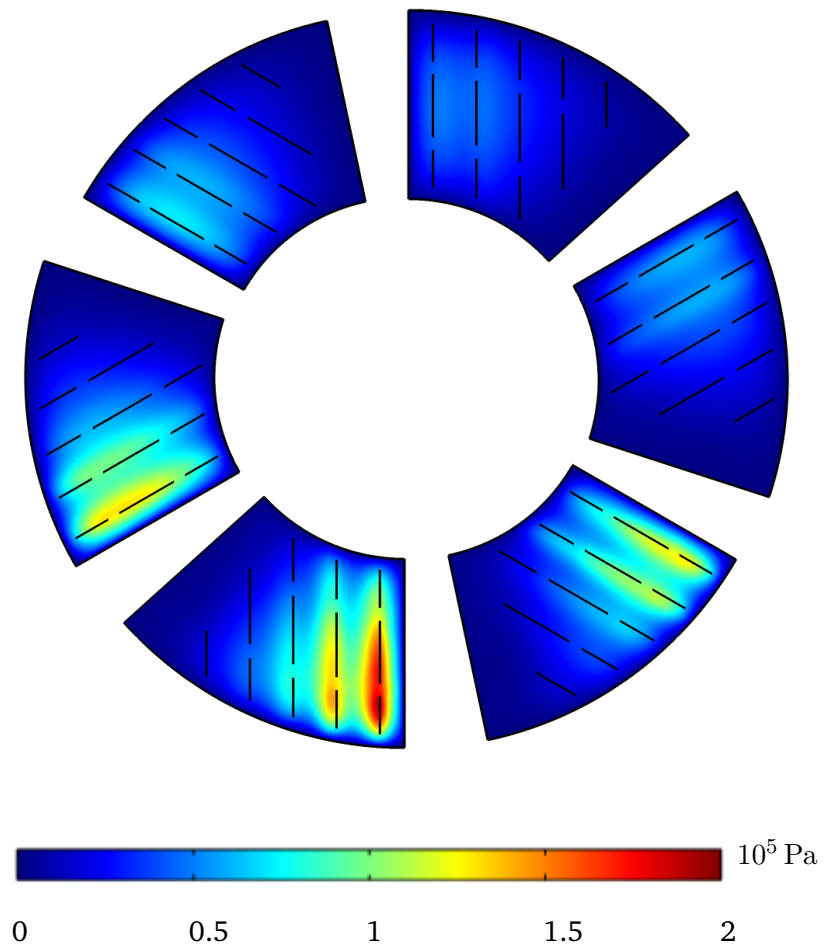


Abbildung 2.10: Pressure distributions $p_i - p_0$ for misalignment angle $\alpha_{\text{mis}} = 3 \times 10^{-4}$ rad.

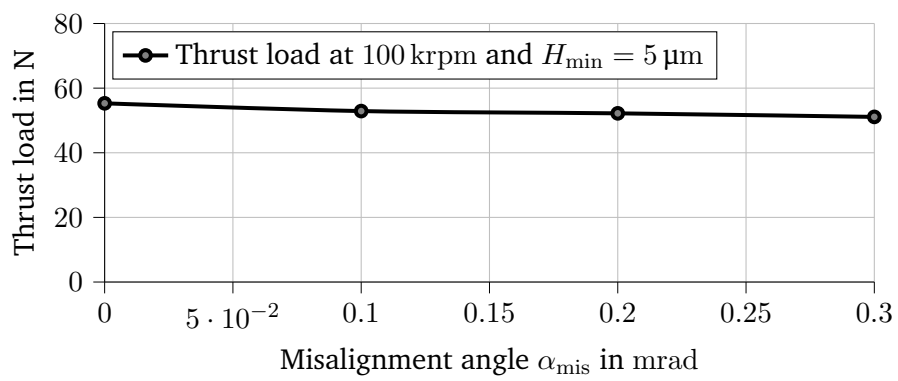


Abbildung 2.11: Thrust load over the misalignment angle α_{mis} .

3 Conclusions

This synopsis presents the summary and synthesis of the publications that are part of this thesis. The global scientific problem lies in the analysis and optimization of air foil thrust bearings with single-foil and multi-foil design. With the use of detailed thermo-elasto-hydrodynamic fully coupled finite element models, heat transfer mechanisms, load generation and bearing failure have been studied extensively for both designs. The models take into account thermoelastic deformations of the rotor, heat transfer in the rotor combined with a detailed analysis of heat transfer to the rotor surroundings (either based on CFD analysis or on a transitional FE flow analysis), air film temperature with a 3D energy equation, air film pressure with a 2D compressible Reynolds equation, elastomechanic deformations of top and bump foil via a nonlinear shell model including contacts, heat conduction in the top foil, and the heat transfer through the bump foil and into the base plate.

It is evident that foil thrust bearing optimization has to take into account thermal management due to the high power losses and the resulting heat generation within the bearing. One of the main mechanisms for performance reduction lies in the thermally induced bending of the runner disk. Hot temperatures at the loaded bearing side in combination with a cooler, unloaded bearing or secondary side cause axial temperature gradients in the disk which in turn cause thermo-elastic deformations (thermal bending). Although these deformations may be partly compensated by the compliance of the foil bearing, they often cause performance degradations up to bearing failure (thermal runaway). The most popular approach to reduce this effect is the introduction of a forced cooling flow underneath the top foil. However, this means that an additional expenditure in pressurized air has to be spent which reduces overall machine efficiency. Furthermore, the machine design gets more complex due to the integration of cooling channels. In this thesis, different ways of reducing or compensating the thermally induced bending deformations are illustrated. Firstly, choosing an alternative foil material with beneficial properties such as high thermal conductivities will reduce the thermal resistance of the foil sandwich and in turn increase the amount of heat that can be conducted into the base plate. The more heat enters the base plate through the foil sandwich, the less heat enters the runner disk so that thermo-elastic bending deformations can be reduced significantly. Even compared

to the impact of typical forced cooling flows, it has been shown that the impact of an optimized foil material is still marked.

A second approach lies in the use of disk bending compensating mechanisms based on centrifugal effects. Small changes in the runner disk design may be used to exploit centrifugal forces acting on the runner disk in order to generate deformations opposite to the thermal bending deformation. The considered approaches include asymmetric rotor disk mass distributions (the resulting centrifugal force does not act along the rotor disk centerline, therefore causing a bending moment for the rotor disk), recesses or asymmetrically placed radii or notches at the base of the rotor disk, isolation layers or cuts to reduce the axial temperature gradient and reduce thermal bending, and different materials (with different densities or thermal expansion properties) for dual-material rotor disks (making use of centrifugal and thermal expansion effects).

The significance of the individual design changes varies, the overhung mass possesses the highest impact. Based on these compensating design changes, an optimized design shows a markedly improved load capacity with increases of up to 40%.

For single-foil thrust bearings with an annular top foil, bearing behavior has to be analyzed using a cyclic coupling approach for a single bearing sector. This approach makes use of the cyclic symmetry of the bearing, enabling bearing parameter changes with feasible computation times. Based on an in-depth analysis of the bearing behavior in combination with experimental testing, two main model improvements were identified. *Firstly*, the real top foil geometry was investigated in measurements. It was found that the real geometry of the top foil deviates markedly in 3 main ways in comparison to the ideal geometry: As a result of the embossing process of the top foils, a parabolically shaped geometry as well as an extended, non-vertical step of the metal top foil are observed. Furthermore, a non-homogeneous coating distribution with accumulations at the inner and outer radius of the bearing sector are found. *Secondly*, a wear algorithm has been developed and implemented in order to take into account the coating wear. The quasi-static, iterative wear routine for the contact wear of the (hard) rotor disk and the (soft) top foil coating is able to predict wear states of the top foil coating. The height function is corrected by a wear height function representing the amount of abraded PTFE coating.

For the maximum operating point with a thrust load of 100 N at a rotational speed of 120 krpm, a wear series has been showcased. The resulting wear from the model matches experimentally observed wear patterns. Furthermore, the bearing performance is analyzed in detail with the resulting wear pattern. A good agreement with performance data from the test rig with regard to a characteristic power loss curve over the thrust load is observed. Thrust bearings with an annular top foil and embossed height profile can only be analyzed when wear is taken into account. Moreover, the real top foil geometry is of key importance in the analysis. Otherwise, numerically obtained load capacity and power loss

are significantly decreased in comparison with experimental data. The coating wear is beneficial and leads to a significantly improved bearing performance.

As a last aspect of foil thrust bearing analysis, it is shown that misalignment causes an uneven distribution of the load onto the bearing pads. This study was carried out with a multi-foil bearing design. By contrast to the reduced investigations which consider symmetric conditions and analyze a single bearing pad, only the presented fully coupled approach considering all individual pads is appropriate for TEHD simulations with misalignment. The detailed model allows for the investigation of foil thrust bearings under misalignment conditions in great depth. Results indicate that, for the presented misalignment cases, the compliant foil thrust bearing was able to compensate and still show similar load capacities. As a downside, the power loss of the thrust bearing is increased due to the uneven loading. The computational effort for each simulation is highly increased when compared to a model with a reduced approach considering only a single bearing pad. With this level of model complexity, an extensive parameter variation for geometrical dimensions is no longer possible.

For future studies, the aspect of real foil and bearing geometries could be investigated for multi-foil bearings. Moreover, wear studies might also advance the research not only for multi-foil thrust bearings, but also for journal bearings. It is expected that the impact of top foil coating wear is also prominent for journal bearings with regard to the initial run-in, but also for lifetime analysis.

Literatur

- [1] Markus Rieken, Marcel Mahner und Bernhard Schweizer. „Thermal optimization of air foil thrust bearings using different foil materials“. In: *Journal of Turbomachinery* 142.10 (2020), S. 101003.
- [2] Markus Eickhoff, Andre Theile, Michael Mayer und Bernhard Schweizer. „Analysis of Air Foil Thrust Bearings with annular top foil including wear prediction, Part I: Modeling and simulation“. In: *Tribology International* 181 (2023), S. 108174.
- [3] Markus Eickhoff, Johannis Triebwasser und Bernhard Schweizer. „Thermo-elasto-hydrodynamic analysis of bump-type air foil thrust bearings considering misalignment“. In: *Bulletin of the Polish Academy of Sciences. Technical Sciences* 71.6 (2023).
- [4] Markus Eickhoff, Johannis Triebwasser, Andre Theile und Bernhard Schweizer. „Compensating thermal bending of the runner disk in hydrodynamic thrust bearings: Simple approach for passively improving the performance of gas bearings“. In: *Tribology International* (2024), S. 109632.
- [5] Markus Rieken. *Numerical Investigations of a Rotor in Journal Bearings with Adjustable Geometry*. Bachelor’s thesis, Technical University of Darmstadt. 2014.
- [6] Bastian Pfau, Markus Rieken und Richard Markert. „Numerische Untersuchungen eines verstellbaren Gleitlagers zur Unterdrückung von Instabilitäten mittels Parameter-Antiresonanz“. In: *First IFToMM DA-CH Conference 2015: 11. März 2015, TU Dortmund*.
- [7] Markus Rieken. *The Finite Element Method Integrated with Floquet Theory for a Column with Harmonic Axial Forcing*. Master’s thesis, Technical University of Darmstadt. 2018.
- [8] Eoin Clerkin und Markus Rieken. „FEM with Floquet Theory for Non-slender Elastic Columns Subject to Harmonic Applied Axial Force Using 2D and 3D Solid Elements“. In: *IUTAM Symposium on Recent Advances in Moving Boundary Problems in Mechanics: Proceedings of the IUTAM Symposium on Moving Boundary Problems, Christchurch, New Zealand, February 12-15, 2018*. Springer. 2019, S. 267–282.

-
-
- [9] Markus Rieken, Marcel Mahner und Bernhard Schweizer. „Thermal optimization of air foil thrust bearings using different foil materials“. In: *Turbo Expo: Power for Land, Sea, and Air*. Bd. 58691. American Society of Mechanical Engineers. 2019, V07BT34A031.
- [10] Pascal Zeise, Marcel Mahner, Marcel Bauer, Markus Rieken und Bernhard Schweizer. „A Reduced Model for Air Foil Journal Bearings for Time-Efficient Run-Up Simulations“. In: *Turbo Expo: Power for Land, Sea, and Air*. Bd. 58691. American Society of Mechanical Engineers. 2019, V07BT34A004.
- [11] P Zeise, M Mahner, M Bauer, M Rieken und B Schweizer. „A reduced semi-analytical gas foil bearing model for transient run-up simulations“. In: *12th International Conference on Vibrations in Rotating Machinery*. CRC Press. 2020, S. 575–587.
- [12] Bernhard Schweizer, Marcel Bauer, Marcel Mahner, Markus Rieken und Pascal Zeise. *Gaslager und ein Verfahren zu dessen Herstellung*. Patent DE50 2019 004 472.2, 2020.
- [13] M Rieken, P Zeise, M Bauer und B Schweizer. „Multiphysical Finite Element Model for Air Foil Thrust Bearing Optimization“. In: *25th International Congress of Theoretical and Applied Mechanics*. IUTAM, 2021, S. 1627–1628.
- [14] Bernhard Schweizer, Marcel Bauer, Pascal Zeise und Markus Rieken. *Axiales federblechfreies Foliengaslager*. Patent DE10 2020 132 177.5, 2022.
- [15] Andre Theile, Markus Eickhoff, Felix Foerster und Bernhard Schweizer. „Analysis of air foil thrust bearings with annular top foil including wear prediction, Part II: Experimental investigations“. In: *Tribology International* 188 (2023), S. 108742.
- [16] Andre Theile, Markus Eickhoff und Johannis Triebwasser. *Rotor mit Rotorscheibe, Strömungsmaschine mit Rotor sowie Verfahren zum Betreiben einer Strömungsmaschine*. Patent DE10 2022 120 067.1, 2024.
- [17] Giri L Agrawal. „Foil Air/Gas Bearing Technology—an Overview“. In: *Turbo Expo: Power for Land, Sea, and Air* 78682 (1997), V001T04A006.
- [18] P Samanta, NC Murmu und MM Khonsari. „The evolution of foil bearing technology“. In: *Tribology international* 135 (2019), S. 305–323.
- [19] Luis San Andrés und Thomas Abraham Chirathadam. „A Metal Mesh Foil Bearing and a Bump-Type Foil Bearing: Comparison of Performance for Two Similar Size Gas Bearings“. In: *Journal of Engineering for Gas Turbines and Power* 134.10 (Aug. 2012), S. 102501. ISSN: 0742-4795. DOI: 10.1115/1.4007061.
- [20] Edward S Zorzi und AIRESEARCH MFG CO OF ARIZONA PHOENIX. *Gas Lubricated Foil Bearing Development for Advanced Turbomachines, Volume II*. 1977.

-
- [21] Kevin C Radil und Christopher DellaCorte. „The effect of journal roughness and foil coatings on the performance of heavily loaded foil air bearings“. In: *Tribology transactions* 45.2 (2002), S. 199–204.
- [22] Franck Balducchi, Mihai Arghir, Romain Gauthier und Emelyne Renard. „Experimental Analysis of the Start-Up Torque of a Mildly Loaded Foil Thrust Bearing1“. In: *Journal of Tribology* 135.3 (2013). ISSN: 0742-4787. DOI: {10.1115/1.4024211}.
- [23] C.-P. Roger Ku und H. Heshmat. „Compliant Foil Bearing Structural Stiffness Analysis: Part I—Theoretical Model Including Strip and Variable Bump Foil Geometry“. In: *Journal of Tribology* 114.2 (Apr. 1992), S. 394–400. ISSN: 0742-4787. DOI: 10.1115/1.2920898.
- [24] C.-P. Roger Ku und Hooshang Heshmat. „Compliant Foil Bearing Structural Stiffness Analysis—Part II: Experimental Investigation“. In: *Journal of Tribology* 115.3 (Juli 1993), S. 364–369. ISSN: 0742-4787. DOI: 10.1115/1.2921644.
- [25] Abdelrasoul M Gad und Shigehiko Kaneko. „A new structural stiffness model for bump-type foil bearings: application to generation II gas lubricated foil thrust bearing“. In: *Journal of Tribology* 136.4 (2014), S. 041701.
- [26] Franck Balducchi, Mihai Arghir und Romain Gauthier. „Experimental analysis of the dynamic characteristics of a foil thrust bearing“. In: *Journal of Tribology* 137.2 (2015), S. 021703.
- [27] Donghyun Lee und Daejong Kim. „Design and Performance Prediction of Hybrid Air Foil Thrust Bearings“. In: *Journal of Engineering for Gas Turbines and Power* 133.4 (Nov. 2010), S. 042501. ISSN: 0742-4795. DOI: 10.1115/1.4002249.
- [28] I Iordanoff. „Analysis of an aerodynamic compliant foil thrust bearing: Method for a rapid design“. In: *Journal of tribology* 121.4 (1999), S. 816–822.
- [29] Donghyun Lee und Daejong Kim. „Design and performance prediction of hybrid air foil thrust bearings“. In: *Journal of Engineering for Gas Turbines and Power* 133.4 (2011).
- [30] Donghyun Lee und Daejong Kim. „Three-Dimensional Thermohydrodynamic Analyses of Rayleigh Step Air Foil Thrust Bearing with Radially Arranged Bump Foils“. In: *Tribology Transactions* 54.3 (2011), S. 432–448. ISSN: 1547-397X. DOI: {10.1080/10402004.2011.556314}.
- [31] Andreas Lehn. „Air Foil Thrust Bearings: A Thermo-Elasto-Hydrodynamic Analysis,“ *Ph.D. thesis, Technische Universität Darmstadt*. 2017.

-
-
- [32] Nguyen LaTray und Daejong Kim. „Design of Novel Gas Foil Thrust Bearings and Test Validation in a High-Speed Test Rig“. In: *Journal of Tribology* 142.7 (2020). ISSN: 0742-4787. DOI: {10.1115/1.4046412}.
- [33] Steve Bauman. „An oil-free thrust foil bearing facility design, calibration, and operation“. In: *58th Annual Meeting*. NASA/TM-2005-213568. 2005.
- [34] Joseph Robert Dickman. „An investigation of gas foil thrust bearing performance and its influencing factors“. Diss. Case Western Reserve University, 2010.
- [35] Robert Jack Bruckner. *Simulation and modeling of the hydrodynamic, thermal, and structural behavior of foil thrust bearings*. Case Western Reserve University, 2004.
- [36] Robert J Bruckner, Christopher DellaCorte und Joseph M Prah. „Analytic modeling of the hydrodynamic, thermal, and structural behavior of foil thrust bearings“. In: *2005 Annual Meeting and Exhibition, 60th Society of Tribologists and Lubrication Engineers*. NASA/TM-2005-213811. 2005.
- [37] Robert J Bruckner. „Performance of simple gas foil thrust bearings in air“. In: *Supercritical CO2 Power Cycle Symposium*. E-18016. 2012.
- [38] Cheng Xiong, Bo Xu, Huanchun Yu, Zhongwen Huang und Zhenqian Chen. „A thermo-elastic-hydrodynamic model for air foil thrust bearings considering thermal seizure and failure analyses“. In: *Tribology International* 183 (2023), S. 108373.
- [39] Brian Dykas, Joseph Prah, Christopher DellaCorte und Robert Bruckner. „Thermal management phenomena in foil gas thrust bearings“. In: *Turbo Expo: Power for Land, Sea, and Air*. Bd. 42401. 2006, S. 1417–1423.
- [40] Yong-Bok Lee, Tae Young Kim, Chang Ho Kim und Tae Ho Kim. „Thrust bump air foil bearings with variable axial load: theoretical predictions and experiments“. In: *Tribology transactions* 54.6 (2011), S. 902–910.
- [41] Brian Dykas, Robert Bruckner, Christopher DellaCorte, Brian Edmonds und Joseph Prah. „Design, fabrication, and performance of foil gas thrust bearings for microturbomachinery applications“. In: *Journal of Engineering for Gas Turbines and Power* 131.1 (2009).
- [42] Zeyuan Zhou, Hekun Jia und Bifeng Yin. „A fully coupled 3D elastohydrodynamic model built with MITC element for static performance analysis of gas foil bearings“. In: *Industrial Lubrication and Tribology* ahead-of-print (2022).
- [43] Kai Feng, Liang-Jun Liu, Zhi-Yang Guo und Xue-Yuan Zhao. „Parametric study on static and dynamic characteristics of bump-type gas foil thrust bearing for oil-free turbomachinery“. In: *Proceedings of the Institution of Mechanical Engineers, Part J: Journal of Engineering Tribology* 230.8 (2016), S. 944–961.

-
- [44] Crystal A Heshmat, David S Xu und Hooshang Heshmat. „Analysis of gas lubricated foil thrust bearings using coupled finite element and finite difference methods“. In: *J. Trib.* 122.1 (2000), S. 199–204.
- [45] Brian David Dykas. „Factors influencing the performance of foil gas thrust bearings for oil-free turbomachinery applications“. Diss. Case Western Reserve University, 2006.
- [46] Marcel Mahner, Andreas Lehn und Bernhard Schweizer. „Thermogas- and thermo-hydrodynamic simulation of thrust and slider bearings: Convergence and efficiency of different reduction approaches“. In: *Tribology International* 93 (2016), S. 539–554. ISSN: 0301-679X. DOI: {10.1016/j.triboint.2015.02.030}.
- [47] Andreas Lehn, Marcel Mahner und Bernhard Schweizer. „Characterization of static air foil thrust bearing performance: an elasto-gasdynamical analysis for aligned, distorted and misaligned operating conditions“. In: *Archive of Applied Mechanics* 88.5 (2018), S. 705–728. ISSN: 0939-1533. DOI: {10.1007/s00419-017-1337-7}.
- [48] Andreas Lehn, Marcel Mahner und Bernhard Schweizer. „A thermo-elasto-hydrodynamic model for air foil thrust bearings including self-induced convective cooling of the rotor disk and thermal runaway“. In: *Tribology International* 119 (2018), S. 281–298. ISSN: 0301-679X. DOI: {10.1016/j.triboint.2017.08.015}.
- [49] Andreas Lehn, Marcel Mahner und Bernhard Schweizer. „Elasto-gasdynamical modeling of air foil thrust bearings with a two-dimensional shell model for top and bump foil“. In: *Tribology International* 100 (2016), S. 48–59. ISSN: 0301-679X. DOI: {10.1016/j.triboint.2015.11.011}.
- [50] Andreas Lehn, Marcel Mahner und Bernhard Schweizer. „A Contribution to the Thermal Modeling of Bump Type Air Foil Bearings: Analysis of the Thermal Resistance of Bump Foils“. In: *Journal of Tribology* 139.6 (2017). ISSN: 0742-4787. DOI: {10.1115/1.4036631}.
- [51] D. Dowson. „A generalized Reynolds equation for fluid-film lubrication“. In: *International Journal of Mechanical Sciences* 4.2 (1962), S. 159–170. ISSN: 0020-7403. DOI: {10.1016/S0020-7403(62)80038-1}.
- [52] Donghyun Lee und Daejong Kim. „Thermohydrodynamic Analyses of Bump Air Foil Bearings With Detailed Thermal Model of Foil Structures and Rotor“. In: *Journal of Tribology* 132.2 (2010). ISSN: 0742-4787. DOI: {10.1115/1.4001014}.

-
-
- [53] Eric Reissner. „The effect of transverse shear deformation on the bending of elastic plates“. In: *Journal of Applied Mechanics* 12 (1945), S. 69–77.
- [54] Yavuz Bařar und Wilfried B. Krätzig. *Mechanik der Flächentragwerke: Theorie, Berechnungsmethoden, Anwendungsbeispiele*. 1. Aufl. Grundlagen der Ingenieurwissenschaften. Wiesbaden: Vieweg+Teubner Verlag, 1985. ISBN: 9783322939845. DOI: {10.1007/978-3-322-93983-8}.
- [55] Martin H. Sadd. *Elasticity: Theory, Applications, and Numerics*. Elsevier, 2005.
- [56] Joachim Rösler, Harald Harders und Martin Bäker. *Mechanical Behaviour of Engineering Materials: Metals, Ceramics, Polymers, and Composites*. Springer Science & Business Media Berlin/Heidelberg, 2007.
- [57] Christopher DellaCorte und Mark J Valco. „Load Capacity Estimation of Foil Air Journal Bearings for Oil-Free Turbomachinery Applications“. In: *Tribology Transactions* 43.4 (2000), S. 795–801.
- [58] CL Ong und JM Owen. „Computation of the Flow and Heat Transfer Due to a Rotating Disc“. In: *International Journal of Heat and Fluid Flow* 12.2 (1991), S. 106–115.
- [59] T. Cebeci und A.M.O. Smith. *Analysis of Turbulent Boundary Layers*. New York: Academic Press, 1974.

Paper 1

Markus Rieken, Marcel Mahner und Bernhard Schweizer. „Thermal optimization of air foil thrust bearings using different foil materials“. In: *Journal of Turbomachinery* 142.10 (2020), S. 101003

<https://doi.org/10.1115/1.4047633>

©2020 by ASME.

This manuscript version is made available under the CCC license 1513092-1.

Thermal Optimization of Air Foil Thrust Bearings Using Different Foil Materials

Markus Rieken¹

Department of Mechanical Engineering,
Institute of Applied Dynamics,
Technical University of Darmstadt,
Darmstadt 64287, Germany
e-mail: rieken@ad.tu-darmstadt.de

Marcel Mahner

Department of Mechanical Engineering,
Institute of Applied Dynamics,
Technical University of Darmstadt,
Darmstadt 64287, Germany
e-mail: mahner@ad.tu-darmstadt.de

Bernhard Schweizer

Department of Mechanical Engineering,
Institute of Applied Dynamics,
Technical University of Darmstadt,
Darmstadt 64287, Germany
e-mail: schweizer@ad.tu-darmstadt.de

Air foil bearings are used in turbomachinery applications with high speeds and in oil-free environments. Their numerical analysis has to account for the multiphysics of the problem. This work features a detailed thermo-elasto-hydrodynamic model of an air foil thrust bearing with bump-type foil-structure. The bearing geometry is designed to produce a high load capacity while maintaining thermally stable conditions. The presented model considers foil deformations using a Reissner–Mindlin-type shell theory. Dry friction (stick-slip approach) between the top foil, the bump foil, and the base plate is taken into account in the model. Reynolds equation from the lubrication theory is used to study the hydrodynamic behavior of the air film. A thermal model of the lubricating gap, the foil sandwich, and the rotor disk including heat fluxes into the rotor and the periphery as well as a cooling flow on the backside of the rotor disk are presented. Elastic deformations of the rotor disk due to centrifugal effects are calculated; deformations caused by temperature gradients are investigated as well. In air foil thrust bearings, very high temperatures are often observed and a forced cooling flow through the foil sandwich has to be applied. Using a cooling flow by applying a pressure difference between the inner and outer radius of the thrust bearing has several drawbacks: the additional cooling flow reduces the overall efficiency of the machine and requires additional constructive measures. In this work, a passive cooling concept is analyzed, where the typical steel foils are replaced with other materials, which have a significantly higher thermal conductivity. The simulation results show that the bearing temperatures can be reduced markedly (up to 70 °C in the considered test case) by this approach. [DOI: 10.1115/1.4047633]

Keyword: heat transfer and film cooling

1 Introduction

Air foil bearings have been developed for the use in air cycle machines starting in the 1960s [1]. High reliability combined with high-speed operation among many other advantages secure their success even though they show comparably low load capacities. Furthermore, high frictional resistances and significant wear during start and stop phases are observed [2].

For the air foil thrust bearing (AFTB), optimizing the load capacity while maintaining compliance for compensation of misalignment and, more importantly, limiting the temperatures that are stressing the rotor disk as well as the foils and their coating is the most important task. Experimental tests are very useful for validation, but too costly for bearing optimization. Therefore, powerful and accurate theoretical models were developed by different authors, e.g., in Refs. [3–6]. This paper features a fully coupled elasto-thermo-hydrodynamic (ETHD) model of an AFTB [7,8] which has been validated by experiment.

In practice, the AFTB is integrated in the stationary housing facing a disk which is part of the rotor. The AFTB possesses a base plate on which multiple bump foils are mounted. The latter are covered with flat and coated top foils. The bumps of the bump foils are manufactured with increasing height, introducing a converging gap between top foil and runner disk. As the rotor disk starts to rotate, air is sucked into the wedge-shaped lubricating gap. This causes a pressure distribution that eventually can carry the axial loads acting upon the rotor system. For lower speeds, dry friction occurs so that top foil and rotor coatings are used [9].

In comparison to rigid air bearings, foil air bearings show lower load capacities due to nonuniform bump foil deformations and foil sagging effects. On the other hand, they are able to compensate for misalignment and centrifugal or thermal growth of the runner disk [10].

This paper gives an overview of the underlying model and discusses the thermal optimization of the bearing by using foil materials with higher thermal conductivity.

2 Multiphysics Model

For the modeling of an AFTB, physical equations from three disciplines are used (see Fig. 1), namely,

- (1) thermo-elasticity (deformations of the top and bump foils and of the rotor disk),
- (2) hydrodynamics (pressure distribution in the lubricating gap and flow in the cooling region), and
- (3) thermodynamics (temperature of top foil, lubricating gap, cooling flow region (CFR), radial gap, rotor and rotor disk).

In the following paragraphs, the main modeling equations for all important components of the bearing are described. Figure 1 gives an overview over the bearing components, the model equations and the main heat flow paths. The governing partial differential equations (PDEs) are discretized using finite elements (FEs). The resulting nonlinear FE model has approximately 425,000 degrees-of-freedom for which stationary studies are carried out. Due to symmetry (misalignment of the rotor disk is not considered here), only one of the altogether six pads has to be investigated. The investigated rotor-bearing system has the following main parameters: rotor diameter $d_R = 27$ mm, disk radius $r_D = 31$ mm, disk thickness $t_D = 4$ mm, inner top foil radius $r_i = 15$ mm, outer top foil

¹Corresponding author.

Contributed by the International Gas Turbine Institute (IGTI) of ASME for publication in the JOURNAL OF TURBOMACHINERY. Manuscript received July 5, 2019; final manuscript received April 29, 2020; published online September 11, 2020. Assoc. Editor: David G. Bogard.

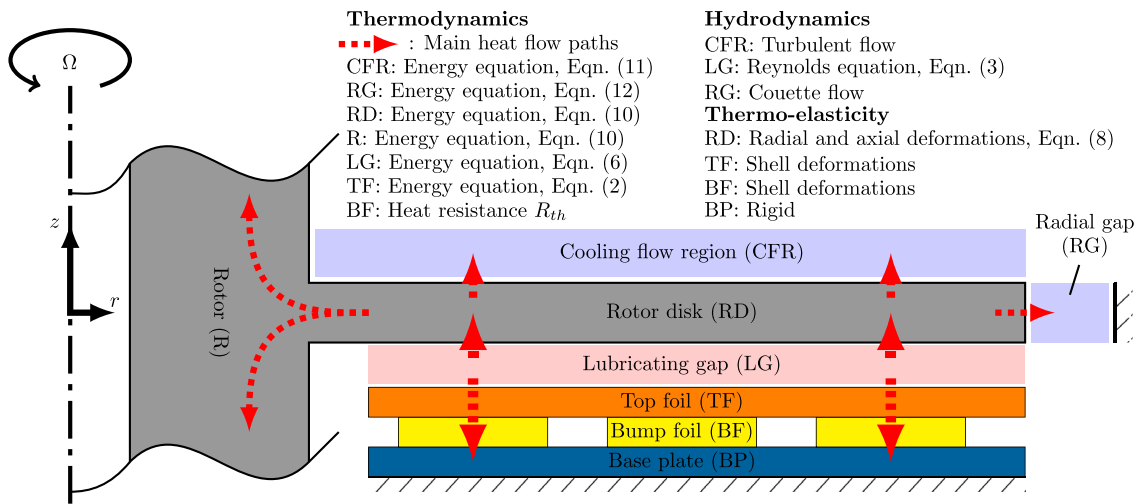


Fig. 1 Overview: model components and equations

radius $r_o = 30$ mm, and maximum rotational speed $\Omega_{\max} = 120$ krpm.

2.1 Top and Bump Foils

2.1.1 Elasto-Mechanics. While the base plate of Fig. 1 is treated as a rigid body, deformations of the thin bump and top foils due to pressure forces can not be ignored. The governing equations used in the current model for the foil deformations originate from the Reissner–Mindlin shell theory [11].

The deformations of the shell are described via the deformations v_i ($i = 1, 2, 3$) of the shell middle surface F in \vec{i}_1 , \vec{i}_2 , and \vec{i}_3 -direction and the two rotations w_α with $\alpha = 1, 2$ of the normal fibers.

The external forces $\vec{p} = p^\alpha \vec{a}_\alpha + p^3 \vec{a}_3$ and the internal force variables $\vec{n}^\alpha = n^{\alpha\beta} \vec{a}_\beta + q^\alpha \vec{a}_3$ and $\vec{m}^\alpha = m^{\alpha\beta} \vec{a}_3 \times \vec{a}_\beta$ with the stress resultant tensor $n^{\alpha\beta}$, the transverse shear stress q^α and the moment tensor $m^{\alpha\beta}$ are connected via the equilibrium equations

$$\begin{aligned} -p^\beta &= n^{\alpha\beta}|_\alpha - q^\alpha b_\beta^\alpha \quad (\beta = 1, 2), \quad -p^3 = n^{\alpha\beta} b_{\alpha\beta} + q^\alpha a_\alpha \\ 0 &= m^{\alpha\beta}|_\alpha - q^\beta \end{aligned} \quad (1)$$

Figures 2(a) and 2(b) give an overview over the used coordinate system, metrical properties of the shell and force variables [11]. Inserting the metrical and curvature properties of the shell (top or bump foil) into Eq. (1) and utilizing constitutive equations from linear elasticity, five differential equations are obtained to solve for the five unknown deformations.

Note that Young's modulus of the materials is assumed to decrease linearly with temperature. The top foil is a flat metal plate and is described by the deformations v_{iT} ($i = 1, 2, 3$) and $w_{\alpha T}$ ($\alpha = 1, 2$). The bump foil geometry is more involved. It consists of several corrugated strips with a pattern of bumps, roundings, and connecting bridges, see Fig. 3(c). Each bump arc possesses a specific height which induces a wedge-shaped height profile for the overlying top foil as shown in Fig. 3(b). Deformations of the bump foils are described by v_{iB} ($i = 1, 2, 3$) and $w_{\alpha B}$ ($\alpha = 1, 2$).

Boundary conditions and coupling

While the bump foils are fixed on their respective trailing edge (left side in Fig. 3(b)), the top foil has its trailing edge fixed as seen in Figs. 3(a) and 3(b). In order to fix the top foil while sustaining compliance a small region without pressure load is added next to the taper region. For the detailed derivation of the formulations and description of the geometry, the interested reader is referred to Refs. [7,12]. The normal contact force F_N between bump and top foil on the one hand and bump foil and base plate on the other hand are

both implemented using a penalty formulation, $F_N = c \Delta v_3$, $c = 1 \times 10^{11}$ N/m being the penalty stiffness, and Δv_3 is the penetration depth. The tangential behavior between top and bump foil is modeled via a stick-slip approach (regularized Coulomb friction, cf. Ref. [13]), $F_{T\alpha} = \mu \cdot \text{step}(\Delta v_\alpha) F_N (|\Delta v_\alpha| / \sqrt{\Delta v_1^2 + \Delta v_2^2}) \vec{i}_\alpha$, ($\alpha = 1, 2$), where $F_{T\alpha}$ is the tangential force in the two directions \vec{i}_1 and \vec{i}_2 , $\Delta v_\alpha = v_{\alpha T} - v_{\alpha B}$, μ is the friction coefficient ($\mu = 0.1$ in this work), and v_α is the tangential deflection in the directions \vec{i}_1 and \vec{i}_2 . The function $\text{step}(\cdot)$ describes a sign function where the sharp jump has been smoothed out over a small transition zone. This approach can also be adapted to the contact between bump foil and base plate. Thus, the foil sandwich is represented as a 2D nonlinear structural shell model (nonlinearity due to contact).

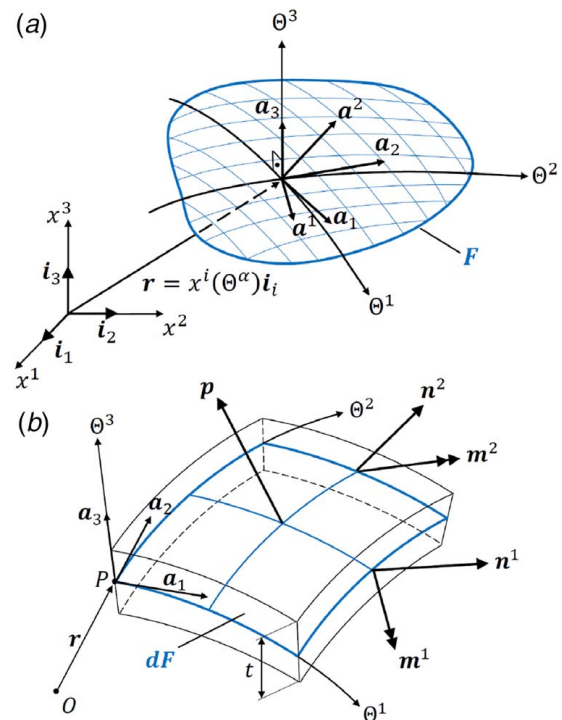


Fig. 2 (a) Metrical properties and (b) force variables

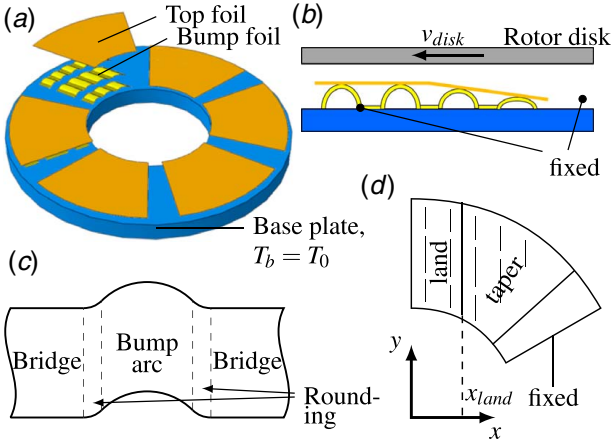


Fig. 3 (a) AFTB with six pads, (b) sectional view, (c) bump sections, and (d) view of single top foil pad

2.1.2 Thermodynamics. For the top foil temperature T_T , a 2D energy equation

$$-\lambda_T t_T \Delta T_T = q_{T,in} + q_{T,out} \quad (2)$$

with thermal conductivity λ_T , thickness t_T and heat fluxes $q_{T,in} = (\lambda_{LG} \partial T_{LG} / \partial z)|_{z=-h}$ and $q_{T,out} = q_b$ at the contact lines and $q_{T,out} = q_c$ everywhere else is solved.

Boundary conditions and coupling

Over the whole top foil, an incoming heat flux from the lubricating gap $q_{T,in}$ is calculated with air conductivity λ_{LG} and temperature T_{LG} from the lubricating gap. A possible cooling heat flux originating from active cooling $q_c = -\alpha_c (T_T - T_0)$ with heat transfer coefficient α_c can be implemented as well (cooling air temperature T_0). Heat conduction from the top foil into the base plate is modeled as an outgoing heat flux $q_b = -2/R_{th}(T_T - T_{Base})$ at the contact lines between top and bump foil, visible in Fig. 3(d). Herein, $R_{th} = R_{TB,air} + R_{bump} + R_{Bb,air}$ is the thermal resistance of a half bump arc composed of the thermal contact resistance between top and bump foil $R_{TB,air}$, thermal conduction resistance of the half bump arc R_{bump} and the contact resistance between bump foil and base plate $R_{Bb,air}$, cf. [14]. The leading edge of the top foil is assumed to have the same temperature as the air in the LG at the inlet (Fig. 4(b)). On the remaining three boundaries, a zero heat flux condition is imposed. Note that the influence of the pressure acting upon the foil sandwich is of subordinate importance for the thermal contact resistances [7].

2.2 Lubricating Gap

2.2.1 Hydrodynamics. Using the generalized Reynolds equation of lubrication theory [15,16] combined with an averaging approach [4,17] for the temperature T_{LG} , a simplified Reynolds equation in 2D cartesian coordinates is obtained to calculate the pressure distribution $p(x, y)$ in the lubricating gap with height profile $h(x, y)$:

$$\frac{\partial}{\partial x} \left[\frac{\rho(p, T_m) h^3}{12\eta(T_m)} \frac{\partial p}{\partial x} \right] + \frac{\partial}{\partial y} \left[\frac{\rho(p, T_m) h^3}{12\eta(T_m)} \frac{\partial p}{\partial y} \right] = \frac{\partial}{\partial x} \left[\frac{\rho(p, T_m) U h}{2} \right] + \frac{\partial}{\partial y} \left[\frac{\rho(p, T_m) V h}{2} \right] \quad (3)$$

Herein, ρ is the density, η is the dynamic viscosity, and U and V are the velocities of the runner disk in x - and y -direction, respectively. The Reynolds number of the flow can be estimated by $Re \approx \Omega_{max} r_o h_{min} \rho / \eta < 100$ with $h_{min} = 5 \mu\text{m}$. The gap height is

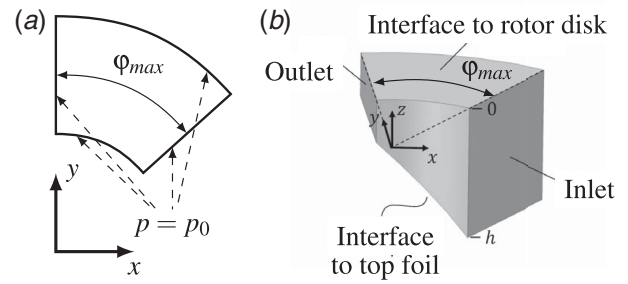


Fig. 4 (a) 2D pressure region and (b) 3D lubricating gap for calculating T_{LG}

calculated as

$$h(x, y) = h_{nom} + d_{mis} + v_{3T} + v_{zD} \quad (4)$$

where d_{mis} is a term from rotor disk misalignment (neglected in this study). v_{3T} is the top foil deformation (perpendicular to the gap). v_{zD} is the thermo-elastic deformation of the rotor disk perpendicular to the gap. This deformation is mainly generated by centrifugal effects and temperature gradients in the z -direction (thermally induced bending of the disk), see Eq. (8). The nominal gap height h_{nom} is defined by the height profile of the bumps (bumps are approximately $500 \mu\text{m}$ high) which is linearly decreasing for $x > x_{land}$: $h_{nom}(x) = h_2 + m(x - x_{land})$ (taper region with slope m , see Fig. 3(d)) and constant for $x \leq x_{land}$ (land region): $h_{nom}(x) = h_2$. Figure 5 shows the iterative procedure of the simulation. The parameter h_2 is updated until a prescribed minimal gap height of $5 \mu\text{m}$ is achieved.

Boundary conditions and coupling

Ambient pressure p_0 is assumed at the boundaries, cf. Fig. 4(a). As the density and viscosity of air are dependent on temperature (and pressure), they are evaluated at a mean temperature T_m :

$$T_m(x, y) = \frac{1}{h(x, y)} \int_0^h T(x, y, z) dz \quad (5)$$

2.2.2 Thermodynamics. For the temperature calculation in the lubricating gap, the 3D energy equation (without external heat source terms) is solved: $\rho(D\epsilon/Dt) = -\text{div} \vec{q} + S \cdot \nabla \vec{u}$. The specific internal energy ϵ for ideal gases is related to the temperature by the isochoric specific heat capacity c_V via $D\epsilon = c_V D T$. The boundary heat flux is $\vec{q} = -\lambda \nabla T$ from Fourier's law with thermal conductivity λ . The Cauchy stress tensor $S = -pI + T$ with $T = 2\eta D - \frac{2}{3}\eta \text{tr}(D)I$ for a Newtonian material law is used. Herein, the rate of strain tensor is defined as $D = \frac{1}{2}(\nabla \vec{u} + \nabla(\vec{u})^T)$ with the fluid velocity vector $\vec{u} = (u, v, w)^T$. If the continuity equation $D\rho/Dt + \rho \text{div} \vec{u} = 0$ for the density ρ and the correlations $p =$

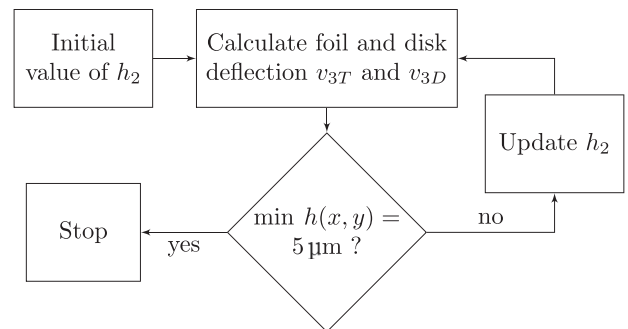


Fig. 5 Flowchart of gap height iteration

$\rho R_{spec} T_{LG}$ and $c_V = c_P - R_{spec}$ for an ideal gas with the specific gas constant R_{spec} and the isobaric specific heat capacity c_P are used, the energy equation reads as $\rho c_P (DT/Dt) = \nabla \cdot (k \nabla T) + (p/\rho)(Dp/Dt) + T \cdot \nabla \vec{u}$. A magnitude of order analysis allows for the following simplifications: (1) pressure gradient $\partial p/\partial z \approx 0$, (2) velocity gradients other than those in z -direction ($\partial u/\partial z$ and $\partial v/\partial z$) are omitted, and (3) planar diffusion (x - and y -direction) and vertical convection (z -direction) are neglected. Finally, the energy equation used for calculating the temperature $T_{LG}(x, y, z)$ in the air film is

$$\rho_{LG} c_{P, LG} \left[u \frac{\partial T_{LG}}{\partial x} + v \frac{\partial T_{LG}}{\partial y} \right] = \left[\frac{\partial}{\partial z} \left(\lambda_{LG} \frac{\partial T_{LG}}{\partial z} \right) \right] + \left[u \frac{\partial p}{\partial x} + v \frac{\partial p}{\partial y} \right] + \eta_{LG} \left[\left(\frac{\partial u}{\partial z} \right)^2 + \left(\frac{\partial v}{\partial z} \right)^2 \right] \quad (6)$$

Boundary conditions and coupling

At the interfaces, the temperature T_{LG} is coupled to the top foil and the rotor disk via interface conditions, i.e., temperatures and heat fluxes are assumed to be equal, cf. Fig. 4(b). At the inlet boundary of the lubricating gap, the temperature is assumed to be the same as the rotor disk temperature. This assumption has been shown to be a good approximation, see Refs. [7,8]. As the energy Eq. (6) is solved in the 3D cartesian region of Fig. 4(b) and the rotor disk is assumed to show axisymmetric behavior (r - z -region as in Fig. 1), the boundary heat flux $q_{LG,D}(x, y, z=0)$ in the lubricating gap at the interface to the rotor disk is transformed and averaged over the circumferential coordinate φ :

$$q_{LG,D}(r) = \frac{1}{r \varphi_{max}} \int_0^{\varphi_{max}} \left[-\lambda_{LG} \frac{\partial T_{LG}}{\partial z} \right]_{z=0} r d\varphi \quad (7)$$

Note that φ_{max} describes the extension of the lubricating gap in circumferential direction. The other three boundaries of the lubricating gap are assumed to be adiabatic (zero flux).

2.3 Rotor Disk and Rotor

2.3.1 Thermo-elasticity. Radial and axial deformations of the rotor disk are calculated based on the Navier-Lamé equations [18] with an account for thermal stresses. Assuming an axisymmetric stress distribution in the rotor and the disk, the equilibrium equations in radial (r -) and axial (z -) direction are as follows:

$$\begin{aligned} \frac{\partial \sigma_{rr}}{\partial r} + \frac{\partial \sigma_{rz}}{\partial z} &= -f_r - \frac{\sigma_{rr} - \sigma_{\phi\phi}}{r} \\ \frac{\partial \sigma_{rz}}{\partial r} + \frac{\partial \sigma_{zz}}{\partial z} &= -f_z - \frac{\sigma_{rz}}{r} \end{aligned} \quad (8)$$

σ_{ij} are the components of the stress tensor and f_i are the external forces. With the assumption of small deformations and the constitutive equations for a linear elastic, homogeneous, isotropic material, the stresses can be expressed as [19]

$$\begin{aligned} \sigma_{rr} &= \xi_1 \xi_2 \left(\frac{\partial v_{rD}}{\partial r} + \frac{v_{rD}}{r} + \frac{\partial v_{zD}}{\partial z} \right) + \xi_1 \frac{\partial v_{rD}}{\partial r} - \xi_3 \\ \sigma_{\phi\phi} &= \xi_1 \xi_2 \left(\frac{\partial v_{rD}}{\partial r} + \frac{v_{rD}}{r} + \frac{\partial v_{zD}}{\partial z} \right) + \xi_1 \frac{v_{rD}}{r} - \xi_3 \\ \sigma_{zz} &= \xi_1 \xi_2 \left(\frac{\partial v_{rD}}{\partial r} + \frac{v_{rD}}{r} + \frac{\partial v_{zD}}{\partial z} \right) + \xi_1 \frac{\partial v_{zD}}{\partial z} - \xi_3 \\ \sigma_{rz} &= \frac{E_D}{2(1 + \nu_D)} \left(\frac{\partial v_{rD}}{\partial z} + \frac{\partial v_{zD}}{\partial r} \right) \end{aligned} \quad (9)$$

with $\xi_1 = E_D/(1 + \nu_D)$, $\xi_2 = \nu_D/(1 - 2\nu_D)$, and $\xi_3 = E_D \alpha_D \Delta T_D / (1 - 2\nu_D)$. Herein, ν_D and E_D are Poisson's ratio and Young's modulus of the disk material, v_{rD} and v_{zD} are the radial and axial deformations of the disk, α_D is the thermal expansion

coefficient, and ΔT_D is the temperature difference between the disk temperature and the reference temperature T_0 . Inserting Eq. (9) in Eq. (8) yields the two governing partial differential equations for $v_{rD}(\Delta T_D, \Omega)$ and $v_{zD}(\Delta T_D, \Omega)$.

Boundary conditions and coupling

The disk and rotor boundary is assumed to be stress-free.

2.3.2 Thermodynamics. The temperature of the rotor disk $T_D(r, z)$ is calculated with the energy equation

$$\frac{\partial}{\partial r} \left[\lambda_{Dr} \frac{\partial T_D}{\partial r} \right] + \frac{\partial}{\partial z} \left[\lambda_{Dr} \frac{\partial T_D}{\partial z} \right] = 0 \quad (10)$$

Herein, λ_D is the thermal conductivity of the disk.

Boundary conditions and coupling.

The temperature boundary conditions are shown in Fig. 6. At the dashed boundaries, zero flux conditions are applied. At the dotted boundaries, interface conditions (same temperature and heat flux) to the adjacent regions are used.

2.4 Cooling Flow Region. At the backside of the rotor disk, the disk rotation causes an airflow. The heat flux that leaves the disk is calculated from the temperature $T_C(r, z)$ in the cooling region which is obtained from the energy equation (assuming axisymmetry):

$$\begin{aligned} \frac{\partial}{\partial z} \left[\lambda_{C,eff} \frac{\partial T_C}{\partial z} \right] &= \rho_C c_{P,C} \left[u_C \frac{\partial T_C}{\partial r} + w_C \frac{\partial T_C}{\partial z} \right] \\ &\quad - \rho_C (\nu_C + \nu_{CT}) \left[\left(\frac{\partial u_C}{\partial z} \right)^2 + \left(\frac{\partial w_C}{\partial z} \right)^2 \right] \end{aligned} \quad (11)$$

Here, $\lambda_{C,eff}$ is an effective thermal conductivity according to Ref. [20], ρ_C is the density, $c_{P,C}$ is the isochoric heat capacity, and ν_C and ν_{CT} are the kinematic viscosity and the turbulent kinematic viscosity according to Cebeci and Smith [21]. The velocity field consisting of the radial velocity u_C , the circumferential velocity v_C and the velocity w_C in the z -direction is calculated from the boundary layer equations for steady incompressible axisymmetric flow (neglecting a radial pressure gradient, see Ref. [21]).

Boundary conditions and coupling

The CFR is coupled to the rotor disk via temperature interface conditions. The radial boundaries are assumed to be adiabatic, while the axial boundary is assumed to be at ambient temperature T_0 , cf. Fig. 6.

2.5 Radial Gap. In the radial gap between the rotor disk and the housing, the disk rotation also causes an airflow. It is assumed to be laminar with purely circumferential flow (Couette flow) and with linearly decreasing velocity over the radial coordinate (disk speed at the inner boundary, zero speed at the outer boundary). This simple

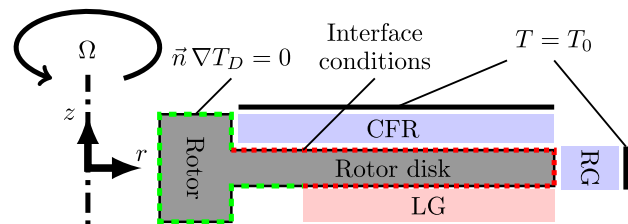


Fig. 6 Rotor disk boundaries and interfaces

assumption is made as the initial gap width t_{RG} is $200\ \mu\text{m}$ and decreases below $100\ \mu\text{m}$ at high rotational speeds due to centrifugal effects. The estimated maximal Reynolds number for the flow is $\text{Re} \approx \Omega r_D t_{RG} \rho / \eta \approx 700\text{--}800$. Thus, the 2D energy equation

$$\frac{\partial}{\partial r} \left[\lambda_{RG} r \frac{\partial T_{RG}}{\partial r} \right] + \frac{\partial}{\partial z} \left[\lambda_{RG} r \frac{\partial T_{RG}}{\partial z} \right] = -r \eta_{RG} \left[\frac{\Omega r_D}{t_{RG}} \right]^2 \quad (12)$$

including dissipative heating is solved to obtain the temperature profile $T_{RG}(r, z)$ in the radial gap. In Eq. (12), λ_{RG} is the thermal conductivity, η_{RG} is the dynamic viscosity of air in the gap, r_D is the disk radius, and the t_{RG} is the gap width with account for disk deformations.

Boundary conditions and coupling

The radial gap is coupled to the rotor disk via temperature interface conditions. The axial boundaries are assumed to be adiabatic, while the outer radial boundary is assumed to be at ambient temperature T_0 , cf. Fig. 6.

3 Simulation Method, Parameters, and Discretization

Through dissipation, high temperatures occur in the lubricating gap owing to the high circumferential velocity of the rotor disk. This heat is mainly flowing into the foil sandwich on the one hand and into the rotor disk on the other hand which leads to thermally induced bending of the rotor disk. These deformations reduce the load capacity of the thrust bearing.

In order to reduce this effect, the heat flow into the foil sandwich can be increased. The first and widespread method is introducing a radial cooling flow under the top foil that decreases the top foil temperature and at the same time reduces the heat flux into the rotor disk. This has a positive effect on the load capacity, cf., Refs. [14,22]. The approach of the current study is to decrease the thermal resistance of the foil sandwich by introducing alternative materials for the bump and top foils (typically, a superalloy-like INCONEL[®] X-750 is used). Due to dynamic loads, spring materials are typically utilized which need to have specific properties: high bending fatigue strength, high tensile strength and resiliency.

If alternative materials are to be considered for the bump and top foils, their maximum operation temperature needs to be higher than the bearing operation temperature as well. With increasing temperature, metals suffer from a weakening of the above-mentioned properties and may experience effects like creep which are to be avoided [23]. For high-temperature applications as in Ref. [24], only specific steels are contemplable. For lower temperature applications, the use of other materials with significantly higher thermal conductivities, albeit with lower maximum operation temperatures, can become interesting.

Therefore, a comparison is drawn here between INCONEL[®] X-750 (Material A), DURACON[®] 17A (Material B), and CuNi1Si (Material C) as foil materials. The important material parameters are Young's modulus at room temperature $E_{A,0} = 210\ \text{GPa}$, $E_{B,0} = 180\ \text{GPa}$, $E_{C,0} = 147.5\ \text{GPa}$, Poisson's ratio $\nu_A = \nu_B = 0.3$, $\nu_C = 0.325$, thermal conductivity $\lambda_A = 12\ \text{W (m K)}^{-1}$, $\lambda_B = 55\ \text{W (m K)}^{-1}$, $\lambda_C = 250\ \text{W (m K)}^{-1}$, top foil thickness $t_{T,A} = 100\ \mu\text{m}$, $t_{T,B} = 105.3\ \mu\text{m}$, $t_{T,C} = 112.5\ \mu\text{m}$, and bump foil thickness $t_{B,A} = 75\ \mu\text{m}$, $t_{B,B} = 79\ \mu\text{m}$, $t_{B,C} = 84.4\ \mu\text{m}$. To make up for the lower Young's modulus of the different materials, the foil thicknesses are increased accordingly to create equal bending stiffnesses at room temperature. The increased foil thickness alongside the higher thermal conductivity contribute to a lower thermal resistance.

The parameters for the rotor disk are $\lambda_D = 12\ \text{W (m K)}^{-1}$, $\nu_D = 0.3$, and $E_D = 210\ \text{GPa}$.

The model has been discretized as follows: bump foil (960 elements), top foil deformation (1233 elements), pressure and top foil temperature (1269 elements), lubricating gap (3384 elements), rotor and rotor disk temperature and deformations (688

elements), cooling flow region (3510 elements), and radial gap (96 elements). Fifth-order elements are chosen for calculating the shell deformations of top and bump foil in order to prevent shear locking effects. The nonlinear fully coupled FE model is solved by a Newton–Raphson method combined with a direct solver (MUMPS). A stationary calculation for a maximum rotational speed of 120 krpm in increments of 10 krpm using the underlying FE model takes approximately 5 h of computation time on a local computer (Win7, Intel i7 3.4 GHz with 12 logical cores, 64 GB RAM).

4 Simulation Results

Figure 7 shows the maximum top foil temperature increase ΔT_T over the rotational speed N for all three foil materials. With increasing rotor speed the maximum top foil temperature increases significantly due to heat accumulation in the lubricating gap. It should be mentioned that for the presented study, the minimal lubricating gap height is iteratively adjusted to $5\ \mu\text{m}$.

For a rotor speed of 120 krpm, the top foil has a maximum temperature increase of 250 K for Inconel foils. Choosing a high-conductive material, this temperature rise can be significantly lowered to around 206 K for Duracon foils or to 182 K for CuNi1Si foils which is a reduction of 17% and 27%, respectively. Figure 8 shows the top foil temperature increase for all three foil materials. The top foil temperature is the hottest at the trailing edge (left side) which is caused by the wedge-shaped lubricating gap. Temperature minima are observed along the contact lines with the bump foil which are visible as distinct vertical lines in the temperature profile. For

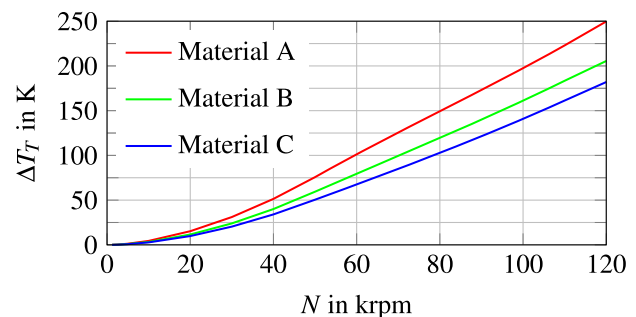


Fig. 7 Maximum top foil temperature increase ΔT_T for different foil materials over the rotational speed N

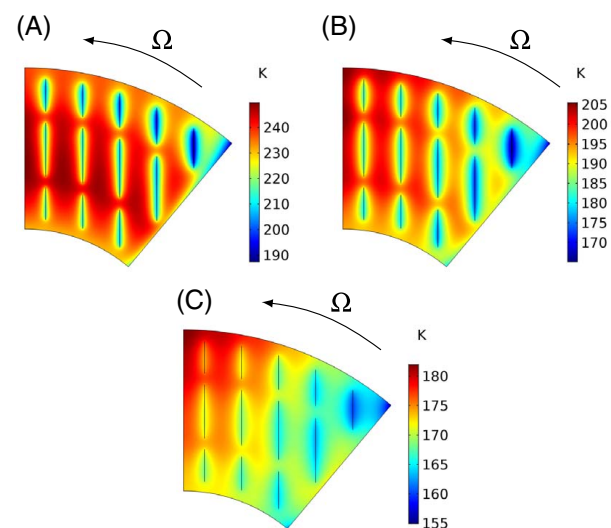


Fig. 8 Top foil temperature increase ΔT_T for the different foil materials A, B and C

materials B and C, the top foil temperature indicates that the heat accumulation in the lubricating gap is significantly reduced.

The main idea of changing the foil material is reducing the thermal resistance of the foil sandwich and therefore lowering the heat flux into the disk. Figure 9 shows the ratio of the heat fluxes Q_D (heat flow from the lubricating gap into the rotor disk) and Q_T (heat flow into the top foil) over the rotational speed for materials B and C with regard to foil material A. The reduced thermal resistance of the foil sandwich allows the heat flux through the foils to be significantly higher. For increasing rotational speeds, the ratios $Q_{T,B}/Q_{T,A}$ and $Q_{T,C}/Q_{T,A}$ increase over the rotational speed as the dissipative heating and thus the gap temperature rise. For material B, this ratio is between 130% and nearly 180%, for material C between 140% and 220%. The ratios $Q_{D,B}/Q_{D,A}$ and $Q_{D,C}/Q_{D,A}$ of heat that enters the disk decrease to 70–85% of the reference case for material B and to 55–75% for material C. The ratios of the two main heat flow paths through the top foil and the disk are displayed by dotted lines. Even for the maximum rotational speed, with foil material C, there is almost as much heat flowing through the foil sandwich as into the disk. Figure 9 shows the cause of the improved performance of the bearing with alternative foil materials. The heat accumulation is reduced due to higher heat conductivity and higher absolute heat fluxes in comparison to material A. Moreover, a larger fraction of the heat passes through the foil sandwich. As a result, disk temperatures are significantly reduced.

Figure 10 depicts the 2D rotationally symmetric temperature of the rotor disk for all three foil materials. The lubricating gap (LG) is located adjacent to the right side of the disk where the highest temperatures occur. Part of the heat is conducted into the rotor, the radial gap (RG), and the CFR. The disk temperature profiles are similar, but the temperature is reduced by around 20 to 30 K for material B and 40 to 50 K for material C.

This also implies a reduction of thermally induced deformations of the rotor disk as shown in Fig. 11(a). The axial rotor disk deformations v_{zD} are visibly lower for foil materials B and C. The graph in Fig. 11(b) shows the axial deformation along the right edge of the disk (dashed line in Fig. 11(a)) for the radial coordinate r , ranging between the inner disk radius r_i and the outer disk radius r_o . This side of the disk is adjacent to the lubricating gap. Therefore, this deformation is directly influencing the lubricating gap height. Clearly, the disk bends away from the lubricating gap due to the axial temperature gradient. The highest deformations are observed at the outer radius. With different foil materials, the rotor disk deformations are lowered by up to 30% at the outer radius r_o . Thus, thermally induced changes in the lubricating gap height are decreased. As the pressure generation in the lubricating gap is mainly

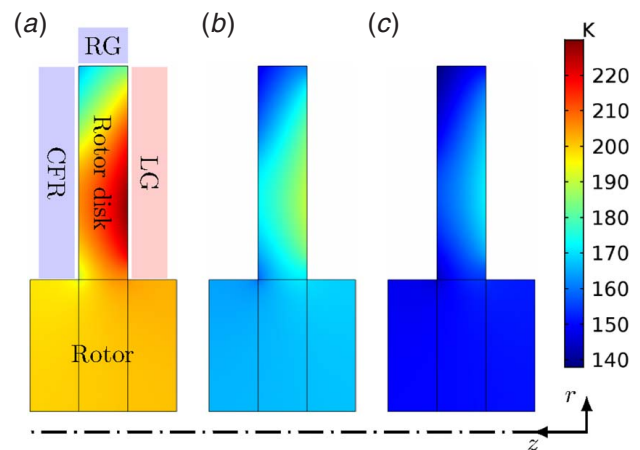


Fig. 10 Disk temperature increase $T_D - T_0$ for the different foil materials A, B, and C

determined by the gap height, lower disk deformations result in an increased load capacity (up to nearly 10% at 120 krpm).

The load capacity W of the thrust bearing is calculated by integrating the 2D pressure field in the lubricating gap over the six pad surfaces. The resulting force is the axial force that acts upon the rotor disk. Figure 12 shows the pressure distribution in the lubricating gap (pressure over the atmospheric pressure). As the bump foil height defines the wedge-shaped lubricating gap, the pressure increases going from the right-hand side (leading top foil edge) towards the left-hand side (trailing edge). The highest pressures are observed in the vicinity of the last two bumps of the bump strips where the lubricating gap height is the smallest. The fact that two distinct pressure peaks are present is caused by top foil sagging. This effect is shown in Fig. 12. The results for the different foil materials only show minor differences. The peak pressure for foil material C is the highest, for foil material A the lowest. This means higher load capacity, but also results in a slightly increased top foil sagging, see Figs. 4 and 13.

Figure 14 shows exemplary temperature calculation results for the CFR and RG region for foil material A at maximum rotational speed.

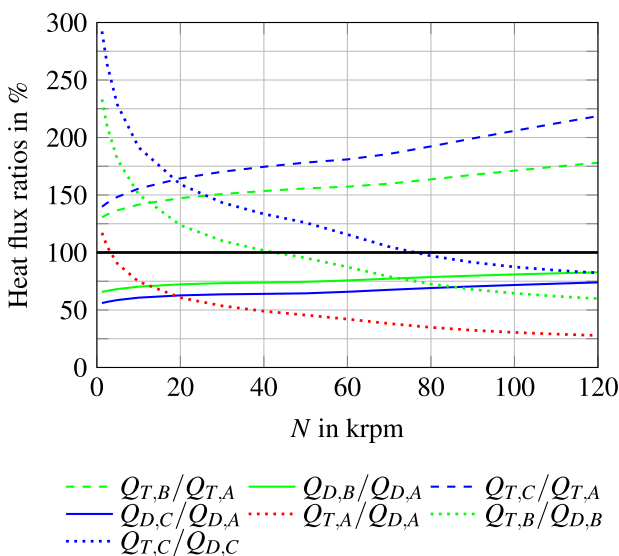


Fig. 9 Heat flux ratios of disk and top foil

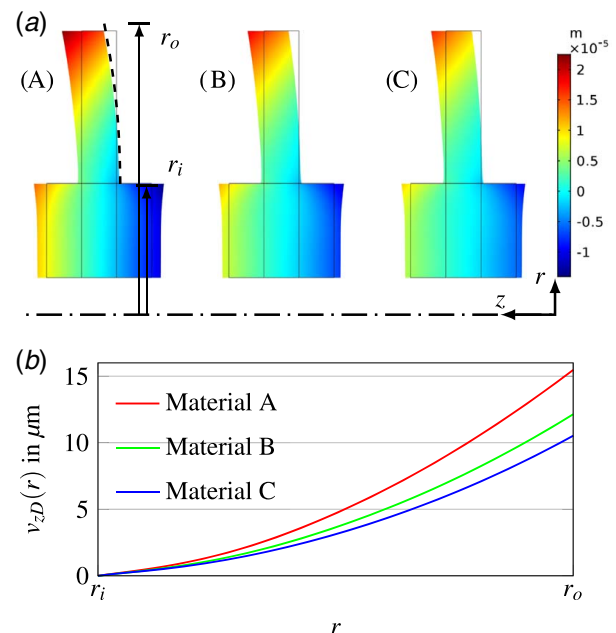


Fig. 11 Thermally induced axial deformations v_{zD} of (a) the rotor disk and (b) the disk underside for foil material A, B, and C

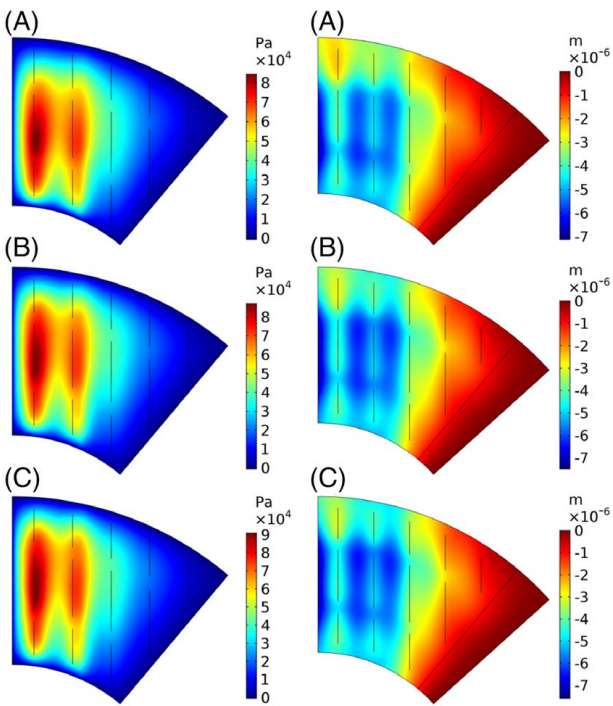


Fig. 12 Pressure distribution $p(x, y)$ (left) and top foil sagging v_{3T} (right) for the different foil materials A, B, and C

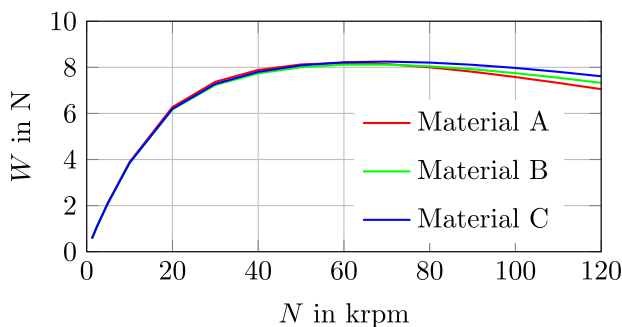


Fig. 13 Load capacity W per pad for different foil materials over the rotational speed N

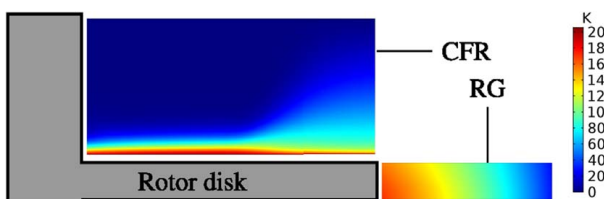


Fig. 14 Temperature increase $T_{RG} - T_0$ in RG and $T_C - T_0$ in CFR at 120 krpm for foil material A

Figure 15 displays the effect of forced cooling (implemented by a properly chosen constant heat-transfer coefficient α_C , see Sec. 2.1.2) on the maximum top foil temperature increase for all 3 materials. Even for very high cooling rates, bearings with foil materials B and C still have visibly lower temperatures.

Figure 16 compares the top foil temperatures of foil material A and C for heat-transfer coefficients $\alpha_C = 200 \text{ W (m}^2 \text{ K)}^{-1}$ and $\alpha_C = 500 \text{ W (m}^2 \text{ K)}^{-1}$. The forced cooling does not change the qualitative temperature distribution significantly. Instead, the overall temperature level is decreased.

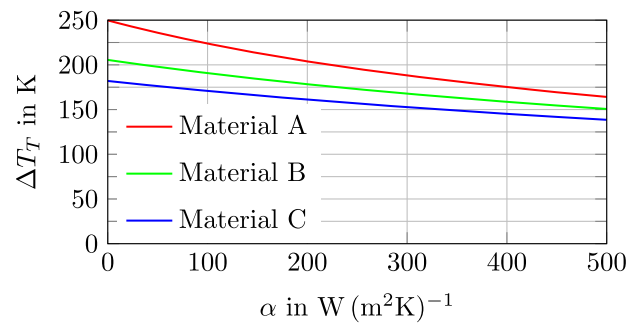


Fig. 15 Maximum top foil temperature increase ΔT_T for different foil materials over cooling heat transfer coefficient α_C at 120 krpm

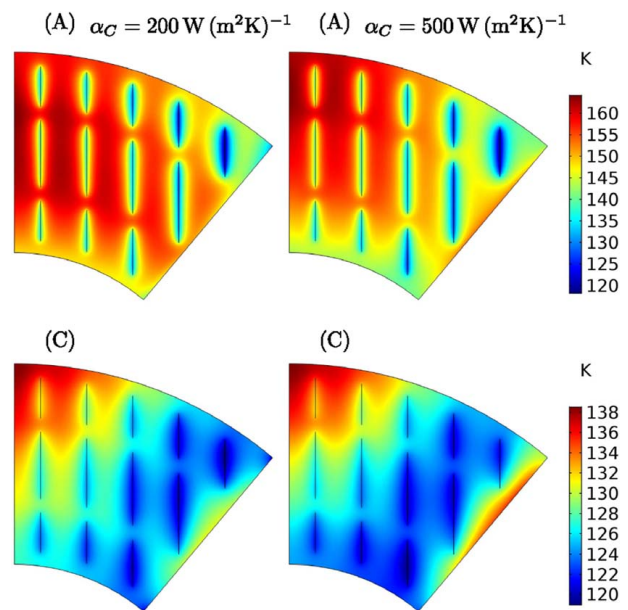


Fig. 16 Top foil temperature increase

As in real machine applications the ambient temperature around the bearing is dependent on the overall machine design and operation parameters, the influence of T_0 on the results has also been studied. In all above studies, $T_0 = 20^\circ \text{C}$ was set. Now, for $T_0 = 100^\circ \text{C}$ and $\alpha_C = 100 (500) \text{ W (m}^2 \text{ K)}^{-1}$, the maximum top foil temperature increase ΔT_T is calculated to 276(200) K for foil material A and 200(162) K for foil material C at 120 krpm.

5 Conclusion

A detailed thermo-elasto-hydrodynamic (TEHD) model for air foil thrust bearings (AFTBs) is used in order to study the effect of different foil materials on the bearing operation temperature. The detailed bearing model allows for the study of various effects like top foil sagging or disk distortions. The thermal balance of AFTBs is known to be one of the critical points in operation and is also challenging for AFTB simulation. The presented study showed the significant influence of different foil materials on temperatures and on the overall bearing performance. The thermal resistance of the foil sandwich was modeled in detail. Due to the reduced thermal resistance of the foil sandwich by using different foil materials, the heat flux into the foil sandwich can be increased. This reduces heat flow into the rotor disk which reduces the axial temperature gradient. It was shown that a high-conductive foil material does not only lower operation temperatures and the thermally

induced rotor disk bending, but as a consequence also increases load capacity (up to 10%). Depending on operation temperatures of the bearing and additional cooling conditions, the use of high-conductive foil materials is expected to be advantageous in practical applications—representing a cost-efficient improvement for the thermal management of AFTBs.

References

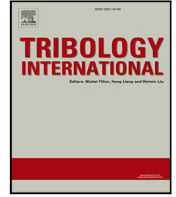
- [1] Agrawal, G. L., 1997, "Foil Air/Gas Bearing Technology—An Overview," ASME 1997 International Gas Turbine and Aeroengine Congress and Exhibition, Orlando, FL, June 2–5, American Society of Mechanical Engineers, pp. 1–11.
- [2] DellaCorte, C., Lukaszewicz, V., Valco, M. J., Radil, K., and Heshmat, H., 2000, "Performance and Durability of High Temperature Foil Air Bearings for Oil-Free Turbomachinery," *Tribol. Trans.*, **43**(4), pp. 774–780.
- [3] Lee, D., and Kim, D., 2010, "Thermohydrodynamic Analyses of Bump Air Foil Bearings With Detailed Thermal Model of Foil Structures and Rotor," *ASME J. Tribol.*, **132**(2), p. 021704.
- [4] Lee, D., and Kim, D., 2011, "Three-Dimensional Thermohydrodynamic Analyses of Rayleigh Step Air Foil Thrust Bearing With Radially Arranged Bump Foils," *Tribol. Trans.*, **54**(3), pp. 432–448.
- [5] San Andrés, L., and Kim, T. H., 2010, "Thermohydrodynamic Analysis of Bump Type Gas Foil Bearings: A Model Anchored to Test Data," *ASME J. Eng. Gas Turbines Power*, **132**(4), p. 042504.
- [6] Sim, K., and Kim, T. H., 2012, "Thermohydrodynamic Analysis of Bump-Type Gas Foil Bearings Using Bump Thermal Contact and Inlet Flow Mixing Models," *Tribol. Int.*, **48**, pp. 137–148.
- [7] Lehn, A., 2017, "Air Foil Thrust Bearings: A Thermo-Elasto-Hydrodynamic Analysis," Ph.D. thesis, Technische Universität Darmstadt.
- [8] Lehn, A., Mahner, M., and Schweizer, B., 2018, "A Thermo-Elasto-Hydrodynamic Model for Air Foil Thrust Bearings Including Self-Induced Convective Cooling of the Rotor Disk and Thermal Runaway," *Tribol. Int.*, **119**, pp. 281–298.
- [9] Balducci, F., Arghir, M., Gauthier, R., and Renard, E., 2013, "Experimental Analysis of the Start-Up Torque of a Mildly Loaded Foil Thrust Bearing," *ASME J. Tribol.*, **135**(3), p. 031702.
- [10] Lehn, A., Mahner, M., and Schweizer, B., 2018, "Characterization of Static Air Foil Thrust Bearing Performance: An Elasto-Gasdynamic Analysis for Aligned, Distorted and Misaligned Operating Conditions," *Arch. Appl. Mech.*, **88**(5), pp. 705–728.
- [11] Basar, Y., and Krätzig, W. B., 1985, *Mechanik Der Flächentragwerke: Theorie, Berechnungsmethoden, Anwendungsbeispiele*, Friedr. Vieweg & Sohn, Braunschweig/Wiesbaden.
- [12] Lehn, A., Mahner, M., and Schweizer, B., 2016, "Elasto-Gasdynamic Modeling of Air Foil Thrust Bearings With a Two-Dimensional Shell Model for Top and Bump Foil," *Tribol. Int.*, **100**, pp. 48–59.
- [13] Wriggers, P., and Laursen, T. A., 2006, *Computational Contact Mechanics*, Vol. 2, Springer, Berlin/Heidelberg.
- [14] Lehn, A., Mahner, M., and Schweizer, B., 2017, "A Contribution to the Thermal Modeling of Bump Type Air Foil Bearings: Analysis of the Thermal Resistance of Bump Foils," *ASME J. Tribol.*, **139**(6), p. 061702.
- [15] Dowson, D., 1962, "A Generalized Reynolds Equation for Fluid-Film Lubrication," *Int. J. Mech. Sci.*, **4**(2), pp. 159–170.
- [16] Hamrock, B. J., Schmid, S. R., and Jacobson, B. O., 2004, *Fundamentals of Fluid Film Lubrication*, Marcel Decker, Inc., New York/Basel.
- [17] Mahner, M., Lehn, A., and Schweizer, B., 2016, "Thermogas- and Thermohydrodynamic Simulation of Thrust and Slider Bearings: Convergence and Efficiency of Different Reduction Approaches," *Tribol. Int.*, **93**, pp. 539–554.
- [18] Nowacki, W., 1986, *Thermoelasticity*, 2nd ed., Pergamon Press, Warsaw.
- [19] Sadd, M. H., 2009, *Elasticity: Theory, Applications, and Numerics*, Academic Press, Burlington.
- [20] Ong, C., and Owen, J., 1991, "Computation of the Flow and Heat Transfer Due to a Rotating Disc," *Int. J. Heat Fluid Flow*, **12**(2), pp. 106–115.
- [21] Cebeci, T., and Smith, A., 1975, *Analysis of Turbulent Boundary Layers*, Academic Press, New York.
- [22] Bruckner, R. J., 2012, "Performance of Simple Gas Foil Thrust Bearings in Air," National Aeronautics and Space Administration, East Lansing, Michigan, Technical Report No. NASA/TM-2012-217262.
- [23] Rösler, J., Harders, H., and Bäker, M., 2007, *Mechanical Behaviour of Engineering Materials: Metals, Ceramics, Polymers, and Composites*, Springer Science & Business Media, Berlin/Heidelberg.
- [24] DellaCorte, C., and Valco, M. J., 2000, "Load Capacity Estimation of Foil Air Journal Bearings for Oil-Free Turbomachinery Applications," *Tribol. Trans.*, **43**(4), pp. 795–801.

Paper 2

Markus Eickhoff, Andre Theile, Michael Mayer und Bernhard Schweizer. „Analysis of Air Foil Thrust Bearings with annular top foil including wear prediction, Part I: Modeling and simulation“. In: *Tribology International* 181 (2023), S. 108174

<https://doi.org/10.1016/j.triboint.2022.108174>

©2022 Elsevier Ltd. All rights reserved.



Analysis of Air Foil Thrust Bearings with annular top foil including wear prediction, Part I: Modeling and simulation

Markus Eickhoff^{a,*}, Andre Theile^b, Michael Mayer^b, Bernhard Schweizer^a

^a Institute of Applied Dynamics, Technical University of Darmstadt, Otto-Berndt-Strasse 2, Darmstadt, Germany

^b Robert Bosch GmbH, Stuttgart, Germany

ARTICLE INFO

Keywords:

Air Foil Thrust Bearing
TEHD model
Annular top foil
Cyclic coupling
Wear prediction

ABSTRACT

This article features an Air Foil Thrust Bearing (AFTB) simulation model including wear prediction for a foil thrust bearing with an annular top foil. The bearing consists of 6 bearing sectors with independent bump foils, but possesses a single annular top foil with an embossed height profile. The bearing is analyzed by a detailed single-sector model utilizing symmetry properties and a cyclic coupling of the components. The compressible Reynolds equation and the 3D energy equation are used to obtain fluid film pressure and temperature. The model further includes thermoelastic deformations of the runner disk, elastomechanic deformations of the top and bump foils, and a detailed thermodynamic model of the rotor. A direct comparison of simulated and experimental results shows that top foil wear has to be taken into account in order to match simulated to measured data. Therefore, a wear algorithm is derived and incorporated into the thermo-elasto-hydrodynamic simulation model. Furthermore, the manufactured real top foil topology is determined by measurements in order to obtain in-depth topology information which is also included in the computation model. Simulation results with the TEHD model including a detailed surface analysis alongside a wear prediction are confirmed by measurements carried out on a dedicated test rig.

1. Introduction

Air foil bearings are becoming more popular with the increasing interest and demand in oil-free machinery. They present a low-cost and robust alternative to rigid air bearings. However, their analysis and optimization is involved due to the multiphysicality of thermodynamic, elastomechanic and hydrodynamic (TEHD) equations and their coupling in the numerical models. In the past, several authors have presented TEHD models for foil bearing analysis for both journal and thrust bearings, see e.g. [1–8]. To this day, the extension of the field of research is conducted intensively. Incorporating tribological aspects in the bearing analysis plays a key role. In [9], the authors present a solution of the Reynolds equation for bearings using a stochastic roughness approach. Alongside advances in the numerical simulation of bearings, experimental works—for example on suitable top foil coatings—are of high value for the optimization of bearing operation, cf. e.g. [10]. For a more detailed review of the literature, we would like to refer the interested reader to [11,12], for instance.

Hydrodynamic bearings represent tribological systems which make use of a lubricating fluid film that causes separation between a stationary and a moving part. They thus allow for their relative movement

with improved friction and wear behavior. In machine operation, different lubrication regimes—including boundary and mixed lubrication—are observed, e.g. for the start-up of a rotor. In tribology, the change and degradation of components under these conditions is a topic of high interest in research, cf. [13]. The influence of wear on the behavior of hydrodynamic bearings has been shown e.g. in [14,15]. In foil bearings, the top foil coating has a huge impact on their performance, see e.g. [16,17]. It is well known that foil bearings undergo a run-in process in which wear occurs. This wear causes the roughness of the foil coating to be reduced, imperfections to be decreased and highly loaded spots to be worn. The following publications give, amongst others, insight into the details of top foil coating wear.

In 2004, Bruckner [18] presented a simulation model as well as experimental test data for AFTBs. He described that the predicted wear location of the top foil matches the observed one very well. In his work, the main wear spot lay in the middle of the top foil pad as a result of the design of the compliant understructure.

In 2006, Dykas [19] presented his largely experimental studies on AFTBs. He states that, during the break-in procedure, wear is observed near the contact points of top and bump foil. Moreover, he concluded that coatings and their wear can have a significant effect on the

* Corresponding author.

E-mail address: eickhoff@ad.tu-darmstadt.de (M. Eickhoff).

Nomenclature**Operators**

Δ	Laplace operator.
∇	Nabla operator.
min	Minimum operator.
ramp	Ramp function as defined in Eq. (34).

Vectors

\vec{n}	Normal vector.
\vec{n}_l	Normal vector of leading edge.
\vec{n}_{in}	Normal vector of inlet.
\vec{n}_{out}	Normal vector of outlet.
\vec{n}_t	Normal vector of trailing edge.

Indices

0	Ambient/reference condition.
A	Air film.
b	Base plate.
B	Bump foil.
l	Leading edge.
in	Inlet surface.
out	Outlet surface.
R	Rotor.
t	Trailing edge.
T	Top foil.

Greek letters

α	Heat transfer coefficient at outer perimeter of the disk.
α_{II}	Heat transfer coefficient of region II in rotor disk.
α_{III}	Heat transfer coefficient of region III in rotor disk.
α_{IV}	Heat transfer coefficient of region IV in rotor disk.
α_C	Heat transfer coefficient of forced cooling and heat conduction below the top foil.
α_R	Thermal expansion coefficient of rotor and disk material.
γ_α	Strain variable in shell theory.
γ_R	Lamé constant of rotor and disk.
Δh_{coat}	Amplitude of top foil coating accumulations.
Δv_3	Penetration depth, relative normal displacement of contact partners.
Δv_{tan}	Relative tangential displacement of contact partners.
δ_{wear}	Wear height increment.
ϵ_R	Thermal expansion parameter of rotor and disk.
η	Air viscosity.
$\kappa_{\lambda\mu}$	Strain variable in shell theory.
λ	Thermal conductivity of air.
λ_{EP}	Thermal conductivity of air in the EP bearing gap.
λ_R	Thermal conductivity of rotor and disk material.
λ_T	Thermal conductivity of top foil material.

μ_R	Shear modulus of rotor and disk.
ν	Poisson's ratio of top and bump foil.
ρ	Air density.
ρ_R	Density of the rotor and disk.
σ_{rr}	Radial component of thermomechanical stress in rotor and disk.
σ_{rz}	Cross-coupling component of thermomechanical stress in rotor and disk.
σ_{zz}	Axial component of thermomechanical stress in rotor and disk.
$\sigma_{\phi\phi}$	Circumferential component of thermomechanical stress in rotor and disk.
$\varphi_{\mu\sigma}$	Strain variable in shell theory.
φ	Circumferential coordinate.
Ω	Angular velocity of the rotor.

Latin letters

$a^{\alpha\lambda}$	Contravariant metric tensor in shell theory.
A_{in}	Inlet surface of air film sector.
A_{mf}	Bearing area of multi-foil bearing.
A_{out}	Outlet surface of air film sector.
A_{sec}	Sector area.
A_{sf}	Bearing area of single-foil bearing.
B	Bending stiffness.
b_λ^σ	Curvature tensor in shell theory.
c	Penalty stiffness of normal contact of top foil/bump foil/base plate.
c_p	Isochoric heat capacity of air.
D	Stretching stiffness.
d_{gap}	Gap height of EP bearings.
E	Young's modulus of top and bump foil material.
E_R	Young's modulus of rotor and disk.
F_n	Normal contact force.
f_r	Radial force due to centrifugal effects.
F_{tan}	Tangential contact force.
G	Shear modulus of the rotor and disk material.
Gt	Shear stiffness of top and bump foil.
H	Air film height.
$H^{(i)}$	Air film height in the i th wear iteration step.
$H^{\alpha\beta\lambda\mu}$	Elasticity tensor.
h_B	Height of bump.
H_{coat}	Film height deviations due to top foil coating defects.
H_{min}	Minimal air film height.
h_{par}	Amplitude of parabolic shape deviation of top foil.
H_{par}	Parabolic shape deviation function of top foil.
h_s	Height of taper/step.
H_{shape}	Film height deviations due to top foil shape defects.
$H_{wear}^{(i)}$	Wear function for the top foil coating in the i th wear iteration step.
i	Wear iteration counter.
i_{end}	Total number of wear iterations.

bearing load capacity. In one test case, the coated top foil showed a load capacity more than twice as high as for the uncoated top foil. This is caused by the favorable wear pattern which decreases the well-known top foil sagging effect. While the top foil sags between the bump supports due to the air pressure, the narrowest gaps are found at the bump support lines. In these areas, wear is observed, partly compensating the top foil sagging.

In 2019, Arghir and Bencheikroun [20] presented a model for journal bearings applicable for start-up conditions including the mixed lubrication regime. They give boundaries for the operation regime of a bearing depending on the respective roughnesses of top foil and rotor disk.

In thrust bearing analysis, the classical *multi-foil* design is frequently applied and has been studied in previous works, cf. Refs. [21,22].

k_S	Shear correction factor.
$m^{\alpha\beta}$	Moment tensor of shell theory.
$n^{\alpha\beta}$	Stress resultant tensor of shell theory.
n_{sec}	Number of sectors.
p	Air film pressure.
p^i	External forces of shell theory for $i = 1, 2, 3$.
p_T^3	External force on top foil in 3-direction.
p_l	Air pressure at leading edge.
P_{loss}	Bearing power loss.
p_t	Air pressure at trailing edge.
q^α	Transverse shear stress of shell theory.
q_{gap}	Averaged heat flux into the rotor disk from the lubricating gap.
$q_{T,\text{in}}$	Heat flux entering the top foil from the air film.
$q_{T,\text{out}}$	Sum of heat fluxes $q_{T,\text{out},\alpha_C}$ and $q_{T,\text{out},R_{\text{th}}}$.
$q_{T,\text{out},\alpha_C}$	Heat flux leaving the top foil through forced cooling and heat conduction in the air gap below the top foil.
$q_{T,\text{out},R_{\text{th}}}$	Heat flux leaving the top foil through bump conduction.
r	Radial coordinate.
R	Radius of curvature in shell theory.
$r_{D,o}$	Outer rotor disk radius.
r_i	Inner top foil radius.
r_m	Mean top foil radius.
r_o	Outer top foil radius.
R_{th}	Thermal resistance of a half bump arc.
R_{bump}	Thermal conduction resistance of a half bump arc.
$R_{\text{TB,air}}$	Thermal resistance of the air gap between top foil and a half bump arc.
$R_{\text{Bb,air}}$	Thermal resistance of the air gap between a half bump arc and the base plate.
t	Shell thickness.
T_0	Ambient reference temperature.
T_A	Air film temperature.
$T_{A,\text{in}}$	Air film temperature at the inlet surface of the air film sector.
$T_{A,\text{out}}$	Air film temperature at the outlet surface of the air film sector.
t_B	Bump foil thickness.
T_{base}	Temperature of base plate.
t_D	Thickness of the rotor disk.
T_{EP}	Temperature of the air supply in the EP bearings.
T_R	Temperature of the rotor and disk.
$\bar{T}_{R,\text{II}}$	Averaged temperature of the rotor disk in Section 2.
T_{ref}	Reference temperature of remaining rotor section.
T_m	Height-averaged air film temperature.
t_T	Top foil thickness.
T_T	Top foil temperature.
$T_{T,l}$	Top foil temperature on leading edge.
$T_{T,t}$	Top foil temperature on trailing edge.
U	x -component of disk velocity.
V	y -component of disk velocity.
u	x -component of air velocity.

This bearing design is displayed in Fig. 2(a) and consists of independent sectors. By contrast, in this paper, a multiphysical model and analysis for air foil thrust bearings with an annular, one-part top foil is presented [23]. This *single-foil* design, where the top foil forms a

v	y -component of air velocity.
v_i	Translational deformations of the shell middle surface of top (T) and bump foil (B) for $i = 1, 2, 3$.
v_r	Radial deformation of the rotor and disk.
v_z	Axial deformation of the rotor and disk.
W	Bearing load capacity.
w_α	Rotational deformations of the shell middle surface of top and bump foil for $\alpha = 1, 2$.
x	Cartesian coordinate.
y	Cartesian coordinate.
z	Axial coordinate.
\bar{z}	Transformed axial coordinate for air film sector.
z_R	Axial position of rotor.

closed and ring-shaped geometry, is displayed in Fig. 2(b). The height profile of the top foil is embossed in order to create a wedge-shaped converging lubricating gap. It should be mentioned that, in case of the classical multi-foil bearing, a taper-land geometry is commonly applied, see right side of Fig. 2(a). The bearing under investigation in the paper at hand possesses a taper-step geometry, cf. Fig. 2(b). Although this again makes for altogether 6 sectors, they are fully coupled. In both bearing designs, the top foils are mounted on independent bump foils. The single-foil design is advantageous with regard to the number of parts. By contrast to the multi-foil design, only a single top foil has to be manufactured, which reduces the system complexity. Also, the bearing assembly is improved through the single-foil design and the simpler method of fixation. It also allows for small-scale applications. Downsides of the single-foil design lie in the occurring non-uniform wear of the top foil coating and the distinctive deformation profile of the top foil, the latter causing a suboptimal pressure profile. These effects are analyzed in detail in Section 3 in this paper. The single-foil bearing design has the same field of application as the classical multi-foil design. Appendix C contains a short comparison of the two bearing designs with regard to their performance.

To the best of the authors' knowledge, these single-foil thrust bearings have not been analyzed and discussed in literature until now. One study with a single top foil design has recently been presented [24]. However, the discussed bearing design lacks the distinctive embossed height profile which is innate to the design at hand.

Here, a detailed simulation model for single-foil bearings with embossed height profile is presented. In contrast to simulations models for multi-foil bearings, see e.g. [25–28], several modifications and extensions must be considered here, since the bearing sectors are fully coupled through the single-part top foil. The new contributions of this work are:

- A fully coupled TEHD model for stationary simulations for single-foil AFTBs with an annular, one-part top foil is presented. The model takes into account
 - thermoelastic deformations of the rotor due to thermal stresses and centrifugal effects,
 - a detailed thermodynamic model for the rotor temperature with a heat transfer model from CFD analysis,
 - air film temperature and pressure through a 3D energy equation and a 2D Reynolds equation, respectively,
 - elastomechanic deformations of top and bump foil via a nonlinear shell model including normal and tangential contact forces,
 - as well as a detailed model for the top foil temperature and the heat transfer through the bump foil and the air gap between top foil and base plate.

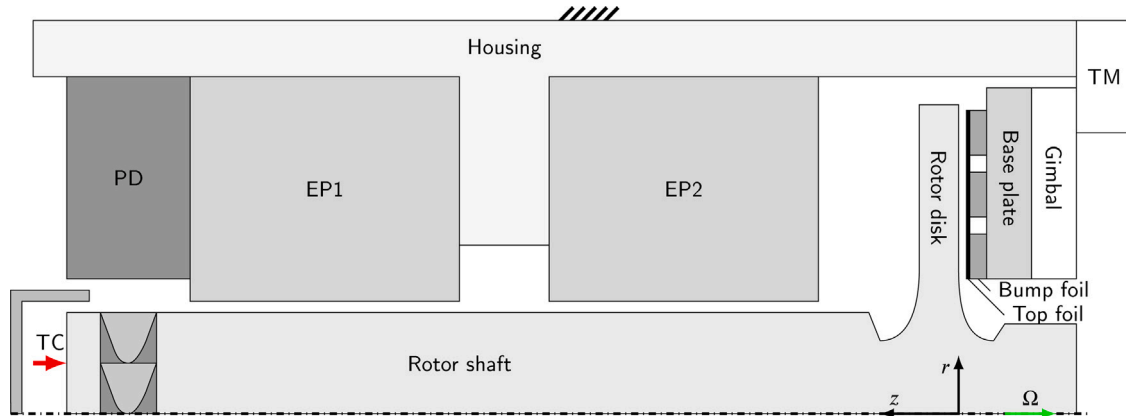


Fig. 1. Schematic overview of the rotor and the surrounding components: thrust chamber (TC) for applying thrust load (arrow), pelton drive (PD), externally pressurized journal bearings (EP1 and EP2), torque measurement (TM), and the thrust bearing consisting of the base plate, the bump foil, and the top foil.

- A direct implementation of the full bearing would require extreme simulation times which would not allow for parameter studies and optimizations. Therefore, a reduction approach is presented which makes use of the cyclic symmetry. The cyclic coupling conditions for the top foil and the air film are derived and explained in detail. Of course, misalignment may not be considered in this case.
- A direct comparison of simulation results with measurements shows large discrepancies. It is observed that significant wear occurs upon the loading of the bearing, especially for the first break-in. Therefore, an appropriate algorithm for the simulation of wear is derived and incorporated into the model.
- The top foil geometry as well as the coating topology deviate significantly from their nominal design values. Therefore, the real geometry of top foil and coating is included in the model.
- Without the use of the real top foil topology and the consideration of wear, bearing performance cannot be analyzed by the model. With the extended model, numerical results agree well with experimental data.
- It is shown in the later sections of this paper that each sector of the one-part top foil deforms from the initial taper-step geometry into a taper-land configuration under pressure load during operation.

Unlike the results of Dykas [19] where the load capacity was approximately doubled, for the current foil design, the calculated load capacity in the numerical model when considering wear is more than 10 times higher than in the unworn condition.

The paper is organized as follows: In Section 2, the bearing model is explained in detail. It consists of the model for the rotor, the air film, and the top and bump foil. Furthermore, the manufactured real top foil topology is discussed in comparison to the nominal foil geometry, the developed wear algorithm is presented, and numerical details are given. Section 3 shows detailed simulation results for the unworn and the worn state of the bearing as well as for intermediate steps. Conclusions are summarized in Section 4. The appendices contain further simulation results for different wear stages and load scenarios.

2. Multiphysics model

In this section, the TEHD model for the single-foil AFTB is presented, showing the governing equations and model assumptions for each component of the bearing. Table 1 lists the most important bearing dimensions. The rotor system under investigation as well as the surrounding components are depicted in Fig. 1. The rotor is driven by a pelton drive (PD) and is supported by 2 externally pressurized rigid air bearings (EP1 and EP2). The thrust bearing investigated here,

Table 1
Foil bearing specifications, dimensions and material properties.

Parameter	Value	Description
r_i	14 mm	inner top foil radius
r_o	27 mm	outer top foil radius
h_s	145 μm	step height
n_{sec}	6	number of sectors
t_B	100 μm	bump foil thickness
t_T	127 μm	top foil thickness
h_B	254 μm	bump height
$E = E_R$	210 GPa	Young's modulus
$\nu = \nu_R$	0.3	Poisson's ratio
ρ_R	7800 kg/m^3	density of rotor material
α_R	10.9E-6 /K	thermal expansion coefficient

consisting of the base plate, the bump foils and the top foil, is also shown. All these surrounding components are encased in the housing. Thrust loads can be applied through a thrust chamber at the front face of the rotor in order to test the thrust bearing performance.

Please note that—for alignment purposes and for being able to measure the friction torque of the foil bearing—the base plate is not directly connected to the housing. Instead, the base plate is connected to a gimbal suspension mechanism that can compensate misalignment between the rotor disk and the thrust bearing. Moreover, in the connection between the base plate and the housing, the relative torque is measured, which allows for friction torque and power loss measurements of the test bearing.

During the manufacturing process, the annular top foil is embossed, resulting in 6 equal sectors. Each sector possesses a curvilinear taper and a steep, almost vertical step, cf. Fig. 2(b). The embossing line is not straight in radial direction, but slightly curved, cf. Fig. 3(d). The step height is denoted by h_s , see Fig. 3(e). The underlying structure of each sector consists of a 3-striped bump foil with parallel arranged bumps. Note that the 6 bump foils are independent, see Fig. 2(b). The bump foil is mounted on the base plate and possesses 3 bump arcs on the outer two stripes and only 2 bump arcs on the inner stripe, see Fig. 3(d). It should be stressed that all bumps possess an equal height h_B , Fig. 3(a) shows the assembly of the whole bearing consisting of the base plate, the bump foils, the top foil and the rotor.

The fact that the top foil is a single part makes for a direct connection of each of the sectors not only in the mechanical part of the model in terms of deformations, but also for the hydrodynamic and thermodynamic behavior of the bearing. If misalignment of the runner disk with regard to the bearing is taken into account as well, a model including the whole bearing is necessary. It has to comprise the entire top foil as well as an air film extending over 360 degrees, and 6 bump foils. Simulations with such a model would take several weeks. Hence, in this work, we assume that misalignment is negligibly

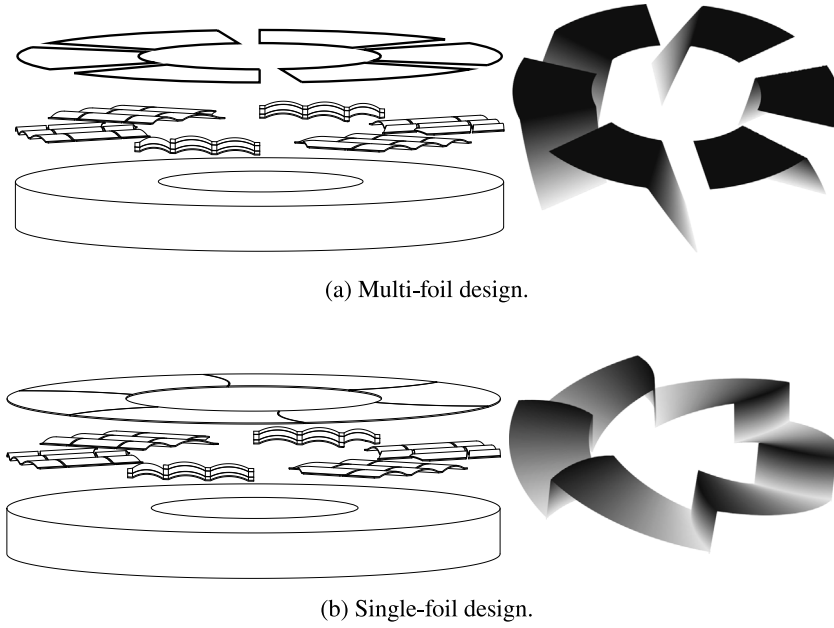


Fig. 2. Comparison of (a) multi-foil and (b) single-foil bearing design. Left side: bearing assembly with base plate, bump foils and top foil(s). Right side: exaggerated height profiles of the top foils, (a) taper-land and (b) taper-step.

small and, therefore, the bearing behaves similarly on each of the 6 sectors (periodicity condition). Therefore, the performance of the entire bearing can be concluded from simulation results of a single sector. Fig. 3 gives an overview over the model components and equations (Fig. 3(a)) as well as of the most important boundary and coupling conditions (Fig. 3(b)–(h)).

2.1. Rotor

This section describes the modeling of the rotor which consists of the rotor disk and the shaft. The direction of rotation is the negative z -direction, cf. Fig. 3(a). Due to the high angular velocity Ω , changes of the rotor temperature and rotor deformations in circumferential direction are negligible. Consequently, the deformations are calculated via a thermoelastic axisymmetric model. The deformations $v_r(r, z)$ in radial and $v_z(r, z)$ in axial direction are obtained by solving the Navier–Lamé equations including centrifugal forces and thermal stresses as in Ref. [29]:

$$\begin{aligned} \mu_R \left(\nabla^2 v_r - \frac{v_r}{r^2} \right) + (\gamma_R + \mu_R) \frac{\partial}{\partial r} \left(\frac{1}{r} \frac{\partial}{\partial r} (r v_r) + \frac{\partial v_z}{\partial z} \right) - \epsilon_R \frac{\partial \Delta T_R}{\partial r} &= -\rho_R r \Omega^2, \\ \mu_R \nabla^2 v_z + (\gamma_R + \mu_R) \frac{\partial}{\partial z} \left(\frac{1}{r} \frac{\partial}{\partial r} (r v_r) + \frac{\partial v_z}{\partial z} \right) - \epsilon_R \frac{\partial \Delta T_R}{\partial r} &= 0 \end{aligned} \quad (1)$$

with

$$\gamma_R = \frac{E_R \nu_R}{(1 + \nu_R)(1 - 2\nu_R)}, \quad \mu_R = \frac{E_R}{2(1 + \nu_R)}, \quad \epsilon_R = \frac{E_R \alpha_R}{1 - 2\nu_R}.$$

γ_R is the Lamé constant and μ_R is the shear modulus (also referred to as G). The constant ϵ_R describes thermoelastic stresses with $\Delta T_R = T_R - T_{\text{ref}}$ being the disk temperature difference with respect to a reference temperature $T_{\text{ref}} = T_0 = 20^\circ\text{C}$. Further, ρ_R is the density of the rotor material. It is assumed that the influence of the fluid film pressure and the fluid film shear stresses on the rotor disk are negligible. The outer edges of the rotor are therefore assumed stress-free.

The temperature field of the rotor $T_R(r, z)$ is obtained through the heat diffusion equation

$$\frac{\partial}{\partial r} \left[\lambda_R r \frac{\partial T_R}{\partial r} \right] + \frac{\partial}{\partial z} \left[\lambda_R r \frac{\partial T_R}{\partial z} \right] = 0. \quad (2)$$

In order to accurately model the bearing behavior, it is important to account for all relevant heat fluxes entering and leaving the rotor. For this purpose, the rotor surface is sectioned into different parts. Fig. 4(a) gives an overview over the different boundary sections I to VIII that are considered.

For the determination of heat fluxes in sections II, III, and IV, a 3D Computational Fluid Dynamics (CFD) analysis is conducted, allowing for the determination of heat transfer coefficients on these 3 boundaries of the rotor. In this paper, the complex CFD model will not be discussed in detail. In short, it contains a fluid dynamics model for the surrounding air as well as a heat conduction model for the simplified rotor. In the CFD simulation, a *total energy* model is used for compressible flow with a *SST* turbulence approach [30,31]. As a boundary condition for the rotor temperature in the CFD model, a representative power loss distribution is applied to section I of the rotor disk. It stems from dissipative losses in the air gap and is dependent on the rotational speed and the load. The output of the CFD simulations are heat transfer coefficients for the disk boundaries II, III, and IV. CFD calculations are carried out for different operating points, i.e. different thrust loads and rotational speeds, so that the heat transfer can be described as a function of the bearing operating conditions. The detailed correlations are described below. Fig. 4(b) shows a section view of exemplary CFD simulation results, displaying the temperature field $T_R(r, z)$ for the rotor in $^\circ\text{C}$ (right scale) as well as the absolute velocity for the surrounding air in m/s (left scale). The temperature distribution in the rotor will be discussed in the results Section 3 of this work.

In the following paragraphs, the boundary conditions for the rotor sections I to VIII are discussed in detail.

Section I: Section I refers to the rotor interface to the load carrying lubricating gap. Here, the disk temperature T_R and air temperature T_A as well as the respective normal heat flux are coupled. On the rotor disk section I, the Neumann boundary condition

$$\lambda_R r \frac{\partial T_R}{\partial z} = q_{\text{gap}}(r) \quad (3)$$

is enforced where $q_{\text{gap}}(r)$ is the averaged heat flux from the lubricating gap. Due to the high rotational speeds of the rotor, an axisymmetric model for rotor temperature calculation according to Eq. (2) is used. Therefore, the rotor temperature $T_R(r, z)$ is not dependent on the circumferential coordinate. This means that different coordinate systems are used for the rotor (axisymmetric, cylindrical r, z -coordinates) and

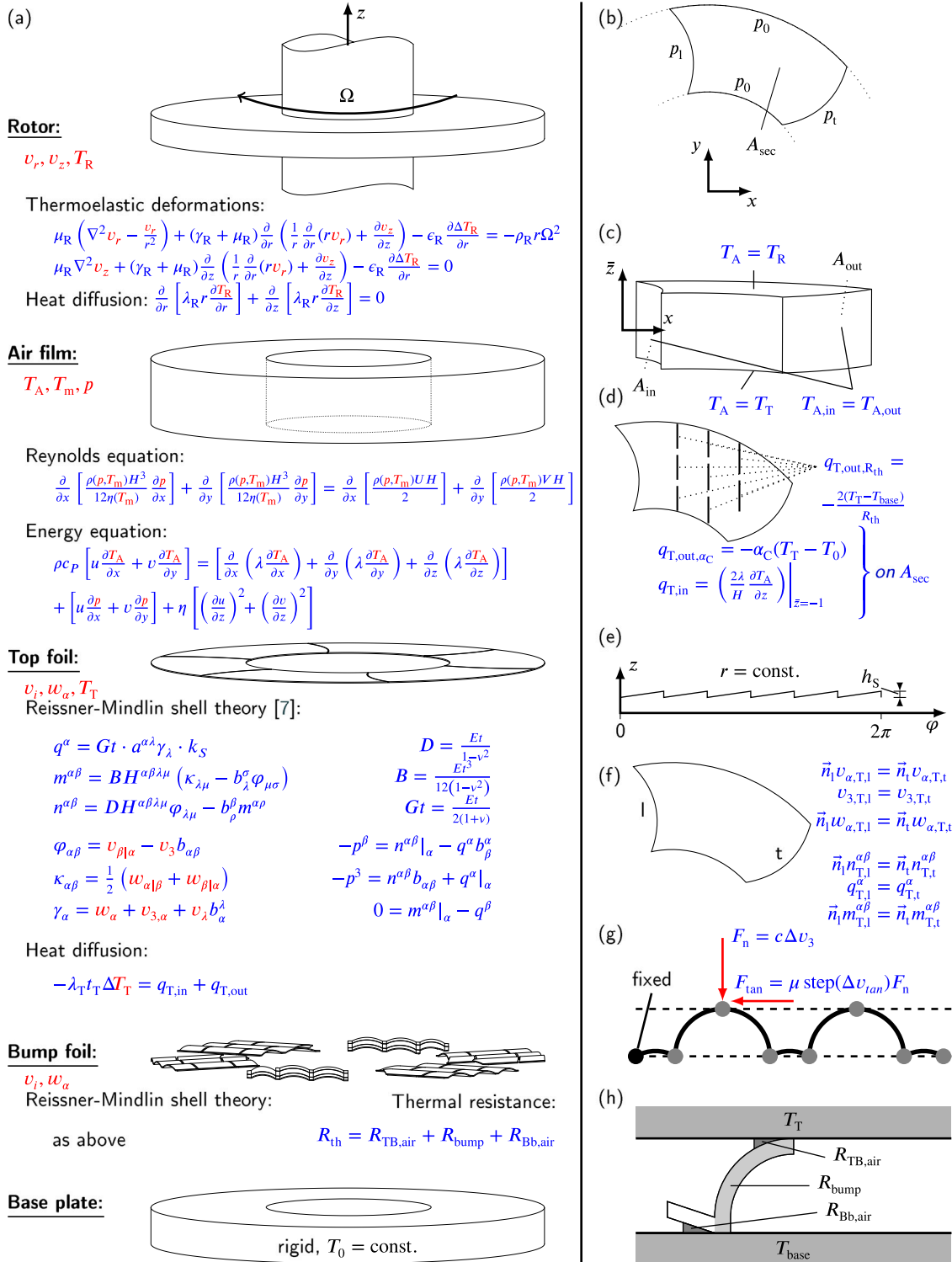


Fig. 3. Bearing model: (a) Components and main equations, (b) pressure boundary conditions (BCs) of single top foil sector, (c) thermal BCs of single air film sector, (d) thermal BCs of top foil sector, (e) nominal height profile, (f) mechanical BCs of single top foil sector (periodic), (g) contact formulation in bump and top foil, and (h) thermal resistance of a half bump.

for the air film component (3D-Cartesian coordinates). Thus, the heat flux from the lubricating gap is firstly transformed into cylindrical coordinates and afterwards averaged over the circumferential coordinate, resulting in

$$q_{gap}(r) = \frac{n_{sec}}{2\pi} \int_{\varphi_l(r)}^{\varphi_t(r)} \left(\frac{2\lambda}{H} \frac{\partial T_A(r, \varphi, \bar{z})}{\partial \bar{z}} \right) \Big|_{\bar{z}=1} r d\varphi. \quad (4)$$

Herein, $\varphi_l(r)$ and $\varphi_t(r)$ are the expressions for the leading and trailing edge angle, respectively. They describe their curved contour as a function of the radial coordinate r . For the definitions of the remaining terms, namely λ , H , T_A , φ , and \bar{z} , see Section 2.2. Note that the rotor disk temperature $T_R(r, z)$ and the air film temperature $T_A(x, y, z)$ are coupled through Eq. (14).

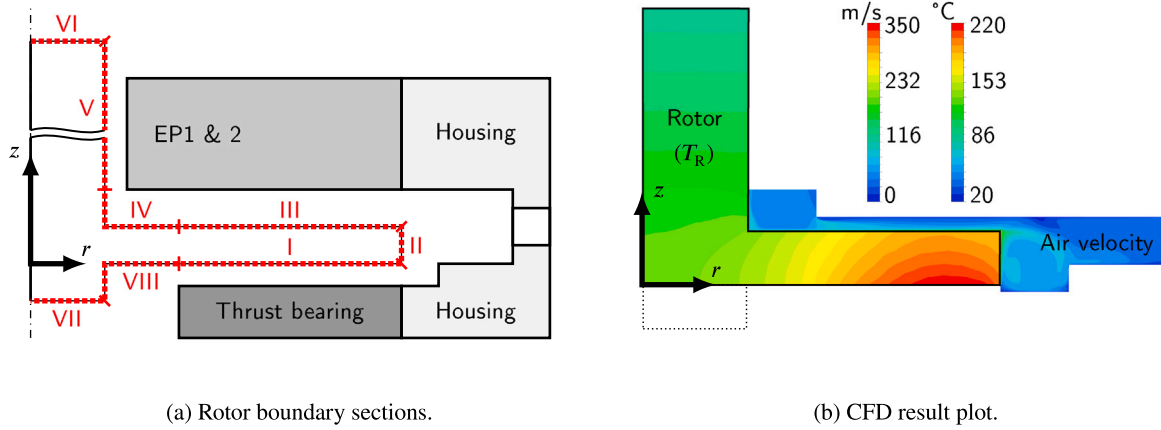


Fig. 4. (a) Definition of rotor boundary sections I to VIII. (b) Result plot section of CFD calculation for heat transfer coefficient determination.

Section II: At the outer perimeter of the rotor disk in Section 2, the heat transfer is described with a Neumann boundary condition

$$-\lambda_R r \frac{\partial T_R}{\partial r} = \alpha_{II} r (T_R - T_0). \quad (5)$$

The heat transfer coefficient α_{II} is a result of CFD calculations:

$$\alpha_{II} = (1.3 \bar{T}_{R,II} + 124) \text{W}/(\text{m}^2 \text{K}). \quad (6)$$

In good approximation, this linear dependency on the mean rotor disk temperature $\bar{T}_{R,II}$ in the small Section 2 is found. It is defined as

$$\bar{T}_{R,II} = \frac{1}{t_D} \int_0^{t_D} T_R(r = r_{D,o}, z) dz. \quad (7)$$

Herein, $t_D = 3.5$ mm is the rotor disk thickness and $r_{D,o} = 27.5$ mm is the outer radius of the rotor disk. Note that this averaged temperature in Section 2 serves as a reference temperature not only for Section 2, but also for Section 3 (see below). It has been found to be representative for the different temperature distributions at the different operation points considered in the CFD simulation.

Section III: A similar Neumann boundary condition as in Eq. (5) is enforced in section III, namely

$$\lambda_R r \frac{\partial T_R}{\partial z} = \alpha_{III} r (T_R - T_0) \quad (8)$$

with the respective heat transfer coefficient

$$\alpha_{III} = (0.63 \bar{T}_{R,II} + 343) \text{W}/(\text{m}^2 \text{K}). \quad (9)$$

Section IV: In the small section with label IV, a small but not negligible heat flux is observed in CFD analysis. Therefore, a heat flux $q = \alpha_{IV} (T_R - T_0)$ is assumed with a constant $\alpha_{IV} = 300$ W/(m²K).

Section V: The journal bearings of the considered rotor system are externally pressurized air bearings (EP) which are opposite of rotor boundary V, see Fig. 4(a). These bearings provide a constant and cool air flow. In experiments, it is found that dissipative losses in the small radial gap of the EP bearings are almost compensated by the fresh air stream which supports the rotor. Therefore, in good approximation, only heat conduction over the air gap of the EP bearings is taken into account so that a following simple Neumann boundary condition can be applied at rotor boundary V:

$$-\lambda_R r \frac{\partial T_R}{\partial r} = r \lambda_{EP} (T_R - T_{ep}) / d_{gap}. \quad (10)$$

Herein, $\lambda_{EP} = \lambda_{EP}(T = [T_R + T_{EP}]/2)$ is the heat conductivity of the air in the bearing gap of the EP bearings. It is defined as the heat conductivity of air at the mean value of the rotor temperature T_R in Appendix A and the temperature of the externally pressurized journal bearings $T_{EP} = 15$ °C. $d_{gap} = 10 \mu\text{m} - v_r$ describes the radial gap size of the EP bearings which is dependent on the thermoelastic radial

deformations of the rotor v_r with an initial value at standstill of 10 μm . The small gap between the two EP bearings visible in Fig. 1 is neglected.

Section VI/VII: The front side rotor boundaries VII (bottom) and VI (top) as well as the inner boundary at $r = 0$ are assumed to be adiabatic with $\vec{n} \nabla T_R = 0$.

Section VIII: Due to their similarity and for simplicity, section VIII is treated like Section 4.

2.2. Air film

Air film pressure $p(x, y)$ is calculated via the generalized Reynolds equation of Ref. [32] using an averaged fluid temperature $T_m(x, y)$ (averaging over the gap height) for the determination of the density ρ and viscosity η , cf. Ref. [28]:

$$\begin{aligned} \frac{\partial}{\partial x} \left[\frac{\rho(p, T_m) H^3}{12 \eta(T_m)} \frac{\partial p}{\partial x} \right] + \frac{\partial}{\partial y} \left[\frac{\rho(p, T_m) H^3}{12 \eta(T_m)} \frac{\partial p}{\partial y} \right] \\ = \frac{\partial}{\partial x} \left[\frac{\rho(p, T_m) U H}{2} \right] + \frac{\partial}{\partial y} \left[\frac{\rho(p, T_m) V H}{2} \right]. \end{aligned} \quad (11)$$

$U = \Omega y$ and $V = -\Omega x$ describe the x - and y -component of the rotor disk velocity, respectively; ρ is the air density and η is the air viscosity. H denotes the height function that is discussed in detail in Section 2.4.

The pressure $p_l(r, \varphi_l(r))$ at the leading and $p_t(r, \varphi_t(r))$ at the trailing edge are coupled periodically, i.e.

$$p_l(r, \varphi_l(r)) = p_t(r, \varphi_t(r)). \quad (12)$$

The respective fluxes are coupled similarly. At the inner ($r = r_i$) and outer ($r = r_o$) boundary, the pressure is set to ambient pressure, $p = p_0$, cf. Fig. 3(b).

The temperature field $T_A(x, y, z)$ results from solving the leading terms of the following 3D compressible energy equation, cf. for example [5]:

$$\begin{aligned} \rho c_p \left[u \frac{\partial T_A}{\partial x} + v \frac{\partial T_A}{\partial y} \right] = \left[\frac{\partial}{\partial x} \left(\lambda \frac{\partial T_A}{\partial x} \right) + \frac{\partial}{\partial y} \left(\lambda \frac{\partial T_A}{\partial y} \right) + \frac{\partial}{\partial z} \left(\lambda \frac{\partial T_A}{\partial z} \right) \right] \\ + \left[u \frac{\partial p}{\partial x} + v \frac{\partial p}{\partial y} \right] + \eta \left[\left(\frac{\partial u}{\partial z} \right)^2 + \left(\frac{\partial v}{\partial z} \right)^2 \right]. \end{aligned} \quad (13)$$

The first term describes the convective heat transfer, the second term diffusive heat transfer (conduction). The third term of the energy equation refers to the power of pressure forces, the last term describes dissipation resulting from shear forces.

In AFTBs, the conductive heat transfer in axial z -direction is dominant over the convective heat transfer due to the dimensions of the air gap. Also, planar heat diffusion in the lubricating gap is usually neglected, cf. [21]. However, the energy equation presented here contains

both convective heat transfer and planar heat diffusion in order to be able to correctly formulate the cyclic boundary conditions shown later.

The film height function H and thus the air film domain changes when rotational speed or load are changed. This is why a coordinate transformation for the energy equation domain is conducted, transforming the gap height ranging between 0 and H to $\bar{z} = -1 \dots 1$. Fig. 3(c) shows the transformed air film domain as well as the boundary conditions of the energy equation. The temperature $T_A(x, y)|_{\bar{z}=1}$ at the top face of the air film is coupled to the rotor disk temperature $T_R(r)$ with the Dirichlet boundary condition

$$T_A(x, y)|_{\bar{z}=1} = T_R(r). \quad (14)$$

Note that the respective heat fluxes are coupled through Eq. (3).

At the bottom surface, the air temperature $T_A(x, y)|_{\bar{z}=-1}$ is coupled to the top foil temperature with the Dirichlet boundary condition

$$T_A(x, y)|_{\bar{z}=-1} = T_T(x, y). \quad (15)$$

The corresponding flux boundary condition is enforced on the top foil, see Eq. (23).

Cyclic boundary conditions are enforced on the inlet surface $A_{in}(r, \varphi_1(r), \bar{z})$ and outlet surface $A_{out}(r, \varphi_2(r), \bar{z})$, cf. Fig. 3(c). This means that the temperature fields as well as the boundary heat fluxes are coupled according to

$$\begin{aligned} T_{A,in}(x, y, z) &= T_{A,out}(x, y, z), \\ -\bar{n}_{in} \nabla T_A(x, y, z)|_{in} &= \bar{n}_{out} \nabla T_A(x, y, z)|_{out} \end{aligned} \quad (16)$$

Herein, \bar{n}_{in} and \bar{n}_{out} describe the face normals of the inlet and outlet which lie parallel to the xy -plane.

Note that the remaining boundaries of the air film are assumed to be adiabatic. It should finally be mentioned that the fluid velocities of Eq. (13) are defined as in [32]:

$$u = \frac{-H^2}{8\eta} \frac{\partial p}{\partial x} (1 - \bar{z}^2) + \frac{U}{2} (\bar{z} + 1), \quad v = \frac{-H^2}{8\eta} \frac{\partial p}{\partial y} (1 - \bar{z}^2) + \frac{V}{2} (\bar{z} + 1). \quad (17)$$

Due to the cyclic coupling of the pressure and pressure gradient, the fluid velocities are also coupled cyclically.

For the bearing designer, two parameters of AFTBs are of special interest, namely the bearing load capacity W and the bearing power loss P_{loss} , which are defined as follows:

$$W = n_{sec} \iint (p - p_0) dA_{sec} \quad (\text{for } H_{min} = 2 \mu\text{m}), \quad (18)$$

$$P_{loss} = n_{sec} \Omega \iint \frac{-2\eta}{H} (x \frac{\partial v}{\partial z} - y \frac{\partial u}{\partial z}) dA_{sec}.$$

Herein, A_{sec} describes the area of the sector. In this work, the load capacity of the thrust bearing is defined as the load at which the minimal film height reaches a threshold value of $H_{min} = 2 \mu\text{m}$. If more load is applied, the minimal film height will decrease and full fluid lubrication will no longer be sustained, i.e. mixed lubrication is assumed to occur. The power loss of Eq. (18) results from integrating the shear stresses over the sector area.

2.3. Top and bump foil

The top foil temperature profile $T_T(x, y)$ is obtained by the planar heat diffusion equation

$$-\lambda_T t_T \Delta T_T = q_{T,in} + q_{T,out} \quad (19)$$

with constant heat conductivity λ_T and thickness t_T of the top foil. Again, a cyclic coupling of the leading and trailing edge temperature is implemented via the Dirichlet boundary condition

$$T_{T,l} = T_{T,t}. \quad (20)$$

The boundary heat flux at the leading and trailing edge is coupled through the Neumann boundary condition

$$-\bar{n}_l \nabla T_T|_l = \bar{n}_t \nabla T_T|_t. \quad (21)$$

The remaining outer boundaries at $r = r_i$ and $r = r_o$ are assumed to be adiabatic:

$$\bar{n} \nabla T_T = 0 \quad \text{at } r = r_i \quad \text{and } r = r_o. \quad (22)$$

The top foil temperature T_T is coupled to the air film temperature T_A via the incoming heat flux

$$q_{T,in} = \left(\frac{2\lambda}{H} \frac{\partial T_A}{\partial \bar{z}} \right) \Big|_{\bar{z}=-1} \quad (23)$$

on the entire sector domain A_{sec} .

Outgoing heat fluxes are described by two separate terms: $q_{T,out} = q_{T,out,\alpha_C} + q_{T,out,R_{th}}$. On the one hand, outgoing heat fluxes are modeled with the heat transfer coefficient α_C on A_{sec} :

$$q_{T,out,\alpha_C} = -\alpha_C (T_T - T_0). \quad (24)$$

The heat transfer coefficient α_C stems from active cooling and heat conduction in the air gap between top and bump foil as well as between top foil and base plate.

On the other hand, heat conduction through the bump foil into the base plate is represented by a resulting thermal resistance R_{th} . It is applied only on the contact lines of top and bump foil, see Fig. 3 d:

$$q_{T,out,R_{th}} = -\frac{2(T_T - T_{base})}{R_{th}}. \quad (25)$$

The thermal resistance of each half bump arc R_{th} consists of the contact resistance between top and bump foil $R_{TB,air}$, the contact resistance between bump foil and base plate $R_{Bb,air}$, and the conduction resistance through the half bump arc R_{bump} , cf. Fig. 3(h). Details can be found in [21].

Deformations of top and bump foil are calculated using the Reissner–Mindlin shell theory [33]. It allows for 3 translational (v_i with $i = \{1, 2, 3\}$) and 2 rotational (w_α with $\alpha = \{1, 2\}$) degrees of freedom. The governing equations depend on the metrical and curvature properties of the shell middle surface.

In good approximation, the top foil can be seen as a planar (flat) shell. Since the step height is similar to the foil thickness, the step can be neglected in the mechanical treatment of the top foil, see e.g. [34]. For the pressure calculation, however, the exact air film height and thus the top foil topology including the step is of highest importance. It is discussed in detail in Section 2.4.

In order to analyze the bump foil, it is sectioned into flat and round sections: the bridges between bumps are modeled as planar shells, while the bumps and the roundings (connections between each bridge and bump arc) are modeled as cylindrical shells, cf. Fig. 3(g).

The 5 governing equations for the deformations of a cylindrical shell with radius of curvature R (centerline along y -axis) are as follows:

$$\begin{aligned} \frac{\partial}{\partial x} \left[D \left(\frac{\partial v_1}{\partial x} + v \frac{\partial v_2}{\partial y} + \frac{1}{R} v_3 \right) + \frac{B}{R} \left(\frac{\partial w_1}{\partial x} + v \frac{\partial w_2}{\partial y} + \frac{1}{R} \frac{\partial v_1}{\partial x} + \frac{1}{R^2} v_3 \right) \right] \\ + \frac{\partial}{\partial y} \left[D \frac{1-v}{2} \left(\frac{\partial v_2}{\partial x} + v \frac{\partial v_1}{\partial y} \right) + \frac{B}{R} \frac{1-v}{2} \left(\frac{\partial w_2}{\partial x} + v \frac{\partial w_1}{\partial y} + \frac{1}{R} \frac{\partial v_1}{\partial y} \right) \right] \\ = -\frac{Gt_S}{R} \left(w_1 + \frac{\partial v_3}{\partial x} - \frac{1}{R} v_1 \right) + p^1, \end{aligned} \quad (26)$$

$$\begin{aligned} \frac{\partial}{\partial x} \left[D \frac{1-v}{2} \left(\frac{\partial v_2}{\partial x} + v \frac{\partial v_1}{\partial y} \right) \right] \\ + \frac{\partial}{\partial y} \left[D \left(\frac{\partial v_2}{\partial y} + v \frac{\partial v_1}{\partial x} + \frac{v}{R} v_3 \right) \right] \\ = p^2, \end{aligned} \quad (27)$$

$$\begin{aligned} \frac{\partial}{\partial x} \left[Gt_S \left(w_1 + \frac{\partial v_3}{\partial x} + \frac{1}{R} v_1 \right) \right] + \frac{\partial}{\partial y} \left[Gt_S \left(w_2 + \frac{\partial v_3}{\partial y} \right) \right] \\ = \frac{D}{R} \left(\frac{\partial v_1}{\partial x} + v \frac{\partial v_2}{\partial y} + \frac{1}{R} v_3 \right) \\ + \frac{B}{R} \left(\frac{\partial w_1}{\partial x} + v \frac{\partial w_2}{\partial y} + \frac{1}{R} \frac{\partial v_1}{\partial x} + \frac{1}{R^2} v_3 \right) + p^3, \end{aligned} \quad (28)$$

$$B \left[\frac{\partial}{\partial x} \left(\frac{\partial w_1}{\partial x} + \nu \frac{\partial w_2}{\partial y} + \frac{1}{R} \frac{\partial v_1}{\partial x} + \frac{1}{R^2} v_3 \right) + \frac{\partial}{\partial y} \left(\frac{1-\nu}{2} \left(\frac{\partial w_1}{\partial y} + \frac{\partial w_2}{\partial x} + \frac{1}{R} \frac{\partial v_1}{\partial y} \right) \right) \right] = Gt k_S \left(w_1 + \frac{\partial v_3}{\partial x} - \frac{1}{R} v_1 \right), \quad (29)$$

$$B \left[\frac{\partial}{\partial x} \left(\frac{1-\nu}{2} \left(\frac{\partial w_1}{\partial y} + \frac{\partial w_2}{\partial x} + \frac{1}{R} \frac{\partial v_1}{\partial y} \right) \right) + \frac{\partial}{\partial y} \left(\frac{\partial w_2}{\partial y} + \nu \frac{\partial w_1}{\partial x} + \frac{1}{R} \frac{\partial v_1}{\partial x} + \frac{\nu}{R^2} v_3 \right) \right] = Gt k_S \left(w_2 + \frac{\partial v_3}{\partial y} \right), \quad (30)$$

where $D = \frac{Et}{1-\nu^2}$ is the stretching stiffness, $B = \frac{Et^3}{12(1-\nu^2)}$ is the bending stiffness, and $Gt = \frac{Et}{2(1+\nu)}$ is the shear stiffness. Note that the 1-, 2-, and 3-direction correspond to the x -, y -, and z -direction of the Cartesian coordinate system of Fig. 3(b), respectively. Fig. 3(a) shows the underlying constitutive equations for the transverse shear stress q^α , the moment tensor $m^{\alpha\beta}$, and the stress resultant tensor $n^{\alpha\beta}$, the kinematic relations for the strain variables $\varphi_{\alpha\beta}$, $\kappa_{\alpha\beta}$, and γ_α , and the 5 equilibrium equations [33,35]. For clarity, the deformation variables of the top foil possess the index T; the index B is used for the bump foil.

The pressure in the lubricating gap causes deformations of the top foil. Thus, the air pressure p is implemented as an external load, i.e.

$$p_T^3 = p - p_0. \quad (31)$$

Secondly, contact forces between the top foil and bump foil as well as between the bump foil and the base plate are incorporated as external loads on the respective component. Contacts are approximated as line contacts at the top line of the bumps and the respective lines on the top foil as visible in Fig. 3(d). Normal contact forces $F_n = c \Delta v_3$ are modeled via a penalty stiffness c allowing only for small penetration depths Δv_3 . Tangential contact forces $F_{tan} = \mu \cdot \text{step}(\Delta v_{tan}) F_n$ are formulated with a generalized Coulomb friction approach [36] as depicted in Fig. 3(g) with a smoothed step-function $\text{step}(\Delta v_{tan})$. Δv_{tan} describes the relative tangential deflection of the contact partners.

As boundary conditions for the top foil sector, cyclic boundary conditions are formulated for the leading (index l) and trailing edge (index t), see Fig. 3(f):

$$\begin{aligned} \vec{n}_l v_{\alpha,T,l} &= \vec{n}_t v_{\alpha,T,t}, & v_{3,T,l} &= v_{3,T,t}, & \vec{n}_l w_{\alpha,T,l} &= \vec{n}_t w_{\alpha,T,t}, \\ \vec{n}_l n_{T,l}^{\alpha\beta} &= \vec{n}_t n_{T,t}^{\alpha\beta}, & q_{T,l}^\alpha &= q_{T,t}^\alpha, & \vec{n}_l m_{T,l}^{\alpha\beta} &= \vec{n}_t m_{T,t}^{\alpha\beta} \end{aligned} \quad (32)$$

\vec{n}_l and \vec{n}_t describe the normal vectors at the leading and trailing edge, respectively. The inner and outer edge at $r = r_i$ and $r = r_o$ are assumed to be stress-free.

For the bump foil, the formulation of the boundary conditions is straightforward as each sector possesses an independent bump foil. Each of the 3 bump strips of a bump foil has a fixed and a free end. The fixed end is implemented as a Dirichlet boundary conditions with zero deflections. For the free end, a zero flux (stress-free) condition is applied, cf. Fig. 3(g). It should be mentioned that thermal stresses are neglected in the shell model for top and bump foil. Due to the limited component temperatures and the boundary conditions of the foils, thermally induced buckling of top and bump foil will not occur. Thermally induced in-plane deformations resulting from thermal expansion are very small and therefore neglected in the analysis (also note that thermally induced in-plane deformations of the top foil only have a marginal influence on the fluid film height and are of lower relevance for the multiphysical model).

2.4. Manufactured real top foil topology

This section discusses the deviation of the real top foil topology from the ideal nominal top foil topology. Simulations have shown that it is necessary to consider the real top foil geometry in order to obtain results in accordance with measurement results. It will be shown that significant deviations of the ideal nominal and the real topology are present. Due to the manufacturing process, these deviations were found consistently in all test specimen and therefore included in the analysis. The description of the mean deviations can be found in this section.

It should be noted, however, that the implementation of the real topology on its own will not be sufficient to yield numerical results in accordance with experiments. It is found that only a combination of the manufactured real top foil topology and a wear algorithm, which will be described in Section 2.5, yields agreement of numerical and experimental results with regard to load capacity, power loss, and wear pattern. The embossing process of the top foil yields a taper-step-type surface as displayed in Fig. 2(b). The nominal profile, plotted over the circumference of a perimeter cut, can be seen in Fig. 3(e). It shows a vertical step between two sectors and a linear taper in between. However, measurements show that the real topology may divert from the ideal one. Firstly, the geometrical shape of the top foil after the embossing process shows a bulging and a non-vertical step between the sectors. Secondly, the top foil coating is found to be non-uniform with accumulations at the inner and outer sector border. It will be shown that it is very important to include this real top foil topology in the simulation model in order to reproduce bearing load capacity and power loss from measurements.

In a first simulation step, the ideal nominal top foil topology has been incorporated in the simulation model. The ideal top foil possesses a uniform coating layer with a nominal thickness of 25 μm , an ideal steep step between the top foil sectors and no radial parabolic shape deviation of the top foil sheet. However, simulation results for this ideal nominal top foil topology showed very large discrepancies when compared to experimental results. Significant deviations are found in the load capacity, the power loss and the deformation profile. Measurements show a load capacity of $W = 100 \text{ N}$ at 120 krpm with a power loss of $P_{\text{loss}} = 333 \text{ W}$. Simulations with the ideal topology, however, show the following results:

- For an isothermal simulation, the thrust bearing shows a maximum load capacity of 38 N, exerting a power loss of only 134.4 W. This amounts to approximately 40% of the experimental data.
- In a TEHD model, results indicate an even lower load capacity and power loss of approximately 25% of experimentally observed results.
- In addition to the global evaluation of the bearing performance, top foil deformations were analyzed in detail. Simulations for the isothermal case as well as with the TEHD model show that the minimal air film gap lies near the middle of the trailing edge of the sector. It is expected that wear will initially occur in this area. However, experimental tests indicate that the main wear is located at the inner and outer radius of the top foil sector, see Section 3.

The reason for these discrepancies can be traced back to the deviation of the real top foil from the ideal nominal topology. A detailed experimental investigation of the real top foil geometry yields the following results:

- The step at the border of adjacent sectors is not ideally vertical but rather extended over a small region. An average step width of 0.66 mm is observed in real top foils.
- In the ideal geometry, the top foil possesses no radial slope or curvature; the ideal taper is a function of the angular position only. Through the embossing process, however, the top foil is also deformed into a parabolic shape. This shape deviation is observable in radial direction, meaning that the inner and outer foil

edge (at the inner and outer radius) is bent upwards. Therefore, radial cuts of the top foil do not yield straight lines. Measurements show that this shape deviation in radial direction can be sufficiently approximated by the parabola expression $H_{\text{par}}(r) = h_{\text{par}}(r - r_m)^2 / (r_i - r_m)^2$ with $r_m = (r_i + r_o)/2$ and $h_{\text{par}} = 20 \mu\text{m}$.

- The top foil is coated with a PTFE layer with a mean coating thickness of $25 \mu\text{m}$. Measurements show that this coating is not uniform. A detailed analysis of the coating thickness reveals that, towards the inner and outer foil edges at $r = r_i$ and $r = r_o$, coating accumulations of $\Delta h_{\text{coat}} = 12 \mu\text{m}$ beyond the mean coating thickness are observed. Measurements further show that the variation of coating height in the circumferential direction is negligible. Consequently, the coating height distribution in radial direction, in the following denoted by $H_{\text{coat}}(r)$, is considered in the simulation model with a spline representation.

These 3 deviations are systematic due to the manufacturing process of the top foil and the coating application. They were found in all the test specimen.

The first two items of the list above—namely the finite step width of 0.66 mm and the parabolic shape deviation in radial direction—are geometrical deviations of the metal foil due to the embossing process in comparison with the ideal geometry. In combination with the ideal taper, they are summarized in the expression $H_{\text{shape}}(x, y)$ below. It should be stressed again that the ideal taper is only a function of the angular position and not of the radial coordinate.

Remark on the influence of these first two defects on the contact formulation: Although the top foil is mechanically treated as an ideal flat plate, its real shape must be taken into account for the contact formulation between the top and the bump foil. Together, the deformations $v_{3,T}$ of the top foil and the real foil topology H_{shape} accurately describe the top foil position. In the normal contact force formulation, the corrected penetration depth thus reads $\Delta v_3 = v_{3,B} - (v_{3,T} + H_{\text{shape}})$. Herein, $v_{3,B}$ is the bump and $v_{3,T}$ the respective top foil deflection at a contact line. As a consequence, the initial air gap between the top foil and the bump foil is hereby correctly taken into account.

The third item of the list above corresponds only to the coating of the top foil. It does not contribute to the foil stiffness and is not part of the mechanical model of the top foil. Images of the real top foil geometry are shown in Section 3.1 (note especially Fig. 6(a)).

Due to the 3 deviations discussed above, the ideal taper-step height function must be corrected in the simulation model. The resulting height function including all deviations reads

$$H(x, y) = z_R + H_{\text{shape}} + H_{\text{coat}} + v_{3,T} - v_z(z = 0, r). \quad (33)$$

Herein, z_R describes the axial position of the rotor and $v_z(z = 0, r)$ with $r_i \leq r < r_o$ is the axial rotor disk deformation in section I of Fig. 4(a). Eq. (33) constitutes the corrected height function H with all the topology details and deviations.

With the height function $H(x, y)$, simulations with the TEHD model show an even lower load capacity and power loss equivalent to only 7% of experimental data. The reason for this significant difference lies in the wear of the top foil coating which occurs due to contact between the rotor disk and the top foil surface. Experiments indicate that parts of the top foil show significant wear after testing. This is why a wear algorithm has been developed and implemented into the simulation model. Only when including the non-uniform wear in the simulation model, experimental results can be reproduced.

2.5. Wear simulation

The wear algorithm that has been developed is described in the upcoming section. It allows to take into account gap height changes due to wear. Basis of the quasi-static wear simulation is the stationary TEHD model described in the previous sections.

```

program WEAR ITERATION
Iteration number  $i = 0$ 
while  $W \leq 100 \text{ N}$ 
  set initial value of  $z_R$ 
  calculate foil and disk deflections
  while  $\min |H(x, y)| \neq H_{\min}$ 
    update  $z_R$ 
    calculate foil and disk deflections
  end while
  calculate  $H_{\text{wear}}^{(i)}$ 
   $H_{\text{wear}}^{(i)} = H_{\text{wear}}^{(i-1)} + \text{ramp}(H^{(i-1)} + H_{\min} + \delta_{\text{wear}})$ 
  increment  $i$ 
end while
 $i = i_{\text{end}}$ 
end program WEAR ITERATION

```

Fig. 5. Pseudocode of the wear algorithm.

With this TEHD model, stationary simulations of the bearing components can be carried out. The minimal gap height $\min |H(x, y)|$ is used as a limit criterion for plausible bearing operation. In this work, $\min |H(x, y)| = H_{\min} = 2 \mu\text{m}$ is chosen as the transition point between fluid lubrication and mixed lubrication. The integrated pressure field at this specific point represents an approximation of the load capacity of the bearing, cf. Eq. (18). If the thrust load on the rotor is further increased, the disk will get closer to the top foil and $\min |H(x, y)| < H_{\min}$. The assumptions for a continuous air flow are no longer met in this case and mixed lubrication is expected to occur.

In experiments, several significant wear marks on the coating are observed during the run-in process. In order to represent this effect in the simulation, a quasi-static wear algorithm is developed. It assumes that the top foil coating is soft compared to the rotor disk and will instantaneously be worn when mixed lubrication occurs.

For the wear algorithm, the function $H_{\text{wear}}(x, y)$ is defined as the wear depth of the top foil. This means that worn areas possess a positive value according to the height of abraded coating, while unworn areas have a wear depth of 0. Initially, H_{wear} is set to zero and a stationary simulation of the bearing is carried out until $\min |H(x, y)| = H_{\min}$ is met, yielding amongst others a load capacity $W^{(0)}$ for the unworn state according to Eq. (33). Note that reaching a specific value of the minimal gap height is achieved by changing the axial position of the rotor z_R . Now, all areas of the height function with $H \geq -(H_{\min} + \delta_{\text{wear}})$ with a small user-defined δ_{wear} are stored in the wear function

$$H_{\text{wear}}^{(1)} = \text{ramp}(H + H_{\min} + \delta_{\text{wear}}) = \begin{cases} H + H_{\min} + \delta_{\text{wear}}, & H + H_{\min} + \delta_{\text{wear}} \geq 0 \\ 0, & H + H_{\min} + \delta_{\text{wear}} < 0 \end{cases}. \quad (34)$$

In the upcoming sections, $\delta_{\text{wear}} = 1 \mu\text{m}$ has been chosen. It represents the wear height increment of each wear step. Note that the bracketed superscript index denotes the wear iteration, ranging from 0 (unworn state) to i_{end} (fully worn state).

While the base iteration with $i = 0$ is carried out with the height function H of Eq. (33), the new height function for iteration step $i = 1$ and the corresponding height functions for the upcoming iteration steps now read

$$\begin{aligned} H^{(0)} &= H, \\ H^{(1)} &= H - H_{\text{wear}}^{(1)}, \\ &\vdots \\ H^{(i)} &= H - H_{\text{wear}}^{(i)}, \\ &\vdots \\ H^{(i_{\text{end}})} &= H - H_{\text{wear}}^{(i_{\text{end}})}. \end{aligned} \quad (35)$$

After each incrementation of H_{wear} , a new simulation of the bearing is conducted. In the proceeding incrementation steps, the old wear result

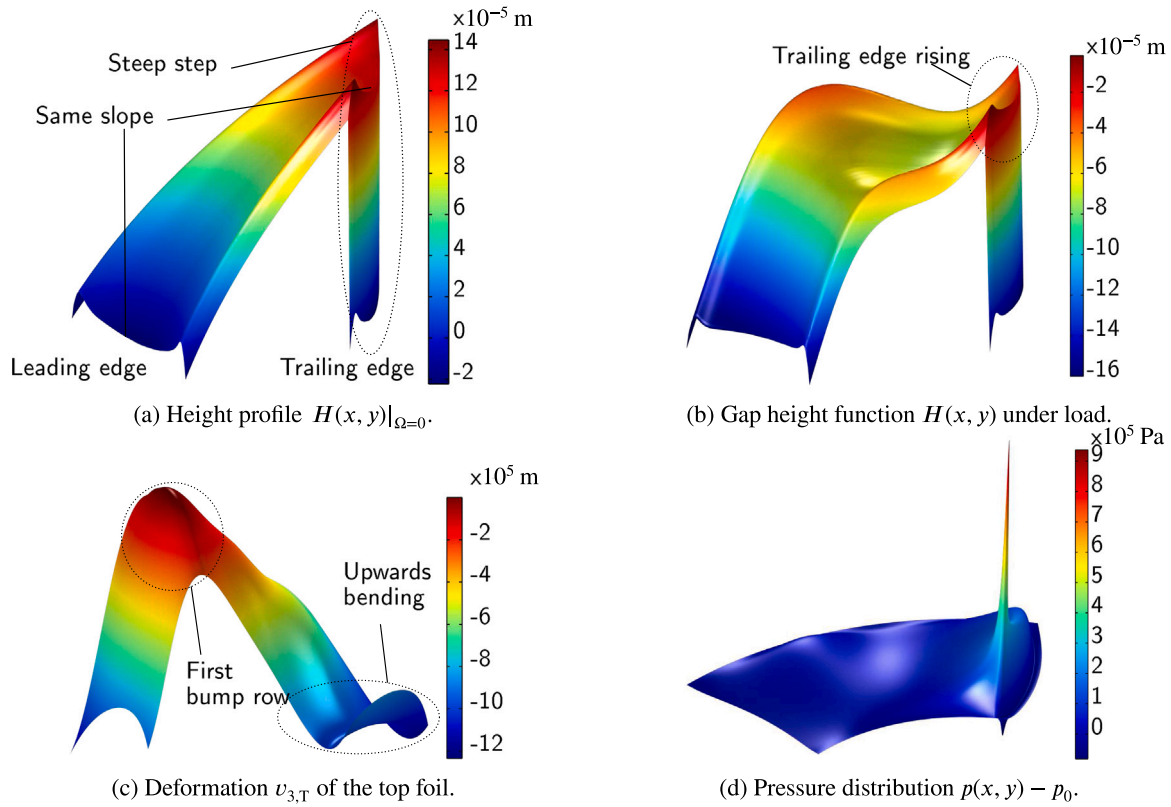


Fig. 6. (a) Height profile after assembly without load, (b) height function $H^{(0)} = H$ for a rotational speed of 120krpm and a minimal gap height $H_{\min} = 2\mu\text{m}$, (c) corresponding top foil deformation v_3 under pressure load showing a kink at the first bump row as well as a cyclic deformation profile, and (d) corresponding pressure distribution.

Table 2
Numerical details of the model.

Component	No. of elements
Bump foil	640
Top foil	1705
Air film	11 840
Rotor	364

Table 2 shows the number of elements for each component. In total, 720824 degrees of freedom are solved for. The discretized integro-differential system is solved by a Newton–Raphson method in combination with a direct solver (MUMPS).

A stationary calculation for one iteration step in the wear simulation using the TEHD model takes approximately 3h of computation time on a local computer (Win10, Intel Xeon E5-1650v4, 3.6 GHz with 12 logical cores, 128 GB RAM).

is added to the new contribution of the current step i , i.e.

$$\begin{aligned}
 H_{\text{wear}}^{(0)} &= 0, \\
 &\vdots \\
 H_{\text{wear}}^{(i)} &= H_{\text{wear}}^{(i-1)} + \text{ramp}(H^{(i-1)} + H_{\min} + \delta_{\text{wear}}), \\
 &\vdots \\
 H_{\text{wear}}^{(i_{\text{end}})} &= H_{\text{wear}}^{(i_{\text{end}}-1)} + \text{ramp}(H^{(i_{\text{end}}-1)} + H_{\min} + \delta_{\text{wear}}).
 \end{aligned}
 \tag{36}$$

Fig. 5 shows the program sequence in a pseudocode representation. It shows the outer while loop for the wear iteration index i and the inner iteration loop for the minimal gap height iteration to H_{\min} .

2.6. Numerical and computational details

This section describes numerical details about the bearing model and the computation. The nonlinear fully coupled TEHD model introduced in Sections 2.1 to 2.5 is described by a nonlinear integro-differential equation system. The set of altogether 16 governing partial differential equations is discretized using a Finite Element approach with Lagrange shape functions. Fifth-order shape functions are chosen for calculating the shell equations of top and bump foil in order to prevent shear locking effects [37], while second-order shape functions are chosen for the remaining variables.

3. Simulation results

In this section, simulation results are presented and compared to experimental results. At first, the condition without wear is discussed in Section 3.1, giving insight in the behavior of thrust bearings with annular top foil. Afterwards in Section 3.2, the wear process is showcased with a wear simulation series. The resulting final state (fully worn top foil) is then analyzed in detail in Section 3.3. Eventually, a comparison to experimental data on a dedicated test rig is drawn for the loss/load-characteristic of the bearing in Section 3.4.

3.1. Simulation without wear algorithm

The unworn state of the bearing is described by the height function of Eq. (33). After assembly of the bearing and for the case that pressure forces are absent, i.e. at $\Omega = 0\text{rad/s}$, the height function possesses a taper-step topology, depicted in Fig. 6(a). Herein, deformations of the top foil and deformations of the rotor disk are absent, $v_{3,T} = v_z = 0$. The figure shows the characteristic taper profile and the defects described in Section 2.4, namely the parabolic shape deviation in radial direction and the extended step width as well as the coating accumulations at the inner and outer radius. Furthermore, it should be stressed that the leading edge and the trailing edge have an equal slope in the circumferential direction. This is a results of the embossing process

during manufacturing and is of high relevance for the understanding of the upcoming analysis.

A distinct feature of the presented bearing type is the fact that the unloaded height profile of Fig. 6(a) transforms into a taper-land configuration upon loading, i.e. air film pressure acting on the top foil. The height function $H^{(0)}$ for the loaded case ($\Omega = 120$ krpm) is depicted in Fig. 6(b). In comparison with the unloaded assembly state of Fig. 6(a), the height function here is mainly changed by the large deformations of the top foil, shown in Fig. 6(c). Rotor deformations also contribute according to Eq. (33), but are significantly smaller. The gap height profile (Fig. 6(b)) shows a classical taper-land-type topology, with a converging gap at first and an approximately constant gap height towards the trailing edge. However, at the trailing edge, the height profile converges again right before the beginning of the step. This behavior—the rising at the trailing edge—is typical for bearings with an annular top foil. It is caused by the top foil being bent upwards near the trailing edge. It can be explained as follows:

- In the unloaded, assembled state of the bearing, the top foil contacts the bump foil only at the first bump row due to the initial taper geometry.
- When the bearing is loaded and air film pressure pushes the top foil down onto the bump foil, the top foil is bent at the first bump row, cf. Fig. 6(c).
- In the course of the loading, the top foil deforms further and eventually contacts the second and the third row of bumps of the bump foil. It should be stressed again that the bumps are of the same height so that the initial gap between the top and bump foil is therefore larger at the second and third bump row.
- When the trailing edge is deformed down, the leading edge is also pulled down by the trailing edge of the adjacent sector. In the simulation model, this effect is achieved via the cyclic coupling of the leading and trailing edge, cf. Eq. (32).
- The step is acting as a stiff connector both between the leading and the trailing edge in terms of the deflection $v_{3,T}$ as well as for the slope. If the leading edge is pulled down, the slope has to increase due to the contact to the bump foil. Consequently, the slope at the trailing edge has to increase as well, causing the trailing edge to rise.
Note that—due to the high stiffness of the step—the height difference between the leading and trailing edge is nearly constant (initial value h_s).

The upwards bending at the trailing edge is clearly seen in Fig. 6(c). The corresponding pressure $p(x, y)$ is shown in Fig. 6(d). It shows a sharp peak at the trailing edge near the inner radius at the spot of lowest film height. The load capacity for the unworn top foil is only $W^{(0)} = 7.5$ N with a power loss of $P_{\text{loss}}^{(0)} = 51.5$ W.

3.2. Simulation of the wear progress

With the developed wear algorithm, the wear height function H_{wear} is iterated in a loop in order to represent the wear that occurs in the bearing. In the test rig, the rotor is accelerated to a rotational speed of 120 krpm without a thrust load. Afterwards, the thrust load is gradually increased to the target load of $W = 100$ N. In the presented wear algorithm, the iteration of H_{wear} is stopped when this specified load capacity is reached.

Remark on the end condition for the wear calculation: The wear of the top foil coating is limited by the coating thickness. Theoretically, for an infinite coating thickness, the wear algorithm could continue infinitely. In this case, the load capacity would be increased further. At a certain point, however, a maximum load capacity is reached. After that, the load capacity decreases again.

In this subsection, the wear progress is showcased at 3 intermediate wear states between the unworn ($i = 0$) and the fully worn ($i = i_{\text{end}}$) state.

Fig. 7 shows the height function $H^{(i)}$, the pressure distribution $p^{(i)} - p_0$ and the wear function $H_{\text{wear}}^{(i)}$ for the 3 iteration indices $i = \{13, 16, 20\}$ of the wear simulation. All plots are generated for a rotational speed of 120 krpm and a minimal gap height of $H_{\text{min}} = 2$ μm .

In the height function of the slightly worn state of Fig. 7(a) ($i = 13$), only a small peak at the inner radius near the trailing edge reaches the minimal gap height, while the other areas possess much larger film heights and do not substantially contribute to the pressure generation. Therefore, the entire wear in Fig. 7(a) occurs at this very spot.

In the following iterations, wear increases further at this spot. Afterwards, additional wear occurs towards the middle of the sector at the inner and outer radius, cf. Figs. 7(b) and 7(c).

In all 3 iteration steps, the pressure profiles show an increasing peak at the trailing edge. The contribution of the remaining sector area to the load capacity is growing continuously and is most developed in the last wear step of Fig. 7(c).

In Appendix A of this work in Fig. 14, simulation results for the rotor temperature $T_R(r, z)$ and the air film temperature $T_A(x, y, \bar{z})$ are displayed for the wear iteration series.

3.3. Detailed simulation results with the worn top foil

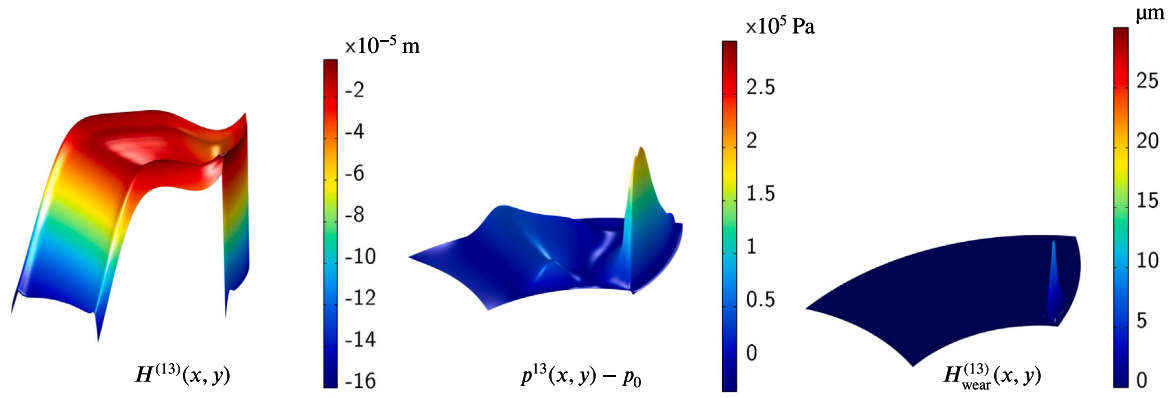
After $i_{\text{end}} = 23$ iterations of the wear algorithm, a load capacity $W = 100$ N is achieved. Fig. 8(a) shows the resulting wear height function $H_{\text{wear}}^{(23)}$. A distinct peak near the trailing edge at the inner radius is observed as well as wear spots near the inner and outer radius in the middle of the sector. The maximum wear depth is 21 μm . Fig. 8(b) shows a photographic image of a corresponding top foil sector after experimental tests. The break-in in the experiment was achieved in two steps. At first, the rotor was run up to 120 krpm without a thrust load. After that, the load was increased incrementally up to the target load of 100 N. Comparing the simulation result of the predicted wear of Fig. 8(a) against the real wear pattern of Fig. 8(b), good agreement is observed. Three characteristic wear locations are visible in both simulation and experiment, highlighted by the red markers in Fig. 8(b).

The respective height function $H^{(23)}$ and pressure profile $p^{(23)} - p_0$ are displayed in Fig. 9. The gap height profile tends towards the desired taper-land topology with a flat land section, although the trailing edge still possesses the distinct positive slope. This is why a part of the land area shows substantially larger film heights. It does therefore not contribute to the pressure generation as much and is less useful. Note that the respective pressure profile of Fig. 9(b) shows a dent in this exact area.

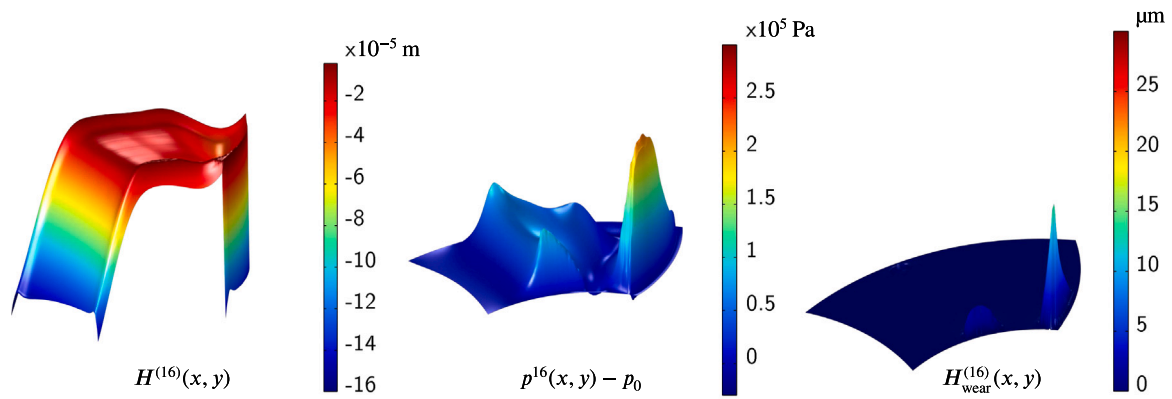
The distinct coating accumulations from the manufacturing process which are concentrated at the inner and outer edges (see Section 2.4) are still visible in Fig. 9(a). Only in the area of largest wear at the trailing edge, the coating accumulations have been erased.

The film height profile of Fig. 9(a) also shows top foil sagging between the lines of contact to the underlying bumps. The bumps are visible as raised lines. Note that the bump design only possesses two bumps at the inner strip, cf. Fig. 3(d). If a third bump would be present near the trailing edge on the inner strip, the trailing edge would be raised even more, making for an increased wear. Alterations of the bump foil design, e.g. a third bump in the inner bump strip, lead to a change in the maximum wear depth at the trailing edge. It should however be stressed that the occurrence of non-uniform wear cannot be prevented for this type of bearing by changing the bump foil design. The non-uniform wear is inherent to the single-foil design because of the cyclic coupling of each top foil sector resulting in the described upwards bending. More precisely, the equal slopes of leading and trailing edge, stemming from the embossing process, cause wear at the trailing edge.

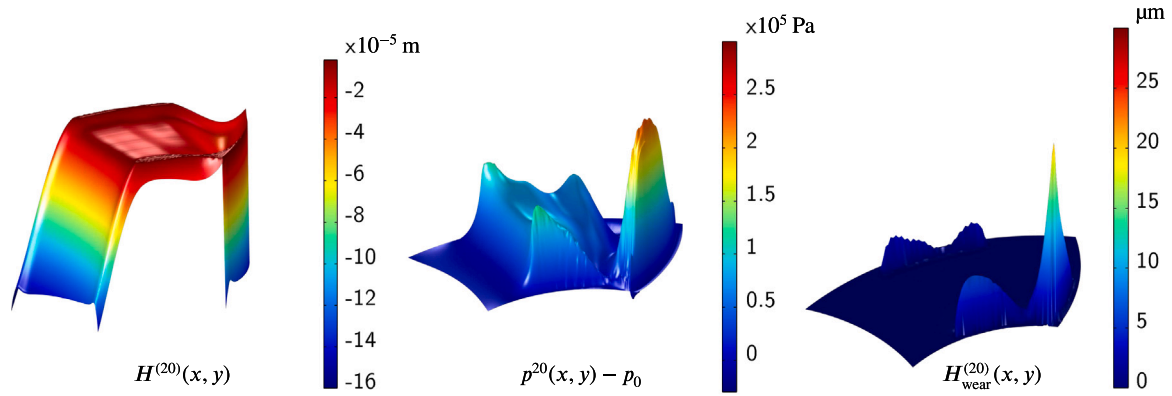
The pressure profile in Fig. 9(b) shows a main peak very close to the position of maximum wear due to the large changes in gap height. Furthermore, 3 distinct pressure lines are observed at the contact lines of top and bump foil. Each of these lines, foremost the first line, shows



(a) Height function, pressure distribution and wear height function for $i = 13$. $W = 30.0$ N and $P_{\text{loss}} = 133.2$ W.



(b) Height function, pressure distribution and wear height function for $i = 16$. $W = 47.5$ N and $P_{\text{loss}} = 182.9$ W.



(c) Height function, pressure distribution and wear height function for $i = 20$. $W = 65.0$ N and $P_{\text{loss}} = 234.7$ W.

Fig. 7. Wear simulation series showing the height function (left), the pressure distribution (center), and the wear function H_{wear} . Rotational speed is 120krpm and minimal gap height is $H_{\text{min}} = 2 \mu\text{m}$.

peaks at the outer edges. These are caused by large gap height gradients at the coating accumulations near $r = r_i$ and $r = r_o$ and the small absolute gap height. Even more precise than the gap height profile, the pressure profile reveals weaknesses in the bearing design. While a large part of the top foil sector contributes to pressure generation and thus carrying rotor thrust loads, the large drop in pressure accompanied with a large single peak at the trailing edge highlights room for improvement in bearing design.

Fig. 10 shows the air film temperature $T_A^{(23)}(x, y, z)$ for different height slices $\bar{z} = \{-1, 0, 1\}$ at a rotational speed of 120krpm with a load of 100N. The bottom slice at $\bar{z} = -1$ corresponds to the top foil interface and shows the top foil temperature $T_T^{(23)}(x, y)$. It shows higher temperatures near the outer edge due to higher fluid velocities and, consequently, more dissipation in the air film. Because of the heat

conduction through the bumps, the temperature drops at the contact lines of top and bump foil.

The top slice at $\bar{z} = 1$ shows the temperature distribution of the rotor disk $T_R^{(23)}(r, z)$ in section I of Fig. 4(a). Due to the high angular velocity Ω of the rotor, an axisymmetric rotor model is used, cf. Section 2.1. This is why there are no temperature changes in circumferential direction. The highest temperatures are observed near the outer radius r_o . A decrease in temperature is found towards the inner radius r_i with temperatures of 160 °C to 225 °C.

The middle slice lies at $\bar{z} = 0$ and shows the temperature field in the middle of the air gap. The contact lines between top and bump foil are still visible as lines of lower temperature. Furthermore, the maximum temperature in this middle slice of the air film is lower than the maximum temperature of the bottom slice (top foil interface). This

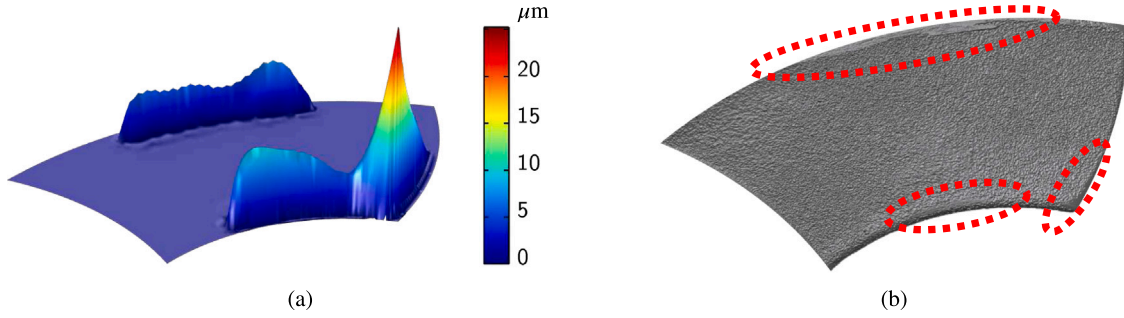


Fig. 8. Calculated wear height function $H_{\text{wear}}^{(23)}$ for a load capacity of $W = 100\text{ N}$ at 120 krpm (a) and photographic image of a top foil sector after the tests where wear marks are visible at the inner and outer radius as well as at the trailing edge (b).

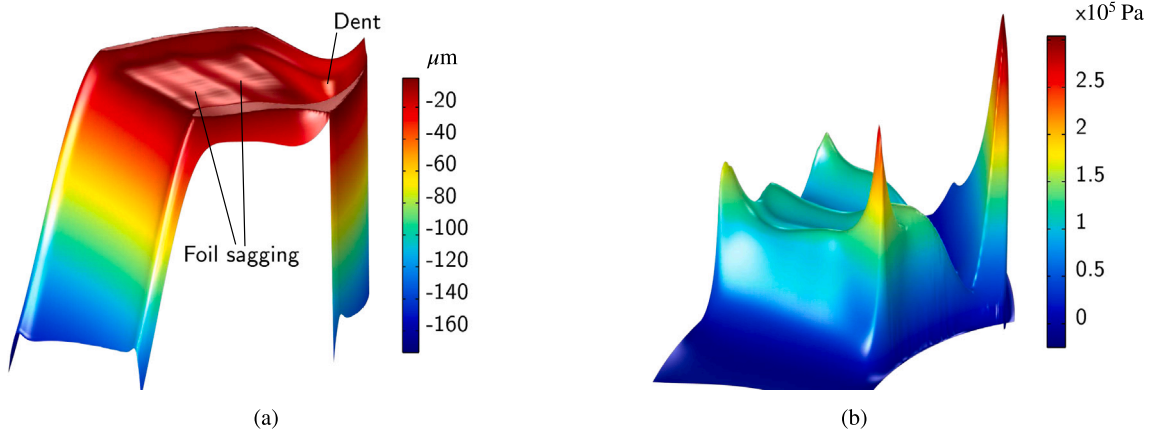


Fig. 9. (a) Height function $H^{(23)}(x, y)$ and (b) pressure distribution $p^{(23)}(x, y) - p_0$ with the calculated $H_{\text{wear}}^{(23)}$ of Fig. 8(a).

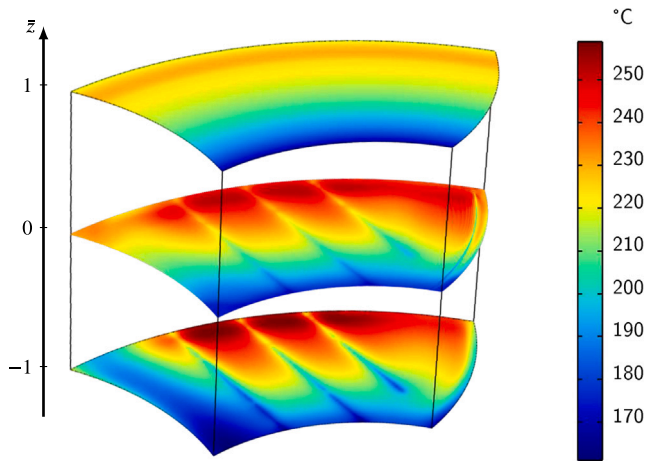


Fig. 10. Air film temperature $T_A^{(23)}$ in degrees Celsius in different layers. The bottom surface corresponds to the top foil interface, the top slice displays the rotor disk temperature.

is a result of the different heat resistances of top foil and rotor disk. The rotation-induced flows and air inlets of the EP journal bearings (see Fig. 1) cause a strong cooling of the rotor disk in sections II to V. Therefore, more heat passes through the rotor disk interface at $\bar{z} = 1$. Note that the top foil—active cooling being absent in this study—displays a larger thermal resistance for the heat flux from the air gap. In all the 3 slices, the cyclic coupling of the air film temperature is observable from inlet to outlet.

Fig. 11 displays the axisymmetric rotor disk temperature field $T_R^{(23)}(r, z)$ at the aforementioned operating point. The disk temperature

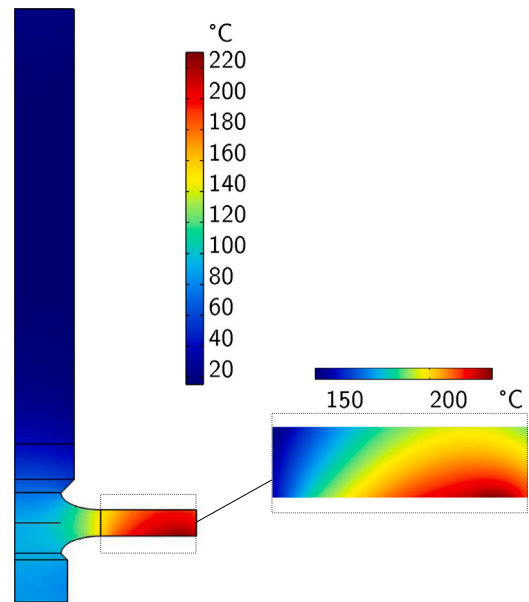


Fig. 11. Rotor temperature $T_R^{(23)}$. Zoom shows a close-up of the rotor disk.

at the interface to the air film has already been discussed with the help of Fig. 10. The most striking feature of the overall rotor temperature lies in the strong cooling induced by the EP journal bearings. They cause the rotor temperatures to immensely decrease towards the rotor shaft. At the recesses of the rotor disk, temperatures have already dropped below $100\text{ }^\circ\text{C}$ with a further decrease to a nearly constant temperature

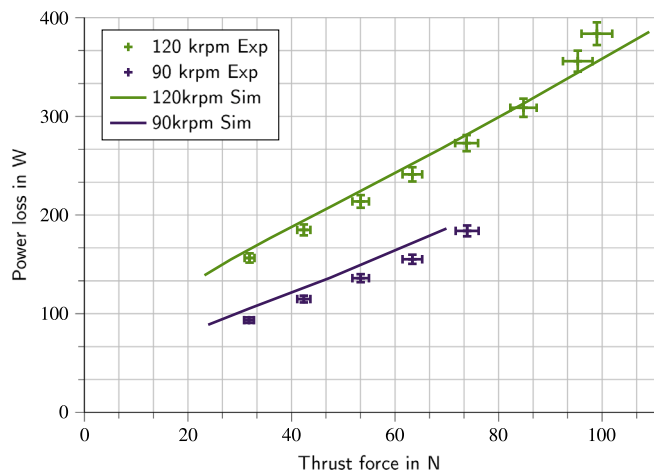


Fig. 12. Performance map of the single-foil thrust bearing for two rotational speeds: power loss in W over the thrust force in N.

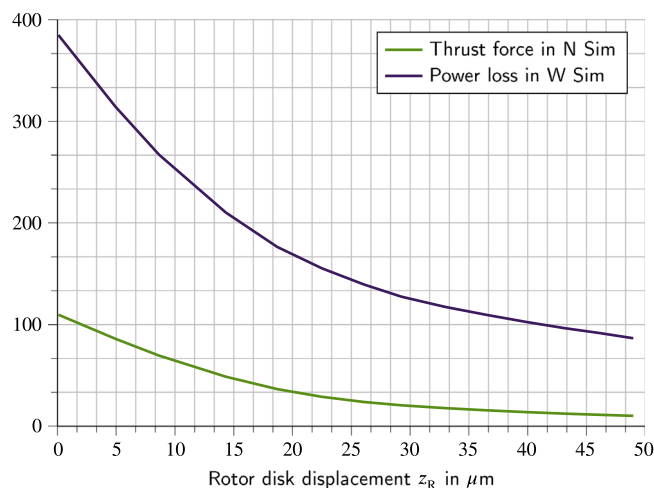


Fig. 13. Simulated power loss in W and thrust force in N for a rotational speed of 120 krpm over the rotor disk displacement z_R in μm .

of 15 °C near the EP journal bearings. Temperatures are highest near the outer radius at the interface to the air film. At the outer perimeter (Section 2), the average temperature is still 201.5 °C. It is interesting to notice that, towards the backside of the disk and the disk basement, temperatures decrease to 145 °C.

It should finally be noted that the resulting thermoelastic bending of the rotor disk, which was showcased in earlier works [18,22,38], influences the observed wear distribution. For more details, please see App. D of the manuscript.

In Appendix B, Figs. 15 and 16 display simulation results for the height function, the pressure distribution, the top foil deflection, the rotor temperature, and the air film temperature for a simulation with $H_{\text{wear}}^{(23)}$, but with different values of $H_{\text{min}} \geq 2 \mu\text{m}$. Therefore, the results in Appendix B refer to different load scenarios.

3.4. Experimental validation

In a so called performance map, Fig. 12 displays the correlation between power loss P_{loss} in W and thrust force W in N for the considered bearing, cf. Eq. (18). Results are shown from simulations and experiments for rotational speeds of 120 krpm and 90 krpm. In experiments, these characteristic curves are recorded after the initial break-in described in Section 3.2. At a constant rotational speed, the worn

bearing is then subjected to a range of loads of up to 100 N. The simulation results were obtained by choosing different values of H_{min} at constant angular velocities Ω and using the wear height function $H_{\text{wear}}^{(23)}$ of Section 3.3.

A near linear increase in power loss is observed with a slight bend towards higher power loss for high loads. The power loss is 50 to 80 W higher at 120 krpm in comparison with 90 krpm for the considered load range. For all considered loads and rotational speeds, the agreement of the results of the numerical simulation and the experiment are good. In the end, this was achieved by not only incorporating a real top foil topology into the model, but also accounting for the coating wear that occurs during operation of the bearing. Note that Fig. 13 shows an alternative representation of the numerical data of Fig. 12 and displays the load capacity and the power loss with regard to the rotor disk displacement z_R . The displacement of the rotor disk is shown relative to the point of maximum thrust load with a minimal gap height of $H_{\text{min}} = 2 \mu\text{m}$ (this corresponds to a rotor disk displacement of $z_R = 0 \mu\text{m}$). It is clearly seen that the load increases nonlinearly when the rotor disk moves closer to the bearing. As displayed in Fig. 12, through the nearly linear correlation between power loss and load, the power loss in Fig. 13 follows a similar trend as the thrust force. It is interesting to notice that a displacement of the rotor disk of less than 15 μm from the point of maximal load leads to a decrease in load to half the maximum value.

4. Conclusions and prospects

A TEHD thrust bearing model for thrust bearings with annular top foil has been presented. In contrast to the frequently used multi-foil design which possesses multiple independent bearing pads, the investigated single-foil design is characterized by fully coupled sectors in the form of a one-part top foil.

The model takes into account thermoelastic deformations of the rotor, heat transfer in the rotor combined with a detailed analysis of heat transfer to the rotor surroundings based on CFD analysis, air film temperature with a 3D energy equation, air film pressure with a 2D compressible Reynolds equation, elastomechanic deformations of top and bump foil via a nonlinear shell model including contacts, heat conduction in the top foil, and the heat transfer through the bump foil and into the base plate.

The governing set of partial differential equations was discretized using a Finite Element Approach. In order to speed up the computation time, studies are conducted using a cyclic coupling approach for a single bearing sector, making use of cyclic symmetry of the bearing. This approach is of course only valid for the case of negligible misalignment of the bearing and the rotor disk.

Simulations with the fully coupled TEHD model based on the nominal, ideal top foil geometry showed significant discrepancies when compared with test rig measurements, where the bearing exerted a power loss of 333 W at a thrust load of 100 N.

The simulation model was enhanced in two ways. *Firstly*, the real top foil geometry was investigated in measurements. It was found that the real geometry of the top foil deviates markedly in 3 main ways in comparison to the ideal geometry: As a result of the embossing process of the top foils, a parabolically shaped geometry as well as an extended, non-vertical step of the metal top foil are observed. Furthermore, a non-homogeneous coating distribution with accumulations at the inner and outer radius of the bearing sector are found.

However, when using a refined height function in the simulation model taking into account these 3 deviations, bearing load capacity and power loss are even lower than with the nominal geometry.

The reason for these significant discrepancies can be traced back to wear of the top foil coating which occurs in the mixed lubrication regime during overloading of the bearing (run-in). In test rig measurements, significant and non-uniform wear of the top foil coating is observed. It is found that, for the single-foil bearing design where

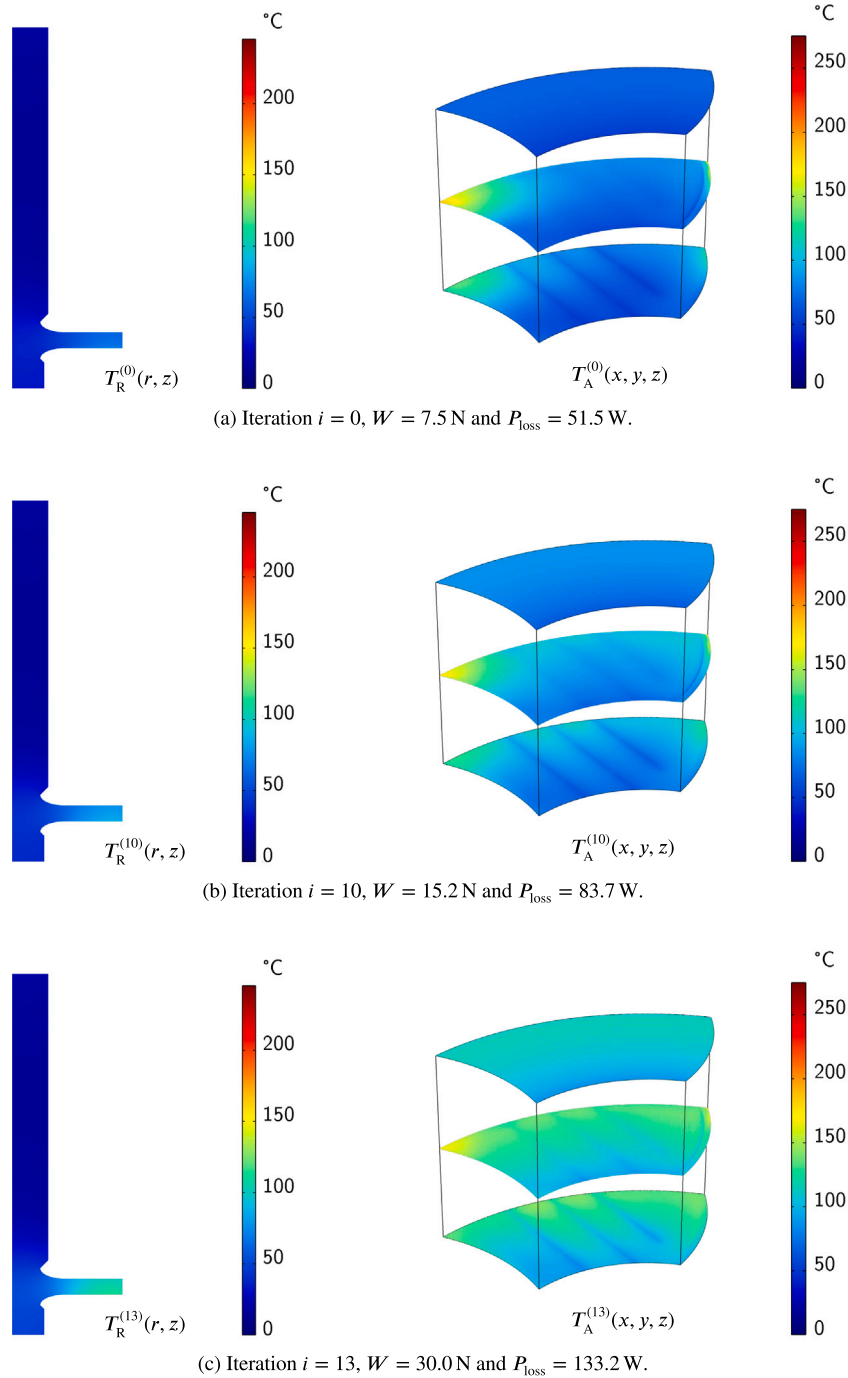


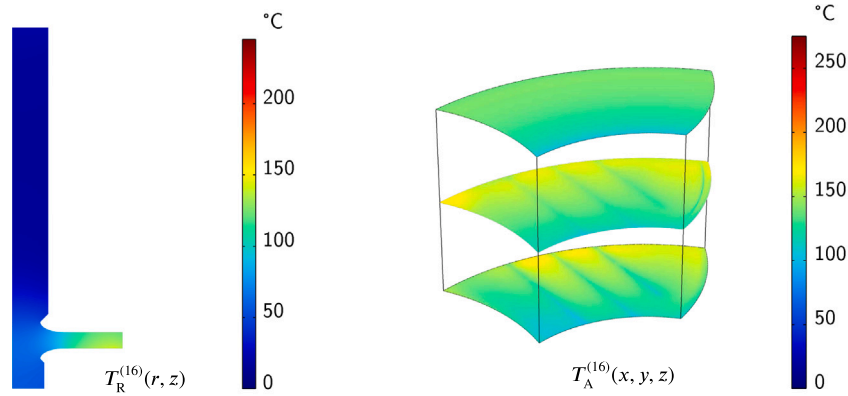
Fig. 14. Wear simulation series showing the rotor disk temperature $T_R(r, z)$ on the left and the air film temperature $T_A(x, y, z)$ on the right. Rotational speed is 120krpm and minimal gap height is $H_{\text{min}} = 2 \mu\text{m}$.

the sectors are coupled, wear has to be taken into account in the model. Therefore, *secondly*, a wear algorithm has been developed and implemented. The quasi-static, iterative wear routine for the contact wear of the (hard) rotor disk and the (soft) top foil coating is able to predict wear states of the top foil coating. The height function is corrected by a wear height function representing the amount of abraded PTFE coating.

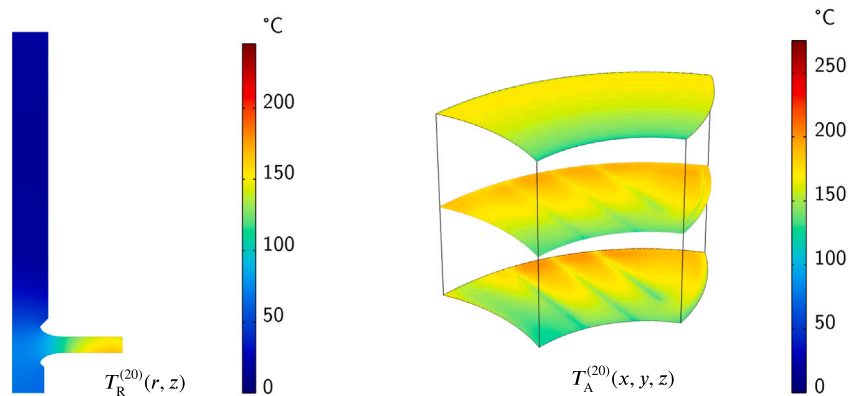
For the maximum operating point with a thrust load of 100 N at a rotational speed of 120krpm, a wear series has been showcased. The resulting wear from the model matches experimentally observed wear patterns. Furthermore, the bearing performance is analyzed in detail

with the resulting wear pattern. A good agreement with performance data from the test rig with regard to a characteristic power loss curve over the thrust load is observed.

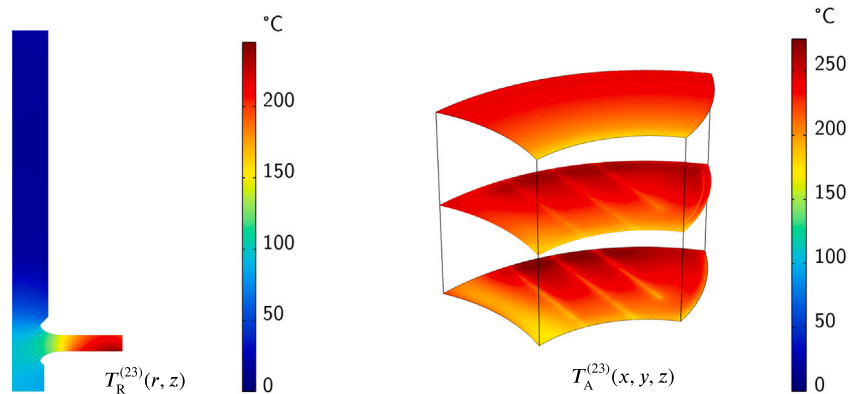
It was shown here that thrust bearings with an annular top foil and embossed height profile can only be analyzed when wear is taken into account. Moreover, the real top foil geometry is of key importance in the analysis. Otherwise, numerically obtained load capacity and power loss are significantly decreased in comparison with experimental data. The coating wear is beneficial and leads to a significantly improved bearing performance. The focus of the current manuscript lies in the modeling and simulation of annular foil thrust bearings including wear



(d) Iteration $i = 16$, $W = 47.5$ N and $P_{\text{loss}} = 182.9$ W.



(e) Iteration $i = 20$, $W = 65.0$ N and $P_{\text{loss}} = 234.7$ W.



(f) Iteration $i = 23$, $W = 100.3$ N and $P_{\text{loss}} = 333.5$ W.

Fig. 14. (continued).

prediction. In a second manuscript to be published soon, experimental details are presented along with an in-depth report on the test rig. Moreover, detailed measurements regarding the real bearing geometry used in the current manuscript in Section 2.4 are presented. The second manuscript includes a comprehensive analysis of the manufactured top foil topology as well as the bearing performance. Furthermore, white-light interferometric measurements of the wear occurring during run-in are shown.

Declaration of competing interest

The authors declare that they have no known competing financial interests or personal relationships that could have appeared to influence the work reported in this paper.

Data availability

The authors are unable or have chosen not to specify which data has been used.

Appendix A. Wear simulation series

This appendix displays additional simulation results for various stages of the wear simulation. For each result plot, the respective iteration number i is given. Fig. 14 shows the rotor disk temperature and the air film temperature for the iteration steps $i = \{0, 10, 13, 16, 20, 23\}$ as an addition for the results given in Section 3.2.

It is interesting to notice that the temperature of the rotor shaft nearly stays constant regardless of the power loss in the bearing gap.

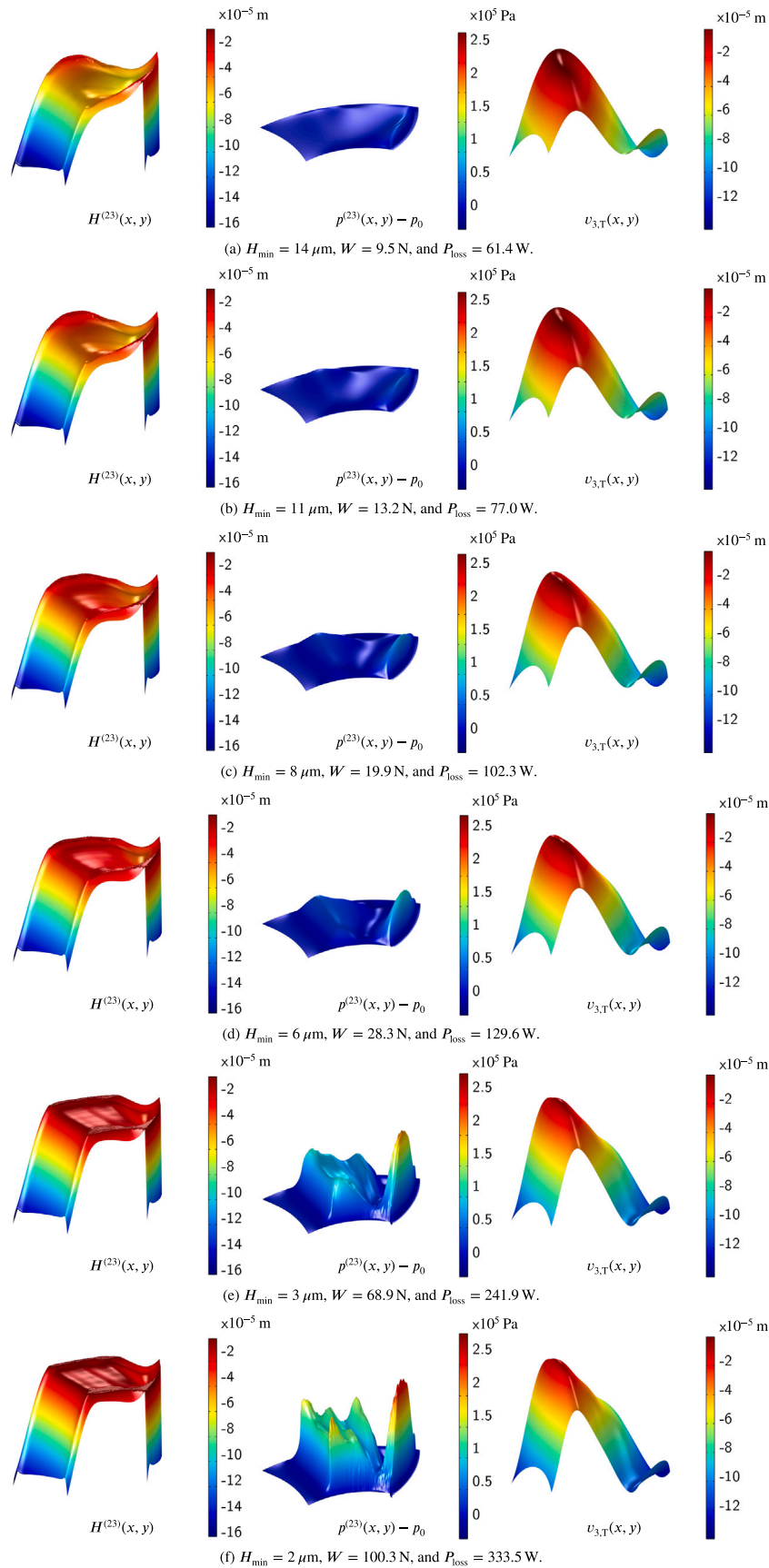


Fig. 15. Minimal gap height sweep with height function H (left), pressure distribution $p - p_0$ (center), and top foil deflection $u_{3,T}$ (right). Rotational speed is 120krpm and wear function H_{wear} implemented for a load capacity of $W = 100 \text{ N}$.

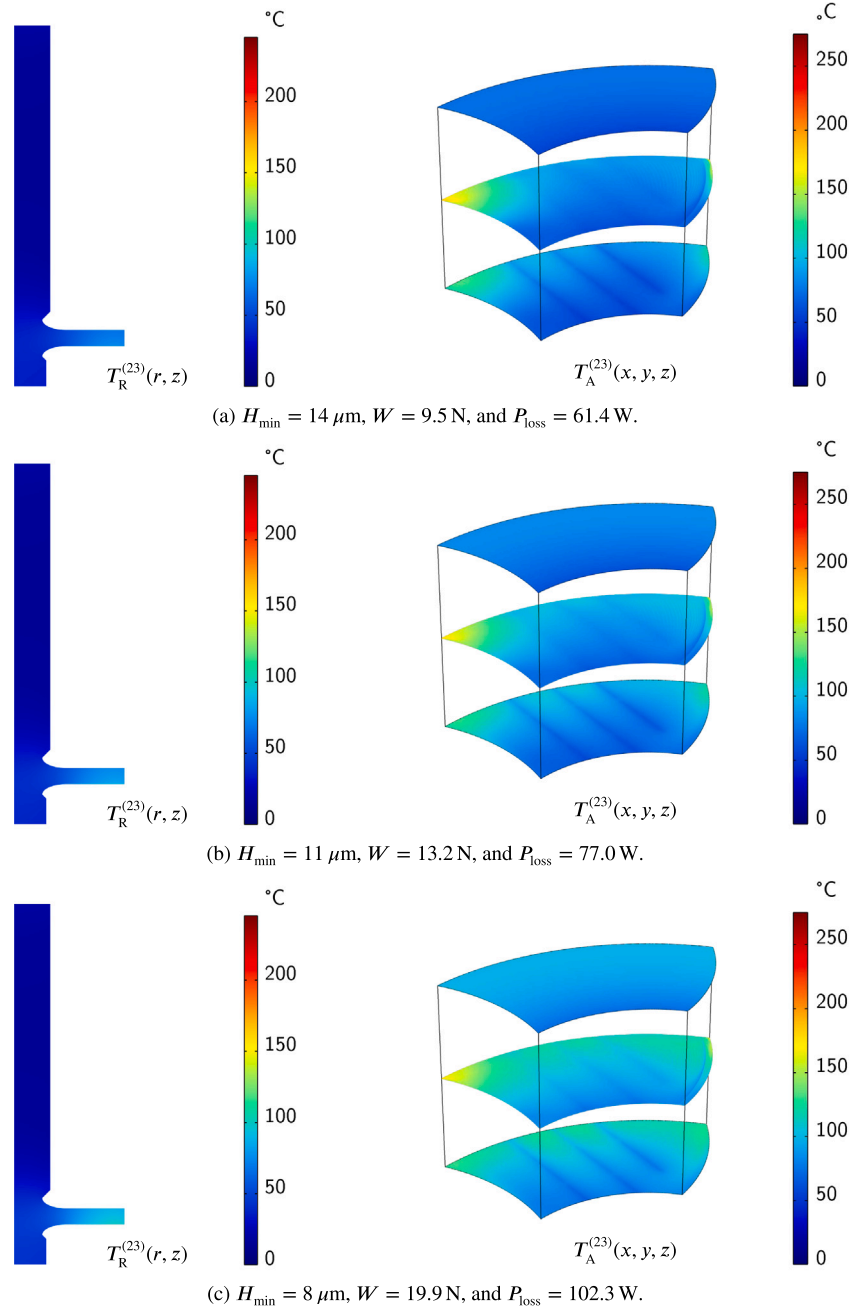


Fig. 16. Load series showing the rotor disk temperature T_R on the left and the air film temperature T_A on the right. Rotational speed is 120krpm and wear function H_{wear} implemented for a load capacity of $W = 100 \text{ N}$.

The heat from the lubricating air film enters the disk in section I (see Fig. 4(a)) and is mostly conducted to the rotor boundaries in Sections 2 and 3 where the heat is transferred into the surrounding air. At the base of the rotor disk, temperatures rise to $100 \text{ }^\circ\text{C}$ only at the last wear iteration step with the highest load. The maximum rotor temperature lies more than twice as high.

The evolution of the air film temperature shows no substantial qualitative change. At the contact lines of top and bump foil, colder stripes are observed due to the heat conduction through the bumps into the base plate.

Appendix B. Load simulation series with the fully worn top foil

Here, the fully worn state of Section 3.3 is investigated for different thrust loads. In the simulation model, different thrust loads can be

created by enforcing different values for the minimal gap height H_{\min} . When the axial rotor position is changed, the minimal gap height can be adapted to a given value. This procedure is the same as conducted in Section 3.4. Fig. 15 shows the height function, the pressure distribution and the top foil deflection for various values of the minimal gap height. For each step, the corresponding loads and power losses are given as well. Like the wear series in Fig. 7, where the increasing wear causes higher exerted thrust loads, this study shows the film height function changing towards an ideal taper-land characteristic with increasing load. The pressure distribution also evolves similar to the case of the wear series. The evolution of the top foil deformation $v_{3,T}$ is particularly interesting, because it shows two things: Firstly, the trend towards an ideal taper-land configuration is repeated in these images by means of an increasing negative slope in the trailing part of the sector. This means that, in combination with the positively inclined taper, a nearly

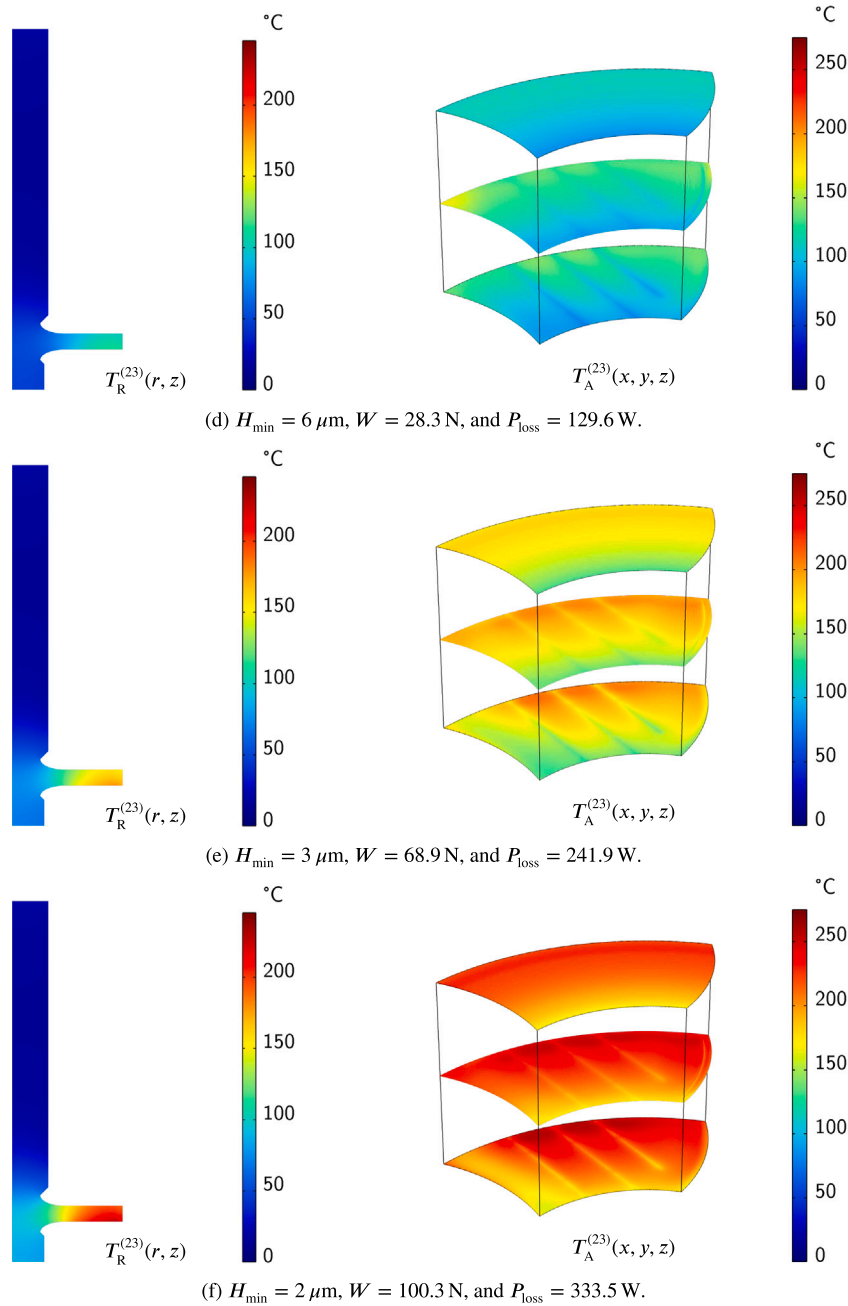


Fig. 16. (continued).

flat section is created which marks the land region of the sector. Secondly, with increasing load, it is evident that the cyclic coupling (which represents the single-foil design) creates a growing upwards bending at the trailing edge. This in turn causes a dent in the height function as well as the trailing edge rising which is the intrinsic reason for the non-uniform wear. Fig. 16 shows the corresponding rotor and air temperature distributions. As mentioned before, similarities between increasing wear on the one hand and increasing load with the fully worn state on the other hand are apparent. The temperature of the rotor shaft stays very low while most of the heat from the lubricating air gap enters and leaves the rotor disk. The air film temperature distributions are very similar to the ones in Fig. 14 as well, which is explained by the similar height functions at similar thrust loads.

Appendix C. Comparison of multi-foil and single-foil thrust bearing design

In this appendix section, a brief comparison of the performance of the single-foil bearing with the multi-foil bearing is conducted, cf. Fig. 2. In general, the two bearing designs are quite similar with regard to their overall layout. Both bearing designs possess a base plate with independent bump foils. The rotor disk design for both bearing types does not vary as both bearing types demand a smooth and flat counter-surface for optimal bearing operation. The differences lie in the design of the bump foil and, of course, in the design of the top foil. While the design change of the top foil is obvious, the bump foil design change is more subtle.

For the classical multi-foil bearing, a taper-land height profile is commonly applied, see e.g. [39,40]. It is realized by manufacturing

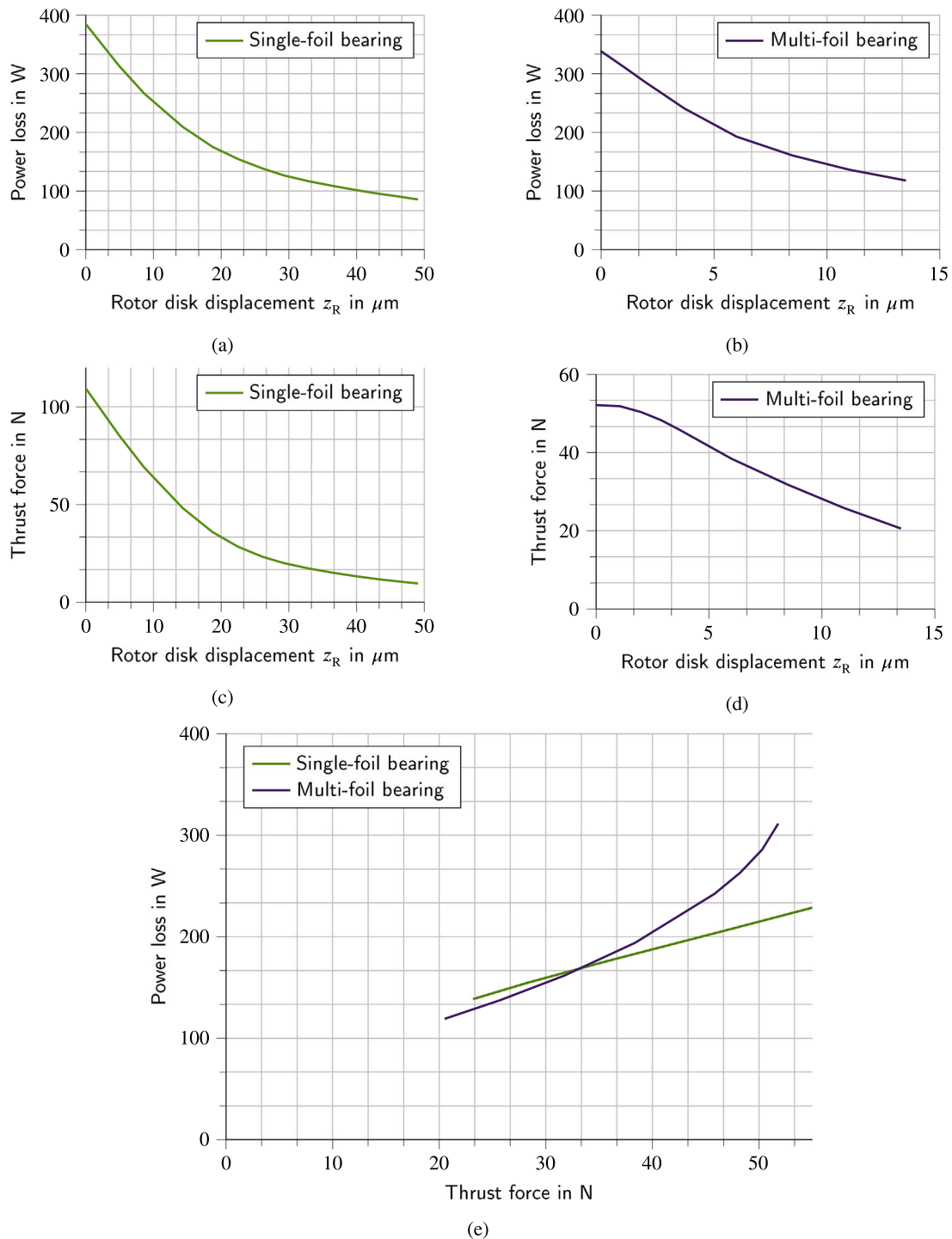


Fig. 17. Numerical comparison between the single-foil thrust bearing investigated here and the multi-foil thrust bearing of Ref. [22]: (a) and (b) power loss over rotor disk displacement, (c) and (d) thrust force over rotor disk displacement, and (e) performance map with power loss in W over the thrust force in N for a rotational speed of 120krpm.

bump foils with varying bump heights, thus transferring the desired height profile onto the top foil under load. Alternatively, a bend may be applied to the top foil at the transition line between taper and land region. In the latter case, bumps of equal height may be used as well.

By contrast, the single-foil design possesses a bump foil with uniform bump height as well as an embossed taper-step topology on the top foil, cf. [23]. The transformation of this initial taper-step profile into the desired taper-land profile under load is inherent to this design and reliant on constant bump heights.

A numerical analysis of a multi-foil bearing is as involved as the analysis of the single-foil bearing. The comparison carried out here is based on a multi-foil bearing model with similar bearing dimensions as the single-foil bearing of Section 2, see [22]. Fig. 17 shows numerical results of the comparison of the two different bearing types. Fig. 17(a) and Fig. 17(b) depict the power loss of both bearing types over the rotor disk displacement z_R . Both bearing types have a regressive relation of power loss and rotor disk displacement. Fig. 17(c) and Fig. 17(d) display the thrust force over the rotor disk displacement z_R which also

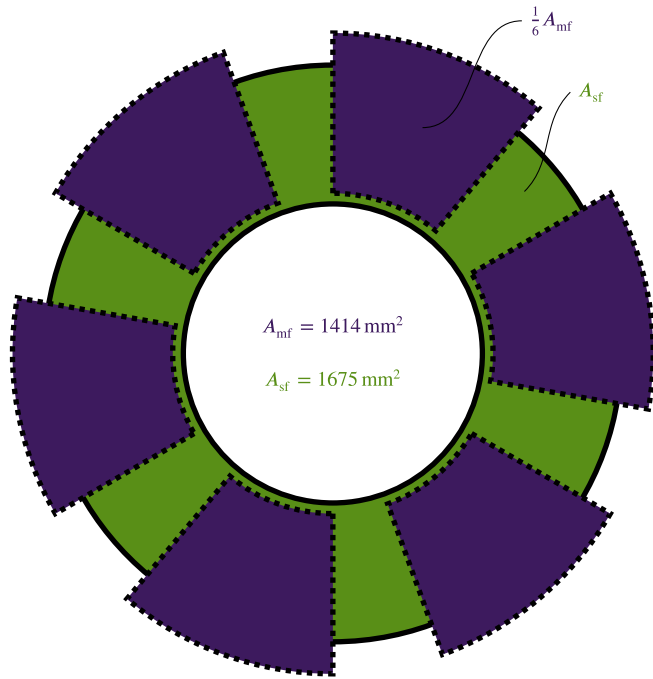


Fig. 18. Bearing areas for the single-foil (A_{sf}) and the multi-foil bearing (A_{mf}).

shows a regressive shape. It is interesting to notice that the thrust force of the multi-foil bearing can only be slightly improved by lowering the rotor disk displacement once the rotor disk displacement approaches zero (nearly horizontal load curve). This is a first indication of a bearing overload, see below. Moreover, the multi-foil bearing appears to be stiffer than the single-foil bearing. This can be explained by the fact that the single-foil bearing first has to transform into a taper-land topology under load, while the taper-land topology is already present in the multi-foil bearing design in the unloaded case.

In Fig. 17(e), the two performance lines of the single-foil bearing and the multi-foil bearing are compared. It is obvious that two very distinct performance characteristics are visible: the single-foil bearing shows a nearly linear relation between power loss and thrust force, while the multi-foil bearing shows a progressive trend, ending in a very steep slope. For low loads, the relation between power loss and thrust force is very similar, both with regard to the absolute values as well as for the slope of the curves. The rise in slope for the multi-foil bearing has been showcased in [41] and numerically explained in [42]. In summary, the uneven deformations of the bump foil cause suboptimal gap functions which lead to a nonlinear increase in power loss. This behavior indicates that the bearing is being operated close to its limit.

The difference in thrust load can be explained by the bearing area difference illustrated in Fig. 18. The single-foil design allows for a full use of the annular bearing surface, while the multi-foil design inherently possesses gaps between the pads. The load-carrying top foil area of the single-foil bearing investigated here is almost 20% higher than the area of the multi-foil bearing despite the slightly larger outer radius of the latter, see [22]. This marks one of the most important advantages of single-foil bearings.

Appendix D. Comparison of thermal and isothermal wear behavior

In this appendix, the patterns of wear under thermal conditions (TEHD) are compared to those with isothermal conditions (EHD). From experiments as well as simulations, it is well known that temperature effects are very important in the analysis of thrust bearings.

However, it is very interesting to compare the wear results with the full TEHD model to those with an isothermal approach. Note again that the procedure of wear-in for the single-foil bearing consists of a load-free acceleration to the target rotational speed of 120 krpm, followed by a successive loading to the target load of $W = 100\text{ N}$ at constant rotational speed. Fig. 19 shows the two resulting wear patterns for thermal and isothermal conditions. Note that the comparison shows two wear patterns with the same maximum wear height in order to compare the wear distribution quantitatively. It should be mentioned that the load capacity and the power loss are higher for the corresponding TEHD simulation.

The comparison shows that the wear patterns are very similar with three regions of wear, see Fig. 8(b). While the main wear spot at the trailing edge near the inner radius does not change substantially, it is obvious that the other two wear regions differ. Near the inner radius of the top foil sector, wear is reduced in the case of the isothermal simulation. Contrary, wear near the outer radius is increased in the isothermal simulation.

This discrepancy can be explained by the thermoelastic bending of the rotor disk, see e.g. [18,22,38]. The rotor disk tends to bend away from the loaded bearing due to the axial temperature gradient. This gradient is caused by the axial temperature difference between the loaded and the unloaded disk side. Dissipation within the lubricating air gap causes higher temperatures, so that a heat flux enters the loaded side of the disk. At the unloaded backside of the disk, heat fluxes leave the rotor disk through active or passive cooling mechanisms.

This means that gap heights tend to be larger towards the outer radius of the bearing in the TEHD simulation, as the rotor disk bends away further with increasing radius. For wear to occur, the minimal gap between the rotor disk and the top foil surface has to get lower than a critical value. If rotor disk bending is taken into account, wear towards the outer radius of the bearing is reduced, while wear near the inner radius is increased.

An interesting conclusion of this comparison is the similarity of the obtained wear patterns. As can be seen, the thermal bending of the rotor disk only causes small deviations between the isothermal wear

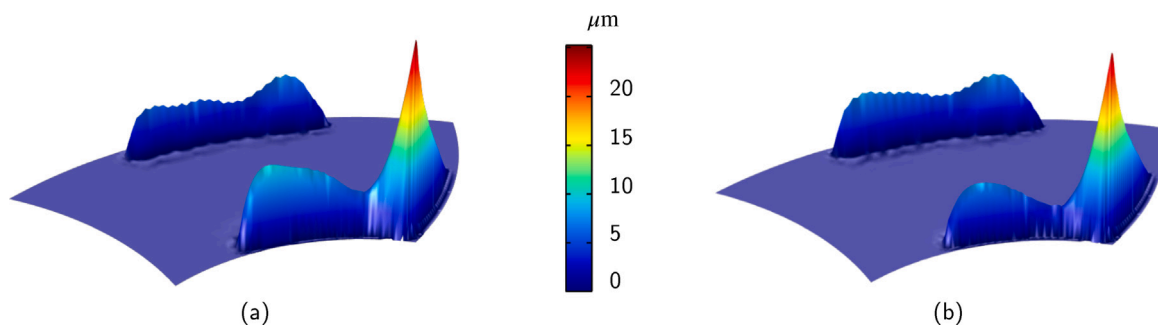


Fig. 19. Comparison of the numerical patterns of wear (a) under thermal conditions (TEHD) and (b) under isothermal conditions (EHD)..

result of Fig. 19(b) and the TEHD wear result of Fig. 19(a). Obviously, the location of the three characteristic wear spots of the single-foil bearing can be traced back to the specific design of this bearing type. Due to the upwards bending of the trailing edge as depicted in Fig. 6(c), the main wear spot always lies near the trailing edge of the top foil sector. The size of the other two wear areas near the inner and the outer radius—as marked in Fig. 8(b)—depend on the temperature distribution.

References

- [1] Arghir M, Benchekroun O. A simplified structural model of bump-type foil bearings based on contact mechanics including gaps and friction. *Tribol Int* 2019;134:129–44.
- [2] Fu G, Untaroiu A, Swanson E. Effect of foil geometry on the static performance of thrust foil bearings. *J Eng Gas Turbines and Power* 2018;140(8).
- [3] Heshmat CA, Xu DS, Heshmat H. Analysis of gas lubricated foil thrust bearings using coupled finite element and finite difference methods. *J Tribol* 2000;122(1):199–204.
- [4] LaTray N, Kim D. Novel thrust foil bearing with pocket grooves for enhanced static performance. *J Tribol* 2021;143(11).
- [5] Lee D, Kim D. Thermohydrodynamic Analyses of Bump Air Foil Bearings With Detailed Thermal Model of Foil Structures and Rotor. *J Tribol* 2010;132(2). <http://dx.doi.org/10.1115/1.4001014>.
- [6] Mahner M, Bauer M, Schweizer B. Numerical analyzes and experimental investigations on the fully-coupled thermo-elasto-gasdynamic behavior of air foil journal bearings. *Mech Syst Signal Process* 2021;149:107221.
- [7] San Andrés L, Kim TH. Thermohydrodynamic Analysis of Bump Type Gas Foil Bearings: A Model Anchored to Test Data. *J Eng Gas Turbines Power* 2010;132(4). <http://dx.doi.org/10.1115/1.3159386>.
- [8] Sim K, Kim TH. Thermohydrodynamic analysis of bump-type gas foil bearings using bump thermal contact and inlet flow mixing models. *Tribol Int* 2012;48:137–48. <http://dx.doi.org/10.1016/j.triboint.2011.11.017>.
- [9] Skaltsas D, Rossopoulos GN, Papadopoulos CI. A comparative study of the Reynolds equation solution for slider and journal bearings with stochastic roughness on the stator and the rotor. *Tribol Int* 2022;167:107410. <http://dx.doi.org/10.1016/j.triboint.2021.107410>.
- [10] Zhou Z, Jia H, Yin B. A fully coupled 3D elasto-hydrodynamic model built with MITC element for static performance analysis of gas foil bearings. *Indust Lubricat Tribol* 2022;(ahead-of-print).
- [11] Agrawal GL. Foil Air/Gas Bearing Technology—An Overview. *Turbo Expo: Power for Land, Sea, and Air* 1997.
- [12] Samanta P, Murmu NC, Khonsari MM. The evolution of foil bearing technology. *Tribol Int* 2019;135:305–23.
- [13] Li B, Li P, Zhou R, Feng X-Q, Zhou K. Contact mechanics in tribological and contact damage-related problems: A review. *Tribol Int* 2022;107534.
- [14] Dufrane KF, Kannel JW, McCloskey TH. Wear of steam turbine journal bearings at low operating speeds. 1983.
- [15] Alves DS, Fieux G, Machado TH, Keogh PS, Cavalca KL. A parametric model to identify hydrodynamic bearing wear at a single rotating speed. *Tribol Int* 2021;153:106640.
- [16] Heshmat H, Hryniewicz P, Walton Li JF, Willis JP, Jahanmir S, DellaCorte C. Low-friction wear-resistant coatings for high-temperature foil bearings. *Tribol Int* 2005;38(11–12):1059–75.
- [17] Radil KC, DellaCorte C. The effect of journal roughness and foil coatings on the performance of heavily loaded foil air bearings. *Tribol Trans* 2002;45(2):199–204.
- [18] Bruckner RJ. Simulation and modeling of the hydrodynamic, thermal, and structural behavior of foil thrust bearings. Case Western Reserve University; 2004.
- [19] Dykas BD. Factors influencing the performance of foil gas thrust bearings for oil-free turbomachinery applications (Ph.D. thesis), Case Western Reserve University; 2006.
- [20] Arghir M, Benchekroun O. A New Structural Bump Foil Model With Application From Start-Up to Full Operating Conditions. *J Eng Gas Turb Power* 2019;141(10). <http://dx.doi.org/10.1115/1.4044685>.
- [21] Lehn A, Mahner M, Schweizer B. A Contribution to the Thermal Modeling of Bump Type Air Foil Bearings: Analysis of the Thermal Resistance of Bump Foils. *J Tribol* 2017;139(6). <http://dx.doi.org/10.1115/1.4036631>.
- [22] Rieken M, Mahner M, Schweizer B. Thermal Optimization of Air Foil Thrust Bearings Using Different Foil Materials. *J Turbomach* 2020;142(10). <http://dx.doi.org/10.1115/1.4047633>.
- [23] Brockett TS, Chinta M, Weissert DH. Compliant foil thrust bearing. Capstone turbine corp; 2004, US6702463 (B1).
- [24] Shi T, Huang H, Chen Q, Peng X, Feng J. Performance investigation and feasibility study of novel gas foil thrust bearing for hydrogen fuel cell vehicles. *Int J Energy Res*.
- [25] Balducchi F, Arghir M, Gauthier R. Experimental analysis of the dynamic characteristics of a foil thrust bearing. *J Tribol* 2015;137(2):021703.
- [26] Conboy TM. Real-gas effects in foil thrust bearings operating in the turbulent regime. *J Tribol* 2013;135(3).
- [27] Dickman JR. An investigation of gas foil thrust bearing performance and its influencing factors (Ph.D. thesis), Case Western Reserve University; 2010.
- [28] Lee D, Kim D. Three-Dimensional Thermohydrodynamic Analyses of Rayleigh Step Air Foil Thrust Bearing with Radially Arranged Bump Foils. *Tribol Trans* 2011;54(3):432–48. <http://dx.doi.org/10.1080/10402004.2011.556314>.
- [29] Sadd MH. Elasticity: Theory, Applications, and Numerics. 2009.
- [30] Ferziger JH, Perić M, Street RL. Computational methods for fluid dynamics. vol. 3, Springer; 2002.
- [31] Menter FR. Two-equation eddy-viscosity turbulence models for engineering applications. *AIAA J* 1994;32(8):1598–605.
- [32] Dowson D. A generalized Reynolds equation for fluid-film lubrication. *Int J Mech Sci* 1962;4(2):159–70. [http://dx.doi.org/10.1016/S0020-7403\(62\)80038-1](http://dx.doi.org/10.1016/S0020-7403(62)80038-1).
- [33] Başar Y, Krätzig WB. Mechanik der Flächentragwerke: Theorie, Berechnungsmethoden, Anwendungsbeispiele. In: Grundlagen der Ingenieurwissenschaften. Wiesbaden and s.l.: Vieweg+Teubner Verlag; 1985. <http://dx.doi.org/10.1007/978-3-322-93983-8>.
- [34] Lee D, Kim D. Design and performance prediction of hybrid air foil thrust bearings. *J Eng Gas Turbines Power* 2011;133(4).
- [35] Reissner E. The effect of transverse shear deformation on the bending of elastic plates. American Society of Mechanical Engineers; 1945.
- [36] Wriggers P. Computational contact mechanics: With 12 tables. 2. ed.. Berlin: Springer; 2006. <http://dx.doi.org/10.1007/978-3-540-32609-0>.
- [37] Zienkiewicz OC, Taylor RL, Zhu JZ. The finite element method: Its basis and fundamentals. Elsevier; 2005.
- [38] Lehn A, Mahner M, Schweizer B. A thermo-elasto-hydrodynamic model for air foil thrust bearings including self-induced convective cooling of the rotor disk and thermal runaway. *Tribol Int* 2018;119:281–98. <http://dx.doi.org/10.1016/j.triboint.2017.08.015>.
- [39] Dykas BD, Bruckner R, DellaCorte C, Edmonds B, Prah J. Design, fabrication, and performance of foil gas thrust bearings for microturbomachinery applications. *J Eng Gas Turb Power* 2009;131(1).
- [40] Lee Y-B, Kim TY, Kim CH, Kim TH. Thrust bump air foil bearings with variable axial load: theoretical predictions and experiments. *Tribol Trans* 2011;54(6):902–10.
- [41] Iordanoff I. Analysis of an aerodynamic compliant foil thrust bearing: Method for a rapid design. *J Tribol* 1999;121(4):816–22.
- [42] Lehn A. “Air foil thrust bearings: A thermo-elasto-hydrodynamic analysis”. (Ph.D. thesis), Technische Universität Darmstadt; 2017.

Paper 3

Markus Eickhoff, Johannis Triebwasser und Bernhard Schweizer. „Thermo-elasto-hydrodynamic analysis of bump-type air foil thrust bearings considering misalignment“. In: *Bulletin of the Polish Academy of Sciences. Technical Sciences* 71.6 (2023)

<https://doi.org/10.24425/bpasts.2023.147917>

©2023. The journal content is available under the licence CC BY 4.0
<https://creativecommons.org/licenses/by/4.0/>



Thermo-elasto-hydrodynamic analysis of bump-type air foil thrust bearings considering misalignment

Markus Eickhoff[✉], Johannis Triebwasser, and Bernhard Schweizer*

Institute of Applied Dynamics, Technical University of Darmstadt, Germany

Abstract. In this study, a multi-pad bump-type foil thrust bearing with a taper-land height profile is investigated. A detailed thermo-elasto-hydrodynamic (TEHD) finite element (FE) model is used comprising all bearing pads instead of only a single pad. Although the single-pad reduction approach is commonly applied, it can not accurately account for the different temperatures, loads, and power losses for individual pads in the case of misalignment. The model accounts for the deformations of the foils on each pad via a Reissner-Mindlin-type shell model. Deformations of the rotor are calculated via the Navier-Lamé equations with thermoelastic stresses and centrifugal effects. The temperature of the top foil and the rotor are calculated with the use of heat diffusion equations. The temperature of each lubricating air film is obtained through a 3D energy equation. Film pressures are calculated with the 2D compressible Reynolds equation. Moreover, the surrounding of the bearing and runner disk is part of the thermodynamic model. Results indicate that the thermal bending of the runner disk as well as top foil sagging are key factors in performance reduction. Due to the bump-type understructure, the top foil sagging effect is observed in simulation results. The study at hand showcases the influence of misalignment between the rotor and the bearing on the bearing performance.

Key words: air foil thrust bearing; simulation; misalignment.

1. INTRODUCTION

Foil bearing technology has its roots over half a century ago, when foil bearings were developed for the use in air cycle machines in aviation, [1, 2]. With an increasing demand in sustainable and oil-free technology today, the use of air foil bearings gains popularity quickly. Further advantages of these bearings consist in their reliability and their tolerance of manufacturing errors as well as misalignment of the rotor system.

In a machine application, the air foil thrust bearing (AFTB) is usually integrated in the stationary machine housing. The rotor possesses a smooth rotor disk acting as a counterpart. As the rotor disk starts to rotate, an air stream into the wedge-shaped lubricating gap between the rotor disk and the bearing surface is created. The generated pressure can eventually carry the thrust loads acting upon the rotor system. For lower speeds, dry friction occurs so that top foil and rotor coatings are used [3, 4]. In comparison to rigid air bearings, foil air bearings possess lower load capacities due to nonuniform bump foil deformations and foil sagging effects.

The investigation of AFTB performance has been conducted by numerous authors in the past. Experimental testing plays a key role in the analysis, see e.g. [5–7].

With numerical models, the foil thrust bearing behavior can be studied and optimized in great detail, see e.g. [8–15].

The thrust foil bearing design with multiple pads and a nominal taper-land topology has been the focus of previous works,

cf. [16–18]. In this study, the influence of misalignment on the bearing performance is studied in a detailed TEHD FE model, which requires the following substantial extensions:

- When considering misalignment, the height function of each bearing pad is individual.
- Each bearing pad exerts a different pressure load and power loss.
- Therefore, the analysis of a single bearing pad as a representation for the overall bearing behavior is no longer valid. The successive calculation of each bearing pad individually is sufficient only for the isothermal case. For the thermal model of the bearing, the fully coupled model of all individual air films presented in this paper can solve this issue.
- Through the use of a single rotor model combined with multiple individual bearing pads (air films and foil understructure), the case of misalignment is adequately represented in the thrust bearing model.
- This extension displays huge additional computational expenses. In comparison with a reduced model where only a single bearing pad is taken into account, computation times are increased by a factor of 8–10 when considering a bearing with six bearing pads.

In this manuscript, a description of the thrust bearing model is given in Section 2. Section 3 presents numerical results for simulations considering misalignment of the rotor disk. The paper is concluded in Section 4.

2. THRUST BEARING MODEL

This section presents the fully coupled TEHD model for the analysis of the AFTB. The bearing design of the current study is displayed in Fig. 1. The rotor possesses a smooth rotor disk

*e-mail: eickhoff@ad.tu-darmstadt.de

Manuscript submitted 2023-05-05, revised 2023-08-22, initially accepted for publication 2023-10-02, published in December 2023.

which is mounted opposite to the thrust bearing of Fig. 1a. The bearing consists of a base plate and 6 individual bearing pads with one bump foil and one top foil each. The bump foil is made up of 3 bump strips with three, four, and five bumps, respectively. The bumps of the bump foil are arranged parallel to the trailing edge of the top foil. The bump foil creates a compliant understructure for the smooth top foil. Through the use of bumps with specific heights, a taper-land height profile is created as depicted in Fig. 1b. The land area is flat, while the taper region ascends from the fixation at the leading edge towards the transition line. The angular velocity Ω of the rotor is marked in Fig. 1b. Figure 2 shows the assembly of the rotor in a cut view with the different model components. Note that the bearing in this analysis possesses an outer diameter of 60 mm.

The model contains the calculation of the air film pressure in the lubricating air gap between the rotor disk and the top foils (Section 2.1), the calculation of bump and top foil deformations (Section 2.2) as well as rotor disk deformations (Section 2.3), the calculation of the air film temperature (Section 2.4), and the calculation of the rotor temperature (Section 2.5) as well as the

top foil temperature (Section 2.6). The section is finished by details on the air film height and misalignment (Section 2.7).

2.1. Air film pressure

The pressure $p_i(x, y)$ in each lubricating air film is calculated via the generalized Reynolds equation in [19]. Herein, the density ρ and the viscosity η are determined using an averaged fluid temperature $T_{m,i}(x, y)$. The latter is calculated by averaging the air film temperature T_i (see Section 2.4) over the gap height H_i (see Section 2.7), cf. [20]. Note that the index i refers to the number of the bearing pad:

$$\frac{\partial}{\partial x} \left[\frac{\rho(p_i, T_{m,i}) H_i^3}{12\eta(T_{m,i})} \frac{\partial p_i}{\partial x} \right] + \frac{\partial}{\partial y} \left[\frac{\rho(p_i, T_{m,i}) H_i^3}{12\eta(T_{m,i})} \frac{\partial p_i}{\partial y} \right] = \frac{\partial}{\partial x} \left[\frac{\rho(p_i, T_{m,i}) U H_i}{2} \right] + \frac{\partial}{\partial y} \left[\frac{\rho(p_i, T_{m,i}) V H_i}{2} \right]. \quad (1)$$

The values $U = \Omega y$ and $V = -\Omega x$ describe the x - and y -component of the rotor disk velocity. The remaining parameters are listed in Table 1.

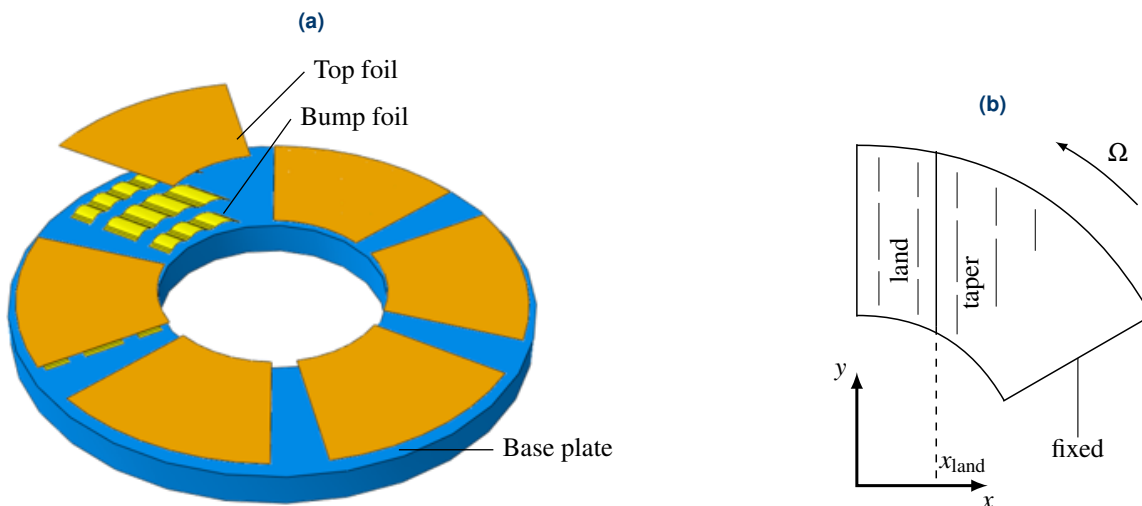


Fig. 1. Overview of the bearing design: (a) Foil thrust bearing with 6 pads consisting of a base plate as well as 6 individual bump and top foils and (b) taper-land profile of one individual bearing pad

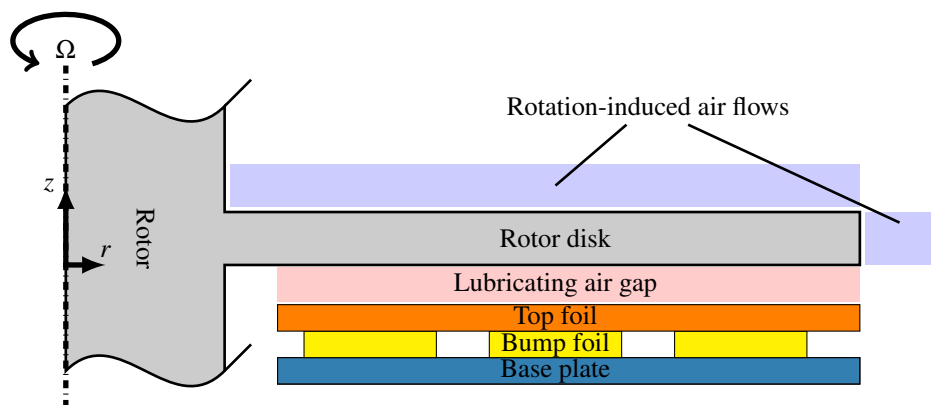


Fig. 2. Model components in cut view

Table 1
Air film parameters

Variable	Value	Description
ρ	$\frac{p}{RT_{m,i}}$	Density
R	0.287 kJ/(kg · K)	Gas constant of air
η	$\left[-1.75 \times 10^{-11} \left(\frac{T_{m,i}}{[K]}\right)^2 + 5.68 \times 10^{-8} \left(\frac{T_{m,i}}{[K]}\right) + 3.06 \times 10^{-6}\right]$ [kg/(m · s)]	Viscosity

The 2D pad region on which equation (1) is solved is equivalent to the bearing pad depicted in Fig. 1b. Due to the sudden increase in film height at the outer borders of the bearing pad, the pressure at the pad edges is assumed to be at ambient pressure p_0 .

2.2. Top and bump foil deformations

This section describes the equations for the calculation of the deformations of top and bump foils in the thrust bearing. Table 2 lists the relevant parameters for the calculation of the foil deformations. For both types of foils, the Reissner-Mindlin shell theory [21] is applied. It allows for three translational degrees of freedom v_k with $k = \{1, 2, 3\}$ and two rotational degrees of freedom w_α with $\alpha = \{1, 2\}$ of the shell middle surface. The constitutive equations of the shell theory are:

$$\begin{aligned} q^\alpha &= Gt \cdot a^{\alpha\lambda} \gamma_\lambda \cdot k_S, \\ m^{\alpha\beta} &= BH^{\alpha\beta\lambda\mu} (\kappa_{\lambda\mu} - b_\lambda^\sigma \varphi_{\mu\sigma}), \\ n^{\alpha\beta} &= DH^{\alpha\beta\lambda\mu} \varphi_{\lambda\mu} - b_\rho^\beta m^{\alpha\rho}. \end{aligned} \quad (2)$$

Note that $n^{\alpha\beta}$ represents the stress resultant tensor, q^α is the transverse shear stress and $m^{\alpha\beta}$ is the moment tensor. The elasticity tensor $H^{\alpha\beta\lambda\mu}$ for a linear elastic, homogeneous and isotropic material reads as

$$H^{\alpha\beta\lambda\mu} = \frac{1-\nu}{2} \left(a^{\alpha\lambda} a^{\beta\mu} + a^{\alpha\mu} a^{\beta\lambda} + \frac{2\nu}{1-\nu} a^{\alpha\beta} a^{\lambda\mu} \right). \quad (3)$$

Table 2
Foil parameters

Variable	Value	Description
E	210 GPa	Young's modulus
ν	0.3	Poisson's ratio
t	75 μ m 100 μ m	Bump foil thickness Top foil thickness
k_S	5/6	Shear correction factor
$d_{i,T}$	30 mm	Top foil inner diameter
$d_{o,T}$	60 mm	Top foil outer diameter

In equation (2), $a^{\alpha\lambda}$ is the metric tensor, b_λ^σ is the curvature tensor, and k_S is the shear correction factor. Furthermore, D is the stretching stiffness, B is the bending stiffness, and Gt is the shear stiffness defined as

$$D = \frac{Et}{1-\nu^2}, \quad B = \frac{Et^3}{12(1-\nu^2)}, \quad Gt = \frac{Et}{2(1+\nu)}, \quad (4)$$

where E is Young's modulus and ν is Poisson's ratio of the steel foils. The three strain variables $\varphi_{\alpha\beta}$, $\kappa_{\alpha\beta}$, and γ_α are given as

$$\begin{aligned} \varphi_{\alpha\beta} &= v_{\beta|\alpha} - \nu_3 b_{\alpha\beta}, \\ \kappa_{\alpha\beta} &= \frac{1}{2} (w_{\alpha|\beta} + w_{\beta|\alpha}), \\ \gamma_\alpha &= w_\alpha + \nu_3 \cdot \alpha + \nu_\lambda b_\alpha^\lambda. \end{aligned} \quad (5)$$

Finally, the equilibrium equations read as follows:

$$\begin{aligned} -p^\beta &= n^{\alpha\beta} |_\alpha - q^\alpha b_\beta^\alpha, \\ -p^3 &= n^{\alpha\beta} b_{\alpha\beta} + q^\alpha |_\alpha, \\ 0 &= m^{\alpha\beta} |_\alpha - q^\beta. \end{aligned} \quad (6)$$

Herein, $\vec{p} = p^\alpha \vec{a}_\alpha + p^3 \vec{a}_3$ are the external forces and $\vec{n}^\alpha = n^{\alpha\beta} \vec{a}_\beta + q^\alpha \vec{a}_3$ and $\vec{m}^\alpha = m^{\alpha\beta} \vec{a}_3 \times \vec{a}_\beta$ are the internal force variables.

External forces on the top foils originate from the pressure in the lubricating air gap. Therefore, the air film pressure is implemented as an external load in the calculation of the top foil deflections. On the other hand, the resulting top foil deformations influence the gap function and – in turn – change the pressure profile in the lubricating air gap. For details on the height function see Section 2.7.

Contacts between the top foil and the bump foil as well as between the bump foil and the base plate are included in the model. The normal contact force F_N is implemented using a penalty formulation, $F_N = c \Delta v_3$, $c = 1 \times 10^{11}$ N/m being the penalty stiffness and Δv_3 the penetration depth.

The tangential behavior between top and bump foil is modeled via a stick-slip approach with regularized Coulomb friction, cf. [22]. The tangential force $F_T = \mu \cdot \text{step}(\Delta v_T) F_N$ acts in the direction opposite to the relative sliding motion Δv_T . μ is the friction coefficient ($\mu = 0.1$ assumed here for all contacts) and step describes a regularized sign function with a small transition zone. In this way, the foil sandwich is represented as a 2D nonlinear structural shell model. The nonlinearity arises from the contact formulation.

It should finally be mentioned that thermal deformations of the foils are not considered in this model. Although the thermal behavior of the thrust bearing is crucial for safe operation, thermal expansion of the top foil can be neglected as it causes in-plane deformations and does not contribute to changes in the lubricating gap height. Furthermore, the design of the bearing with individual pads and independent top and bump foils reduces the impact of thermal deformations further. The top foil temperature and the heat conduction through the bump foil is discussed in Section 2.6.

2.3. Rotor deformations

Due to the high angular velocity Ω , the rotor and rotor disk are modeled with an axisymmetric model, both for the rotor deformations $v_r(r, z)$ in radial and $v_z(r, z)$ in axial direction and the rotor temperature T_R (see Section 2.5). The deformations are obtained through the Navier-Lamé equations with centrifugal forces and thermal stresses, cf. [23, 24]:

$$\begin{aligned} \mu_R \left(\nabla^2 v_r - \frac{v_r}{r^2} \right) + (\gamma_R + \mu_R) \frac{\partial}{\partial r} \left(\frac{1}{r} \frac{\partial}{\partial r} (r v_r) + \frac{\partial v_z}{\partial z} \right) \\ - \varepsilon_R \frac{\partial \Delta T_R}{\partial r} = -\rho_R r \Omega^2, \\ \mu_R \nabla^2 v_z + (\gamma_R + \mu_R) \frac{\partial}{\partial z} \left(\frac{1}{r} \frac{\partial}{\partial r} (r v_r) + \frac{\partial v_z}{\partial z} \right) \\ - \varepsilon_R \frac{\partial \Delta T_R}{\partial r} = 0 \end{aligned} \quad (7)$$

with

$$\begin{aligned} \gamma_R &= \frac{E_R \nu_R}{(1 + \nu_R)(1 - 2\nu_R)}, \\ \mu_R &= \frac{E_R}{2(1 + \nu_R)}, \\ \varepsilon_R &= \frac{E_R \alpha_R}{1 - 2\nu_R}. \end{aligned} \quad (8)$$

γ_R is the Lamé constant and μ_R is the shear modulus. The constant ε_R describes thermoelastic stresses with $\Delta T_R = T_R - T_{\text{ref}}$ being the disk temperature difference with respect to a reference temperature $T_{\text{ref}} = T_0 = 20^\circ\text{C}$. Further, ρ_R is the density, α_R is the thermal expansion coefficient, E_R is Young's modulus, and ν_R is Poisson's ratio of the rotor material. Table 3 lists the relevant parameters for the calculation of the rotor deformations.

Table 3
Rotor parameters

Variable	Value	Description
E_R	210 GPa	Young's modulus
ν_R	0.3	Poisson's ratio
α_R	$13 \times 10^{-6} \text{K}^{-1}$	Thermal expansion coefficient

2.4. Air film temperature

The temperature field $T_{A,i}(x, y, z)$ of each sector is obtained from the 3D compressible energy equation, cf. for example [11]:

$$\begin{aligned} \rho c_P \left[u \frac{\partial T_{A,i}}{\partial x} + v \frac{\partial T_{A,i}}{\partial y} \right] = \left[\frac{\partial}{\partial z} \left(\lambda \frac{\partial T_{A,i}}{\partial z} \right) \right] \\ + \left[u \frac{\partial p}{\partial x} + v \frac{\partial p}{\partial y} \right] + \eta \left[\left(\frac{\partial u}{\partial z} \right)^2 + \left(\frac{\partial v}{\partial z} \right)^2 \right]. \end{aligned} \quad (9)$$

The four terms describe the convective heat transfer, diffusive heat transfer (conduction), the power of pressure forces, and

dissipation resulting from shear forces, respectively. λ is the heat conductivity, c_P is the heat capacity, and u and v are the x - and y -velocities of the lubricating air. Table 4 lists the definition of the heat capacity and the heat conductivity of air depending on the air temperature.

Table 4
Energy equation parameters

Variable	Value	Description
c_P	$\left[2.43 \times 10^{-4} \left(\frac{T_{A,i}}{[K]} \right)^2 - 7.7 \times 10^{-2} \left(\frac{T_{A,i}}{[K]} \right) + 1008 \right] [\text{J}/(\text{kg} \cdot \text{K})]$	Heat capacity
λ	$\left[-2.1 \times 10^{-8} \left(\frac{T_{A,i}}{[K]} \right)^2 + 8.46 \times 10^{-5} \left(\frac{T_{A,i}}{[K]} \right) + 2.89 \times 10^{-3} \right] [\text{W}/(\text{m} \cdot \text{K})]$	Heat conductivity

At the interfaces of the air films to the respective top foils, the temperature $T_{A,i}$ is coupled via interface conditions to the top foil temperature T_T (see Section 2.6), i.e. temperatures and heat fluxes are set to be equal. At the inlet boundary of the lubricating gap, the temperature is assumed to be the same as the rotor disk temperature. This assumption has been shown to be a good approximation, see [17, 25]. As the model contains 6 individual air films and a single rotor model, the heat fluxes of all air film sectors into the rotor disk can be given as a flux boundary condition for the rotor disk temperature. For the individual air films, the temperature at the interface to the rotor disk is set to the rotor disk temperature T_R (see Section 2.5).

2.5. Rotor temperature

The rotor and rotor disk temperature $T_R(r, z)$ is calculated via the heat conduction equation

$$\frac{\partial}{\partial r} \left[\lambda_R r \frac{\partial T_R}{\partial r} \right] + \frac{\partial}{\partial z} \left[\lambda_R r \frac{\partial T_R}{\partial z} \right] = 0. \quad (10)$$

The heat conduction of the rotor material is $\lambda_R = 12 \text{W}/(\text{m} \cdot \text{K})$. The boundary conditions of the rotor and rotor disk are crucial for the determination of the rotor temperature T_R . As mentioned in Section 2.4, the incoming heat flux into the rotor disk from all lubricating air gaps is enforced as a heat flux boundary condition at the interface to the bearing pad, cf. [17]. The heat flux $q_{\text{gap},i}(r)$ of each individual air film can be calculated as

$$q_{\text{gap},i}(r) = \frac{1}{2\pi} \int_{\varphi_l}^{\varphi_l} \left(\lambda \frac{\partial T_{A,i}}{\partial z} \right) \Big|_{\text{Interface}} r d\varphi, \quad (11)$$

where the temperature gradient is evaluated at the interface to the rotor disk. The angles φ_l and φ_t are the angles of the leading

edge and the trailing edge of the bearing pad, respectively. The total heat flux $q_{\text{gap}}(r)$ into the rotor disk now reads as follows:

$$q_{\text{gap}}(r) = \sum_{i=1}^6 q_{\text{gap},i}(r). \quad (12)$$

At the backside of the rotor disk, the disk rotation causes an airflow. The heat flux that leaves the disk is calculated from the temperature $T_C(r, z)$ in this region which is obtained from the energy equation (assuming axisymmetry):

$$\frac{\partial}{\partial z} \left[\lambda_{C,\text{eff}} \frac{\partial T_C}{\partial z} \right] = \rho_C c_{P,C} \left[u_C \frac{\partial T_C}{\partial r} + w_C \frac{\partial T_C}{\partial z} \right] - \rho_C (v_C + v_{CT}) \left[\left(\frac{\partial u_C}{\partial z} \right)^2 + \left(\frac{\partial v_C}{\partial z} \right)^2 \right]. \quad (13)$$

Here, $\lambda_{C,\text{eff}}$ is an effective thermal conductivity according to [26], ρ_C the density, $c_{P,C}$ the isochoric heat capacity and v_C and v_{CT} are the kinematic viscosity and the turbulent kinematic viscosity according to Cebeci and Smith [27]. The velocity field consisting of the radial velocity u_C , the circumferential velocity v_C and the velocity w_C in z -direction is calculated from the boundary layer equations for steady incompressible axisymmetric flow (neglecting a radial pressure gradient), see [27].

In the radial gap between the rotor disk and the housing, the disk rotation also causes an airflow. It is assumed to be laminar with purely circumferential flow (Couette flow) and with linearly decreasing velocity over the radial coordinate (disk speed at the inner boundary, zero speed at the outer boundary). This simple assumption is made as the initial gap width t is 200 μm and decreases below 100 μm at high rotational speeds due to centrifugal effects. Thus, the 2D energy equation

$$\frac{\partial}{\partial r} \left[\lambda_{RG} r \frac{\partial T_{RG}}{\partial r} \right] + \frac{\partial}{\partial z} \left[\lambda_{RG} r \frac{\partial T_{RG}}{\partial z} \right] = -r \eta_{RG} \left[\frac{\Omega r_D}{t} \right]^2 \quad (14)$$

including dissipative heating is solved to obtain the temperature profile $T_{RG}(r, z)$ in the radial gap. In equation (14), λ_{RG} is the thermal conductivity, η_{RG} is the dynamic viscosity of air in the radial gap, r_D is the disk radius and t is the gap width with account of disk deformations.

2.6. Top foil temperature

The top foil temperature profile $T_{T,i}(x, y)$ of each top foil is obtained by the planar heat conduction equation

$$-\lambda_T t_T \Delta T_{T,i} = q_{T,\text{in}} + q_{T,\text{out}} \quad (15)$$

with constant heat conductivity $\lambda_T = 12 \text{ W}/(\text{m} \cdot \text{K})$ and thickness t_T of the top foils. The heat fluxes $q_{T,\text{in}} = \left(\lambda \frac{\partial T_{A,i}}{\partial z} \right) \Big|_{\text{Interface}}$ as well as $q_{T,\text{out}} = q_b$ at the contact lines and $q_{T,\text{out}} = q_c$ everywhere else is solved. Over each top foil, an incoming heat flux from the lubricating gap is calculated. A possible cooling heat flux q_c originating from active cooling can be implemented as well, but is neglected in the present study. Heat conduction from each top foil into the base plate

is modeled as an outgoing heat flux $q_b = -\frac{2}{R_{\text{th}}}(T_{T,i} - T_{\text{Base}})$ at the contact lines between top and bump foil, visible in Fig. 1b. Herein, $R_{\text{th}} = R_{\text{TB,air}} + R_{\text{bump}} + R_{\text{BB,air}}$ is the thermal resistance of a half bump arc composed of the thermal contact resistance between top and bump foil $R_{\text{TB,air}}$, thermal conduction resistance of the half-bump arc R_{bump} and the contact resistance between bump foil and base plate $R_{\text{BB,air}}$, cf. [28]. The leading edge of the top foil is assumed to have the same temperature as the air at the inlet. On the remaining three boundaries, a zero heat flux condition is imposed. Note that the influence of the pressure acting upon the foil sandwich is of subordinate importance for the thermal contact resistances [17].

2.7. Air film height and misalignment

For the numerical analysis of the thrust bearing, the film height function $H(x, y)$ is crucial. It is affected by the bearing design, but also includes the deformations of the bearing components. Each bearing pad possesses an individual height function $H_i(x, y)$:

$$H_i(x, y) = z_R - v_{3,T,i} + v_z(z=0, r) + H_{\text{mis}}. \quad (16)$$

Herein, $v_{3,T,i}$ is the deformation of the i -th top foil and is individual for each pad. The remaining values are the same for each bearing pad: z_R displays the axial position of the rotor, $v_z(z=0, r)$ is the deformation of the rotor disk underside (see Fig. 2), and H_{mis} represents the misalignment between the rotor disk and the bearing:

$$H_{\text{mis}} = -\tan(\beta_{\text{mis}})x + \frac{\tan(\alpha_{\text{mis}})}{\cos(\beta_{\text{mis}})}y. \quad (17)$$

The two misalignment angles α_{mis} and β_{mis} are displayed in Fig. 3.

2.8. Computational details

This section describes details of the computation of the fully coupled TEHD FE model. The model has roughly 2.1 million degrees of freedom (DOF) plus approximately 320 000 internal DOFs. A direct MUMPS solver is used to find the stationary solution for a given set of parameters. While the bearing design and the underlying geometrical parameters for the various components obviously play a key role in the performance of thrust bearings, the main parameters for the presented study comprise the angular velocity Ω , the minimal gap height H_{min} and the misalignment angles α_{mis} and β_{mis} .

In order to generate a solution for the full model, a multi-step approach is used for convergence improvement. This approach starts with different segregated parts of the model (energy equation, shell equations, surrounding) in order to generate adequate starting solutions for the complete fully coupled model. The first fully coupled simulation starts with very low rotational speeds and relatively large gap heights (i.e. low loads) and without misalignment of the components. In the next step, the rotational speed is increased in steps up to the desired speed of 100krpm. Next, the minimal gap height parameter H_{min} is decreased in order to obtain higher loads. In the last step, the

M. Eickhoff, J. Triebwasser, and B. Schweizer

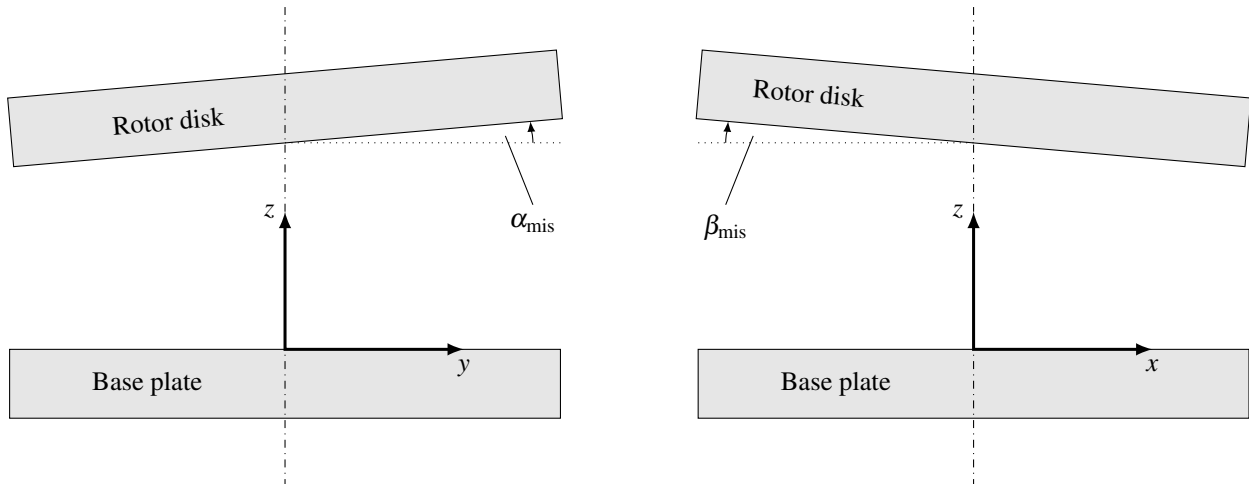


Fig. 3. Definition of the two misalignment angles α_{mis} and β_{mis} of equation (17)

misalignment angles may be increased to study the influence of misalignment.

On a local machine (Win 7) with a 4th generation Intel Xeon processor with 12 logical cores and 128 GB of RAM, the described process of generating a full solution with the model takes approximately 40 hours. It should be mentioned that computation times increase significantly with increasing misalignment angles. Compared to the corresponding single-pad model, computation times are increased by a factor of 8–10.

3. RESULTS

This section presents numerical results of the fully coupled TEHD model considering misalignment. In Fig. 4, the nominal design height function and the real height function are compared. While the nominal height function without deformations in Fig. 4a shows the ideal taper-land topology, Fig. 4b shows the deformed height function which is affected by the top foil deformations as well as the rotor disk deformations. As the top foil is subject to pressure loading from the lubricating air gap,

it is forced downwards onto the bump foil support. As the contact between top and bump foils only forms at the peak line of the bumps, the top foil does not possess any structural support in between these lines, cf. Fig. 4b. The sagging of the top foil between the bump lines is widely known as top foil sagging effect. It is responsible for a degradation of the height function and a decrease in load capacity.

Deformations of the rotor disk stem from centrifugal forces as well as axial temperature gradients. Figure 5 displays the rotor disk temperature for a rotational speed of 100krpm and a power loss of 154 W. The underside of the rotor disk is at the interface to the lubricating air gaps where dissipation causes high air temperatures. The dissipation is dependent on the shear velocity within the air film. Therefore, the rotor disk temperature is highest near its outer radius where circumferential velocities are highest. Towards the base of the rotor disk (attachment to the rotor) and towards the backside of the disk, its temperature gets cooler. The temperature gradient of the rotor disk temperature, which is proportional to the heat flux, is also depicted in Fig. 5 by black arrows.

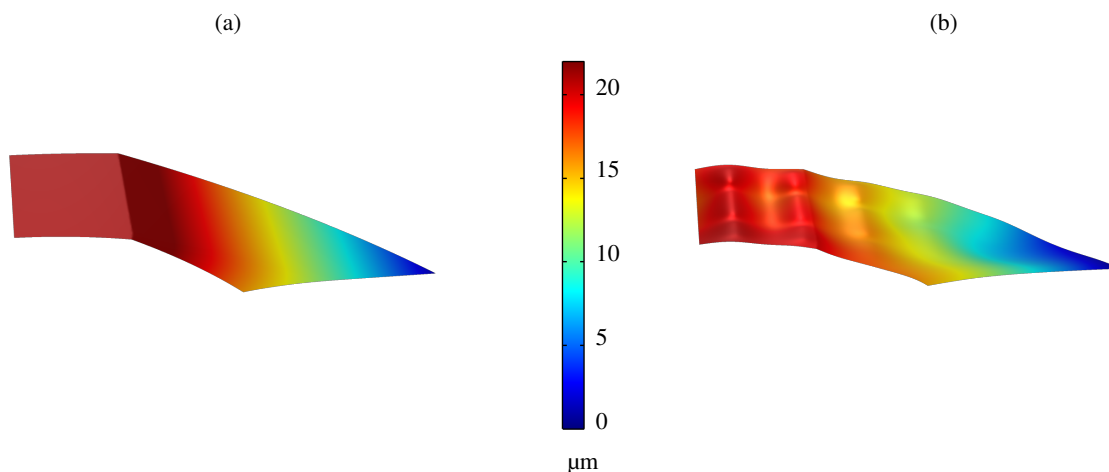


Fig. 4. Height function (relative scale) of equation (16) without misalignment: (a) nominal height function without deformations $v_{3,T}$ and $v_z(z=0, r)$ and (b) height function with top foil and rotor disk deformations showing top foil sagging

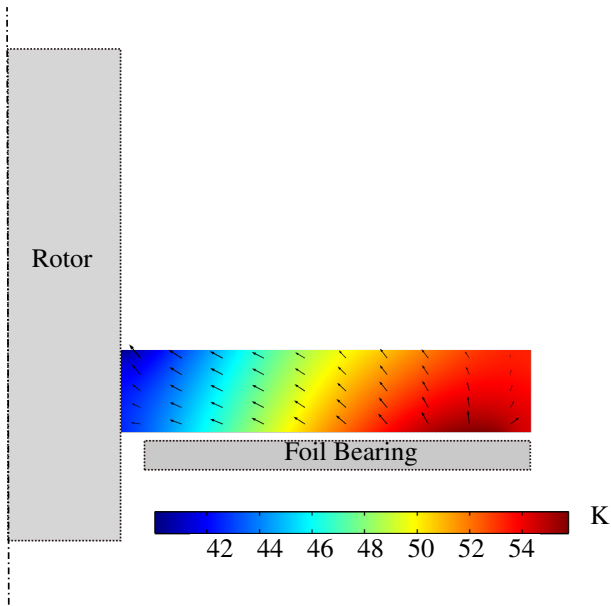


Fig. 5. Rotor disk temperature $T_R - T_0$ as well as rotor disk temperature gradient marked by black arrows

The axial temperature gradient of the rotor disk causes thermal bending and is included in the deformed height function of Fig. 4b.

Figure 6 now displays the pressure distributions p_i for all bearing pads with different misalignment angles α_{mis} . Note that the second misalignment angle β_{mis} is set to 0 in all studies. The pressure profiles are displayed on a common pressure scale also depicted in Fig. 6. As expected, the case without misalignment between the rotor disk and the bearing ($\alpha_{\text{mis}} = \beta_{\text{mis}} = 0 \text{ rad}$) yields identical pressure distributions across all bearing pads. In general, the highest pressures are observed in the land region of the pad with distinct pressure peaks at the contact lines between top foils and bump foils. These contact lines are marked by black lines in Fig. 6. Please note again that the direction of rotation of the rotor disk in the displayed views is counter-clockwise (positive z -direction).

When the misalignment angle is increased in Figs. 6b-d, the rotor disk tilts towards the lower half of the bearing (negative y -direction). For comparability, all simulations were carried out with a constant minimal air gap height. While all six pads of Fig. 6a (no misalignment) show a spot where this minimal gap

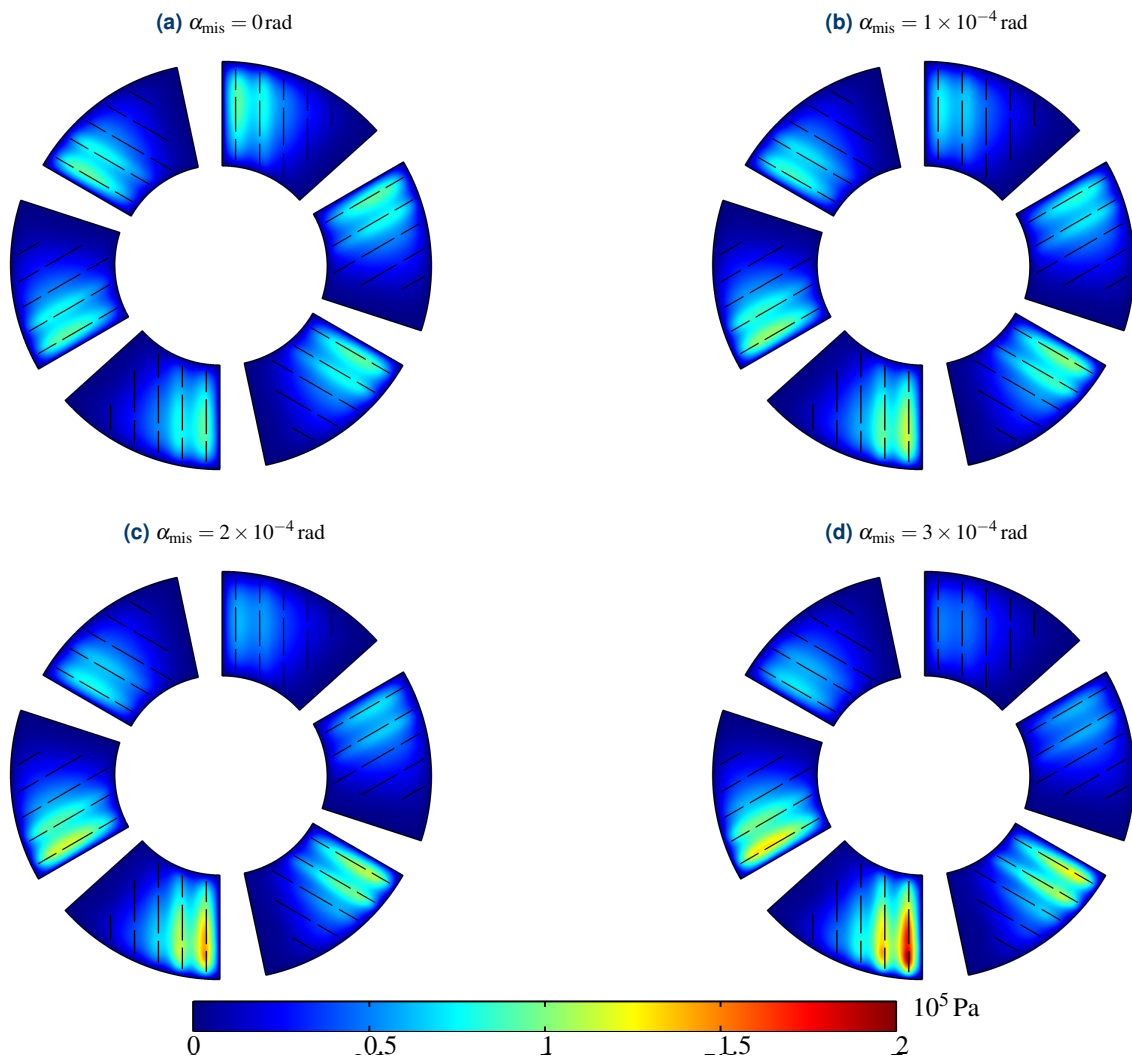


Fig. 6. Pressure distributions $p_i - p_0$ for various misalignment angles α_{mis}

height is observed, for the remaining cases, the minimal gap height is only achieved on the bottom left pad in Figs. 6b–d. It is interesting to notice that – by contrast to rigid thrust bearings – the compliant foil thrust bearing can compensate a portion of the misalignment. This is why the bearing pads in the top half of Figs. 6b–d still show significant pressure buildup. For the last case of Fig. 6d, the pad with the highest load generates two times as much load capacity as the least loaded pad on the top right. However, the overall load capacity of the bearing is very similar with a value of 55 N at a rotational speed of 100 krpm at a minimal gap height of $5 \mu\text{m}$ when compared to results without misalignment. The compliant foil thrust bearing is able to compensate and still show similar load capacities. Figure 7 shows the thrust load over the misalignment angle α_{mis} . For the investigated misalignment angle range, the thrust load is nearly constant. As a downside, the power loss of the thrust bearing is increased due to the uneven loading.

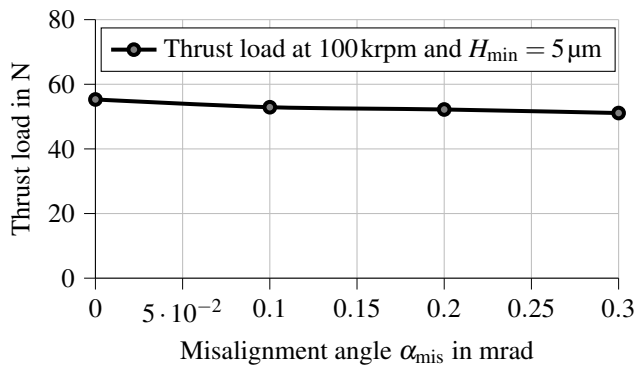


Fig. 7. Thrust load over the misalignment angle α_{mis}

Simultaneously, through the uneven loading of the bearing, the exerted power loss increases by approximately 6.5% to 164 W.

Short remark on the misalignment angles displayed in this manuscript: A misalignment configuration with $\alpha_{\text{mis}} = 1 \times 10^{-4}$ rad and $\beta_{\text{mis}} = 0$ rad refers to a maximum misalignment of $3 \mu\text{m}$ at the outer radius of the thrust bearing.

Figure 8 shows the impact of thermal bending of the rotor disk. The 3D image of the disk as well as the cross-sectional view both show a dished rotor disk. The graph at the bottom of the figure displays the axial deformation of the disk on the side facing the thrust bearing. It is typical for this hot side of the rotor disk to bend away from the bearing due to an axial temperature gradient inside the rotor disk. At the outer radius of the disk, the resulting bending is substantial and causes an uneven gap height, which in turn reduces the load capacity of the bearing.

Figure 9 shows the air film temperature in all six bearing sectors via a slice plot for the misalignment case of $\alpha_{\text{mis}} = 3 \times 10^{-4}$ rad. Herein, the top slice corresponds to the interface with the rotor disk. Note again that the rotor disk temperature does not depend on the circumferential coordinate. Therefore, the top slice temperature is equal for all bearing sectors. Differences are observed when the bottom slice of the air film temper-

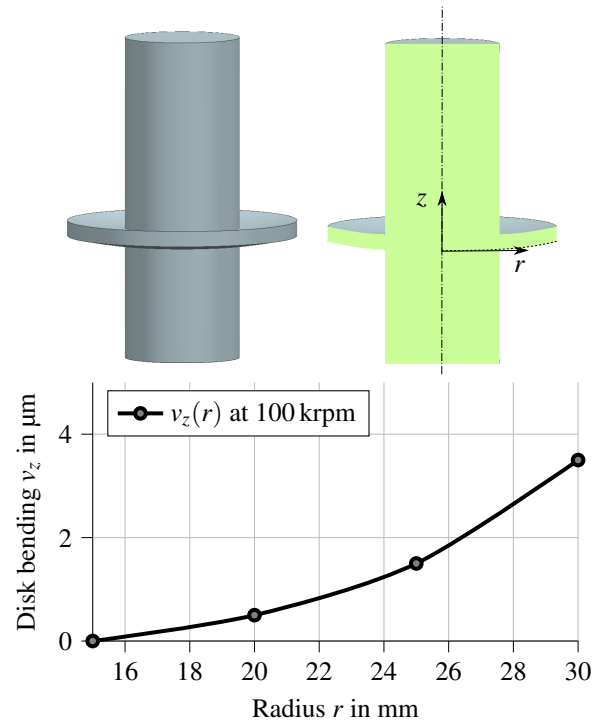


Fig. 8. Rotor disk bending (dishing) illustrated in a 3D view of the rotor shaft and the rotor disk as well as a cross section view, graph (bottom) shows the axial rotor disk deformation v_z over the radial coordinate r

atures is investigated. This slice corresponds to the interfaces with the top foils. In the bottom half of the bearing in Fig. 9, the maximum temperatures are slightly higher than those in the top half due to higher power losses in the lubricating air film.

The temperature distribution in the air films is qualitatively similar with two distinct patterns: a temperature rise towards the outer edge due to higher dissipation as well as temperature drops near the contact lines of top and bump foil due to the heat conduction through the bumps into the base plate.

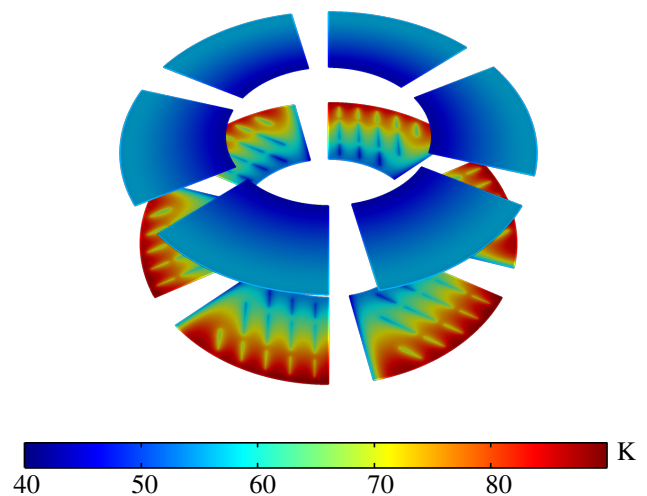


Fig. 9. Air film temperatures $T_{A,i} - T_0$ in slices at the top foil interface and at the rotor disk interface for $\alpha_{\text{mis}} = 3 \times 10^{-4}$ rad

4. CONCLUSIONS

A detailed TEHD model for air-foil thrust bearings considering misalignment between the rotor disk and the bearing has been presented. The model contains an in-depth description of the foil deformations via a shell model as well as a model for rotor and rotor disk deflections. The 2D compressible Reynolds equation and the 3D energy equation are solved for each bearing pad. Furthermore, the temperatures of the top foils, the rotor, and the surrounding air are calculated in the model. This allows for the fully coupled analysis of bump-type thrust bearings with full account of the thermal influences of individual pads when misalignment is present.

Numerical results with this model show the influence of component deformations on the height function and, subsequently, on the bearing performance. The initial taper-land height function is degraded by top foil sagging and thermal bending of the rotor disk. While top foil sagging is caused by the pressure load onto the top foil combined with line-type support of the bump foil understructure, thermal bending of the rotor disk is a result of the axial temperature gradient in the rotor disk. This temperature gradient is caused by the hot temperatures in the lubricating gap through dissipation on the one hand and the cooling of the rotor disk through conduction into the surroundings on the other hand. The rotation-induced airflows around the runner disk at the outer perimeter and at the disk backside play a key role in this regard.

It is shown that misalignment causes an uneven distribution of the load onto the bearing pads. However, results indicate that, for the presented misalignment cases, the compliant foil thrust bearing was able to compensate and still show similar load capacities. As a downside, the power loss of the thrust bearing is increased due to the uneven loading.

Through the modeling of the full bearing with account for all individual bearing pads with individual height functions, small temperature differences in the lubricating air temperature can be observed. The computational effort for each simulation is highly increased when compared to a model with a reduced approach considering only a single bearing pad. By contrast to the reduced investigation, only this fully coupled approach is appropriate for TEHD simulations with misalignment. The detailed model allows for the investigation of foil thrust bearings under misalignment conditions in great depth. However, with this level of model complexity, an extensive parameter variation for geometrical dimensions is no longer possible.

REFERENCES

- [1] G.L. Agrawal, "Foil air/gas bearing technology – an overview," in *Volume 1: Aircraft Engine; Marine; Turbomachinery; Micro-turbines and Small Turbomachinery*, ser. Turbo Expo: Power for Land, Sea, and Air. American Society of Mechanical Engineers, 1997, p. V001T04A006, doi: [10.1115/97-GT-347](https://doi.org/10.1115/97-GT-347).
- [2] P. Samanta, N. Murmu, and M. Khonsari, "The evolution of foil bearing technology," *Tribol. Int.*, vol. 135, pp. 305–323, 2019.
- [3] K.C. Radil and C. DellaCorte, "The effect of journal roughness and foil coatings on the performance of heavily loaded foil air bearings," *Tribol. Trans.*, vol. 45, no. 2, pp. 199–204, 2002.
- [4] F. Balducchi, M. Arghir, R. Gauthier, and E. Renard, "Experimental Analysis of the Start-Up Torque of a Mildly Loaded Foil Thrust Bearing1," *J. Tribol.*, vol. 135, no. 3, 2013, doi: [10.1115/1.4024211](https://doi.org/10.1115/1.4024211).
- [5] B.D. Dykas, "Factors influencing the performance of foil gas thrust bearings for oil-free turbomachinery applications," Ph.D. dissertation, Case Western Reserve University, 2006.
- [6] F. Balducchi, M. Arghir, and R. Gauthier, "Experimental analysis of the dynamic characteristics of a foil thrust bearing," *J. Tribol.*, vol. 137, no. 2, p. 021703, 2015.
- [7] N. LaTray and D. Kim, "Design of Novel Gas Foil Thrust Bearings and Test Validation in a High-Speed Test Rig," *J. Tribol.*, vol. 142, no. 7, p. 071803, 2020, doi: [10.1115/1.4046412](https://doi.org/10.1115/1.4046412).
- [8] I. Iordanoff, "Analysis of an aerodynamic compliant foil thrust bearing: Method for a rapid design," *J. Tribol.*, vol. 121, no. 4, pp. 816–822, 1999.
- [9] C.A. Heshmat, D.S. Xu, and H. Heshmat, "Analysis of gas lubricated foil thrust bearings using coupled finite element and finite difference methods," *J. Tribol.*, vol. 122, no. 1, pp. 199–204, 2000.
- [10] R.J. Bruckner, *Simulation and modeling of the hydrodynamic, thermal, and structural behavior of foil thrust bearings*. Case Western Reserve University, 2004.
- [11] D. Lee and D. Kim, "Thermohydrodynamic Analyses of Bump Air Foil Bearings With Detailed Thermal Model of Foil Structures and Rotor," *J. Tribol.*, vol. 132, no. 2, p. 021704, 2010, doi: [10.1115/1.4001014](https://doi.org/10.1115/1.4001014).
- [12] L. San Andrés and T. H. Kim, "Thermohydrodynamic Analysis of Bump Type Gas Foil Bearings: A Model Anchored to Test Data," *J. Eng. Gas Turbines Power*, vol. 132, no. 4, p. 042504, 2010, doi: [10.1115/1.3159386](https://doi.org/10.1115/1.3159386).
- [13] K. Sim and T. H. Kim, "Thermohydrodynamic analysis of bump-type gas foil bearings using bump thermal contact and inlet flow mixing models," *Tribol. Int.*, vol. 48, pp. 137–148, 2012, doi: [10.1016/j.triboint.2011.11.017](https://doi.org/10.1016/j.triboint.2011.11.017).
- [14] T. Conboy, "Real-gas effects in foil thrust bearings operating in the turbulent regime," *J. Tribol.*, vol. 135, no. 3, p. 031703, 2013.
- [15] K. Feng, L.-J. Liu, Z.-Y. Guo, and X.-Y. Zhao, "Parametric study on static and dynamic characteristics of bump-type gas foil thrust bearing for oil-free turbomachinery," *Proc. Inst. Mech. Eng. Part J.-J. Eng. Tribol.*, vol. 230, no. 8, pp. 944–961, 2016.
- [16] J.R. Dickman, "An investigation of gas foil thrust bearing performance and its influencing factors," Ph.D. dissertation, Case Western Reserve University, 2010.
- [17] A. Lehn, "Air Foil Thrust Bearings: A Thermo-Elasto-Hydrodynamic Analysis," Ph.D. thesis, Technische Universität Darmstadt, 2017.
- [18] M. Rieken, M. Mahner, and B. Schweizer, "Thermal Optimization of Air Foil Thrust Bearings Using Different Foil Materials," *J. Turbomach.*, vol. 142, no. 10, p. 101003, 2020, doi: [10.1115/1.4047633](https://doi.org/10.1115/1.4047633).
- [19] D. Dowson, "A generalized Reynolds equation for fluid-film lubrication," *Int. J. Mech. Sci.*, vol. 4, no. 2, pp. 159–170, 1962, doi: [10.1016/S0020-7403\(62\)80038-1](https://doi.org/10.1016/S0020-7403(62)80038-1).
- [20] D. Lee and D. Kim, "Three-Dimensional Thermohydrodynamic Analyses of Rayleigh Step Air Foil Thrust Bearing with Radially Arranged Bump Foils," *Tribol. Trans.*, vol. 54, no. 3, pp. 432–448, 2011, doi: [10.1080/10402004.2011.556314](https://doi.org/10.1080/10402004.2011.556314).
- [21] Y. Başar and W.B. Krätzig, *Mechanik der Flächentragwerke: Theorie, Berechnungsmethoden, Anwendungsbeispiele*, 1st ed., ser. Grundlagen der Ingenieurwissenschaften. Wiesbaden: Vieweg + Teubner Verlag, 1985, doi: [10.1007/978-3-322-93983-8](https://doi.org/10.1007/978-3-322-93983-8).

M. Eickhoff, J. Triebwasser, and B. Schweizer

- [22] P. Wriggers, *Computational contact mechanics*, 2nd ed. Berlin: Springer, 2006, doi: [10.1007/978-3-540-32609-0](https://doi.org/10.1007/978-3-540-32609-0).
- [23] M.H. Sadd, *Elasticity: Theory, Applications, and Numerics*. Elsevier, 2005.
- [24] M. Mahner, A. Lehn, and B. Schweizer, "Thermogas- and thermohydrodynamic simulation of thrust and slider bearings: Convergence and efficiency of different reduction approaches," *Tribol. Int.*, vol. 93, pp. 539–554, 2016, doi: [10.1016/j.triboint.2015.02.030](https://doi.org/10.1016/j.triboint.2015.02.030).
- [25] A. Lehn, M. Mahner, and B. Schweizer, "Characterization of static air foil thrust bearing performance: an elasto-gasdynamic analysis for aligned, distorted and misaligned operating conditions," *Arch. Appl. Mech.*, vol. 88, no. 5, pp. 705–728, 2018, doi: [10.1007/s00419-017-1337-7](https://doi.org/10.1007/s00419-017-1337-7).
- [26] C.L. Ong and J.M. Owen, "Computation of the flow and heat transfer due to a rotating disc," *Int. J. Heat Fluid Flow*, vol. 12, no. 2, pp. 106–115, 1991, doi: [10.1016/0142-727X\(91\)90036-U](https://doi.org/10.1016/0142-727X(91)90036-U).
- [27] T. Cebeci and A. Smith, *Analysis of Turbulent Boundary Layers*. New York: Academic Press, 1974.
- [28] A. Lehn, M. Mahner, and B. Schweizer, "A Contribution to the Thermal Modeling of Bump Type Air Foil Bearings: Analysis of the Thermal Resistance of Bump Foils," *J. Tribol.*, vol. 139, no. 6, p. 061702, 2017, doi: [10.1115/1.4036631](https://doi.org/10.1115/1.4036631).

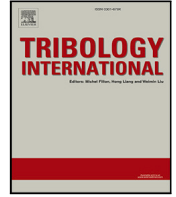
Paper 4

Markus Eickhoff, Johannis Triebwasser, Andre Theile und Bernhard Schweizer.
„Compensating thermal bending of the runner disk in hydrodynamic thrust bearings:
Simple approach for passively improving the performance of gas bearings“. In:
Tribology International (2024), S. 109632

<https://doi.org/10.1016/j.triboint.2024.109632>

©2024. The journal content is available under the licence CC BY 4.0
<https://creativecommons.org/licenses/by/4.0/>





Full Length Article

Compensating thermal bending of the runner disk in hydrodynamic thrust bearings: Simple approach for passively improving the performance of gas bearings

Markus Eickhoff^{a,*}, Johannis Triebwasser^a, Andre Theile^b, Bernhard Schweizer^a

^a Institute of Applied Dynamics, Technical University of Darmstadt, Otto-Berndt-Strasse 2, Darmstadt, Germany

^b Robert Bosch GmbH, Wernerstraße 51, Stuttgart, Germany

ARTICLE INFO

Keywords:

Thermal Bending
Hydrodynamic bearing
Thrust bearing
Air bearing

ABSTRACT

This paper presents a method for passively compensating thermal bending distortions of the thrust disk in gas thrust bearings by passive approaches. Thermal bending displays a prominent problem in hydrodynamic thrust bearings, especially in connection with air bearings. Axial temperature gradients cause the rotor disk to dish which in turn diminishes the lubricating gap topology and reduces the load capacity of the bearing. Consequently, the bearing performance is decreased and the bearing may even fail. The here proposed straightforward solutions are small changes in the rotor and runner disk design and are therefore rather simple and inexpensive to adopt. They comprise asymmetric mass distributions, recesses, disk cuts, and dual-material rotor disks. In order to show the benefit for the thrust bearing performance, detailed multiphysical numerical simulations of a representative rotor assembly with a foil thrust bearing are presented. The fully coupled finite element model calculates the deformations of the foil package (2D Reissner–Mindlin type shell equations), lubricating air film pressure (2D compressible Reynolds equation), air film temperatures (3D energy equation), and thermo-elastic deformations of the rotor and rotor disk (2D Navier–Lamé equations including centrifugal forces and thermal stresses). When the proposed design changes are applied, the model predicts reduced thermal bending, marked improvements in load capacity as well as decreased temperatures. The load capacity increase ranges up to 43% for an optimized design when compared against a standard symmetric design. Also, the sensitivity of different design parameters is discussed in detail. The suggested disk design changes may be applied to a broad variety of rotor-bearing systems. However, the design has to be tailored to the specific and individual machine operating conditions.

1. Introduction

Hydrodynamic thrust bearings are a very popular and widely used machine part that supports axial loads in various machines. Depending on the application, expected relative speeds and loads, thermal and environmental conditions or the available space, different lubricants are eligible for the bearings. Possible lubricants comprise gases such as air or CO₂ [1,2]. Gas bearings can again be divided into compliant [3–9] and rigid [10–12] bearing types. Other possible lubricating fluids are water [13,14] or oil [15,16]. The oil-lubricated hydrodynamic thrust bearing can be used in various applications such as turbochargers, gearboxes, generators, etc. [17,18]. In this manuscript, air foil bearings are considered. However, the main findings are applicable to other thrust bearing types in a similar manner.

For all of the aforementioned bearings, a thrust disk on the rotor is necessary in order to act as a counterpart for the bearing surface. Due to

the rotational speed of the rotor disk with respect to the stationary bearing and the wedge-shape of the resulting lubricating gap, hydrodynamic pressure is generated that can carry thrust loads acting upon the rotor. Fig. 1 shows a typical high-speed rotor-bearing assembly comprising a rotor with a rotor shaft, a rotor disk, a compressor wheel and two journal bearings (green) as well as a dual-sided thrust bearing (base plate in blue, bearing foils not shown). The air film (red) separates the rotor disk and the top foil of the thrust bearing. The structure of the air foil thrust bearing is described in detail in Section 3. In typical applications of air bearings, the high rotational speeds of the rotor cause high gas temperatures through dissipation in the lubricating gap. The resulting heat fluxes into the surrounding components are mainly directed into the bearing itself and into the runner disk. While the heat entering the bearing is usually noncritical for bearing operation and can be faced with active or passive cooling, the heat fluxes entering

* Corresponding author.

E-mail address: eickhoff@ad.tu-darmstadt.de (M. Eickhoff).

<https://doi.org/10.1016/j.triboint.2024.109632>

Received 2 November 2023; Received in revised form 18 March 2024; Accepted 31 March 2024

Available online 1 April 2024

0301-679X/© 2024 The Authors. Published by Elsevier Ltd. This is an open access article under the CC BY license (<http://creativecommons.org/licenses/by/4.0/>).

Nomenclature

Δ	Laplace operator.
∇	Nabla operator.
B	Bending stiffness in shell theory in N/m^2 .
c	Penalty stiffness in contact formulation in N/m^2 .
c_p	Heat capacity of air film in $J/(kg K)$.
$c_{p,air}$	Heat capacity of air in $J/(kg K)$.
$c_{p,C}$	Heat capacity of flow on disk backside in $J/(kg K)$.
D	Stretching stiffness in shell theory in N/m^2 .
E	Young's modulus in shell equations in N/m^2 .
E_R	Young's modulus of the rotor material in N/m^2 .
F_n	Normal contact force in N.
F_t	Tangential contact force in N.
Gt	Shear stiffness in shell theory in N/m^2 .
H	Air film height in m.
H_0	Initial taper-land air film height in m.
H_{min}	Minimal air film height in m.
k_S	Shear correction factor in shell theory (unitless).
n	Rotational speed in rpm.
\vec{n}	Normal vector.
p	Air film pressure in Pa.
p_0	Ambient pressure in Pa.
p^1	External load in shell theory in N/m^2 .
p^2	External load in shell theory in N/m^2 .
p^3	External load in shell theory in N/m^2 .
p_T^3	External axial load on top foil in N/m^2 .
$q_{T,in}$	Heat flux into the top foil from the air film in W.
$q_{T,out}$	Heat flux from the top foil into the understructure in W.
r	Radial coordinate in m.
R	Radius of curvature in shell theory in m.
R_{air}	Specific gas constant of air in $J/(kg K)$.
r_D	Outer radius of rotor disk in m.
R_{th}	Thermal resistance between top foil and base plate (bump resistance) in W/K .
step	Regularized step function for contact formulation.
t	Shell thickness in m.
T	Air film temperature in K.
T_0	Ambient temperature in K.
T_1	Hot test temperature in K.
T_2	Cold test temperature in K.
t_B	Bump foil thickness in m.
T_{base}	Base plate temperature in K.
T_C	Temperature of the flow on disk backside in K.
t_{init}	Initial radial gap thickness in m.
T_m	Height-averaged air film temperature in K.
T_R	Temperature of the rotor shaft and disk in K.

T_{ref}	Reference temperature in K.
t_{RG}	Radial gap thickness in K.
T_{RG}	Temperature of the radial air gap in K.
t_T	Top foil thickness in m.
T_T	Top foil temperature in K.
u	Air film velocity in x -direction in m/s.
U	x -component of disk velocity in m/s.
u_C	Radial velocity of flow on disk backside in m/s.
v	Air film velocity in y -direction in m/s.
V	y -component of disk velocity in m/s.
v_1	Shell deformation in x -direction in m.
v_2	Shell deformation in y -direction in m.
v_3	Shell deformation in z -direction in m.
$v_{3,B}$	Axial bump foil deformation in m.
$v_{3,T}$	Axial top foil deformation in m.
v_C	Circumferential velocity of flow on disk backside in m/s.
v_r	Radial deformation of the rotor in m.
v_z	Axial deformation of the rotor in m.
w_1	Angular shell deformation.
w_2	Angular shell deformation.
w_C	Axial velocity of flow on disk backside in m/s.
x	Cartesian coordinate.
x_{land}	Location of taper-land transition in m.
y	Cartesian coordinate.
z	Axial coordinate.
\bar{z}	Scaled axial coordinate of air film.
z_R	Axial rotor position in m.
α_R	Thermal expansion coefficient of the rotor material in K^{-1} .
γ_R	Lamé constant of the rotor in N/m^2 .
ΔT	Temperature difference for thermal bending example in K.
ΔT_R	Temperature difference of the rotor in K.
Δv_3	Penetration depth, relative normal displacement of contact partners in m.
Δv_{tan}	Relative tangential displacement of contact partners in m.
ϵ_R	Thermo-elastic constant for rotor deformations in Pa/K .
η	Viscosity of air film in $Pa \cdot s$.
η_{air}	Viscosity of air in $Pa \cdot s$.
η_{RG}	Viscosity of air in radial gap in $Pa \cdot s$.
λ	Thermal conductivity of air film in $Pa \cdot s$.
λ_{air}	Thermal conductivity of air in $W/(m K)$.
$\lambda_{C,eff}$	Effective thermal conductivity of flow on disk backside in $W/(m K)$.
λ_R	Thermal conductivity of rotor material in $W/(m K)$.
λ_{RG}	Thermal conductivity of air in radial gap in $W/(m K)$.

the runner disk cause an axial temperature gradient which in turn causes thermoelastic bending of the runner disk directed away from the bearing. This bending changes the shape of the lubricating gap and

reduces the load capacity of the bearing, which can lead to even higher temperatures and machine failure (thermal runaway).

The thermal bending effect has been described for hydrodynamic oil bearings by ROBINSON and CAMERON [19]. They present a three-part study on the theory and experiments regarding thrust bearing distortion

λ_T	Thermal conductivity of top foil material in W/(m K).
μ	Coefficient of friction in contact formulation.
μ_R	Shear modulus of the rotor in N/m ² .
ν	Poisson's ratio in shell equations.
ν_C	Kinematic viscosity of flow on disk backside in m ² /s.
ν_{CT}	Turbulent kinematic viscosity of flow on disk backside in m ² /s.
ν_R	Poisson's ratio of the rotor material.
ρ_C	Density of flow on disk backside in kg/m ³ .
ρ_R	Density of the rotor material in kg/m ³ .
Ω	Angular velocity of the rotor in rad/s.

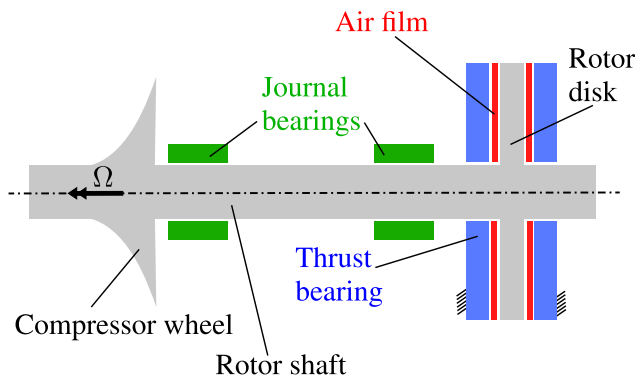


Fig. 1. Cut-view of an exemplary rotor-bearing assembly.

lubrication, stating that the thermal bending of the collar (rotor disk) is a result of the axial temperature gradient.

With regard to foil thrust bearings, it should be stressed that pioneering and comprehensive work on the behavior of foil journal and thrust bearings has been carried out by researchers from NASA and the Case Western Reserve University in the 2000s and the following years [20–28]. Thermal bending of the rotor disk has been highlighted in DYKAS et al. [23] and DYKAS [24]. It is explained that the thermal modeling of thrust bearings is highly important as the thermal distortions of the runner disk may significantly influence the gas film height inside the bearing.

In [24], DYKAS also presents specific recommendations and examples of alternative runner disk designs, mostly aimed at the improvement of heat transfer from the disk towards the surrounding. He even mentions the possibility of runner disk designs aiming at the reduction of thermally-induced convexity (thermal bending). The designs stated there are not usable in a dual-sided bearing as they possess a non-flat backside.

Several other authors have contributed to the improvement of the analysis of gas (foil) thrust bearings [5,20]. The significance of the thermal bending effect has been analyzed further by LEHN [6] and recently by XIONG et al. [29].

Fig. 2 illustrates the thermal bending which is directed away from the hot, loaded bearing side.

There is an established way to reduce the thermal bending effect which consists of an active cooling of the thrust bearing. However, an active cooling—typically guided underneath the top foil—poses an additional expenditure in power, the need for cooling channels and cooling air supply and results in a decrease in machine efficiency.

The main new contributions of this work are:

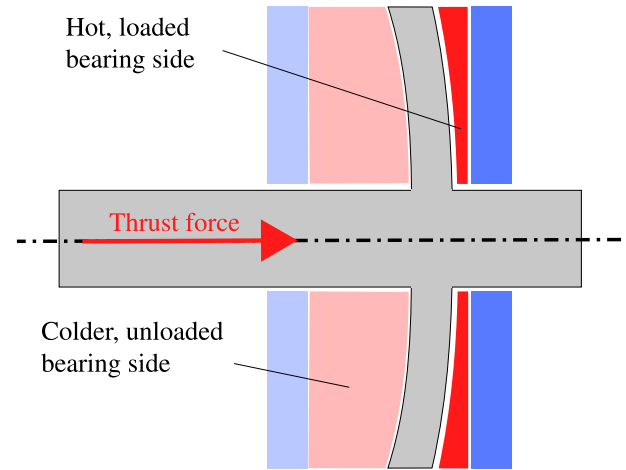


Fig. 2. Thermal bending of the rotor disk (exaggerated) directed away from the hot bearing side resulting from the supported thrust force.

- Compensation approaches for the commonly observed thermal bending phenomenon of the rotor disk in thrust bearings are presented using passive effects without additional expenditure of energy.
- The main idea is to make use of centrifugal forces that generate a bending moment in the rotor disk that causes a deformation counteracting the thermal bending effect. Different measures can be considered in order to generate a compensating effect.
 - Using asymmetric rotor disk mass distributions causing a bending moment through centrifugal forces, see Fig. 3. The resulting centrifugal force does not act along the rotor disk centerline depicted by the dotted line, therefore causing a bending moment for the rotor disk.
 - Applying recesses or asymmetrically placed radii or notches at the base of the rotor disk causing a bending moment through centrifugal forces.
 - Implementing isolation layers or cuts to reduce the axial temperature gradient and reduce thermal bending.
 - Utilizing different materials (with different densities or thermal expansion properties) for dual-material rotor disks and making use of centrifugal and thermal expansion effects.
- A fully coupled air foil thrust bearing finite element (FE) model is presented incorporating a standard rotor disk geometry S as well as a new proposed optimized design O in order to compensate the thermal bending of the rotor disk.
- Detailed results of the fully coupled thermo-elasto-hydrodynamic (TEHD) thrust bearing model including pressure distributions, height functions and rotor temperatures at high rotational speeds and loads are presented.
- A direct comparison is drawn between the standard design S and different optimized designs. Temperatures, deformations, thrust loads and power losses are shown in order to evaluate the benefit of the proposed design changes.
- The impact of changes in single design parameters is investigated and a second optimization step for maximum load capacity of the bearing is presented.

While the focus of this work lies on the improvement of gas bearings, it should be mentioned that oil thrust bearings possess a very similar design when compared to gas bearings. Researchers report runner disk distortions in oil bearing applications as well which may influence their performance [30,31]. However, due to the higher viscosity of oil and the resulting smaller runner disk diameters as well as the different heat

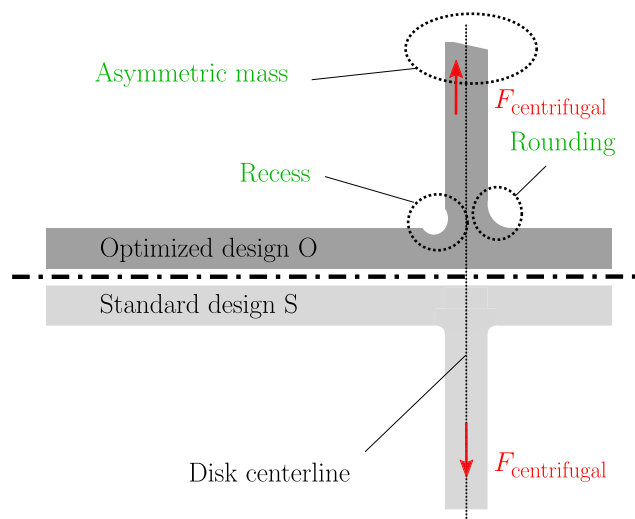


Fig. 3. Comparison of the optimized rotor disk design O (top half) including an asymmetric mass distribution as well as a combination of a recess and a rounding at the base of the disk vs. the standard symmetric design S (bottom half).

transfer mechanisms, it is expected that the impact of the proposed approaches is most significant in air bearing applications.

Moreover, it should be emphasized that the current study is a purely numerical analysis of the effect of runner disk design changes for thrust bearing performance. The presented results have not yet been validated by test rig measurements. The development of the necessary test rig setup and validation of the results in this paper may be accomplished in future works. The detailed multiphysical TEHD finite element model presented here has been validated in previous works for different bearing designs [6,8,9]. Therefore, the presented numerical study with a modified runner disk design should give a reasonable insight in the qualitative and quantitative impact of the design changes for the overall bearing performance.

This paper is organized as follows: Section 2 gives insight into the different approaches for compensating the thermal bending effect. Section 3 presents the detailed TEHD model for the air foil thrust bearing and the rotor. Section 4 shows results of stationary numerical analyses of the rotor-bearing system including a comparison of a standard rotor disk design S and optimized design variants incorporating the aforementioned compensation approaches. The paper is concluded in Section 5.

2. Technical solution approach

This article presents straightforward measures for passively compensating thermal bending of the rotor disk in hydrodynamic thrust bearings [32]. Fig. 4 depicts the different measures that are considered here. Thermal bending is the result of an axial temperature gradient in the rotor disk that develops during operation (hot air film on the loaded bearing side, colder surrounding air on the opposite side, see Fig. 2). This thermal bending is directed away from the loaded bearing and reduces load capacity by causing increasing film heights towards the outer radius, leading to an uneven load distribution. The design changes of the runner disk that are proposed here introduce a positive second bending deformation that compensates the negative and unwanted thermal bending deformation. Fundamentally, centrifugal forces caused by the rotation of the runner disk are exploited to cause disk bending in the direction opposite to the thermal bending. The following list explains different measures to generate centrifugal-induced disk bending as displayed in Fig. 4.

- **A:** The rotor disk possesses an asymmetric design with mass overhangs or bulges on a single disk side. The resulting asymmetric mass distribution leads to an offset between the center of mass of the disk and the disk centerline. In this configuration, centrifugal forces cause a bending moment on the disk, resulting in a bending deformation directed towards the loaded bearing side.
- **B:** When the rotor disk possesses two different radii at its base at the connection to the rotor shaft or a single notch, the strains resulting from centrifugal stresses are different on the two disk sides, resulting in a bending deformation of the rotor disk. This effect can also be achieved by applying recesses or undercuts.
- **C:** The rotor disk possesses a cut in its center. The resulting gap is either filled with air or with an additional isolating layer. This reduces the axial heat flow and favors radial heat flow, leading to a reduced axial temperature gradient. Consequently, the thermal bending deformations of the rotor disk are reduced.
- **D:** The rotor disk is designed as a two-part disk with two different materials. Due to differences in the densities of the materials, the resulting centrifugal force is again offset from the disk centerline. Alternatively, the different coefficients of thermal expansion of the two materials can be exploited to cause a favorable bending deformation when the rotor disk temperature is increased during operation.

Based on a detailed parametric optimization study with the TEHD bearing model of Section 3, an optimized new design O has been developed, comprising a combination of the effects A and B (effects C and D are not considered further). Fig. 3 (above) displays the prototype design of the optimized disk which is—in Section 4—used for a comparison with the standard design S. The presented optimized design O is based on simple manufacturing steps, allowing for fast and cost-efficient production. The optimized design O features an asymmetric mass distribution of the rotor disk that is achieved by applying a chamfer to one side of the rotor disk at the outer disk radius. Additionally, a specific layout of a recess at the base of the disk on one side and a rounding on the other side is used, see Fig. 6. For comparison, the standard, traditional rotor disk design S with simple symmetric roundings, displayed in the bottom half of Fig. 3 is used.

It should be mentioned that the shafts depicted in the sketches are solid. For weight saving and for multi-part shaft designs, hollow shafts are also frequently applied. The shaft design (solid or hollow) does not markedly influence the solution approaches given in this section and the optimization results of Section 4. The calculations in Section 4 have been carried out with hollow shafts, depicted in Fig. 3.

It should be noted that the applicability of the proposed design changes might be limited:

- Concerning the generation of asymmetric mass distributions by a mass overhang as in approach A, the designer might be limited by housing or overall machine dimensions. For the slight increase in outer diameter of the rotor disk, the housing has to possess additional space. However, the required additional space is only in the order of millimeters, cf. Section 4.2.
- Furthermore, it should be stressed that the shafts in this study are assumed to be manufactured as a single part. In practice, multi-part shaft designs are also frequently applied. For multi-part shafts, the recess feature approach of approach B may not be applicable in the same way as for single-part shaft designs.
- Another very important aspect of the proposed approaches is the increase in stresses for the rotor material if approach B is applied (recess feature). The designer has to include the geometry changes in the design stage in order to account for stress concentrations in the rotor, which are mainly caused by the application of recesses or notches. Please note that the designs shown in this work do not cause critical stress values.

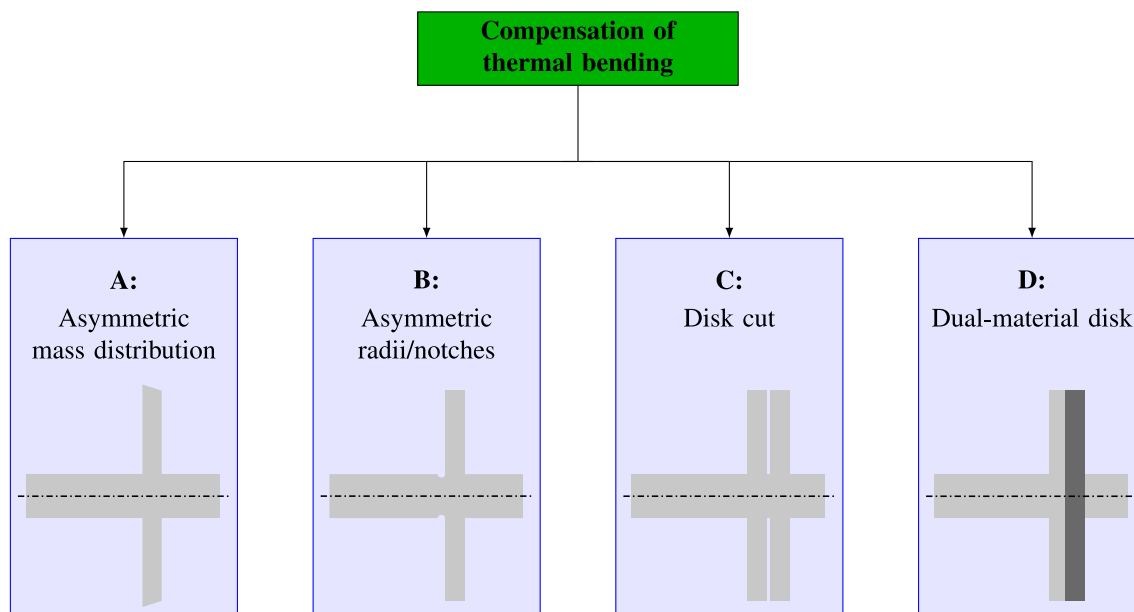


Fig. 4. Different technical approaches for compensating thermal bending.

Pre-study: Explanation of the basic compensation mechanism

This section is dedicated to the description of the extent of the thermal bending effect and the proposed compensating design approaches. For this purpose, three simplified models have been set up in order to illustrate and quantify thermal bending deformations and the compensation mechanism:

- 1 The first model investigates the thermal bending deformations of the symmetric rotor disk design S at standstill. This is achieved by imposing different temperatures to the two sides of the runner disk. The results are displayed in Fig. 5(a).
- 2 The second model investigates the bending deformations of the alternative runner disk designs RD1, RD2, and RD3 with different mass overhangs. In this model, no temperature difference is imposed to the runner disk. The results are displayed in Fig. 5(b).
- 3 The third model investigates the bending deformations of the optimized runner disk design O for three different rotational speeds. Again, no temperature difference is imposed to the runner disk which means that no thermal bending is observed with this model. The results are displayed in Fig. 5(c).

Fig. 5(a) shows the first test case where the thermo-elastic deformations caused by an axial temperature gradient of the runner disk are calculated for a symmetric disk design S at standstill ($n = 0$ rpm). A high temperature T_1 is imposed to the bottom edge of the runner disk which is located at the loaded bearing side of the rotor-bearing assembly (red line). This line represents the interface between the runner disk and the hot air film. The top edge refers to the cooler, unloaded bearing side with the colder temperature T_2 (blue line). All remaining boundaries of the rotor disk are assumed to be adiabatic. The imposed temperature difference $\Delta T = T_1 - T_2$ causes an axial temperature gradient and consequently thermal bending deformations of the runner disk. Details on the thermo-elastic model of the runner disk are found in Section 3.1. Note that this model only accounts for thermo-elastic deformations of the rotor at $n = 0$ rpm. With the help of this rather simple model, the disk deformations for various temperature differences can be analyzed. Fig. 5(a) displays the resulting thermal bending deformations for temperature differences of up to 40 K evaluated at the interface between the rotor disk and the air film (red line in Fig. 5(a)). The thermal bending causes the rotor disk to deform away from the loaded bearing side by up to 25 μm at the outer disk radius for $\Delta T = 40$ K. It should be stressed

that the axial temperature gradient in a real machine application is not known a priori so that estimating thermal bending deformations without a detailed full bearing model is not feasible.

Through the alteration of the classical symmetric rotor disk design S of Fig. 3 in test case 2, the rotor disk deforms due to centrifugal effects when it is rotating. In order to illustrate the impact of the suggested geometry changes, Fig. 5(b) shows the deformation of modified runner disks for three different mass overhangs (outer radius $r_D = 31, 32, 33$ mm) which represent different mass overhangs. The resulting deformation lines can be observed on the right side of Fig. 5(b). Note that these designs are later called RD1, RD2, and RD3 in Section 4.2, respectively. All calculations were carried out at the maximum rotational speed of $n = 120$ krpm. The disk deformation is directed towards the thrust bearing surface with a progressive slope towards the outer diameter. Of course, the larger mass overhangs produce larger disk deformations. For an outer radius of $r_D = 33$ mm, the disk deflects up to 30 μm at the outer radius. It will be explained in the later sections of this manuscript that—among all proposed design changes—the mass overhang has the most significant impact for compensating thermal bending deformations of the runner disk.

As for test case 3, Fig. 5(c) shows the resulting deformation of the runner disk of the optimized design O at the interface to the air film for different rotational speeds. For increasing rotational speeds, the resulting disk deformations increase nonlinearly. The shape of the deformation lines is again showing increasing slopes towards the outer radius of the runner disk as in Fig. 5(b).

It is easy to imagine that a combination of the unwanted thermal bending deformations with these opposite centrifugal deformations of the runner disk may improve the shape of the lubricating gap height towards a more uniform shape. It should also be mentioned that the increase of these deformations with speed is rather convenient as the thermal bending deformations are also increasing with higher temperatures (connected to higher speeds) and are of a very similar—but opposite—shape. This is the reason why the rotor disk design changes may be used to compensate thermal bending deformations passively.

However, it is highly important that these countermeasures or compensation approaches are tailored to the actual bearing application. It is evident from Figs. 5(b) and 5(c) that the centrifugal deformations might even exceed thermal bending deformations if the design changes are not made with caution. An improper use of these design changes

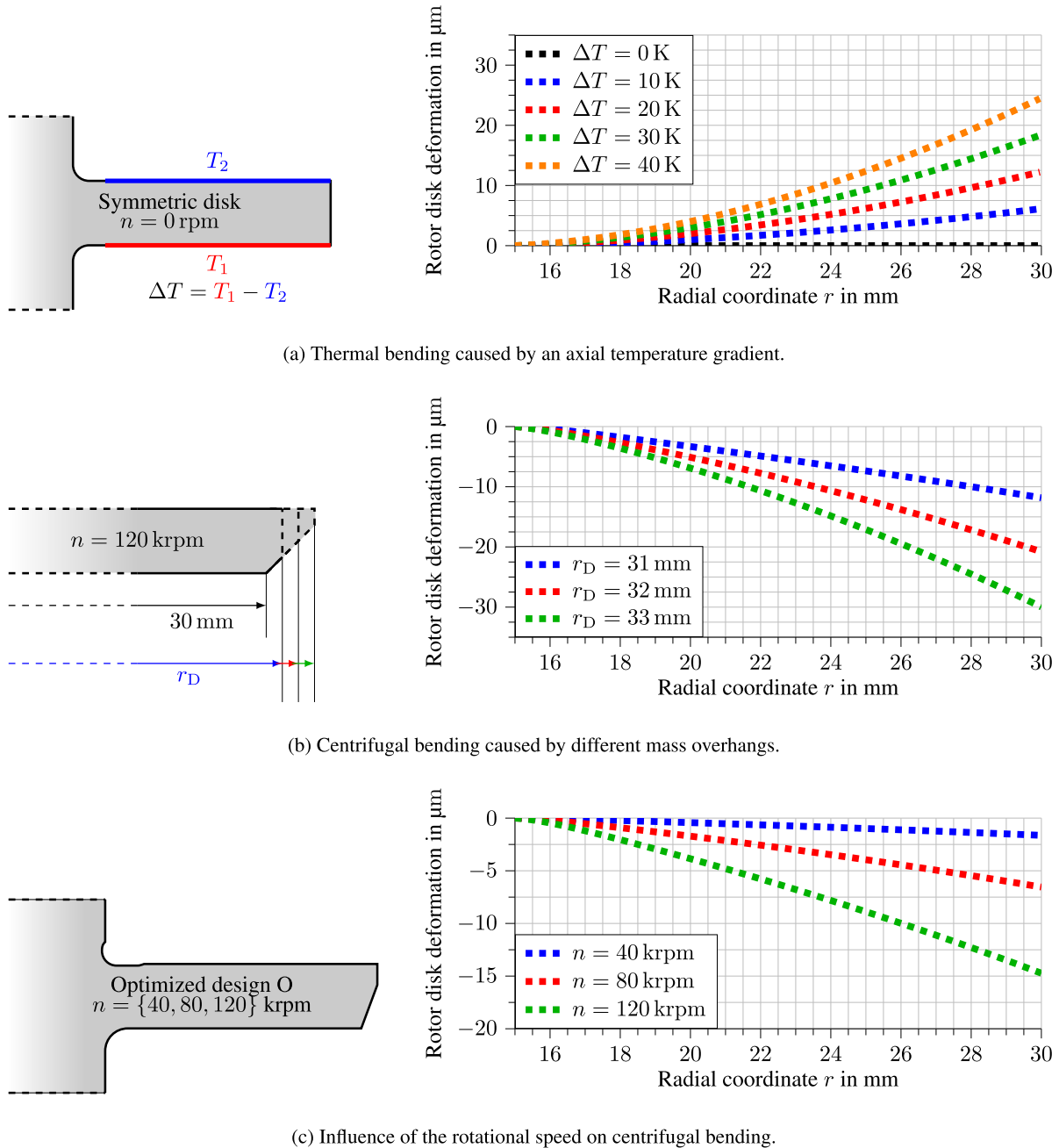


Fig. 5. Rotor disk bending mechanisms.

might even lead to a significant decrease in bearing as well as overall machine performance.

In order to adequately, i.e. qualitatively and quantitatively, present the impact on the performance of a representative bearing, the application of the design approaches in an air foil thrust bearing assembly is considered in this paper. Although the expected rotation-induced bending of the rotor disk due to centrifugal effects can be predicted with the help of a much more basic model (cf. Fig. 5), the consequences for the bearing performance can only be quantified with a detailed investigation.

3. Numerical model

This section describes the numerical model used to analyze the foil thrust bearing assembly with the standard (S) and the newly optimized (O) rotor disk design. Although the proposed design changes of the

runner disk may be analyzed by a simple (thermo)-mechanical model of the rotor, the significance of these alterations for bearing and machine performance is showcased with the application in a foil thrust bearing assembly. A fully coupled, multiphysical finite element model is used to investigate the thermo-elastic, hydrodynamic and thermodynamic behavior of the various bearing components. In typical applications, a dual-sided bearing guarantees that axial loads in both directions can be carried, e.g. in shock loading scenarios, cf. Fig. 1. Frequently, turbomachines possess one main thrust direction in which loads have to be supported by the thrust bearing. This means that dual-sided bearings usually have a highly loaded and less loaded side. For the present study, the numerical analysis focuses on stationary investigations of the loaded bearing side in order to compare the plain standard rotor disk design S with one of the featured optimized designs of this article. Details on the modeling of the secondary less loaded side of the rotor disk are given in Section 3.1.

Subsequently, the individual bearing components and their modeling are described here. Section 3.1 describes the thermo-elastic and thermodynamic behavior of the rotor shaft and the rotor disk which is the focus of the presented design modification. Section 3.2 describes the governing shell equations for top and bump foils as well as the modeling approaches for the foil temperatures and the heat flow through the foil sandwich. Section 3.3 displays the Reynold's equation and the energy equation for the calculation of air pressure and air temperature. Moreover, the boundary conditions and the coupling of the various bearing components and governing equations is described. In Section 3.4, important numerical details of the solution process and the solver strategy are presented.

3.1. Rotor shaft and disk

The thermo-elastic behavior of the rotor shaft and disk is analyzed by coupled equations for the rotor disk deformations v_r and v_z and the rotor temperature T_R . Changes of temperature and deformations are calculated with a rotationally symmetric model [6]. Thus, the temperature and the deformations are a function of the radial coordinate r and the axial coordinate z only, i.e. $T_R = T_R(r, z)$. The radial deformation is denoted by $v_r(r, z)$ and the axial deformation analogously $v_z(r, z)$.

Deformations are calculated using the Navier-Lamé equations [33, 34]:

$$\begin{aligned} \mu_R \left(\nabla^2 v_r - \frac{v_r}{r^2} \right) + (\gamma_R + \mu_R) \frac{\partial}{\partial r} \left(\frac{1}{r} \frac{\partial}{\partial r} (r v_r) + \frac{\partial v_z}{\partial z} \right) \\ - \epsilon_R \frac{\partial \Delta T_R}{\partial r} = -\rho_R r \Omega^2, \\ \mu_R \nabla^2 v_z + (\gamma_R + \mu_R) \frac{\partial}{\partial z} \left(\frac{1}{r} \frac{\partial}{\partial r} (r v_r) + \frac{\partial v_z}{\partial z} \right) \\ - \epsilon_R \frac{\partial \Delta T_R}{\partial r} = 0 \end{aligned} \quad (1)$$

with the density of the rotor material $\rho_R = 8200 \text{ kg/m}^3$, the angular velocity $\Omega = \frac{2\pi n}{60}$, and the temperature difference $\Delta T_R = T_R - T_{\text{ref}}$ of the rotor temperature to a reference temperature $T_{\text{ref}} = T_0 = 20^\circ\text{C}$. Eq. (1) contains the constants

$$\begin{aligned} \gamma_R &= \frac{E_R \nu_R}{(1 + \nu_R)(1 - 2\nu_R)}, \\ \mu_R &= \frac{E_R}{2(1 + \nu_R)}, \\ \epsilon_R &= \frac{E_R \alpha_R}{1 - 2\nu_R}. \end{aligned} \quad (2)$$

Herein, $E_R = 210 \text{ GPa}$ is Young's modulus, $\nu_R = 0.3$ is Poisson's ratio and $\alpha_R = 13 \times 10^{-6} \text{ K}^{-1}$ is the thermal expansion coefficient of the rotor material. The first two constants in Eq. (2) are the Lamé constant γ_R and the shear modulus μ_R . The third constant ϵ_R describes thermo-elastic stresses.

The only external force in Eq. (1) is the centrifugal force in radial direction, while gravity and the impact of the fluid pressure as well as shear forces from the air film can be neglected. Fig. 6 depicts the rotor domain of the optimized design O including the most important geometrical dimensions and the mechanical boundary conditions. The depicted design is the result of a parametric optimization study and possesses an asymmetric mass distribution as well as a combination of a recess and a rounding at the disk base, see Section 2. The rotors investigated in this paper are hollow (inner radius 2.7 mm). All boundaries are assumed to be stress-free. The centrifugal force is implemented as a body force, see Eq. (1). It should be mentioned that the standard rotor disk design S is symmetric ($r_D = 30 \text{ mm}$, symmetric roundings with radius 1.4 mm, see Fig. 11(a)).

For the calculation of the rotor temperature T_R , the following heat conduction equation is solved:

$$\frac{\partial}{\partial r} \left[\lambda_R r \frac{\partial T_R}{\partial r} \right] + \frac{\partial}{\partial z} \left[\lambda_R r \frac{\partial T_R}{\partial z} \right] = 0. \quad (3)$$

The thermal conductivity of the rotor material is $\lambda_R = 12 \text{ W/(m K)}$. The rotor boundary is subdivided into 8 different sections a–h (see Fig. 7). The following list describes the corresponding boundary conditions for these sections:

- **Boundary a:** At this interface, the remaining rotor is cut off. It is assumed that only a small portion of the heat entering the rotor shaft passes this interface. Therefore, this boundary is assumed to be adiabatic.
- **Boundary b:** Due to the low tangential velocities of the rotor on this boundary and the small size, this boundary is assumed to be adiabatic, i.e. diffusive and convective heat transfer is neglected.
- **Boundary c:** This boundary represents the interface to the lubricating air gap. This gap's thickness is in the order of microns when a thrust load is applied to the rotor (negative z -direction in Fig. 7). Due to high shear velocities, dissipative heating causes a heat flux into the surrounding components, one of which being the rotor disk at the interface boundary c. Details on the calculation of the air temperature in the lubricating gap can be found in Section 3.3. The rotor temperature T_R is coupled to the lubricating air gap temperature T via a Dirichlet and a Neumann boundary condition, meaning that the interface temperatures and heat fluxes are equal.
- **Boundary d:** The temperature $T_{RG}(r, z)$ of the air in the radial gap between rotor boundary d and the stationary housing is calculated by the energy equation

$$\begin{aligned} \frac{\partial}{\partial r} \left[\lambda_{RG} r \frac{\partial T_{RG}}{\partial r} \right] + \frac{\partial}{\partial z} \left[\lambda_{RG} r \frac{\partial T_{RG}}{\partial z} \right] \\ = -r \eta_{RG} \left[\frac{\Omega r_D}{t_{RG}} \right]^2. \end{aligned} \quad (4)$$

As the properties of air are temperature-dependent [35], the thermal conductivity λ_{RG} is a function of the radial air gap temperature T_{RG} , i.e. $\lambda_{RG} = \lambda_{\text{air}}(T_{RG})$ with

$$\begin{aligned} \lambda_{\text{air}}(T) &= \left[-2.1 \times 10^{-8} \left(\frac{T}{[\text{K}]} \right)^2 \right. \\ &\quad + 8.46 \times 10^{-5} \left(\frac{T}{[\text{K}]} \right) \\ &\quad \left. + 2.89 \times 10^{-3} \right] [\text{W}/(\text{m K})]. \end{aligned} \quad (5)$$

Analogously, the viscosity η_{RG} is defined as $\eta_{RG} = \eta_{\text{air}}(T_{RG})$ with

$$\begin{aligned} \eta_{\text{air}}(T) &= \left[-1.75 \times 10^{-11} \left(\frac{T}{[\text{K}]} \right)^2 \right. \\ &\quad + 5.68 \times 10^{-8} \left(\frac{T}{[\text{K}]} \right) \\ &\quad \left. + 3.06 \times 10^{-6} \right] [\text{kg}/(\text{ms})]. \end{aligned} \quad (6)$$

Furthermore, $r_D = 31 \text{ mm}$ is the outer disk radius and t_{RG} is the thickness of the radial gap between the outer disk radius and the housing. Due to the radial deformation of the rotor disk v_r , the gap height decreases during operation.

The formulation of the energy equation (4) is based on the assumption that the flow in this air volume is a laminar circumferential Couette flow with a linear velocity profile over the gap radius. Dissipative heating in the radial gap is included on the right-hand side of Eq. (4). It should be mentioned that the initial radial gap height between the rotor disk and the housing is $200 \mu\text{m}$.

The rotor temperature T_R is coupled to the radial gap temperature T_{RG} with a Dirichlet boundary condition (equal temperature) and a Neumann boundary condition (equal heat flux).

- **Boundary e:** This boundary represents the unloaded backside of the disk. Note again that only a single-sided thrust bearing is used for the numerical analysis. Therefore, a rotation-induced passive airflow is assumed in the volume adjacent to boundary

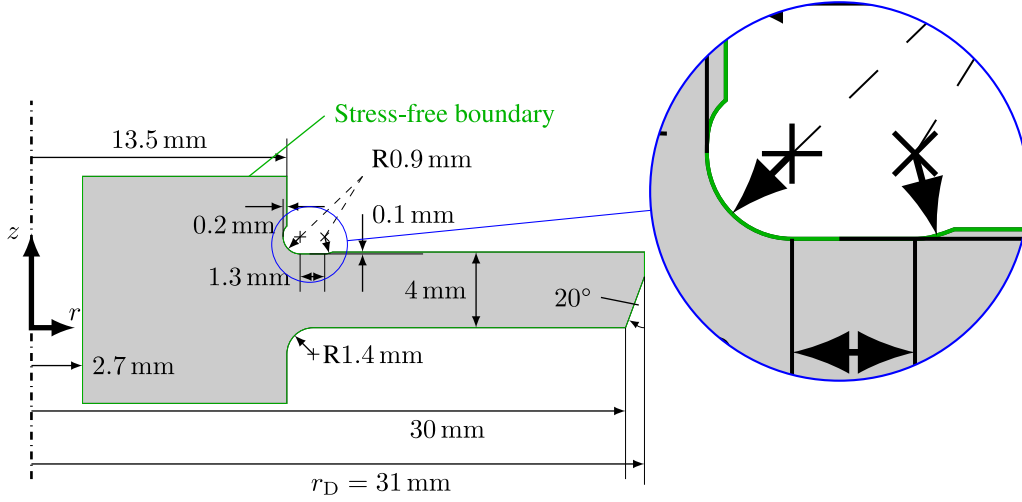


Fig. 6. Rotor domain of the optimized design O with geometric dimensions.

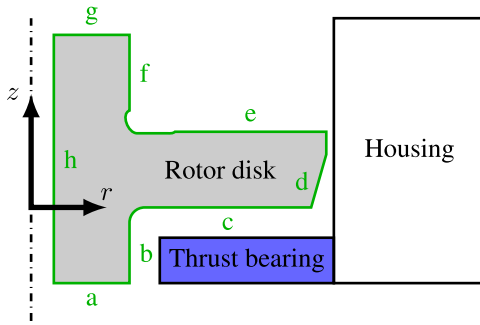


Fig. 7. Thermal boundary conditions of the rotor in the different sections a–h.

e. The airflow is modeled using the boundary layer equations for a steady incompressible axisymmetric flow, while neglecting the radial pressure gradient [36]. The temperature T_C in this volume is calculated via the axisymmetric energy equation

$$\frac{\partial}{\partial z} \left[\lambda_{C,\text{eff}} \frac{\partial T_C}{\partial z} \right] = \rho_C c_{p,C} \left[u_C \frac{\partial T_C}{\partial r} + w_C \frac{\partial T_C}{\partial z} \right] - \rho_C (v_C + v_{CT}) \left[\left(\frac{\partial u_C}{\partial z} \right)^2 + \left(\frac{\partial v_C}{\partial z} \right)^2 \right]. \quad (7)$$

It contains heat conduction with the effective thermal conductivity $\lambda_{C,\text{eff}}$, convective heat transfer with the density ρ_C and the heat capacity $c_{p,C}$ as well as dissipative terms with the kinematic viscosity ν_C and the turbulent kinematic viscosity ν_{CT} , all according to Cebeci and Smith [6,36]. The air velocities are u_C in radial direction, v_C in circumferential direction and w_C in axial direction.

The airflow temperature $T_C(r, z)$ and the rotor temperature T_R are then coupled via a Dirichlet and a Neumann boundary condition, meaning that the interface temperature is equal and that the heat flux leaving the rotor via this boundary enters the airflow volume adjacent to boundary e.

- **Boundary f:** See boundary b.
- **Boundary g:** See boundary a.
- **Boundary h:** This boundary describes the inside of the hollow shaft which is assumed to be adiabatic due to the insulating properties of the air inside the shaft.

3.2. Bearing foils

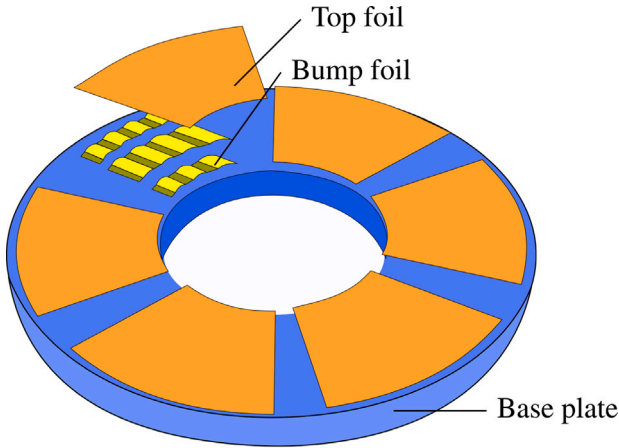
In this section, the mechanical and thermodynamic models of the top and bump foils are described. Fig. 8 displays a foil bearing assembly consisting of a base plate (blue), on which 6 bearing pads are mounted, each consisting of a corrugated bump foil understructure combined with a smooth and coated top foil. The bump foil elastically supports the top foil and also provides a taper-land topology. This is achieved by embossing the bump foil with ascending bump heights in the taper-part of the pad and constant bump heights in the land part of the pad. The location of the transition between taper-region and land-region is located at $x = x_{\text{land}}$.

For this study, it is assumed that there is no misalignment between the rotor disk and the foil thrust bearing. This allows for a reliable comparison of the impact of different rotor disk designs within the numerical model with acceptable simulation times. Several simplifications in the modeling of the thrust bearing can be made when no misalignment is present. Due to symmetry, it is then sufficient to analyze a single bearing pad representative for all bearing pads.

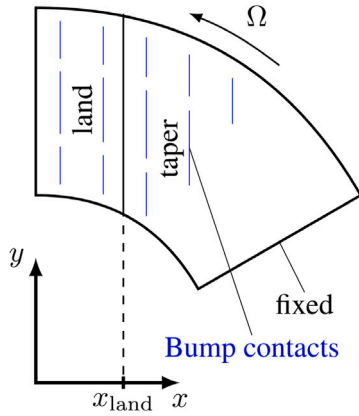
The deformations of the top and bump foil are calculated using a Reissner–Mindlin type shell theory [37,38]. Each shell possesses 5 degrees of freedom (DOFs), namely 3 translational DOFs $v_1(x, y)$, $v_2(x, y)$, and $v_3(x, y)$ in x -, y -, and z -direction, respectively, as well as 2 rotational DOFs denoted by $w_1(x, y)$ and $w_2(x, y)$. Eqs. (8) to (12) are used for the calculation of the deformations of a cylindrical shell with radius of curvature R along the y -direction under the external loads p^1 , p^2 , and p^3 in x -, y -, and z -direction, respectively:

$$\begin{aligned} & \frac{\partial}{\partial x} \left[D \left(\frac{\partial v_1}{\partial x} + v \frac{\partial v_2}{\partial y} + \frac{1}{R} v_3 \right) \right. \\ & \left. + \frac{B}{R} \left(\frac{\partial w_1}{\partial x} + v \frac{\partial w_2}{\partial y} + \frac{1}{R} \frac{\partial v_1}{\partial x} + \frac{1}{R^2} v_3 \right) \right] \\ & + \frac{\partial}{\partial y} \left[D \frac{1-v}{2} \left(\frac{\partial v_2}{\partial x} + v \frac{\partial v_1}{\partial y} \right) \right] \end{aligned} \quad (8)$$

$$\begin{aligned} & + \frac{B}{R} \frac{1-v}{2} \left(\frac{\partial w_2}{\partial x} + v \frac{\partial w_1}{\partial y} + \frac{1}{R} \frac{\partial v_1}{\partial y} \right) \\ & = -\frac{Gt k_S}{R} \left(w_1 + \frac{\partial v_3}{\partial x} - \frac{1}{R} v_1 \right) + p^1, \\ & \frac{\partial}{\partial x} \left[D \frac{1-v}{2} \left(\frac{\partial v_2}{\partial x} + v \frac{\partial v_1}{\partial y} \right) \right] \\ & + \frac{\partial}{\partial y} \left[D \left(\frac{\partial v_2}{\partial y} + v \frac{\partial v_1}{\partial x} + \frac{v}{R} v_3 \right) \right] \\ & = p^2, \end{aligned} \quad (9)$$



(a)



(b)

Fig. 8. (a) Foil thrust bearing with 6 bearing pads with base plate (blue), bump foils (yellow), and top foils (orange). (b) Individual bearing pad with taper-region and land-region.

$$\begin{aligned}
 & \frac{\partial}{\partial x} \left[Gt k_S \left(w_1 + \frac{\partial v_3}{\partial x} + \frac{1}{R} v_1 \right) \right] \\
 & + \frac{\partial}{\partial y} \left[Gt k_S \left(w_2 + \frac{\partial v_3}{\partial y} \right) \right] \\
 & = \frac{D}{R} \left(\frac{\partial v_1}{\partial x} + v \frac{\partial v_2}{\partial y} + \frac{1}{R} v_3 \right) \\
 & + \frac{B}{R} \left(\frac{\partial w_1}{\partial x} + v \frac{\partial w_2}{\partial y} + \frac{1}{R} \frac{\partial v_1}{\partial x} + \frac{1}{R^2} v_3 \right) + p^3,
 \end{aligned} \tag{10}$$

$$\begin{aligned}
 & B \left[\frac{\partial}{\partial x} \left(\frac{\partial w_1}{\partial x} + v \frac{\partial w_2}{\partial y} + \frac{1}{R} \frac{\partial v_1}{\partial x} + \frac{1}{R^2} v_3 \right) \right. \\
 & \left. + \frac{\partial}{\partial y} \left(\frac{1-v}{2} \left(\frac{\partial w_1}{\partial y} + \frac{\partial w_2}{\partial x} + \frac{1}{R} \frac{\partial v_1}{\partial y} \right) \right) \right] \\
 & = Gt k_S \left(w_1 + \frac{\partial v_3}{\partial x} - \frac{1}{R} v_1 \right),
 \end{aligned} \tag{11}$$

$$\begin{aligned}
 & B \left[\frac{\partial}{\partial x} \left(\frac{1-v}{2} \left(\frac{\partial w_1}{\partial y} + \frac{\partial w_2}{\partial x} + \frac{1}{R} \frac{\partial v_1}{\partial y} \right) \right) \right. \\
 & \left. + \frac{\partial}{\partial y} \left(\frac{\partial w_2}{\partial y} + v \frac{\partial w_1}{\partial x} + \frac{v}{R} \frac{\partial v_1}{\partial x} + \frac{v}{R^2} v_3 \right) \right] \\
 & = Gt k_S \left(w_2 + \frac{\partial v_3}{\partial y} \right).
 \end{aligned} \tag{12}$$

Table 1

Foil parameters.

Parameter	Value
Inner top foil radius	15 mm
Outer top foil radius	30 mm
Top foil angle	48°
Number of pads	6
Bump height	500 μm
Number of bump strips	3
Number of bumps	Inner strip: 3 Middle strip: 4 Outer strip: 5
Bump radius	2 mm
Bridge length	0.8 mm
Bump slope	2.9 μm mm ⁻¹

This formulation contains the stretching stiffness $D = \frac{Et}{1-\nu^2}$, the bending stiffness $B = \frac{Et^3}{12(1-\nu^2)}$ and the shear stiffness $Gt = \frac{Et}{2(1+\nu)}$ with Young's modulus $E = 210$ GPa, Poisson's ratio $\nu = 0.3$ and the shell thickness $t = t_B = 75$ μm for the bump foils and $t = t_T = 100$ μm for the top foils. In this study, a shear correction factor of $k_S = \frac{5}{6}$ is used [38]. While the top foil is considered a flat metal sheet with $R \rightarrow \infty$, the bump foil possesses cylindrical bumps (constant radius R) combined with flat bridges ($R \rightarrow \infty$). The most important geometrical parameters are listed in Table 1.

The top foil is fixed at the leading edge, while the remaining boundaries are stress-free. The bump foil is fixed on the edge corresponding to the top foil trailing edge. Loads on the top foil stem from the fluid pressure p (see Section 3.3). Therefore, the external load on the top foil in axial direction can be expressed as

$$p_T^3 = -(p - p_0) \tag{13}$$

with the ambient pressure p_0 . Note that the pressure acts in negative z -direction. Furthermore, contacts between the top foil and the bump foil are considered. The locations of these line-contacts are depicted in Fig. 8(b). For the normal contact forces F_n , a penalty contact formulation is used:

$$F_n = c \Delta v_3. \tag{14}$$

Herein, $c = 1 \times 10^{11}$ N m⁻² is the penalty stiffness and $\Delta v_3 = v_{3,B} - v_{3,T}$ is the local penetration depth between the axial top foil deformation $v_{3,T}$ and the corresponding bump foil deformation $v_{3,B}$. Tangential contact forces F_t are formulated with a generalized Coulomb friction approach [39] with a smoothed step-function $\text{step}(\Delta v_{\text{tan}})$:

$$F_t = \mu \cdot \text{step}(\Delta v_{\text{tan}}) F_n. \tag{15}$$

Δv_{tan} describes the relative tangential displacement of the contact partners and $\mu = 0.1$ is the coefficient of friction. The contacts between the bump foil and the base plate are modeled analogously.

The top foil temperature is denoted by $T_T(x, y)$ and is calculated via the heat diffusion equation

$$-\lambda_T \nabla_T^2 T_T = q_{T,\text{in}} + q_{T,\text{out}} \tag{16}$$

with a constant thermal conductivity $\lambda_T = 12$ W/(m K) for the top foil material. Eq. (16) is a two-dimensional equation in the top foil plane. Heat flow in thickness direction is neglected due to the small thickness of the foil. On its top surface, the top foil adjoins the thin air film described in Section 3.3. The hot air temperatures cause an incoming heat flow $q_{T,\text{in}}$ into the top foil which is described in Eq. (22). At the bottom surface of the top foil, it adjoins the bump foil understructure. For the present study, it is assumed that there is no cooling airflow guided between top foil and base plate which is a common practice for active thrust bearing cooling. Note that the bump height of 500 μm means that the air gap between base plate and top foil can be seen as an

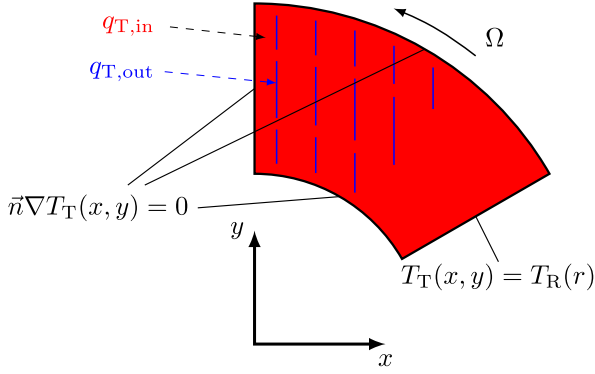


Fig. 9. Thermal boundary conditions for the top foil energy equation (16).

insulator. Therefore, only the heat flux passing the bump foil is taken into account in the outgoing heat flux $q_{T,out}$. The heat transfer between top foil and bump foil, the heat flow through the bumps as well as the heat transfer between bump foil and the base plate is modeled via thermal resistances [40]. The resulting thermal resistance R_{th} for one half arc is then used to formulate the heat flux from the top foil into the base plate,

$$q_{T,out} = -\frac{2(T_T - T_{base})}{R_{th}}, \quad (17)$$

where $T_{base} = 20^\circ\text{C}$ denotes the prescribed base plate temperature. Fig. 9 depicts the thermal boundary conditions and the incoming and outgoing heat fluxes. Note that the incoming heat flux $q_{T,in}$ is enforced over the entire top foil domain while the outgoing heat flux $q_{T,out}$ is only applied to the contact lines of top and bump foil. As each of these lines contacts two half arcs of the bump foil, the thermal resistance R_{th} in Eq. (17) is halved (heat flux is doubled). For the top foil boundaries, adiabatic conditions are applied except for the leading edge. Here, it is assumed that the top foil temperature is equal to the rotor temperature. This assumption is based on calculations for the heat transfer between the rotor disk and the air gap between two pads, which are not discussed here. These calculations show that the air enters each pad with a temperature very close to the rotor disk temperature, cf. [40].

3.3. Air film

The lubricating air film develops between the thrust bearing pads and the rotor disk. For the air film temperature $T(x, y, z)$, a 3D energy equation is solved [41]:

$$\rho c_p \left[u \frac{\partial T}{\partial x} + v \frac{\partial T}{\partial y} \right] = \frac{\partial}{\partial z} \left(\lambda \frac{\partial T}{\partial z} \right) + \left[u \frac{\partial p}{\partial x} + v \frac{\partial p}{\partial y} \right] + \eta \left[\left(\frac{\partial u}{\partial z} \right)^2 + \left(\frac{\partial v}{\partial z} \right)^2 \right]. \quad (18)$$

It should be mentioned that the energy equation (18) is solved on a scaled air film domain with the new coordinate $\bar{z} = 1 + \frac{z}{H}$ [6]. This way, the air film gap domain with the gap height H is transformed into a constant domain limited by the top surface at $\bar{z} = 1$ representing the interface to the rotor disk and the bottom surface at $\bar{z} = -1$ representing the interface to the top foil. The transformed domain is shown in Fig. 10.

The air density ρ , the thermal conductivity λ of air, and the air viscosity η are temperature-dependent. While the thermal conductivity and the viscosity are calculated based on the temperature-dependent functions in Eqs. (5) and (20), the density is calculated via the ideal gas law

$$\rho = p/(R_{air}T) \quad (19)$$

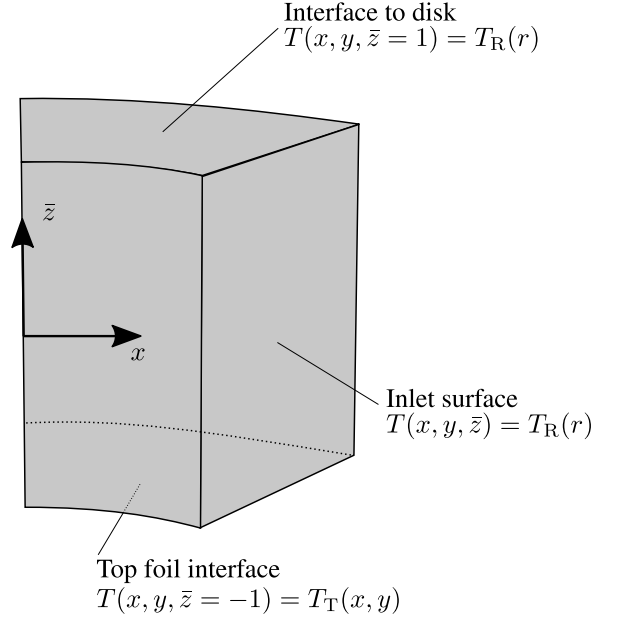


Fig. 10. Scaled air film domain with thermal boundary conditions for the air film temperature T .

with the specific gas constant of air $R_{air} = 287.1\text{J}/(\text{kg K})$. The temperature-dependency of the isochoric heat capacity of air c_p is given as

$$c_p(T) = c_{p,air}(T) = \left[2.43 \times 10^{-4} \left(\frac{T}{[\text{K}]} \right)^2 - 7.7 \times 10^{-2} \left(\frac{T}{[\text{K}]} \right) + 1008 \right] [\text{J}/(\text{kg K})]. \quad (20)$$

The air film velocities $u(x, y, \bar{z})$ in x -direction and $v(x, y, \bar{z})$ in y -direction are defined as in [42]:

$$u = \frac{-H^2}{8\eta} \frac{\partial p}{\partial x} (1 - \bar{z}^2) + \frac{U}{2} (\bar{z} + 1), \quad (21)$$

$$v = \frac{-H^2}{8\eta} \frac{\partial p}{\partial y} (1 - \bar{z}^2) + \frac{V}{2} (\bar{z} + 1).$$

At the boundaries, the air film is coupled with the adjoining domains. At its top surface, the air film temperature T is coupled with the rotor disk temperature T_R via a Dirichlet boundary condition (same temperature) and a Neumann boundary condition (same normal heat flux). In a similar way, the air film is coupled with the top foil at the bottom surface. The heat flux from the air gap into the top foil $q_{T,in}$ in Eq. (16) reads as follows:

$$q_{T,in} = \left(\frac{2\lambda}{H} \frac{\partial T}{\partial \bar{z}} \right) \Big|_{\bar{z}=-1}. \quad (22)$$

It describes the axial (z - or \bar{z} -direction, respectively) heat flux into the top foil at the interface of air film and top foil. As mentioned in Section 3.2, the inlet air temperature is assumed to be equal the rotor disk temperature T_R , cf. Fig. 10.

The generalized compressible Reynolds equation [42] is used for the calculation of the air film pressure $p(x, y)$:

$$\frac{\partial}{\partial x} \left[\frac{\rho(p, T_m) H^3}{12\eta(T_m)} \frac{\partial p}{\partial x} \right] + \frac{\partial}{\partial y} \left[\frac{\rho(p, T_m) H^3}{12\eta(T_m)} \frac{\partial p}{\partial y} \right] = \frac{\partial}{\partial x} \left[\frac{\rho(p, T_m) U H}{2} \right] + \frac{\partial}{\partial y} \left[\frac{\rho(p, T_m) V H}{2} \right]. \quad (23)$$

The air density ρ and the air viscosity η are evaluated at an averaged fluid temperature $T_m(x, y)$ [5]:

$$T_m(x, y) = \frac{1}{2} \int_{-1}^1 T(x, y, \bar{z}) d\bar{z}. \quad (24)$$

The variables U and V describe the velocity of the disk in the Cartesian x - and y -direction:

$$\begin{aligned} U &= -\Omega y, \\ V &= \Omega x. \end{aligned} \quad (25)$$

The height function H is generally of taper-land-topology, but is influenced by the rotor movement z_R , the deformation of the rotor disk v_z and the deformation of the top foil $v_{3,T}$:

$$H(x, y) = H_0 + z_R - v_{3,T}(x, y) + v_z(z = 0, r). \quad (26)$$

H_0 describes the taper-land-topology that is predetermined by the different bump heights, cf. Section 3.2.

3.4. Numerical solution strategy

The equations of Sections 3.1 to 3.3 are discretized using a finite element approach. Generally, second order shape functions for all equations except for the shell equations of Section 3.2 are used. In order to avoid shear locking, fifth-order shape functions are applied here [43]. The complete fully coupled nonlinear model has 488708 DOFs. The damped Newton method is used for solving the system of nonlinear equations (linear direct stationary solver: MUMPS).

The highly nonlinear system of equations requires an advanced solution strategy with regard to the key model parameters, including the use of parameter sweeps and continuation solvers. The most important parameters are the angular velocity Ω and a parameter representing the loading condition of the bearing. The axial rotor position would be a suitable value indicating the current load acting on the thrust bearing. However, for better comparability, the minimal gap height of the air film H_{\min} is used as a reference value instead of the axial rotor position. Each simulation is controlled so that the gap height H reaches a given minimal value H_{\min} so that $\min[H(x, y)] = H_{\min}$ holds. A small minimal gap height corresponds to a high-load scenario, while large minimal gap heights refer to a low-load scenario. Moreover, due to surface roughness and the onset of mixed lubrication, the minimal gap height cannot be reduced arbitrarily. In this manuscript, a limit value of $H_{\min} = H_{\min, \text{limit}} = 2 \mu\text{m}$ is assumed as the transition value between mixed lubrication (bearing damage and wear) and full fluid lubrication (nominal operation). Note that at this minimal gap height value, the thrust load reaches its maximum.

On a desktop PC (Win 10, 64 GB of RAM, Intel Xeon E5 CPU with 12 cores), each simulation including a run-up from low to maximum speed ($n = 120 \text{krpm}$) and a sweep for the minimal gap height takes roughly 4 h.

4. Results

The numerical foil thrust bearing model of Section 3 is used to compare the bearing performance of a standard rotor disk geometry S with different optimized rotor disk design variants. As described in Section 3.4, the minimal gap height H_{\min} is considered to define the different loading scenarios (operating points) for the bearing. In this study, H_{\min} varies between a value of $20 \mu\text{m}$ (low load) down to the limit gap height of $2 \mu\text{m}$ (highest load). The rotational speed is kept constant at $n = 120 \text{krpm}$. In a first step, the standard design S and the optimized design O of Fig. 3 are compared in detail in Section 4.1. In the following sections, different parameter studies are presented.

- The mass overhang is varied in Section 4.2.
- The influence of the recess depth on the bearing performance is investigated in Section 4.3.
- In Section 4.4, the impact of the notch depth at the rotor disk base is described.

With the help of these single-parameter optimizations, Section 4.5 displays a new optimized design O2 with an even higher thrust load capability compared to the optimized design O according to Fig. 3.

It should be mentioned that the optimization of the rotor disk design may lead to an increase in mechanical stresses at the connection between the rotor disk and the shaft if recesses are applied. The optimized designs presented in this paper do not cause the occurring stresses to exceed design limits for the given rotor material and rotational speeds.

4.1. Comparison of the standard (S) and the optimized (O) rotor design

Fig. 11 presents a comparison of the standard design S and the optimized design O with regard to the rotor temperature, rotor deformations and the global bearing performance parameters, namely thrust load and power loss.

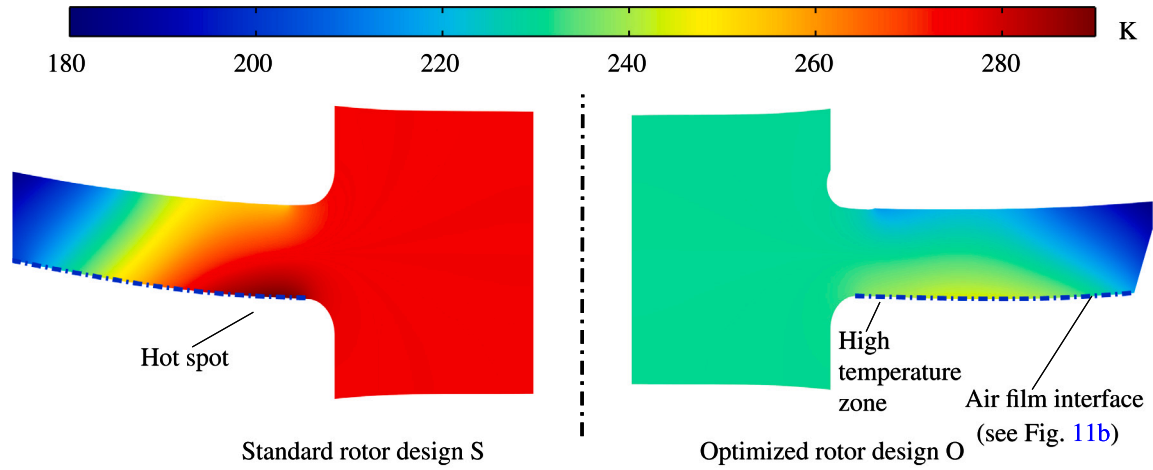
In Fig. 11(a), the rotor temperature is displayed for both designs at a thrust load of 95 N. Short remark on the chosen operating point: The thrust load of 95 N represents the limit thrust load for the standard design S with $H_{\min} = H_{\min, \text{limit}} = 2 \mu\text{m}$. In order to achieve a fair comparison of the two rotor designs, the same thrust force (95 N) is applied to the bearing with the optimized rotor disk design O. This means that the minimal gap height H_{\min} in the simulation of the optimized design O is larger than $2 \mu\text{m}$. Specifically, for a load of 95 N, the minimal gap height is $H_{\min} = 5.3 \mu\text{m}$ for the optimized design O.

The plot also shows the rotor deformations for the standard rotor design S with two symmetric roundings on the left and the optimized rotor design O with a combination of rounding, recess and asymmetric mass distribution on the right. It is obvious that the rotor temperatures for the standard rotor design S are substantially higher than with the optimized design O. This is the case because—at the same thrust load—the corresponding power loss is higher for the standard rotor design S.

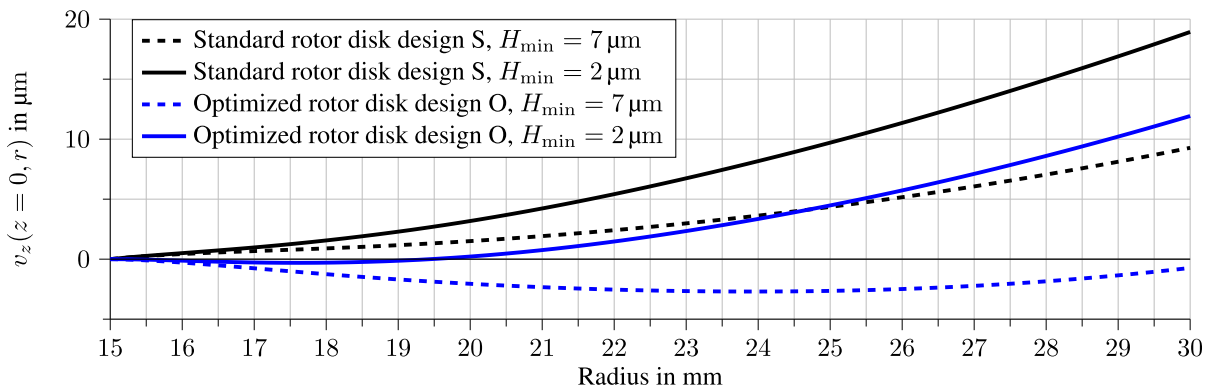
The bending deformation of the rotor disk, evaluated at the air film interface, is shown in Fig. 11(b) for two different operating points, namely $H_{\min} = 7 \mu\text{m}$ and $H_{\min} = 2 \mu\text{m}$. The deformation of the standard rotor disk S has a progressive slope and reaches a maximum value of $9.3 \mu\text{m}$ for $H_{\min} = 7 \mu\text{m}$ and $18.9 \mu\text{m}$ for $H_{\min} = 2 \mu\text{m}$. The deformation of the optimized rotor disk O (blue) is a combination of the thermal bending deformations with the compensating deformations from centrifugal forces, see Section 2. For the highest load configuration at $H_{\min} = 2 \mu\text{m}$, the maximum rotor deformation $v_z(z = 0, r = r_D)$ is reduced by $7 \mu\text{m}$. For the medium load at $H_{\min} = 7 \mu\text{m}$, a large part of the thermal bending is compensated so that only a maximum deformation of $2.7 \mu\text{m}$ remains. It can be concluded that, with the optimized rotor disk design O, the compensating effect is largest for the case $H_{\min} = 7 \mu\text{m}$, while thermal bending deformations are still present for the case $H_{\min} = 2 \mu\text{m}$.

The power loss is plotted over the thrust force for both designs in Fig. 11(c). For this simulation and also for upcoming simulations that investigate different load scenarios of the bearing, the minimal gap height is varied, taking values of $H_{\min} = \{2, 3, 4, 5, 6, 7, 8, 9, 10, 12, 14, 16, 18, 20\} \mu\text{m}$. For a large portion of the range of operation, both graphs are nearly linear. It is worth mentioning that the evaluated operating points for different values of H_{\min} do usually not coincide. However, the ratio of power loss and thrust load is approximately the same in the thrust force region up to 80 N. For higher loads ($>80 \text{N}$), the power loss of the standard design S increases markedly, while the linear behavior continues up to 100 N for the optimized design O. The reason for the higher power loss of the standard design S lies in the sub-optimal gap height function due to significant thermal bending of the rotor disk. This is also visible in the temperature distribution in Fig. 11(a): the standard design S possesses a small hot spot, while the optimized rotor disk O shows a more distributed and extended higher temperature area on its underside. Consequently, the maximum temperature of the optimized rotor disk O is reduced markedly.

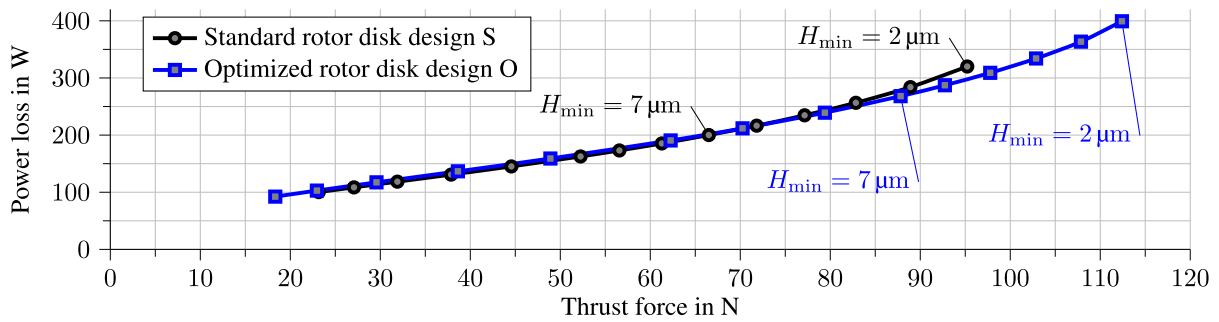
Fig. 12 displays the gap height distribution for the standard design S (a) and the optimized design O (b) at the described operating point



(a) Temperature difference $T_R - T_0$ and deformation v_z (scale factor 100). Left side standard design S (thrust force 95 N, $H_{\min} = H_{\min,limit} = 2 \mu\text{m}$), right side optimized design O (thrust force 95 N, $H_{\min} = 5.3 \mu\text{m}$).



(b) Rotor disk deformation $v_z(z = 0, r)$ at the air film interface for two parameter cases: $H_{\min} = 2 \mu\text{m}$ and $H_{\min} = 7 \mu\text{m}$.



(c) Performance map: Power loss vs. thrust force.

Fig. 11. (a) Rotor disk temperature and deformation for standard (S) and optimized (O) rotor disk configuration, (b) rotor disk deformation on the interface to the air film, and (c) performance map of the two rotor disk designs variants.

with a thrust load of 95 N and a rotational speed of $n = 120 \text{krpm}$. As mentioned before, the minimal gap height for the standard design S reaches $H_{\min} = H_{\min,limit} = 2 \mu\text{m}$ (limit load), while the film height is larger for the optimized design O ($H_{\min} = 5.3 \mu\text{m}$). Additionally, the height distribution is more even along the radial direction, which is a direct result from the reduced thermal bending of the rotor disk. Although the compliant foil bearing can partly adapt to rotor disk deformations and distortions, the effect is still clearly visible. It is worth mentioning that the lowest air film heights are observed at the bump

contacts. This phenomenon is typical for foil thrust bearings as the top foil will sag between the bump supports, leaving elevated areas near the bump contacts (top foil sagging effect). The corresponding pressure distribution for both designs is depicted in Fig. 13. Note again that the thrust load, i.e. the integrated pressure distribution, is the same in both cases. While the pressure distribution with the standard design S possesses high pressure peaks near the trailing edge and a significant pressure drop towards the outer radius, the pressure distribution for the optimized design O is more evenly distributed and does not show very

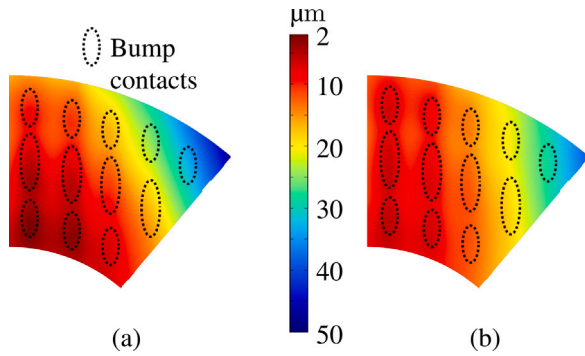


Fig. 12. Gap height function $H(x, y)$ at a load of 95 N: standard rotor design S (a) and optimized rotor design O (b).

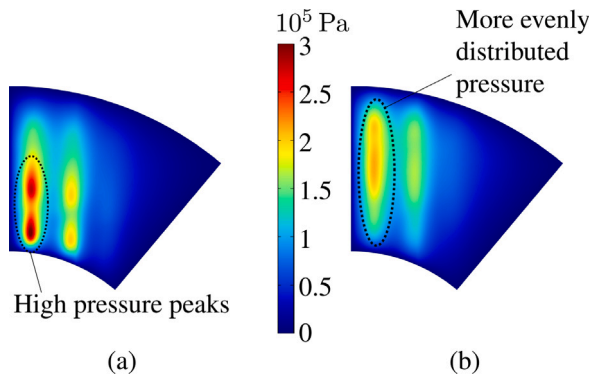


Fig. 13. Pressure distribution $p - p_0$ at a thrust load of 95 N: standard rotor disk design S (a) vs. optimized rotor disk design O (b).

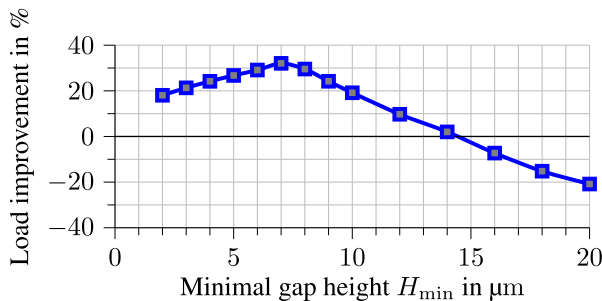


Fig. 14. Thrust load improvement over the minimal gap height H_{min} for the optimized design O vs. the standard design S.

sharp peaks. The lack of pressure buildup near the outer radius for the standard rotor design S stems from the increased gap heights towards the outer radius due to thermal bending, cf. Fig. 12. In both design variants, high pressure areas are observed near the bump contacts as a result of the aforementioned top foil sagging effect.

Although the optimized design O improves the film height distribution and consequently the pressure buildup and the load capacity, the compensation effect due to centrifugal forces is still not fully balancing the thermal bending deformation at the limit load with $H_{min} = 2 \mu\text{m}$, cf. Fig. 11(b). This conclusion is supported by the following analysis: Fig. 14 investigates the thrust load improvement of the optimized design O for different values of the minimal gap height H_{min} . As can be seen, the highest load improvements are in fact found for a minimal gap height of $H_{min} = 7 \mu\text{m}$. For higher and lower values of H_{min} , the improvement is smaller. For very large gap heights and consequently very low loads, even a decline of the load capacity is observed (negative improvement at low loads). It should however be noted that the load

reduction is small in absolute values, as the thrust load is very small for high gap heights. The only consequence in this operating range is a very slight increase in power loss for very low loads (less than 3 W at 23 N).

As can be seen in Fig. 14, it is obvious that a larger compensation effect would further benefit the ultimate load capacity of the thrust bearing. With regard to the diagram in Fig. 14, this would mean a shift of the improvement maximum towards smaller minimal gap heights. The potential of a second optimization step O2 is investigated in Sections 4.3 to 4.5.

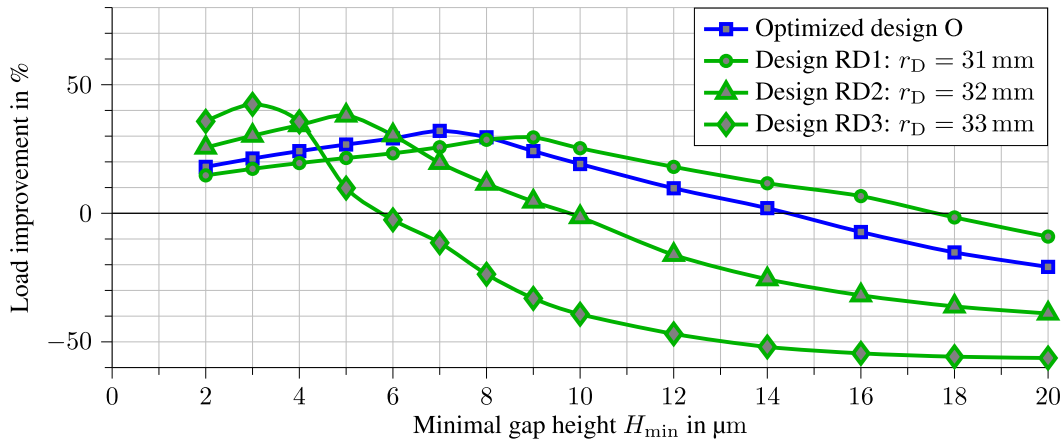
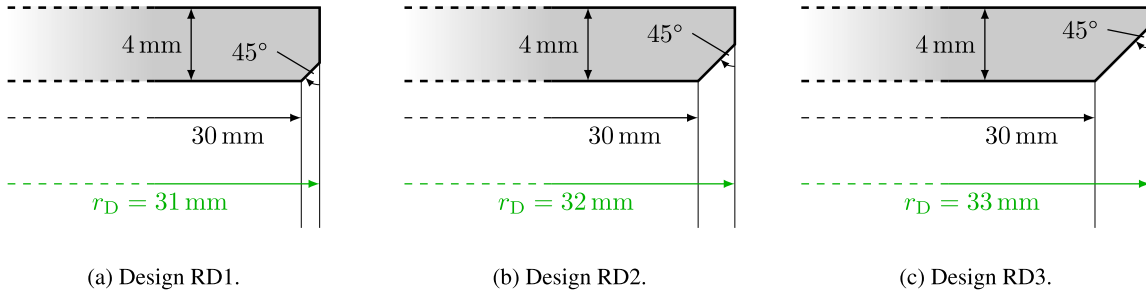
4.2. Influence of the mass overhang

This section studies the influence of the mass overhang at the outer radius of the rotor disk. While the rotor disk of the standard design S possesses a rectangular cross-section, the optimized design O features a 20° chamfer towards the loaded bearing side, cf. Fig. 6. This chamfer causes an offset between the center of mass of the rotor disk and the disk centerline, which in turn leads to a bending moment from the offset centrifugal force, cf. Fig. 3. In order to study the influence of different mass distributions in the rotor disk, three different variants of the optimized rotor disk design O are created. These three design variants are shown in Fig. 15. They only differ from the optimized design O with respect to the disk shape at the outer radius. For this parameter analysis, the chamfer angle has been changed from 20° to 45° . Secondly, the outer disk radius r_D is varied from 31 mm (RD1) over 32 mm (RD2) to 33 mm (RD3). Fig. 15(d) presents the thrust load improvements compared against the standard design S that can be achieved with these different outer disk radii r_D . Evidently, a larger outer radius causes a higher compensating effect due to centrifugal forces. This means that, for increasing disk radii, the highest improvement is achieved at higher loads. This is visible in the maximum of the load improvement curves of the different variants. The maximum points shift towards lower minimal gap heights (higher loads) with increasing outer disk radius. On the other hand, the higher centrifugal deformations of the design variants with a large outer disk radius also cause a slight decline in load capacity for larger minimal gap heights H_{min} , which is—of course—not a practical problem.

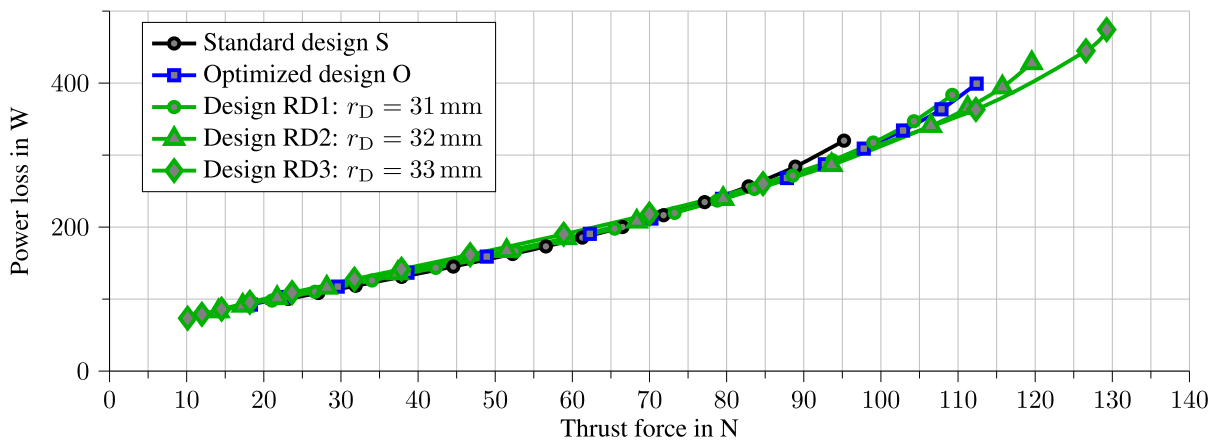
The improvement can also be observed in the corresponding performance map for the three design variants in Fig. 15(e). While the low and medium load region (up to 80 N) is very similar among all designs, a larger outer disk radius can increase the load capacity of the thrust bearing markedly. For an outer radius of $r_D = 33 \text{ mm}$ (design RD3), the load capacity reaches 129 N (for $H_{min} = H_{min,limit} = 2 \mu\text{m}$). It should again be mentioned that this advantage comes at the small cost of slightly increased power losses at low and medium thrust loads.

4.3. Influence of the recess depth

In a similar manner to Section 4.2, this section describes the impact of a deeper recess on the disk backside. For this purpose, the optimized design O of Fig. 6 is again taken as the reference. In two small steps of 0.1 mm, the recess depth is increased to 0.2 mm in the design R1 and to 0.3 mm in the design R2. Due to the centrifugal force, the local strains near the recess are increased. They cause a favorable bending deformation of the disk, which can enhance the compensation of the thermal bending deformation. Fig. 16 displays the three different recess depths that are investigated here. Fig. 16(a) corresponds to the optimized design O of Fig. 6, Fig. 16(b) possesses a deeper recesses with a depth of 0.2 mm, and Fig. 16(c) with a recess depth of 0.3 mm. For larger recess depths, the load capacity is markedly improved when compared against the optimized design O. With a recess depth of 0.3 mm, the optimal compensation effect is achieved at a minimal gap height of $H_{min} = 5 \mu\text{m}$, see Fig. 16(d). This means that the investigated recess depths did not outperform the effect of the mass overhangs in Section 4.2. The deepest recess that has been considered here has a similar impact as the medium rotor disk radius of $r_D = 32 \text{ mm}$. The performance map in Fig. 16(e) also reveals the improvement in thrust load capacity.



(d) Load improvement curves.



(e) Power loss vs. thrust force.

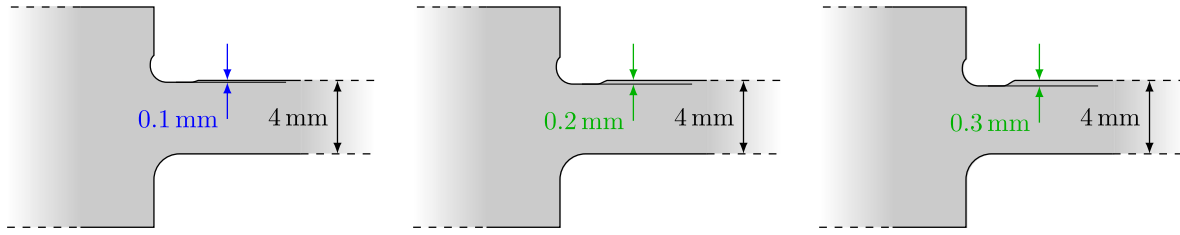
Fig. 15. (a–c) Mass overhang variants with different outer radii r_D , (d) thrust load improvement over the minimal gap height H_{min} for the three designs, and (e) performance map of the design variants with different mass overhangs.

4.4. Influence of the notch depth

Another approach of achieving the beneficial compensation of thermal bending deformations lies in the application of different notch depths at the rotor disk base. This effect has been studied with the three design variants depicted in Figs. 17(a) to 17(c). The first design with a notch depth of 0.2 mm again corresponds to the optimized design O of Fig. 6. In the other two variants, the notch depth is increased to 0.3 mm (N1) and 0.4 mm (N2), respectively. As can be seen in Fig. 17(d) (load improvement curves) and Fig. 17(e) (performance map), the effect of this design parameter is rather small. There is only a slight improvement when compared to the optimized design O.

4.5. Second optimization step

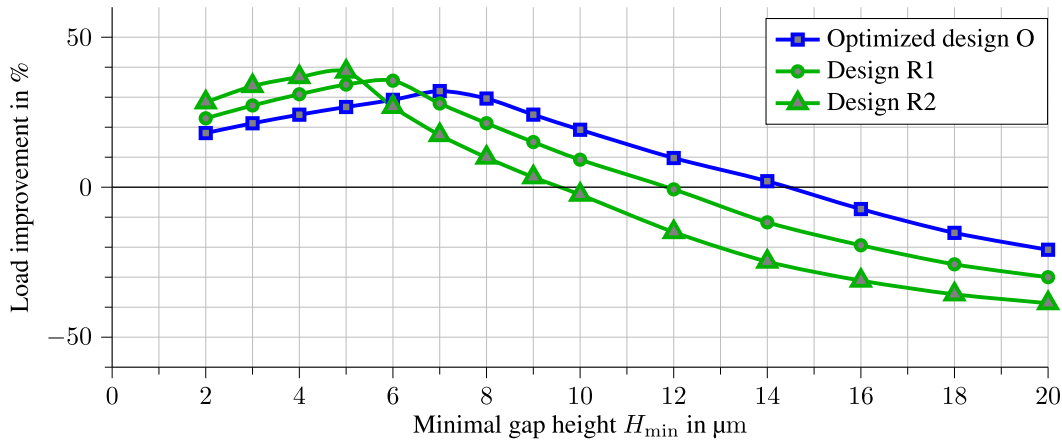
From the previous single-parameter investigations (Sections 4.2 to 4.4) it is obvious that the highest effect can be achieved by applying a mass overhang to the rotor disk. Additionally, a deeper recess also markedly improves the bearing performance. On the other hand, a deeper notch into the rotor disk at the disk base does not show substantial effects. In order to combine these effects and find a design that yields further improvements near the ultimate thrust load (at $H_{min} = H_{min,limit} = 2 \mu m$), this section presents a second optimized design O2, combining the findings of the previous sections. Fig. 18 displays the simulation results for this design. In Fig. 18(a), the second optimized geometry O2 is shown which combines a large mass overhang ($R_D =$



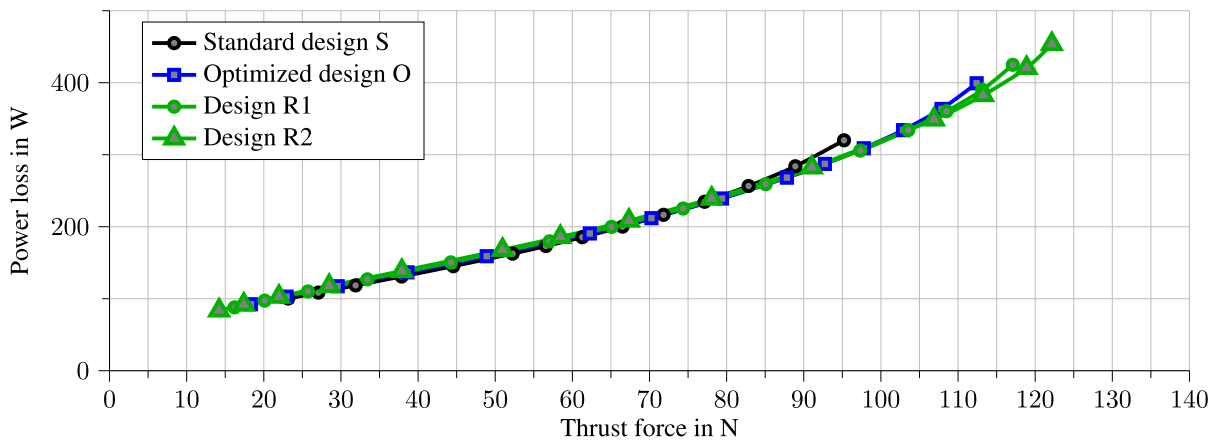
(a) Optimized design O.

(b) Design R1.

(c) Design R2.



(d) Load improvement curves.



(e) Power loss vs. thrust force.

Fig. 16. (a) Optimized design O, (b-c) recess depth variants R1 and R2, (d) thrust load improvement over the minimal gap height H_{min} for the three designs vs. the standard design S, and (e) performance map of the design variants.

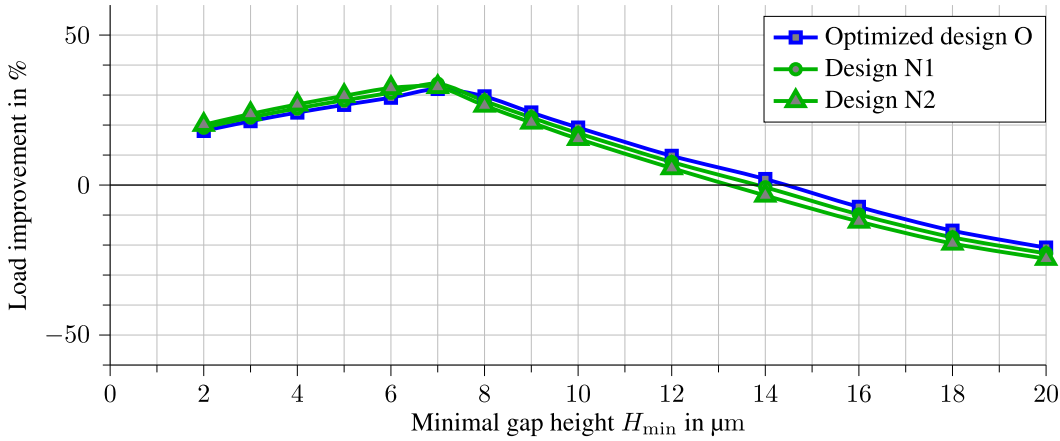
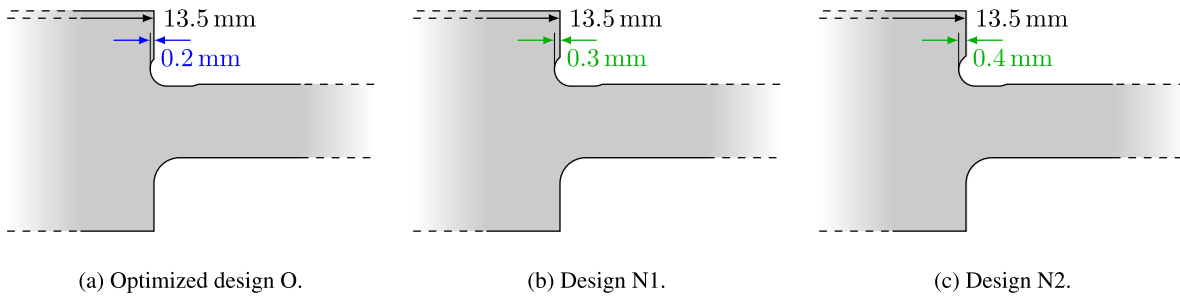
33 mm) with a deep recess (0.26 mm) and the standard notch depth (0.2 mm). With this design, a very high load capacity of approximately 136 N can be achieved, which is equal to a 43% increase compared to the standard rotor disk design S. The corresponding load improvement curve in Fig. 18(b) has its maximum very close to the limit gap height of $H_{min} = H_{min,limit} = 2 \mu\text{m}$, meaning that the compensating effect of the asymmetric rotor disk design is optimal near the limit load.

The performance map of Fig. 18(c) also shows a marked improvement in load capacity when comparing the second optimized design O2 with the previous optimized design O of Fig. 6 and with the standard design S. While the second optimized design O2 of Fig. 18(a) reveals a very little increase in power loss for low loads, a significant increase of

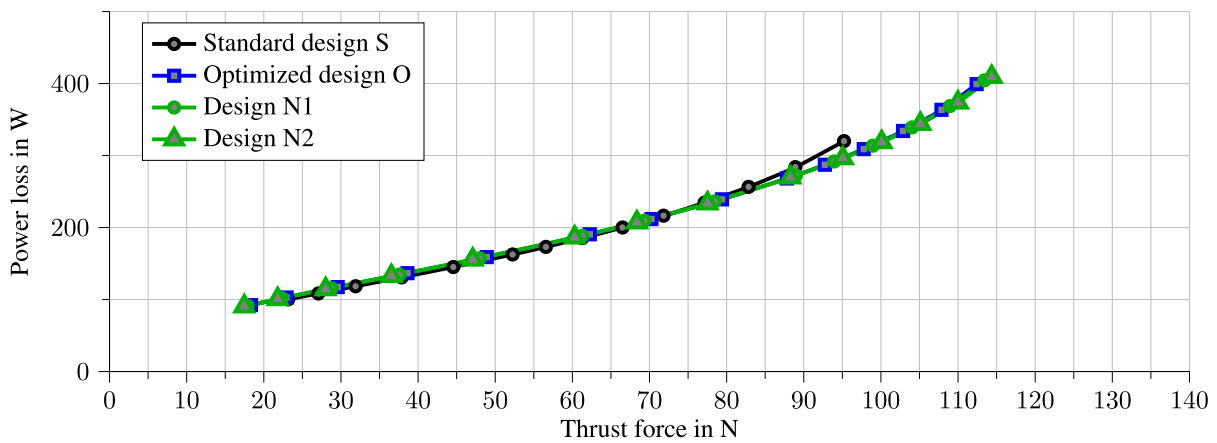
the load capacity by 24 N in comparison to the optimized design O of Fig. 6 and 41 N with regard to the standard design S is achieved.

5. Conclusions

In this paper, a simple and cost-efficient method for the performance improvement of hydrodynamic thrust bearings has been presented. Thermal bending of the rotor disk is a result of an axial temperature gradient that is caused by dissipation in the fluid film. This bending deformation diminishes the film thickness distribution and reduces the



(d) Load improvement curves.



(e) Power loss vs. thrust force.

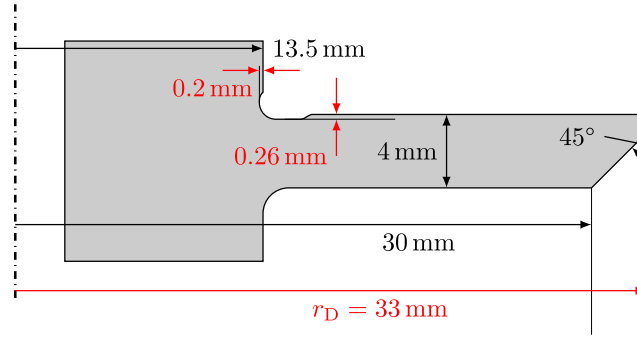
Fig. 17. (a) Optimized design O, (b-c) notch depth variants N1 and N2, (d) thrust load improvement over the minimal gap height H_{min} for the three designs vs. the standard design S, and (e) performance map of the design variants.

load capacity. The distorted disk causes increased gap heights near the outer radius of the bearing. This reduces the pressure buildup and the thrust load. The thermal bending phenomenon is very prominent in air thrust bearings and thus critical for safe bearing and machine operation. Therefore, the focus of this study has been the analysis of an air foil thrust bearing with optimized rotor disk geometries.

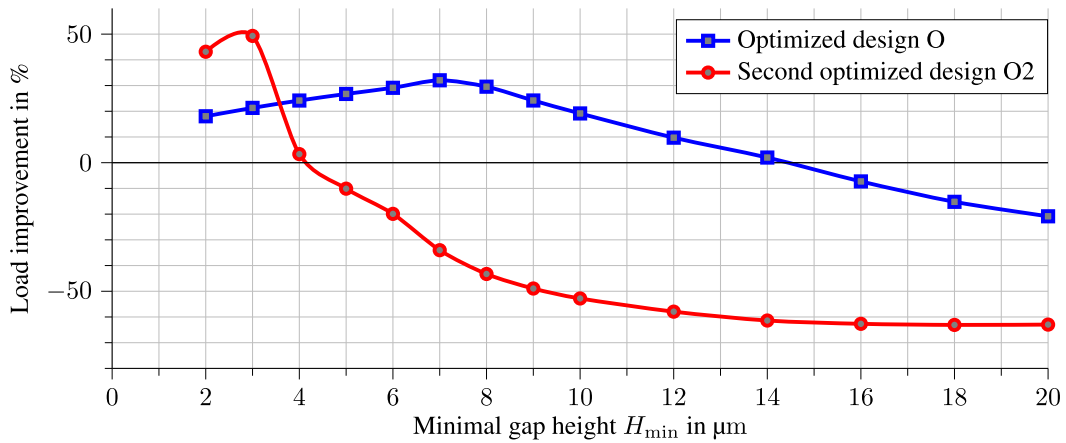
By small changes in the rotor disk design, centrifugal forces can be exploited to cause a second kind of bending deformation that counteracts and compensate the unwanted thermal bending. These design changes comprise asymmetric mass distributions as well as

small roundings and recesses at the disk base which are inexpensive modifications that are easy to apply.

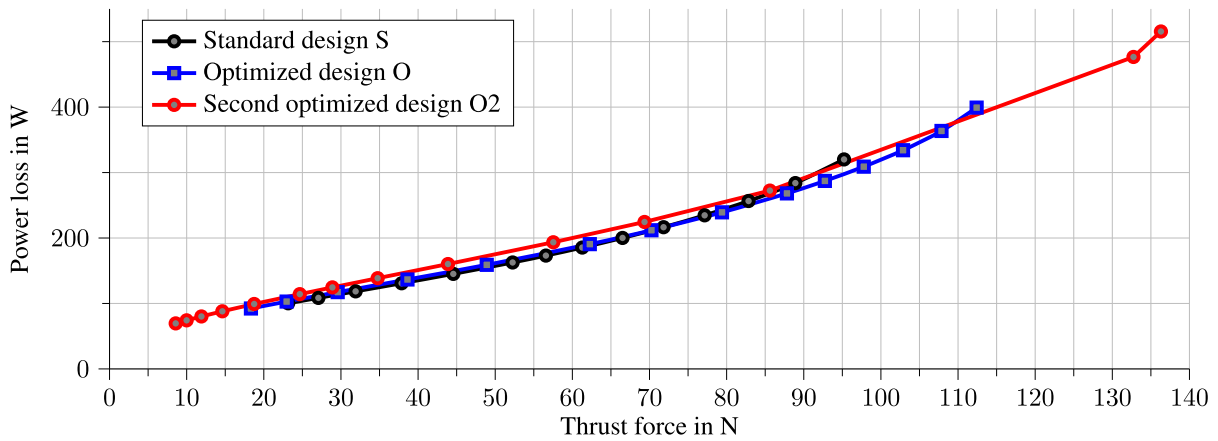
With the help of a detailed multiphysical TEHD thrust bearing model, an optimized rotor disk design has been identified. The optimization parameters were mainly focused on the mass overhang at the outer disk radius and the recess at the disk base. The final optimized design shows a marked improve in load capacity of up to 40%. With the help of an elaborate and complex multi-parameter optimization, further improvements may be achieved. The compensating effect is of course only influencing a single bearing side. Therefore, this improvement can



(a) Second optimized design O2.



(b) Load improvement curves.



(c) Power loss vs. thrust force.

Fig. 18. (a) Second optimized design O2, (b) thrust load improvement over the minimal gap height H_{min} , and (c) performance map of the standard (S), the optimized (O, cf. Fig. 6) and the second optimized design (O2).

be applied in machine designs with a main thrust direction. For thrust bearings that have to support similar loads in both axial directions, the proposed design adaptations are unsuitable.

Additionally, it should be mentioned that the proposed design changes are limited by the admissible stresses of the rotor material or the available space in a machine housing. Especially the mentioned

recess features may cause a stress concentration near the shoulder of the runner disk.

The presented modifications of the rotor disk show a promising behavior for an improved bearing performance. While this study focuses on the application in air foil thrust bearings, the method can also be applied to oil thrust bearings with the same proposed measures.

CRediT authorship contribution statement

Markus Eickhoff: Investigation, Methodology, Project administration, Resources, Software, Supervision, Validation, Visualization, Writing – original draft, Writing – review & editing, Conceptualization, Data curation, Formal analysis. **Johannis Triebwasser:** Conceptualization, Data curation, Investigation, Software. **Andre Theile:** Conceptualization, Data curation, Investigation, Software. **Bernhard Schweizer:** Conceptualization, Investigation, Methodology, Project administration, Supervision, Writing – original draft, Writing – review & editing.

Declaration of competing interest

The authors declare that they have no known competing financial interests or personal relationships that could have appeared to influence the work reported in this paper.

Data availability

The authors are unable or have chosen not to specify which data has been used.

References

- [1] Conboy T. Real-gas effects in foil thrust bearings operating in the turbulent regime. *J Tribol* 2013;135(3).
- [2] Qin K, Jahn IH, Jacobs PA. Effect of operating conditions on the elastohydrodynamic performance of foil thrust bearings for supercritical CO₂ cycles. *J Eng Gas Turbines Power* 2017;139(4):042505.
- [3] Agrawal GL. Foil air/gas bearing technology—an overview. *Turbo Expo: Power Land Sea Air* 1997;78682:V001T04A006.
- [4] Iordanoff I. Analysis of an aerodynamic compliant foil thrust bearing: Method for a rapid design. *J Tribol* 1999;121(4). 816–822.
- [5] Lee D, Kim D. Three-dimensional thermohydrodynamic analyses of Rayleigh step air foil thrust bearing with radially arranged bump foils. *Tribol Trans* 2011;54(3). 432–448.
- [6] Lehn A. Air foil thrust bearings: A thermo-elasto-hydrodynamic analysis (Ph.D. thesis), Technische Universität Darmstadt; 2017.
- [7] LaTray NT, Kim D. A high speed test rig capable of running at 190,000 rpm to characterize gas foil thrust bearings. *Turbo Expo: Power Land Sea Air* 2018;51142:V07BT34A043.
- [8] Eickhoff M, Theile A, Mayer M, Schweizer B. Analysis of air foil thrust bearings with annular top foil including wear prediction, part I: Modeling and simulation. *Tribol Int* 2023;181:108174.
- [9] Theile A, Eickhoff M, Foerster F, Schweizer B. Analysis of air foil thrust bearings with annular top foil including wear prediction, part II: Experimental investigations. *Tribol Int* 2023;188:108742.
- [10] Yue Y, Stolarski T. Numerical prediction of the performance of gas-lubricated spiral groove thrust bearings. *Proc Inst Mech Eng J* 1997;211(2). 117–128.
- [11] Wong CW, Zhang X, Jacobson SA, Epstein AH. A self-acting gas thrust bearing for high-speed microrotors. *J Microelectromech Syst* 2004;13(2). 158–164.
- [12] Schiffmann J, Favrat D. Integrated design and optimization of gas bearing supported rotors. *J Mech Des* 2010;132(5):051007.
- [13] San Andrés L, Phillips S, Childs D. A water-lubricated hybrid thrust bearing: measurements and predictions of static load performance. *J Eng Gas Turbines Power* 2017;139(2):022506.
- [14] Lin X, Jiang S, Zhang C, Liu X. Thermohydrodynamic analysis of high speed water-lubricated spiral groove thrust bearing considering effects of cavitation, inertia and turbulence. *Tribol Int* 2018;119. 645–658.
- [15] Frene J, Nicolas D, Degueurce B, Berthe D, Godet M. Hydrodynamic lubrication: bearings and thrust bearings. Elsevier; 1997.
- [16] Glavatskih SB, Fillon M, Larsson R. The significance of oil thermal properties on the performance of a tilting-pad thrust bearing. *J Tribol* 2002;124(2). 377–385.
- [17] Zhou J, Blair B, Argires J, Pitsch D. Experimental performance study of a high speed oil lubricated polymer thrust bearing. *Lubricants* 2015;3(1). 3–13.
- [18] Chambers WS, Mikula AM. Operational data for a large vertical thrust bearing in a pumped storage application. *STLE Trans* 1988;31(1). 61–65.
- [19] Robinson C, Cameron A. Studies in hydrodynamic thrust bearings I. Theory considering thermal and elastic distortions. *Philos Trans R Soc Lond Ser A Math Phys Eng Sci* 1975;278(1283). 351–366.
- [20] Bruckner RJ. Simulation and modeling of the hydrodynamic, thermal, and structural behavior of foil thrust bearings. Case Western Reserve University; 2004.
- [21] Bauman S. An oil-free thrust foil bearing facility design, calibration, and operation. In: 58th annual meeting, no. NASA/TM-2005-213568. 2005.
- [22] Bruckner RJ, DellaCorte C, Prah J. Analytic modeling of the hydrodynamic, thermal, and structural behavior of foil thrust bearings. In: 2005 annual meeting and exhibition, 60th society of tribologists and lubrication engineers, no. NASA/TM-2005-213811. 2005.
- [23] Dykas B, Prah J, DellaCorte C, Bruckner R. Thermal management phenomena in foil gas thrust bearings. In: *Turbo expo: power for land, sea, and air*, vol. 42401, 2006, 1417–1423.
- [24] Dykas BD. Factors influencing the performance of foil gas thrust bearings for oil-free turbomachinery applications (Ph.D. thesis), Case Western Reserve University; 2006.
- [25] DellaCorte C, Radil KC, Bruckner RJ, Howard SA. Design, fabrication, and performance of open source generation I and II compliant hydrodynamic gas foil bearings. *Tribol Trans* 2008;51(3). 254–264.
- [26] Dykas B, Bruckner R, DellaCorte C, Edmonds B, Prah J. Design, fabrication, and performance of foil gas thrust bearings for microturbomachinery applications. *J Eng Gas Turbines Power* 2009;131(1).
- [27] Dickman JR. An investigation of gas foil thrust bearing performance and its influencing factors (Ph.D. thesis), Case Western Reserve University; 2010.
- [28] Bruckner RJ. Performance of simple gas foil thrust bearings in air. In: *Supercritical CO₂ power cycle symposium*, no. E-18016. 2012.
- [29] Xiong C, Xu B, Yu H, Huang Z, Chen Z. A thermo-elastic-hydrodynamic model for air foil thrust bearings considering thermal seizure and failure analyses. *Tribol Int* 2023;183:108373.
- [30] Ahmed S, Fillon M, Maspeyrot P. Influence of pad and runner mechanical deformations on the performance of a hydrodynamic fixed geometry thrust bearing. *Proc Inst Mech Eng J* 2010;224(4). 305–315.
- [31] Karadere G. The effects of the total bearing deformation on the performance of hydrodynamic thrust bearings. *Ind Lubr Tribol* 2010;62(4). 207–213.
- [32] Theile A, Eickhoff M, Triebwasser J. Rotor mit Rotorscheibe, Strömungsmaschine mit Rotor sowie Verfahren zum Betreiben einer Strömungsmaschine. Patent DE10 2022 120 067.1 2024.
- [33] Noda N, Hetnarski RB, Tanigawa Y. Thermal stresses. Taylor & Francis; 2003.
- [34] Sadd MH. Elasticity: Theory, applications, and numerics. Elsevier; 2005.
- [35] Baehr HD, Stephan K. Heat and mass transfer. Heidelberg: Springer Berlin; 2011.
- [36] Cebeci T, Smith A. Analysis of turbulent boundary layers. New York: Academic Press; 1974.
- [37] Reissner E. The effect of transverse shear deformation on the bending of elastic plates. *J Appl Mech* 1945;12. 69–77.
- [38] Başar Y, Krätzig WB. Mechanik der Flächentragwerke: Theorie, Berechnungsmethoden, Anwendungsbeispiele, 1st ed. Grundlagen der Ingenieurwissenschaften, Wiesbaden: Vieweg+Teubner Verlag; 1985.
- [39] Wriggers P. Computational contact mechanics. 2nd ed.. Berlin: Springer; 2006.
- [40] Lehn A, Mahner M, Schweizer B. A contribution to the thermal modeling of bump type air foil bearings: Analysis of the thermal resistance of bump foils. *J Tribol* 2017;139(6).
- [41] Lee D, Kim D. Thermohydrodynamic analyses of bump air foil bearings with detailed thermal model of foil structures and rotor. *J Tribol* 2010;132(2).
- [42] Dowson D. A generalized Reynolds equation for fluid-film lubrication. *Int J Mech Sci* 1962;4(2). 159–170.
- [43] Zienkiewicz OC, Taylor RL, Zhu JZ. The finite element method: its basis and fundamentals. Elsevier; 2005.